A Study of the Observational and Data Analysis Techniques of Extragalactic Supernova Remnants: The Case of the Sculptor Group Galaxy NGC 300

Thesis submitted by
William Charles MILLAR, M.A.
in May 2012

for the degree of Doctor of Philosophy
in the Centre for Astronomy
James Cook University

Statement of Sources:

I declare that this thesis is my own work and has not been submitted in any form for another degree or diploma at any university or other institution of tertiary education. Information derived from the published or unpublished work of others has been acknowledged in the text and a list of references given.

This thesis contains material originally published in the journal *Astrophysics and Space Sciences* (Millar et al., 2011) and used here with permission from Springer-Verlag Publishing, license #2796170023827.

This thesis contains material originally published in the *Serbian Astronomical Journal* (Millar et al., 2012) and is used here with copyrights retained.

Contributors:

The following people made contributions to this thesis:

Name	Chapter(s)	Contribution(s)	Signature
Miroslav Filipović	All	Principal Research Adviser. Coauthor of published papers.	
Graeme White	All Optical Spectra of Supernova Remnant Candidates in NGC 300	Research Adviser. Coauthor of published papers. Co-observer, contributed error analysis techniques.	
Jeff Payne	Optical Spectra of Supernova Remnant Candidates in NGC 300	Coauthor of published paper, contributed object observation selections.	
Thomas Pannuti	Optical Spectra of Supernova Remnant Candidates in NGC 300	Coauthor of published paper, original suggestion of re-observing NGC 300 supernova remnant candidates from Blair & Long (1997).	
Evan Crawford	Optical Spectra of Supernova Remnant Candidates in NGC 300	Coauthor of published paper.	
Wayne Staggs	Optical Spectra of Supernova Remnant Candidates in NGC 300	Coauthor of published paper, contributed Section 6.2.2.	

Acknowledgements:

From Chapter 6: I thank the Australian National University Research School of Astronomy and Astrophysics (RSAA) for the use of the 2.3 meter Advanced Technology Telescope (ATT) at Siding Spring Observatory (SSO), Australia. I used the NOAO (National Optical Astronomical Observatory) IRAF (Image Reduction and Analysis Facility) software package with Brent Miszalski's "Planetary Nebula Extractor" task for IRAF, and the Figaro software package from the Starlink Project. IRAF is distributed by the NOAO which are operated by the Association of Universities for Research in Astronomy, Inc. (AURA), under cooperative agreement with the National Science Foundation (of the United States). I also used the KARMA software package from the Australian Telescope National Facility (ATNF).

From Chapter 7: I gratefully acknowledge the generosity of Professor William Blair who provided the original CCD image files from the Blair & Long (1997) survey observations. Thanks also go to the Hubble Space Telescope (HST) archival team for their work in maintaining the archives thus making the telescope's original data available to all. I used the Smithsonian Astrophysical Observatory's (SAO) DS9 software package to process the images from both the original survey (Blair & Long, 1997) and from the Hubble Space Telescope. I also used software ("CCDOps") from the Santa Barbara Imaging Group (SBIG).

I thank the many people involved with the creation and development of these software programs and packages, and for making them available free of charge for use by astronomical researchers.

This thesis makes use of data products from the Two Micron All Sky Survey (2MASS), which is a joint project of the University of Massachusetts and the Infrared Processing and Analysis Centre, funded by the National Aeronautics and Space Administration and the National Science Foundation.

A grant from the Access to Major Research Facilities Program (AMRFP) from the Australian Nuclear Science and Technology Organisation provided for travel and lodging for observations at the South African Astronomical Observatory made during this thesis research.

Dedications:

Nothing worth doing can be done alone.

I dedicate this work to my wife,

Sheri Lynn Millar

whose love, patience and understanding of the international travel and

many long days at my desk made this advanced degree obtainable.

I also dedicate this work to my father and mother,

William Harold and Margie Jane Millar

whose encouragement and support throughout my

education has led to a successful career

and an intense desire for lifelong learning.

Abstract

This thesis is based on multi-wavelength observations of supernova remnants in the nearby Sculptor Group galaxy NGC 300. A survey of the literature provides a set of observations of supernova remnants and candidate supernova remnants within NGC 300 in the X-ray, optical and radio spectral regions. A radio survey published by Payne et al. (2004) presents a number of new candidate supernova remnants. Blair & Long (1997) published an optical survey of supernova remnant candidates that have not been re-observed before this thesis and some of which had never had optical spectra taken. These two candidate sets were used to create a set of objects which were observed with the Advanced Technology Telescope at Siding Spring Observatory, using its moderate-resolution (< 5 Å) dual-beam spectrometer (Millar et al., 2011). Most of the radio sources of Payne et al. (2004) did not meet the accepted optical requirement of [S II]:H$\alpha > 0.4$ while most of the optical sources from Blair & Long (1997) did meet this requirement.

With multiple sources of observations of the optical supernova remnant candidates (Blair & Long, 1997) a problem appears. Comparing observations of the supernova remnant candidate labelled N300-S16 made by Blair & Long (1997) with those published in Millar et al. (2011) and also compared with an archival observation from the Hubble Space Telescope provides conflicting evidence as to the true nature of this particular object. Although there are known problems with the [S II]:H$\alpha > 0.4$ criterion for identifying supernova remnants and there are reported resolutions to these problems, there appear to be more problems that may as yet be unrecognised.

The spectral line flux levels from N300-S16 are low and this may cause a large error in spectral line flux measurement. This error source was investigated in Millar et al. (2011). The sulphur/oxygen gradient of NGC 300 has been studied (Christensen et al., 1997) and NGC 300 has a high level of diffuse ionised gas (Hoopes et al., 1996). There are no studies into how these factors may affect the [S II]:Hα measurements for object identification. Telescope pointing errors, astrometry errors and seeing conditions all act adversely to the correct measurement of flux density from extragalactic candidate supernova remnants. The effects of these

errors was investigated in particular for the N300-S16 object. I find that other observation techniques may be needed along with optical spectra – preferably very high-resolution optical imaging with space-based or ground-based adaptive optics capable telescopes – to confirm the true identity or even to validate the existence of some extragalactic supernova remnants. In the process of comparing Hubble Space Telescope images of NGC 300 with radio emission sources consistent with supernova remnants, I have found four locations where the Hubble Space Telescope's images support the radio sources as being supernova remnants.

Contents

List of Tables

List of Figures

Chapter 1

Introduction

For all living organisms the most important events in the universe are the energetic explosions known as supernovae and the distribution of the supernova remnants' debris through the body of the host galaxy. The distributed debris from this stellar death event becomes the building material of planets, plants and animals (Prantzos, 2007). To understand the origins of living organisms, the origins of life's building blocks – carbon (C), nitrogen (N), oxygen (O) and the other chemical elements must first be understood. The even numbered elements up to iron (Fe) are produced within the cores of main-sequence stars and the remaining elements during the stars' death stages (principally as red giants). The elements above iron are produced during a supernova explosion. Supernovae are probably a galaxy's greatest source of life's elements (Prantzos et al., 1994; Prantzos, 2007). Supernova remnants have been associated with the production of cosmic rays (Zwicky, 1939; Biermann et al., 2010) which pass through living organisms, causing mutations and thus providing one of the fundamental mechanisms for the evolution of living organisms (Goldsmith, 1989). The creation of living organisms requires the death of stars.

The study of stellar death is a merger of many fields of science: astronomy, physics, chemistry, spectroscopy, electronics and computers – to name a few. Within the science of astronomy, stellar death is a combination of the study of stellar structure, life and death, the interstellar matter and the chemical evolution of galaxies.

The first step in distributing new chemical elements throughout any galaxy is the production and ejection of those elements during the death of a star. Most supernovae are the implosion of the core of a high-mass star and is just one form of stellar death. A more common form of stellar death creates a planetary nebula. Planetary nebulae are also a major contributor of the elements of life (Kwok, 2000). Unlike planetary nebulae

however, a supernova explosion creates high-energy shock waves within the interstellar matter which can trigger the formation of more stars (Xu et al., 2011). In turn, the deaths of these stars increase the abundance of the chemical elements within their galaxy. As evidenced by the observation of interstellar matter super-bubbles created by supernovae, the shock waves can directly affect the surrounding environment up to 200 light-years away. Many of the stars whose formation is triggered by a supernova may have planetary systems supporting living organisms built from the chemicals produced by the supernova. Because of the presence of supernovae produced heavy elements like Uranium, this is thought to be the case for our own planet, Earth.

While it is known that supernova remnants emit over the entire electromagnetic spectrum the observation of supernova remnants and candidate supernova remnants is concentrated mainly in the radio, X-ray and optical regions. This is particularly true for extragalactic supernova remnants because of limitations in current detector technology. The primary criteria for finding and confirming candidate supernova remnants include prominent, polarised radio emissions (synchrotron radiation), the [S II]:Hα ratio in optical, and X-ray emissions from shocked (and therefore high temperature) gasses. Kinematic studies (mostly by observation of optical diameter and Doppler effect) help to determine the probable age of a Galactic[1] supernova remnant. Age determination is supported (in the case of very young supernova remnants) by the gamma-ray (gamma-ray) observation of elemental decay (e.g. ^{44}Ti). Age determination of large (older) Galactic supernova remnants is difficult when there is no known, associated supernova event. Historical records are most helpful for determining supernova remnant age. The interactions of expanding supernova remnants with the circumstellar matter and interstellar matter can provide insight into the structure and composition of the circumstellar or interstellar matter. This is critical for understanding the dispersion of new elements in, and the chemical evolution of, a galaxy.

Identification of supernova remnants in the radio region is done primarily by the value of the spectral index of the emissions. This index and its values are discussed in sections 3.5.6, 4.4 and 6.3.5. The optical identification of a supernova remnant is primarily made through the total, singly ionised sulphur ([S II] $\lambda\lambda$ 6713, 6732 Å)[2] to hydrogen-alpha (Hα λ 6564 Å) line flux ratio [S II]:Hα; secondly through the presence of [O I] λ 6300 Å which is energised by the shock front of the expanding supernova remnant; and thirdly by the temperature of the material[3] which in the case of supernova remnants, is generally due to shock heating. X-ray emissions are

[1] From here after any form of the word galaxy which is capitalised refers to the Milky Way galaxy.

[2] See Section 4.10 for an explanation of this spectral notation.

[3] The [O III] and [N II] line fluxes are electron temperature dependent (Osterbrock & Ferland, 2006).

identified by a positional linking of the X-ray source to known supernova remnants from radio or optical studies.

Over 270 supernova remnants are known within the Galaxy (Green, 2009). However, the study of supernova remnants within the Galaxy is hampered by the Galaxy's interstellar matter (extinction and reddening effects) and problems with measuring the distance to these objects. These effects of these problems are decreased by observing supernova remnants in other galaxies. The galaxies chosen for observation are those which are spiral types, are face-on or nearly face-on, and have a high Galactic latitude so the effects of both the host galaxy's and the Galaxy's interstellar matter are of far less concern. Because the extragalactic supernova remnants are located within a host galaxy whose distance can be measured by various techniques, the distance to the extragalactic supernova remnants is also known. With known distance and apparent angular size the physical size of the supernova remnant can be determined and from this an estimate of the age of the supernova remnant can be made. The list of published extragalactic supernova remnants has grown to nearly 500 entries (e.g. Urošević et al., 2005; Chomiuk & Wilcots, 2009).

Problems with the [S II]:Hα ratio being influenced by background (interstellar matter) emissions are discussed in Petuchowski & Bennett (1995). They found that [S II] $\lambda\lambda$ 6716, 6731 Å and [O I] $\lambda\lambda$ 6300, 6363 Å emissions have a natural positional correlation due to the heated electrons providing the energy for the respective transitions. There is significant contribution to the [S II] emissions in the neutral interstellar matter from far-ultraviolet sources. This produces an average large-scale galactic [S II]:Hα on the order of 0.4. This background emission ratio can cast doubt on the validity of the [S II]:Hα measurement for detecting extragalactic supernova remnants particularly when there is no evidence of supernova remnant-like structure in the interstellar matter. This may be the situation I have found with the Blair & Long (1997) NGC 300 supernova remnant candidate N300-S16, thus giving support to the need for high-resolution optical imaging of these candidates.

1.1 An Overview of this Thesis

This thesis is based on original research concerning the discovery, identification and confirmation of supernova remnants in nearby galaxies – specifically the Sculptor Group galaxy, NGC 300. The goals of the research are:

- To identify the sources of errors in observational and data analysis techniques used for identifying and confirming supernova remnants in nearby galaxies.
- To determine the effects of those errors on the data and the conclusions drawn from the data.

- To propose changes to the observation and data analysis techniques or procedures to estimate the size of and decrease the impact of these errors.

This research led to questioning the reliability of the optical criterion of [S II]:H$\alpha \geq 0.4$ for these purposes. There are observational and measurement difficulties – seeing conditions, telescope pointing, flux measurement errors, background flux, effects of a galaxy's diffuse ionised gas, and astrometry errors – which have not been clearly addressed in the extragalactic supernova remnant research thus far. These difficulties could not be addressed separately because many have an interrelationship which was also investigated. This investigation of these errors and effects used multi-wavelength astronomy (see Appendix A), spectral line flux measurement error analysis, astrometry error analysis, high-resolution optical image evidence of possible supernova remnant structure within N300-S300's interstellar matter, and the metallicity (Z) of the galaxy's interstellar matter to determine the effectiveness of the detection and observing techniques for extragalactic supernova remnants.

It was found that when the data collected with the telescopes and instruments typically used for the discovery and confirmation of extragalactic supernova remnants was compared to data from higher-resolution instruments that the reliability of these techniques may be questionable. A strict flux density measurement error analysis shows that large errors in the [S II]:Hα ratio occur when the ratio is based on low flux density levels (Millar et al., 2011) which are typical for extragalactic supernova remnants. Seeing conditions may hamper (manual) telescope fine positioning of the spectrograph's slit, thus producing a pointing error which may impinge in the reliability of the flux measurements and on the confidence of exactly what object is being measured. The seeing can produce the possibility that the spectrograph slit is completely off the candidate's reported position – yet return positive [S II]:H$\alpha > 0.4$ results. In cases where the target galaxy has high level emission from its diffuse ionised gas, the spectroscopic signal may not be sufficient to confirm the presence of a extragalactic supernova remnant. This is particularly true if the remnant is the result of a Balmer dominated Type Ia event which is not near any H II regions. High resolution optical images from space-based telescopes or from ground-based telescopes using adaptive optics may be necessary for confirming the existence of these extragalactic supernova remnants. These telescopes should be able to detect structure in the interstellar matter to help confirm the existence of the supernova remnant.

Here is a list and brief description of the chapters:

1. "Introduction" — An introduction to the purpose, goals and general results of this thesis research.

2. "Supernovae: The Progenitors of Supernova Remnants" — A description of the general properties of supernovae including their proposed existence, classification into types and subtypes, and the role of historical supernovae in understanding supernova remnants.

3. "Supernova Remnants" — An overview of supernova remnants – their properties, time evolution, classification, electromagnetic emissions including a description of observations of supernova remnants over the entire electromagnetic spectrum. The need for multi-wavelength observations of supernova remnants and for observation of extragalactic supernova remnants is established.

4. "Emission Mechanisms" — A discussion of the physical mechanisms by which the observed emissions are created within the supernova remnant. The main purpose of this chapter is to introduce the reader to concepts, terms and symbols used in this thesis.

5. "Extragalactic Supernova Remnants and NGC 300" — A literature review of the observations of supernova remnants in nearby galaxies with a focus on the observations made of supernova remnants in NGC 300.

6. "Optical Spectra of Supernova Remnant Candidates in NGC 300" — Based on an original research paper previously published in the journal *Astrophysics and Space Sciences* (Millar et al., 2011, here after, MWF11). This paper describes optical (spectral) observations of optical and radio candidate supernova remnants in NGC 300 with an analysis of the flux measurement errors.

7. "Optical Observing Techniques: NGC 300" — Based on an original research paper published in the *Serbian Astronomical Journal* (Millar et al., 2012, here after, MWF12). This chapter discusses the search for the supernova remnants of Blair & Long (1997, here after, BL97) and Payne et al. (2004, here after, PF04) within the archives of the Hubble Space Telescope with analysis of the astrometry of the BL97 images, the astrometry of the radio observations of PF04 and the telescope pointing errors found in MWF11.

8. "Conclusions" — A general discussion of the conclusions drawn from the results of the observations and comparisons.

9. "Future Work" — Suggestions for future observations and studies.

The appendix contains:

A. "Multi-Wavelength Astronomy" — A short introduction to the principles of multi-wavelength astronomy.

B. "Other Known Objects in NGC 300" — A review of observations of objects other than supernova remnants (e.g. planetary nebulae) within NGC 300 and how these objects may be confused with supernova remnants when observed in distant galaxies.

C. "HST File Search Data and Results" — A description of Hubble Space Telescope filter data.

D. "HST Proposal Abstracts" — The Hubble Space Telescope observation proposals related to the archival Hubble Space Telescope images used in this thesis.

E. "DS9 Settings for Figures" — Various options/settings for images produced with the SAO's DS9 software.

F. "Author's Publications List" — A list of my publications released during the research period of this thesis. This includes publications for which I am the principal author and those for which I am a contributing author.

Chapter 2

Supernovae: The Progenitors of Supernova Remnants

Supernova remnants are the high-speed outward flow of the outer layers of a star – the result of a supernova explosion. Supernova remnant electromagnetic emissions are sourced from both thermal (black body radiation, see Section 4.2) and non-thermal (e.g. synchrotron radiation, see Section 4.4) mechanisms, and includes spectral-line emissions and absorptions by atoms from essentially every chemical element[1]. Band spectra from dust particles and molecules in supernova remnants have also been observed. For examples of recent observations and how the presence of dust and molecules is used in understanding of supernova remnants, see Rho et al. (2009) and Su et al. (2011). Type II supernovae may be the major source of dust in a galaxy (Dunne et al., 2003). To discuss the analysis of supernova remnants an understanding of their progenitors – supernova explosions – is needed.

2.1 Supernovae

Supernova explosions were proposed by Walter Baade and Fritz Zwicky in 1934 (Baade & Zwicky, 1934). Analysis of transient, extremely bright stars led to the proposal of explosions of much greater energy than ordinary novae – supernovae – with no observed intermediate luminosity objects. From calculations for the total radiation emitted from a supernova Baade & Zwicky (1934) concludes, "*the phenomena of a super-nova*

[1] Note the list of elements shown in Table C.2.

represents the transition of an ordinary star into a body of considerably smaller mass" (italics original). The calculations showed that a considerable amount of the mass of the star was converted into energy. This paper also proposed that these explosions should able to produce the neutron stars predicted three years earlier by Russian physicist, Lev Landau[2].

With 12 supernova observations resulting from a multiple-year survey (Zwicky, 1938), Minkowski (1941) divided supernova explosions into two types: Type I and Type II. Later, Zwicky extended this scheme to Types III, IV and V, where Type V had only one example[3]. These later classes were based mainly on variations in the optical light intensity curves[4]. Now, only Type I and Type II supernovae with a few subtypes for each (Figure 2.1) are accepted[5]. The fundamental difference between Type I and Type II supernovae is the presence of hydrogen (H) in its optical spectrum at the maximum of the supernova's light curve. The subtypes are labelled with upper or lower case Latin letters. Subtypes with lowercase letters are defined by spectral differences. Subtypes with uppercase letters are defined by the time-dependent shape of the light curve.

A correlation between the host galaxy (Hubble) type and observed supernovae type has been found. While Type Ia supernovae occur in all Hubble types, core collapse supernovae (non Type Ia) occur mainly in late type galaxies (van den Bergh et al., 2003). Another notable difference between Type Ia and core collapse types is their locations within a late-type galaxy. The core collapse types are found mainly in the dusty arms of the galaxies where the young, population I stars are found and generally also near hydrogen cloud (H I, H II) regions. Type Ia supernovae are found in all regions of a galaxy. There is a possibility that Type Ia supernovae are associated mainly with older population II stars (Wheeler & Benetti, 2000), which could explain why they are found in all galaxy types.

[2] A presentation by D. G. Yakovlev in 2008 discusses the history behind this prediction.
`http://www.ift.uni.wroc.pl/~karp44/talks/yakovlev.pdf`

[3] Shklovsky (1968) contains a discussion of the characteristics of supernova types III, IV and V.

[4] "Optical light intensity curves" are also known simply as "light curves."

[5] da Silva (1993) has proposed a classification scheme for supernovae based on physical mechanisms rather than spectra but this has not been accepted.

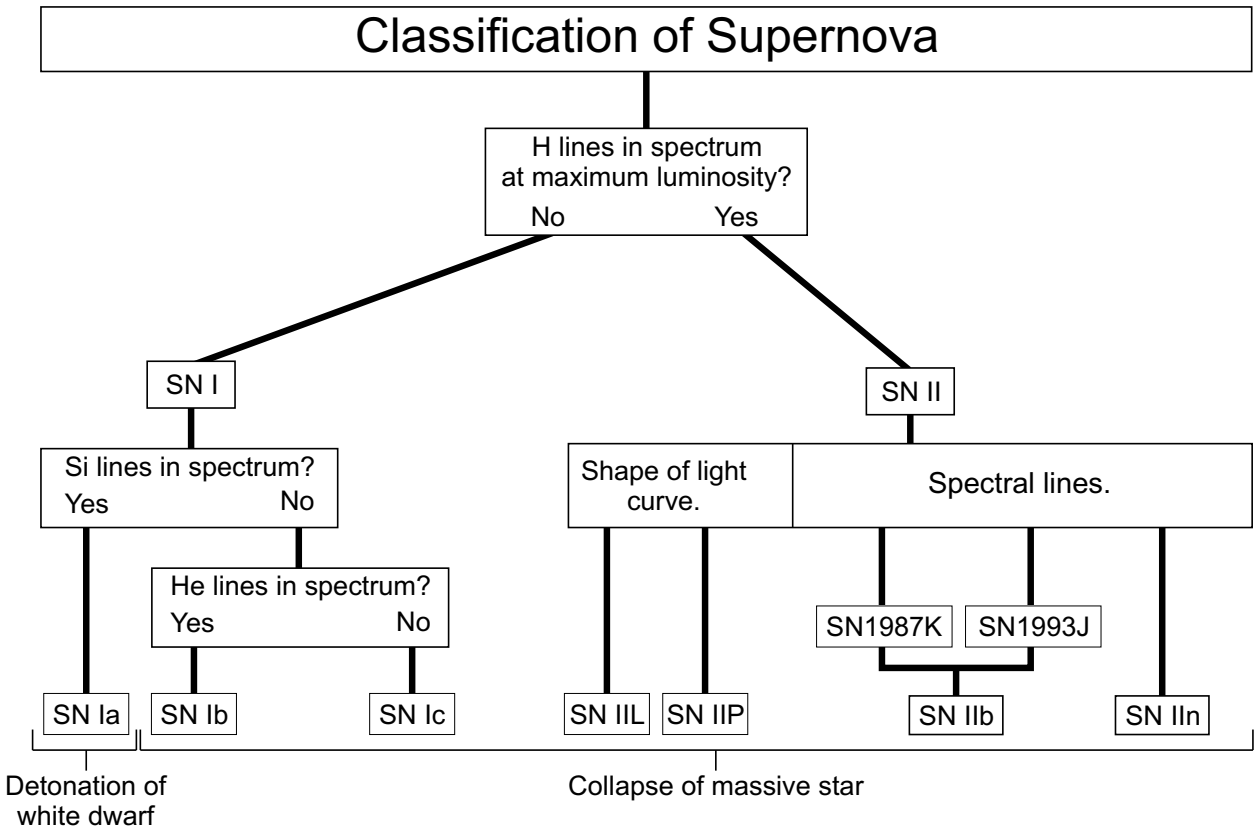

Figure 2.1: The classification of supernovae. The subtypes are divided by spectra or light-curve shape. The physical mechanism causing the explosion is shown at the bottom. SN 1987K and SN 1993J were originally separate subclasses but have since been combined into subclass IIb. (Based partly on Harkness & Wheeler, 1990).

2.2 Type I Supernovae

A representative light curve of a Type I supernova is shown in Figure 2.2. Type I supernovae rise to maximum brightness very quickly (about two weeks) and fall off in brightness at the same rate for about two more weeks. After this, the dimming slows and follows an exponential fall-off with the luminosity falling to half its value with the same characteristic period of some number of days – essentially acting like a radioactive decay.

Type I supernovae do not have hydrogen in their spectra and are divided into subtypes a, b and c. The first division in these subtypes is based on whether there is silicon (Si) in the spectrum. If there is, the supernova is classified as Type Ia. Type Ia supernovae exhibit a S II absorption feature at λ 6150 Å that is unique to this supernova type. If not, a second division is based on the presence of helium (He) in the spectrum. Supernovae with helium are classified as Type Ib and supernovae without are Type Ic. However, using single parameter differences between the subtypes and even within each subtype can be problematic (Benetti et al., 2004). Like all Type II supernovae, Type Ib and Type Ic are due to the collapse of the core of a high-mass star. Supernovae were classified by spectra rather than the mechanism of the explosion (Marschall, 1988).

2.2.1 Type Ia Supernovae

Type Ia supernovae occur in binary star systems where one of the stars is a white dwarf and its companion is most likely a dying star in one of its red giant stages. A detailed discussion of Type Ia models is given in Hillebrandt & Niemeyer (2000). The white dwarf gathers material from its giant companion[6] until its mass is sufficient for gravity to overwhelm the core pressure produced by its degenerate electrons and the white dwarf collapses. The collapse heats the core to temperatures sufficient to fuse carbon and oxygen[7] forming about 1 $M_\odot$ (1 solar mass) of nickel (^{56}Ni), which is unstable. ^{56}Ni decays with a half-life of 6 days to cobalt (^{56}Co) which decays with a half-life of 77 days to ^{56}Fe, which is stable. Nickel, cobalt and iron are collectively called the "iron group" because they have a similar atomic weight and are next to each other on the periodic table. These nuclear decays produce a set of characteristic gamma-rays which have been observed (Marschall, 1988; Goldsmith, 1989). The absorption of these gamma-rays by, and subsequent ionisation of, the outer layer gasses expelled by the supernova explosion accounts for the characteristic decay in luminosity of the supernova in its later days (see Figure 2.2). The luminosity decay rate may also be wavelength dependent.

[6] Through a process known as *mass transfer*.

[7] In lower-mass white dwarfs the increased heat may initiate helium fusion.

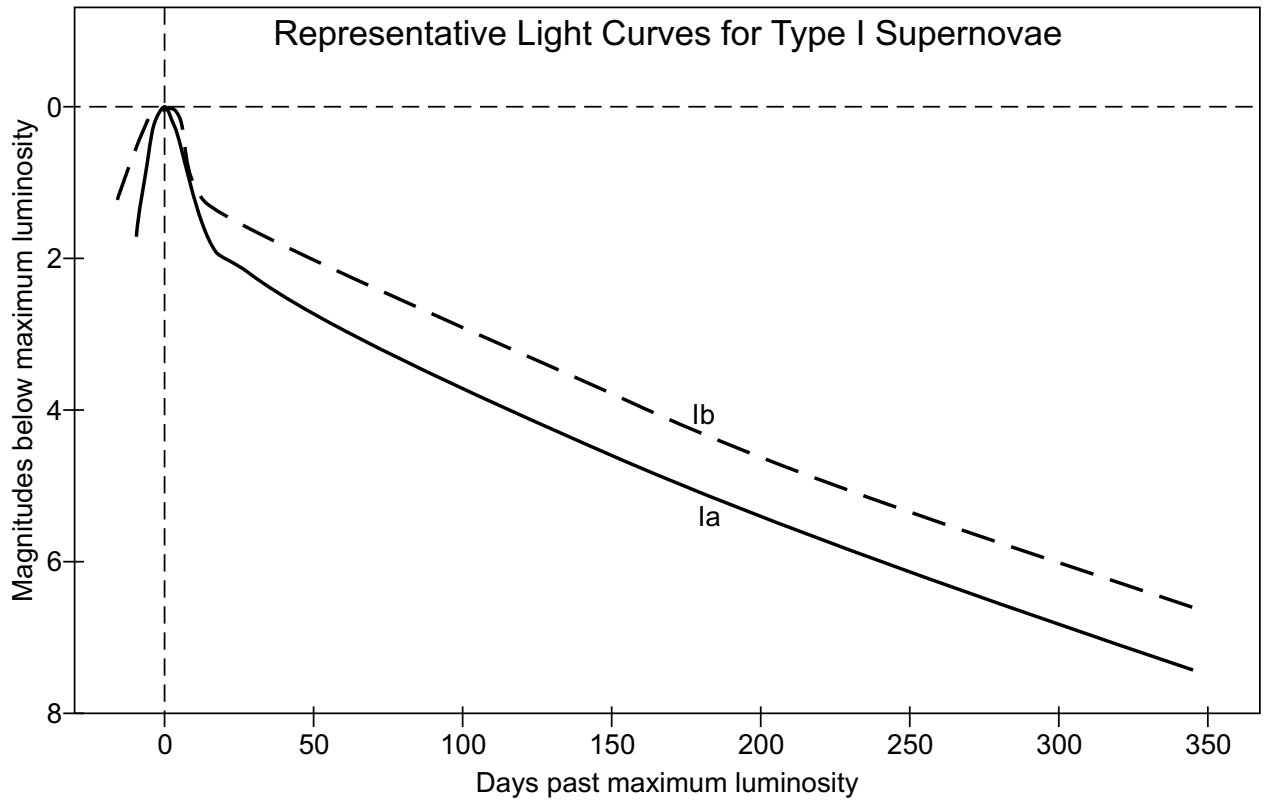

Figure 2.2: Representative light curves for Type I supernova (after Marschall, 1988; Kirshner, 1990).

Some of the problems with understanding the evolution of binary star systems producing Type Ia explosions are discussed by Wheeler (1996). For example, there is no general theory for the evolution of such binary systems and there is little understanding of the explosion mechanism (the physical process of the white dwarf core collapse). However, progress has been made in determining the progenitor supernova type by careful observations of the X-ray spectrum of the supernova remnant (Lopez et al., 2010). Not only can X-ray observations be used to determine the supernova type (Ia or core collapse, Lopez et al., 2011) but also the mechanism of the Type Ia explosion (detonation or deflagration, see Woosley, 1990, for a discussion of these mechanisms).

No radio emissions have been found from Type Ia supernovae suggesting a very low density circumstellar matter around the progenitor star (Panagia et al., 2006). This might be expected from a binary star system undergoing mass transfer. Because the mass of the collapsing star is within a very narrow range of values ($< 1.4\ M_\odot$), Type Ia supernovae produce the same energy (10^{51} ergs = 1 foe)[8] and thus these supernovae have been used as standard candles for galactic distance measurement.

2.2.2 Types Ib and Ic Supernovae

The absence of hydrogen lines in the spectra of Type Ib/c supernovae is generally explained by the progenitor star shedding the majority of its predominantly hydrogen outer layers before the core collapses. It is also thought these progenitor stars may lose their hydrogen by mass-transfer to a companion (Uomoto, 1986; Woosley, 1990). In the case of Type Ic progenitors, the star may also shed the helium layer from around its core.

Type Ib supernovae have helium lines, especially He I λ 5876 Å while Type Ic do not (Filippenko, 2005). Neither subtypes have the Si II λ 6355 Å line in their spectra. Why this is so is still unclear because computer models show a high production rate of silicon. Their spectra often show a [O I] λ 6300 Å emission line, sometimes after 100 days (Woosley, 1990). In infrared, Type Ia supernovae show strong, variable absorption at 1.2 μm and 3.5 μm while Type Ib show no such absorption and have a slower emission decline after maximum (Elias et al., 1985).

These supernovae are apparently the result of the collapse of a star with a main-sequence mass greater than 20 $M_\odot$. One suggestion is that Wolf-Rayet (WR) stars may be (one of) the progenitors of these types of supernovae (particularly Ib) as these stars have intense stellar winds which may be the mechanism of shedding

[8] Because this energy amount is used so often in supernova studies, the energy unit of 1 foe was introduced (Herant et al., 1997). The name is an acronym from the phrase "ten to the **f**ifty-**o**ne **e**rgs." One foe equals 10^{51} ergs.

hydrogen (Filippenko & Sargent, 1986). Type Ib supernovae have always been observed in spiral galaxies near H II regions where Wolf-Rayet stars are typically found (Woosley, 1990). There is also evidence to support Type Ib as the result of the explosion of a white dwarf in a binary system, with the difference in the type being caused by the effective flame speed in the white dwarf's collapse (Woosley, 1990).

2.3 Type II Supernovae

A Type II supernova is the final event in the life of a star with a main-sequence mass of at least 8 $M_{\odot}$. If the main-sequence mass is less than this the most likely result of the star's death is a planetary nebula with a central white dwarf star. At the end of the star's life its internal structure of nuclear fusion shells has an onion-layer appearance with progressively higher numbered elements inward to an iron core. The fusion products of each shell become a fuel source for the shell immediately below. The outer most (non-fusing) layers are mostly hydrogen with new chemical elements being created by the slow and rapid neutron capture processes. The iron core cannot release energy by nuclear fusion (iron is the most tightly bound nucleus) and is supported against gravitational collapse by electron degeneracy. As nuclear fusion continues above the iron core, the core increases in mass and temperature until it reaches approximately 7×10^9 K at which time it undergoes photodisintegration ($^{56}\mathrm{Fe} + \gamma \rightarrow 13\ ^4\mathrm{He} + 4\mathrm{n}$) producing helium and neutrons. The iron nuclei are literally knocked apart by the extremely high-energy gamma-rays.

The iron core begins to collapse creating an enormous burst of neutrinos (symbol, ν) which leave the core at nearly the speed of light[9]. The neutrino burst is created by the neutronization ($\mathrm{p} + \mathrm{e}^- \rightarrow \mathrm{n} + \nu$) of the core. As the electrons are being absorbed the electron degeneracy drops faster which increases the rate of core collapse with a corresponding increase in core temperature. The neutrinos carry energy away from the core, cooling it and thus causing a drop in core pressure which increases the rate of core collapse. This entire catastrophic core collapse process happens in less than three seconds (Smith, 1995). The neutrinos carry away nearly 99% of the energy released by the collapse (Burrows, 1990).

When the collapsing core reaches high enough (nearly nuclear) density it will achieve neutron degeneracy, which stops the collapse and the core will rebound slightly. The outer layers which were falling onto the collapsing core suffer a shock wave from the core's rebound and are pushed back out into space. The shock wave from the core's rebound is not sufficient to sustain the expulsion of the outer layers and their continued

[9] Neutrinos a have mass of about 16 eV and thus they travel at nearly the speed of light.

expansion is caused by the extremely high neutrino flux (Fryer & Kusenko, 2006). This mechanism was verified by the observation of neutrinos from SN 1987A, a Type II supernova. A more detailed discussion of the core collapse is given by Burrows (1990) and by Herant et al. (1997).

The expanding shell of the star's outer layers mixing and interacting with the circumstellar matter and interstellar matter become the supernova remnant. The spectral lines of Type II are narrower than those of the Type I indicating that the star's outer layers are expelled at a much lower speed (one to three thousand kilometres per second) than in Type I supernovae. This makes identification of the chemical elements in the supernova remnants of Type II supernovae somewhat easier.

The neutron star created by the core collapse plays a major role in the evolution of the supernova remnant if it was not expelled from the supernova remnant by an asymmetrical explosion or some other mechanism. The central neutron star generally has a very high spin rate – on the order of 500 to 2000 revolutions per second – and this rotational energy is generally coupled to the supernova remnant material through the neutron star's intense magnetic field. The interactions between the supernova remnant debris and the neutron star's magnetic field provides testable predictions about the nature of supernovae, neutron stars and supernova remnants through the electromagnetic emissions created by their interactions. The supernova remnant and the neutron star within must evolve together.

2.3.1 Type II Supernovae Subtypes

The two principal Type II supernovae subtypes are P and L. Representative light curves for these Type II supernovae are shown in Figure 2.3. At maximum, a Type II supernovae is three to ten times dimmer than a Type I (Kirshner, 1990). The shape of the luminosity decline is controlled by the gamma-rays from the radioactive decay of ^{56}Co to ^{56}Fe. After a quick rise in brightness to maximum, Type II-P supernovae show a two to three month long plateau followed by a radioactive decay shaped decline in brightness (Kirshner, 1990). Type II-L supernovae have a fast, fairly linear decay after maximum followed by an exponential decay similar to Type II-P.

The progenitor of a Type IIb supernova may have lost most of its outer hydrogen to a companion star. The exposed core consists mostly of helium. The spectrum of the explosion initially shows weak hydrogen lines (hence the Type II designation) but after a second light curve peak, shows a spectrum similar to a Type Ib explosion – hence the "b" designation for this subtype. This subtype was created from two supernovae which

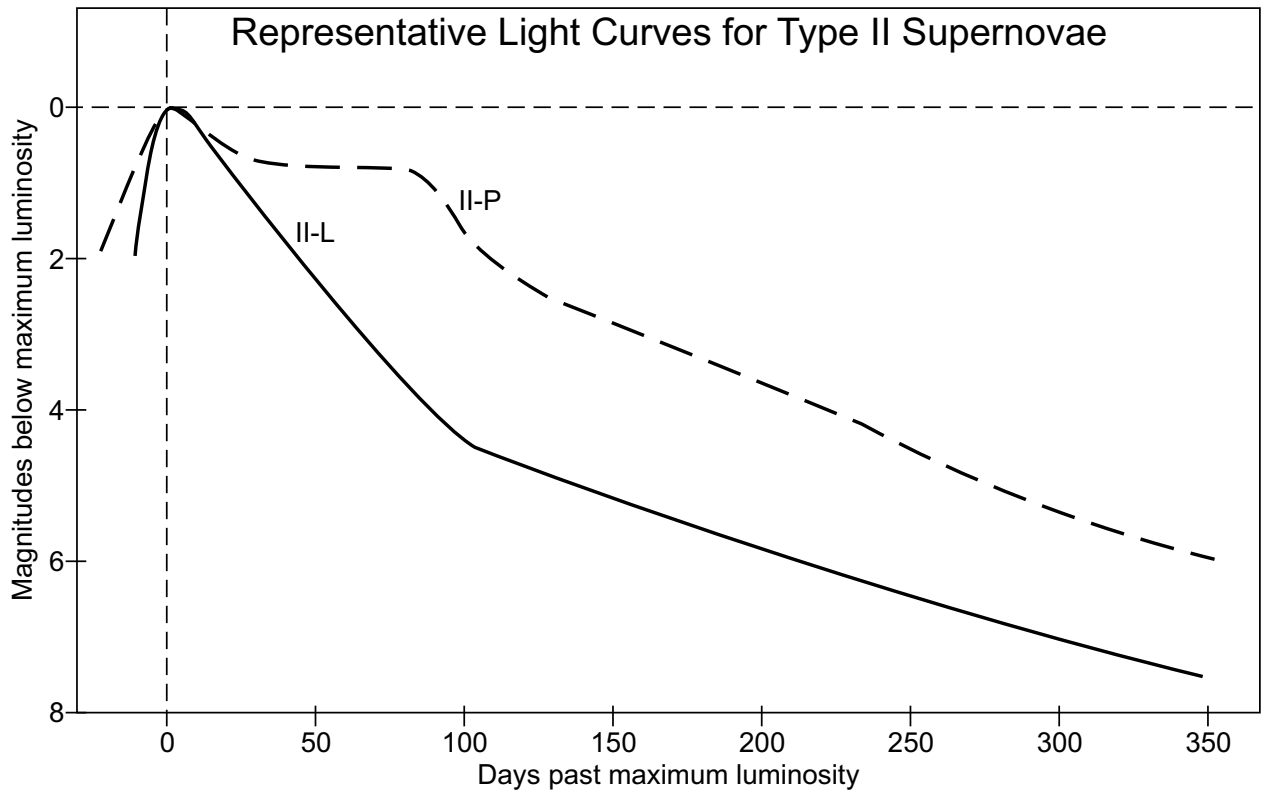

Figure 2.3: Representative light curves for the principal Type II supernovae (after Marschall, 1988; Kirshner, 1990).

were originally (temporarily) separate subclasses. SN 1987K and SN 1993J are now the classic examples of the IIb subtype and Cas A may also have been such an explosion (Chevalier & Soderberg, 2010).

SN 2005gl and SN 2006gy are two possible examples of Type IIn supernovae. The "n" indicates the presence of very narrow to intermediate width hydrogen emission lines in the spectra with little P-Cygni[10] absorption. At the intermediate range of line-width the expanding remnant may be interacting with the dense circumstellar matter (Filippenko, 1997, 2005). Type IIn progenitors may be luminous blue variable stars which may have large mass-loss before exploding (Kiewe et al., 2010)

2.4 Historical Supernovae

One of the greatest aids in understanding the evolution of supernova remnants is historical records of observed supernovae[11]. Modern European astronomy begins at roughly the time of Tycho Brahe and Johannes Kepler, and primarily by their work. Before these two men, observations (by European astrologers) of any events other than those of comets and the conjunctions of planets are few and not well documented. This is probably due to the influence of the ancient Greek philosophers (e.g. Aristotle and Ptolemy) on European science and perhaps also to the role of the Church in private, public and most importantly in academic life. Chinese, Japanese and Korean astrologers were not under the same influences. They kept fairly accurate records of any unusual events in the heavens including the appearance of "guest stars[12]." Table 2.1 shows the generally accepted location of these historical supernovae.

The earliest recorded observation is in the 14^{th} century BC, drawn on a piece of bone by Chinese astrologers (Wang, 1996). The first observed extragalactic supernova was SN 1885A, which occurred near the nucleus of M 31 (the Andromeda Galaxy[13]) on 20 August 1885. All historical supernovae are naked-eye events which occurred within the Galaxy.

[10] P Cygni (34 Cyg) is a variable star in the constellation Cygnus originally thought to be a recurring nova (with major outbursts in the 1600s). It is actually a hypergiant luminous blue variable – one of the brightest stars in the Galaxy. The spectrum shows both absorption and emission lines indicating a gaseous envelope is expanding away from the star (a strong stellar wind). The emission lobe (far-side of the star) is red-shifted and the absorption lobe (near-side of the star) is blue-shifted.

[11] The discussion in this section is based on books such as Goldsmith (1989); Marschall (1988); Mitton (1978) and journal papers such as Bamba et al. (2005); van den Bergh (1973).

[12] It is believed that the Asian astrologers called novae or supernovae "guest stars."

[13] It was then known as the Andromeda Nebula.

Table 2.1: Accepted location of historical supernovae, based on known supernova remnants.

Supernova	**Year**	α **(h)**	δ (°)	**Constellation**
SN 185	185	14.5	−60.33	Centaurus
SN 393	393	17.2	−38.33	Scorpius
SN 1006	1006	15.0	−41.75	Lupus
SN 1054	1054	5.5	+22.0	Taurus
SN 1181	1181	2.03	+64.6	Cassiopeia
SN 1572	1572	0.4	+63.8	Cassiopeia
SN 1604	1604	17.5	−21.5	Ophiuchus
SN 1692 (Cas A)	1692	23.38	+58.8	Cassiopeia

The observation record of SN 185 describes the fading of this star and it is very similar to what is observed for supernovae. The well-studied supernova remnant RCW 86 is thought to be the remnant of this proposed Type Ia explosion (Williams et al., 2011). The Chinese also recorded guest stars in AD369, 386 and 393 (Goldsmith, 1989; Marschall, 1988; Mitton, 1978). SN 393 was recorded by two independent observers and was visible for seven months. The Chinese, Japanese, Koreans, Muslims and Europeans (French, Italians and Swiss) observed the first truly significant supernova in the year 1006. This supernova (probably the brightest naked-eye supernova ever seen) is now designated as SN 1006 and it has a remnant which has been well studied in all regions of the spectrum[14].

The event known as SN 1054 and has been linked to the "Crab Nebula" (M 1, NGC 1952). It was recorded by nearly everyone but the Europeans. Why the Europeans failed to record it is a mystery (Goldsmith, 1989). Some point to pictographs in the American southwest claiming that even Native Americans (the Anasazi) noted the event but there are others who say this is not true (Mitton, 1978). The Crab is probably the most well studied of all supernova remnants[15]. The Crab was first observed by the English astronomer John Bevis in 1731. Its name was derived from the drawings made of the nebula by Lord Rosse in the 1840s. Here are some of the intriguing features of the Crab:

1. it has a pulsar (a fast rotating neutron star),
2. it is one of the nearest supernova remnants,
3. it has filaments of gas in a very complex structure,
4. it emits synchrotron radiation from interactions of the supernova remnant electrons with the pulsar's magnetic field.

The Crab was one of the first nebulae subjected to spectral analysis by astronomers, in the early 1900s. Its emissions have been used as an X-ray intensity measurement standard. In the X-ray energy range from 2 to 10 keV, 1 crab $= 2.4 \times 10^{-8}$ erg cm^{-2} s^{-1} $= 15$ keV cm^{-2} s^{-1} $= 2.4 \times 10^{-11}$ W m^{-2}. One crab is also equal to 1060 μjansky, where 1 μjansky [μJy] $= 0.242 \times 10^{-11}$ erg cm^{-2} s^{-1} KeV^{-1}. However, the reliability of this standard has been disputed (Wilson-Hodge et al., 2011). Because this unit of energy is quite large, the millicrab is used more often.

[14] NASA/ADS text search returns over 650 results.

[15] NASA/ADS text search returns at least 2960 results.

The event of 1181 was recorded in China and Japan. It was visible for 185 days. The radio source 3C 58 might be the remnant of this supernova. One of the most well observed supernovae was Tycho's star (SN 1572). Tycho kept an excellent record of daily observations of the new star from the night of its discovery (11 Nov 1572, in Cassiopeia) to the last night of visibility, recording apparent magnitude and colour. The description of this supernova fits that of a Type I supernova very well. This is the first supernova for which accurate descriptions of the light curve and colour changes were recorded.

Kepler's star (SN 1604) was the last naked-eye supernova within the Galaxy. Kepler made observations of this supernova that are very similar to Tycho's observations of SN 1572. The Chinese observations established the date of the explosion – 9 October 1572. The first European observations were made by two Italian astronomers and reported to Father Clavius (an opponent of Galileo). Only later did Kepler begin his observations. This supernova occurred in Ophiuchus and it was not visible between the end of October 1604 to January 1605 because of its proximity to the Sun. Therefore a significant portion of observation of its light curve is missing.

Cassiopeia A (Cas A) is the strongest radio source in this constellation. It is a supernova remnant and from its size and rate of expansion it exploded about 300 years ago, at the end of the 1600s. It is generally associated with SN 1692. There are no records of anyone observing this supernova from anyplace on Earth. There is a note in John Flamsteed's (the first Astronomer Royal of England) records where he may have observed this supernova in August of 1692, but his observation log is not clear (Goldsmith, 1989). The supernova remnant is easily observed in radio wavelengths but very faint in optical apparently because of the dense interstellar matter (mostly dust) lying in the direction to this supernova remnant. This dust may explain why the event was not seen and thus is a prime example of the reasons why modern astronomy must be able to make observations at all wavelengths. Without these multi-wavelength techniques the presence of many Galactic objects would be unknown. There are more recent discoveries of Galactic supernova remnants using non-optical wavelengths (see for example, Edelstein et al. (2006) or Morris et al. (2006)). Tycho's Star, Kepler's Star, and Cas A are all examples of Type Ia supernovae.

The research significance of these historical supernovae is that they provide the age of the supernova remnants associated with them. Knowing the age of the supernova remnant provides a deeper understanding of the evolution of supernova remnants and their interactions with the interstellar matter by allowing the testing of supernova remnant evolution models against observations of real supernova remnants of known age. Determining the age of a Galactic supernova remnant which has no recorded supernova event is hampered by the inability

to determine the distance to the supernova remnant with reasonable uncertainty. Further discussion of the problems with the Galactic interstellar matter and distance measurements is found in Section 3.3.1.

Chapter 3

Supernova Remnants

There are few papers and fewer books dealing with the general time-evolution of supernova remnants. See for example, Cox (1972); Chevalier (1974); Cioffi et al. (1988); Dwarkadas (2005a,b); Tang & Wang (2005); Balsara et al. (2006); Hanayama & Tomisaka (2006); Shelton (2006) with three distinctive papers by Woltjer (1972); Gull (1973); Chevalier (1977) and significant work by Cioffi (1990). A typical supernova releases about one foe of energy, creating a shock wave that compresses and interacts with the circumstellar matter and eventually the interstellar matter. The interactions between the expanding debris and the circumstellar or interstellar matter (primarily the heating and subsequent cooling of the shocked gas) govern the evolution of the supernova remnant (Cioffi, 1990) and create the electromagnetic emissions we observe.

3.1 The Theoretical (Ideal) Model

The general evolution of supernova remnants is divided into four major stages with each stage described by an expansion parameter m, defined by $R \propto t^m$, where R is the linear radius and t is the supernova remnant age (Tam & Roberts, 2003).

The first stage is called "free expansion." The outer layers of the star expand into the surrounding space relatively unimpeded by the very low density circumstellar matter. During this stage the mass swept-up from the circumstellar matter is insignificant compared to the mass of the expanding stellar ejecta. This stage is characterised by a constant temperature and a constant expansion velocity of the shell so the shock wave expands radial-linearly in time. It can last anywhere from 90 to over 300 years.

The second stage is known as the "adiabatic" or "Sedov" or "Sedov-Taylor" stage (it was well described by

Sedov, 1993). The remnant shell becomes mixed with larger amounts of material swept-up from the circumstellar or interstellar matter and the expanding shell begins to slowdown and cool. The material mixing also enhances the magnetic field inside the remnant shell. This stage can last anywhere from 100 to 10 000 years but in some cases this stage may be missed entirely. On the other hand, this stage can be very long in its duration (the radius of an SNR could reach 180 pc) if the supernova remnant expands in a region of hot interstellar matter (McKee & Ostriker, 1977).

The third stage, known as the "snowplow," the "pressure-driven snowplow," or the "radiative" stage, begins after the shell has cooled down to less than 10^6 K with the radiative interior less than 10^7 K (Cioffi, 1990, figure 1). For a 1 foe supernova expanding into an interstellar matter of typical particle density ($1.0\,\mathrm{cm}^{-3}$) this stage expands the supernova remnant from about 14 pc in diameter to about 50 pc in diameter (Cioffi, 1990). During this stage the shell can radiate electromagnetic energy very efficiently with most of the emissions as optical light. The increase in radiation cools the shell faster, increasing its density, which makes it cool even faster. Because of the snowplow effect the supernova remnant material quickly develops into a thin, dense shell. The expansion velocity decreases fairly rapidly. During this stage the material becomes too cool to produce X-ray and thus optical and radio observations are most likely to detect these middle-aged supernova remnants. If the interior material cools completely the shell continues to expand as a momentum-conserving snowplow. This stage can last up to 20 000 years.

The fourth stage is called "dispersal." The shell breaks up when the velocity of the snowplow becomes sub-sonic (in the interstellar matter) and what is left of the supernova remnant dissipates into the interstellar matter. Typically this begins at the end of the pressure-driven snowplow stage and the supernova remnant never enters the momentum-conserving snowplow stage. The supernova remnant begins to break into segments and the size of the supernova remnant during this last stage ranges from 50 (at the beginning) to over 100 pc. The intensity of electromagnetic emissions drops quickly as the supernova remnant disperses.

3.2 Deviations from the Ideal Model

The ideal model represents a very simplified overview of the general evolution of supernova remnants. Most supernova remnants do not follow this model very well (Harrus et al., 2001) but this should be expected because this model is only a simplified understanding of the evolution of supernova remnants. Some possible reasons for the variation from the ideal are as follows:

1. The interstellar matter in which supernovae occur is rarely of uniform temperature, density or chemical composition which leads to asymmetry within the expanding supernova remnant (Chevalier, 1977; Dohm-Palmer & Jones, 1996; Jones et al., 1997).

2. If the density of the interstellar matter is low enough, the supernova remnant may finish merging with the interstellar matter before cooling becomes important (effectively, no snowplow stage; Asvarov, 2000).

3. Depending on the properties of the interstellar matter, different evolutionary stages can occur in different locations within particular supernova remnants (Asvarov, 2000).

4. If the supernova occurs in a pre-existing (evacuated) bubble in the interstellar matter which is surrounded by a massive shell of material (the "bubble walls"), the Sedov stage may not occur (Franco et al., 1991). In this case, the supernova remnant may not be detected at all unless the expanding shell reaches the wall of the bubble where the collision results in shock heating and produce excessive X-ray emissions (Chu, 1997; Koo & Heiles, 1995).

There are many papers dealing with the evolution of specific supernova remnants, some of which add support to this list of reasons for the deviation of observation from idealised theory. See for example, Aharonian et al. (2005); Badenes et al. (2005); Harrus et al. (2001); Heng et al. (2006); Park et al. (2006); Williams et al. (2005).

3.3 The Classification of Supernova Remnants

Supernova remnants are currently described by three (morphological) classes. These classes are based on Galactic supernova remnants, most of which are visible only in radio. Thus these classifications are also based mainly on radio emissions.

1. Shell-type: As the shock wave from the supernova expands into the interstellar matter it heats and stirs the material it encounters producing a large shell of hot gas (and some dust). This supernova remnant class presents a ring-like structure to the observer because at the limb of the shell there is more hot gas in the line of sight than in the middle. Typical examples include the Cas A (Figure 3.1) and Vela supernova remnants. This class comprises about 80% of Galactic supernova remnants.

2. Crab-like: These supernova remnants are also known as "filled-shell" or "plerions." (A name proposed by Weiler & Panagia (1978) from the Greek word meaning "full.") This class is named for its progenitor,

the Crab Nebula (M 1, Figure 3.2). They are similar to shell-type remnants except that they contain a central pulsar producing bipolar jets of very high speed electrons (and possibly protons) filling and usually asymmetrically reshaping the expanding outer shell. These remnants look more like a messy "blob" than a "ring." Their radio and X-ray emissions are mostly synchrotron radiation. This class comprises about 10% of Galactic supernova remnants.

3. Composite: These supernova remnants appear as a shell or a plerion depending on the electromagnetic region of the observation. This class comprises about 10% of Galactic supernova remnants. There are two subtypes of composite supernova remnants; thermal and plerionic.

   (a) A thermal composite appears as a shell-type in radio wavelengths due to synchrotron radiation. However, in X-ray wavelengths it looks like a plerion. Unlike the true crab-like supernova remnants, its X-ray spectrum has lines indicating the presence of hot gas (thermal emissions). Many X-ray bright supernova remnants fall into this class and many of these are found in proximity to molecular clouds. Observations of such a remnant are presented by Shelton et al. (2004).

   (b) A plerionic composite looks crab-like in both radio and X-ray wavelengths but it also has a shell. The X-ray spectrum from the centre does not show spectral lines but the X-ray spectrum near the shell does.

The population demographics of these classes are most certainly affected by selection effects in the observations and by the evolution of supernova remnants as they age. The crab-like pulsar-nebula type of supernova remnant may be only a stage in the evolution of the supernova remnant (Strom, 1996).

As understanding grows there may be a need to expand the classification schemes of supernova remnants and supernovae. Kesteven & Caswell (1987) suggest a fourth class of remnant – "barrel-shaped" – and also suggest that this is the most common morphological class of supernova remnant. This suggestion is based on data obtained in the radio region with the MOST (Molonglo Observatory Synthesis Telescope) telescope[1]. Rho & Petre (1998) also suggests a fourth class – "mixed morphology" – with shell and filled-shell characteristics similar to the thermal composite type but with little or no limb darkening. The dominant X-ray emission is thermal and the primary source is swept-up interstellar material rather than ejecta[2].

[1] This suggested class has not yet been accepted.

[2] This classification has also not yet been accepted.

Each for their own and various reasons, there is interest in both young and old supernova remnants. For the young supernova remnants, "There are two types of young supernova remnants from a morphological point of view: shell-like structures and those of centre-filled morphology. There are also two types of young supernova remnants from a spectroscopic point of view: thin thermal emission and power-law type spectra" (Tsunemi et al., 2000). Young supernova remnants are studied for their interactions with the circumstellar and interstellar matter. Interest in old supernova remnants lies in understanding the final dissipation or distribution of material into the interstellar matter.

Figure 3.1: A step sequence from an artist's animated rendition of the Cassiopeia A (Cas A) supernova and its expanding remnant. This is a classic example of a Shell-type supernova remnant. (Credit: NASA/ESA and the Hubble Heritage STScI/Aura-ESA/Hubble Collaboration.)

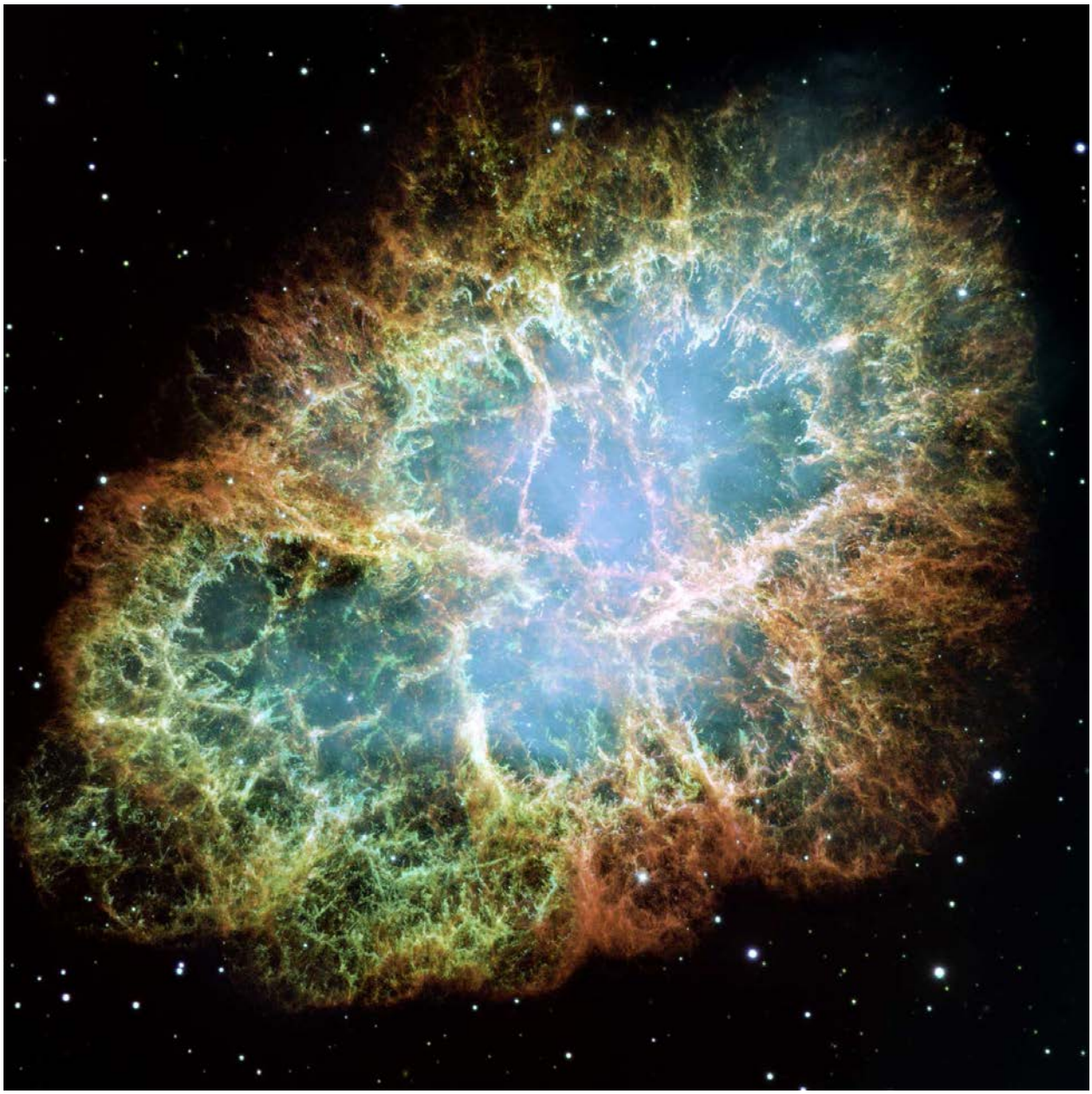

Figure 3.2: M 1, the Crab Nebula: The prototype of the filled-shell (plerion) type supernova remnant. Created by the historical supernova SN 1054. (Credit: NASA, ESA and Allison Loll/Jeff Hester (Arizona State University). Acknowledgement: Davide De Martin (ESA/Hubble).)

3.3.1 Distance and Diameter

Apparent diameter and distance are two important observables of supernova remnants. The apparent supernova remnant diameter can be measured from its radio, infrared, optical or ultraviolet emissions. If the distance to the supernova remnant is also known then its actual size is known. Determining distance is difficult for Galactic supernova remnants. One technique for determining the size is to measure the radial expansion rate with the Doppler effect and compare this with measurements of the shell expansion at the limb from photographs taken years apart. Assuming the expansion is symmetrical, the size, distance and age of the supernova remnant can be determined.

One of the advantages of studying extragalactic supernova remnants is easier determination of distance because it is effectively equal to the distance to the galaxy. From the known distance and diameter measurement, the age of the supernova remnant can be determined. However, as stated by Matonick & Fesen (1997), ground based measurements of supernova remnant diameter should be taken with caution because they can differ from 20% up to a factor of 3 in comparison with the same measurements made with the Hubble Space Telescope (see also, Blair & Davidsen, 1993). The overestimate of size can be blamed mainly on seeing – causing confusion between the supernova remnant and the surrounding material. That is, it is difficult to determine the edge of the supernova remnant. Blair & Davidsen (1993) also note that structure within the supernova remnant can be seen when using space-based observations. These are substantial arguments for using high-resolution imaging (space-based telescopes) for extragalactic supernova remnants.

3.4 The Observational Sample Base

The study of supernova remnants is best based in those found within the Galaxy because they are close enough to observe both the structural and dynamical details. Unfortunately, these observations are hampered by the gas and dust within the Galactic plane (the interstellar matter). Most Galactic supernova remnants are optically hidden (by nebulae or by long optical paths through the interstellar matter) and thus can be observed only in infrared (in nearby cases, if not also hidden by hot interstellar matter, e.g. Isensee et al., 2012), radio or in a very few cases, X-rays. X-rays are also hampered by the interstellar matter (Wilms et al., 2000). Generally, optically hidden supernova remnants are detectable or observable only in radio. It is also very difficult to determine distances to Galactic supernova remnants. The standard catalogue of Galactic supernova remnants currently contains 274 objects (Green, 2009).

Supernovae occur once per second in the universe[3] but they occur as naked-eye events only every few hundred years as can be seen in Table 2.1; and within the Galaxy as a whole about every 50 years (Diehl et al., 2006). To increase understanding of supernova remnants the sample of observable supernova remnants must be increased. This is done by finding and studying supernova remnants in neighbouring galaxies.

Mathewson & Clarke (1972) were the first to successfully argue for the observability and usefulness of extragalactic supernova remnants to increase understanding of supernova remnant properties. The primary galaxies for this task are those in the Local Group. The next closest group of galaxies is the Sculptor Group, of which NGC 300 is a member. Since that publication, almost 500 extragalactic supernova remnants have been discovered (e.g. Pannuti et al., 2007). As discussed below, observations of supernova remnants in all wavelengths are useful. Unfortunately, current technology limits our multi-wavelength observation of extragalactic supernova remnants to X-ray, optical and radio wavelengths (Duric, 2000a,b).

From the discussions in this chapter there are now three primary reasons for observing supernova remnants in nearby galaxies:

1. To further the understanding of supernova remnants by increasing the number of observable supernova remnants.

2. The Galactic interstellar matter blocks observation of all but the nearest supernova remnants within the Milky Way. Most Galactic supernova remnants are known only by their radio emissions. The interstellar matter can also produce significant extinction and reddening effects on those supernova remnants which can be seen optically.

3. Distance measurements to Galactic supernova remnants have large uncertainties which create large uncertainties in size, age and evolutionary stage. Extragalactic supernova remnants are all at the distance of the host galaxy and thus both distance and size are known to the accuracy of the galaxy distance measurement.

3.5 Supernova Remnant Observables

Multi-wavelength observations of supernova remnants provide greater understanding of their structure and dynamics. Figure 3.3 shows a composite image of radio, optical and X-ray emissions from the supernova

[3] A statement made by supernovae theorist, Sterling Colgate in the PBS Nova series episode, "The Death of a Star."

remnant, E0102 (1E0102.2−7219, in the Small Magellanic Cloud). The radio image (red, $\lambda = 6$ cm) was made using the Australia Telescope Compact Array (ATCA) and the radio emission is due to synchrotron radiation (Section 4.4). The optical image (green, [O III] λ 5007 Å) was taken by the Hubble Space Telescope and shows dense clumps of ionised oxygen tracing out a region of plasma with a temperature of about 3×10^5 K. The X-ray image (blue) taken by the Chandra X-ray Observatory shows gas that has been heated to millions of kelvins by a rebounding, or reverse shock wave. The X-ray spectrum shows that this material is rich in oxygen and neon (Ne) (Gaetz et al., 2000).

Supernova remnants are known to emit in all regions of the electromagnetic spectrum. For example, 82 of the known 137 supernova remnants in M 33 are detected in both optical and X-ray wavelengths (Long et al., 2010). Understanding the sources or causes of these emissions provides a deeper understanding of the structure, dynamics and evolution of supernova remnants. Many papers discuss observations from multiple electromagnetic regions, with the discussion including relationships or correlations between the observations (for example: PF04; MWF11; Bouchet & Danziger, 2010). This section provides short descriptions with possible causes of the observable emissions from supernova remnants.

3.5.1 Gamma Rays

Intense gamma-rays are produced by the supernova and by the supernova remnant during the first few months of its existence while the iron-group elements go through their radioactive decays. This was observed in SN 1987A (Sandie et al., 1988). Hundreds of years after the supernova event, gamma-ray emissions may be seen from the decay of other elements, such as the 1.16 MeV line emission of ^{44}Ti observed from the 300 year old supernova remnant, Cas A (Lang et al., 2010). Though it is not well understood, at later evolutionary stages gamma-rays may be produced by relativistic protons (cosmic rays) or other particles accelerated by their interaction with the magnetic fields of the supernova remnant or the neutron star within it (Abdo et al., 2010). High-energy gamma-rays are probably produced by the inverse Compton scattering of electrons (see Section 4.5) or neutral pion decay after proton-proton collisions as the supernova remnant is interacting with nearby molecular clouds (Uchiyama, 2011). Most gamma-ray emissions occur during the first stage of supernova remnant expansion (Section 3.1). Gamma-ray emissions may help to establish the age of the supernova remnant. Unfortunately, current gamma-ray detector technology is not sufficiently sensitive to observe extragalactic supernova remnants.

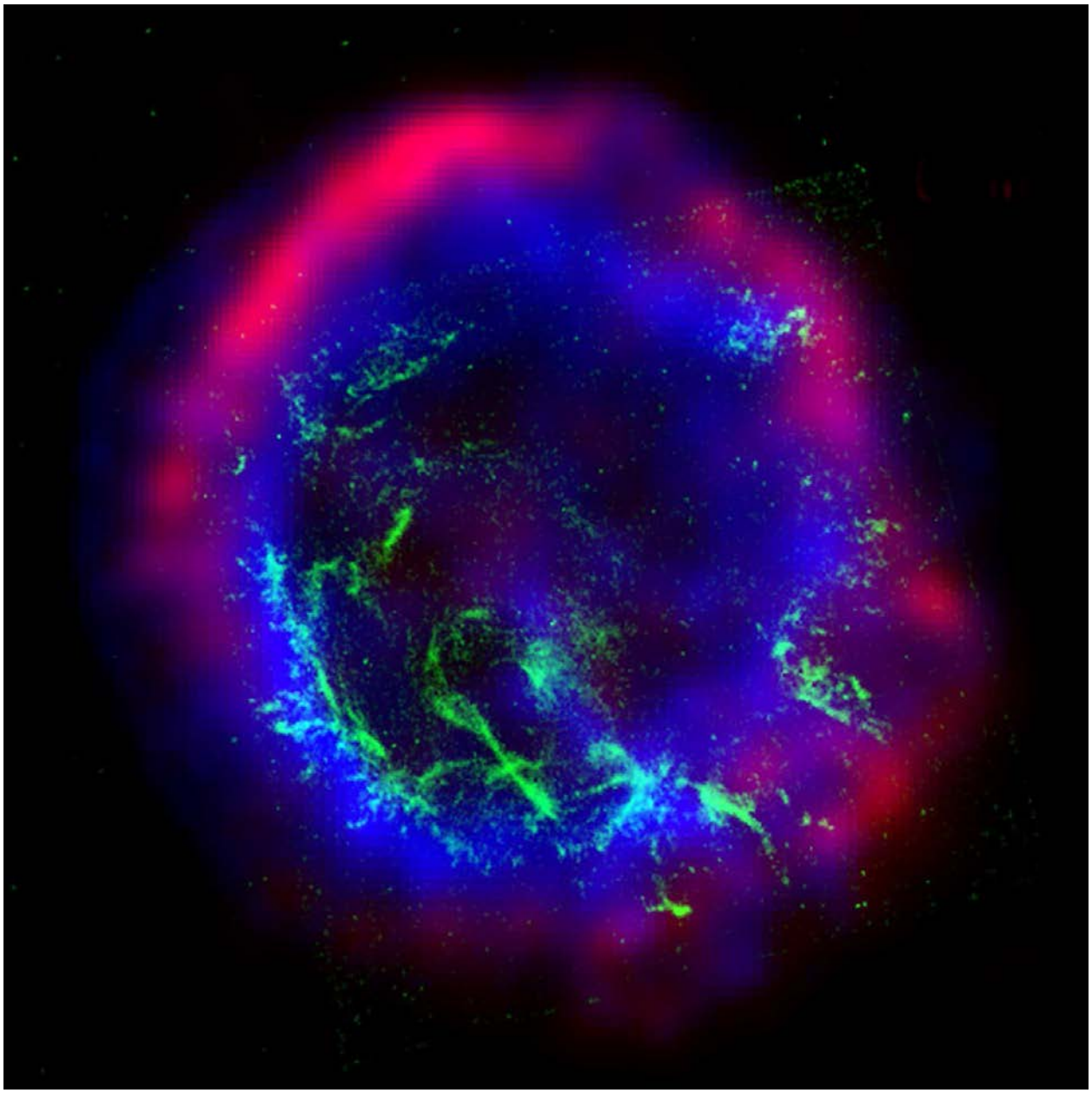

Figure 3.3: A multi-wavelength image of the supernova remnant E0102 in the Small Magellanic Cloud, at a distance of 190,000 light-years. (Credit: X-ray: NASA/CXC/SAO, Optical: NASA/HST, Radio: CSIRO/ATNF/ATCA.)

3.5.2 X-rays

X-ray emissions are important to the study of supernova remnants and supernovae because they provide information about the energy of the explosion and the nature and composition of the stellar ejecta and the interstellar matter (Canizares, 1990). X-ray observatories must be space-based as cosmic X-rays cannot pass through the Earth's atmosphere. The Uhuru satellite (December 1970 to March 1973) was one of the first X-ray observatories and found X-ray emissions from several supernova remnants. The Einstein (November 1978 to April 1981, the first imaging X-ray observatory), Ginga (February 1987 to November 1991) and ROSAT (Röntgensatellit, June 1990 to February 1999) observatories had a large impact on supernova remnant observations.

The most productive observatories were the Chandra X-ray Observatory (launched July 1999) and XMM-Newton (X-ray Multi-Mirror Mission, launched December 1999). A broad overview of these two missions is given by Paerels & Kahn (2003). Section 6 of this paper explicitly states the need for X-ray observations of supernova remnants:

> "The rationale for high-resolution spectroscopy of supernova remnants is clear: Abundance measurements allow typing of the supernova, a direct determination of the outcome of nucleosynthesis and the details of the explosion, and measurement of velocity fields provides information on the dynamics, the explosion energy, and the age of the remnant."

Weisskopf et al. (2002) also gives an overview of the Chandra telescope (covering supernova remnants in section 4.1.3) showing an excellent example of the improved resolution of Chandra over ROSAT by comparing side-by-side images of Cas A from both observatories. The location of the emitting atoms/ions within the supernova remnant structure can be used to infer the intensity and direction of shock fronts. The Chandra X-ray Observatory was able to find such structure in supernova remnants (Paerels & Kahn, 2003).

X-ray emissions can be either thermal or synchrotron – the difference is discerned by polarisation. Thermal X-rays indicate high temperatures (up to $> 10^7$ K) generally seen from the supernova remnant's forward shock front. The supernova remnant ejecta within the shell are initially cold but can be heated by the reverse shock as the shell expands in the interstellar matter. The heated material may emit both thermal (continuous) and spectral-line X-rays. The thermal X-rays will fall off quickly in young supernova remnants (Drury et al., 2009), helping to determine the age of supernova remnants. X-ray band synchrotron radiation indicates relativistic charged particles in strong magnetic fields – for example, the synchrotron radiation caused by TeV electrons being accelerated by the post-shock magnetic field (Bamba et al., 2000). There are thus thermal and non-thermal

X-ray emissions from supernova remnants (Borkowski et al., 2001).

Supernova remnant X-ray emissions are well studied in papers such as Kong et al. (2004), Badenes et al. (2005), Giacani et al. (2005), Immler & Kuntz (2005), Vink (2005, 2006), Rakowski et al. (2006), Lazendic et al. (2006), Torii et al. (2006) and many others. Both Galactic supernova remnants and extragalactic supernova remnants have been studied in X-rays (Pannuti et al., 2007; Long et al., 2010). There are about 50 X-ray supernova remnants in the Galaxy (Canizares, 1990).

The sensitivity and resolution of X-ray detectors are still too low to detect structural detail in extragalactic supernova remnants similar to that made in Galactic supernova remnants. However, spectral X-ray studies can be made on extragalactic supernova remnants. These measurements are converted into "hardness ratios." Unlike optical observations, these low count X-ray observations cannot produce a usable spectral (energy) distribution. Hardness ratios show rough spectral properties for these low count observations (such as extragalactic supernova remnants, e.g., PF04). Hardness ratios (HR) are generally defined as the ratio of counts in different X-ray energy bands.

Haberl & Pietsch (1999) proposed an X-ray hardness ratio test for detecting supernova remnants. Using the ROSAT PSPC instrument for a survey of the Large Magellanic Cloud, they define the following energy ranges: S = 0.1–0.4 keV, H = 0.4–2.0 keV; H1 = 0.5–0.9 keV and H2 = 0.9–2.0 keV. With these energy ranges they define two hardness ratios as: HR1 = (H–S)/(H+S) and HR2 = (H2–H1)/(H1+H2). These hardness ratios are indicators of the X-ray spectrum. Section 3.4 of Haberl & Pietsch (1999) then discusses how these hardness ratios are used to classify the X-ray sources within a parameter space of HR1:HR2. Supernova remnants are found with HR1 > 0.25 and $-0.70 <$ HR2 < 0.25

Because hydrogen atoms are very good at absorbing X-rays (see page 51) the hydrogen column density (N_H) cannot be ignored in X-ray observations (spectra). N_H is not easily determined because there is no reliable spectral fit. Hardness ratios can be used to quantify N_H, which in turn can be used to determine important information such as the characteristics of the interstellar environment surrounding the X-ray source. These topics are discussed further by Jin et al. (2006) and references therein.

3.5.3 Ultraviolet

Ultraviolet line emissions can provide indications of shock velocities in the supernova remnant (Sankrit et al., 2003). Pre-shock densities and the abundance of elements having no bright optical lines (e.g. carbon) can be

derived from ultraviolet observations (Ghavamian et al., 2006). These shock velocity measurements can aid with supernova remnant identification by breaking the abundance/shock velocity ambiguity in the [O III] lines because the ultraviolet emissions are due mainly to shock excitation. The International Ultraviolet Explorer (IUE) was the most prolific observer of cosmic ultraviolet and the nearby Galactic supernova remnants were observed but most extragalactic supernova remnants were too faint to have been seen by the IUE (Blair & Davidsen, 1993). Blair et al. (2006) used the Far Ultraviolet Spectroscopic Explorer (FUSE) observatory to observe supernova remnants in the Large and Small Magellanic Clouds. The detected supernova remnants ranged from "relatively small, bright objects to large (old) shells, and from both X-ray shells and filled-centre morphologies." There are currently no active ultraviolet observatories.

3.5.4 Optical

Both continuous (thermal) and spectral line emissions are observed in optical. Most optical spectrum emissions are caused by shock heated gas and include many ionic forbidden transitions (for examples, see Table C.2). Specific emission line flux density measurements are made and studied for identification of supernova remnants. The most important of these are Hα and the sulphur doublet [S II] $\lambda\lambda$ 6716, 6732 Å (see also Table 4.6). In Galactic supernova remnants the total [S II] flux (λ 6716 Å + λ 6732 Å) to Hα integrated flux density ([S II]:Hα) shows a value of at least 0.4. This ratio value is used as the first step in finding extragalactic supernova remnants (BL97, WMF11, WMF12 and references therein). The [S II] lines may be produced by the abundance of 10^4 K electrons in the shock fronts of the expanding supernova remnants. These electrons have sufficient energy to provide the 1.85 eV excitation for these optical transitions (Dopita et al., 1984).

Also, because [O I] $\lambda\lambda$ 6300, 6364 Å and [O III] λ 5007 Å lines are produced by shocked material, their presence in a candidate supernova remnant's spectra is used to support the identity of the candidate. The ratio of the individual [S II] line fluxes (λ 6716 Å/λ 6732 Å and also [O II] λ 3729 Å/λ 3726 Å) can be used to determine the electron density in the remnant. [O III] and [N II] lines can be used to determine supernova remnant plasma temperatures (Osterbrock & Ferland, 2006).

3.5.5 Infrared

Infrared emissions from supernova remnants are expected from mechanisms such as atomic and molecular line emission (see for example Table 4.1), hot gas free-free emission (bremsstrahlung radiation, see Section 4.3),

synchrotron radiation (Section 4.4), polycyclic aromatic hydrocarbons (PAHs, Rho et al., 2011), and atomic fine-structure lines (Reach & Rho, 1999). The free-free (thermal bremsstrahlung) and synchrotron radiation at infrared wavelengths should be minimal so supernova remnant infrared observations should be dominated by thermal dust emissions or line emissions or both (Williams et al., 2006). Red giant stars are thought to be a significant source of inter-stellar dust with a portion of the dust surviving the supernova and supernova remnant shocks (for discussions see, Dunne et al., 2003; Bianchi & Schneider, 2007; Reynoso et al., 2010). As much as 4 $M_{\odot}$ of dust may be produced by Type II supernovae with infrared thermal continuum emissions due to dust grains heated by radiation or collisions to temperatures of ∼100 K (Williams et al., 2006, and references therein). These dust grains can be slowly destroyed by collisional sputtering, shock waves and intense radiation. There is evidence for suggesting that in the supernova remnant Kes 75 (G29.7-0.3) the dust is collisionally heated by the X-ray emitting gas (Temim et al., 2012).

Inelastic dust-atom/ion collisions tend to cool the supernova remnant plasma. The temperature of the dust is a balance between its radiative and collisional heating and its surface emission (Chevalier, 1990). Infrared research on supernova remnants is mainly concerned with the apparent low amount of dust found in supernova remnants that show thermal dust emission. Observations with the Spitzer Space Telescope show dust levels as much as 100 times too low compared to expected theoretical supernova model results (Stanimirović et al., 2005). Infrared observations are also concerned with dust abundance and dust composition in supernova remnants, and what these data indicate concerning the progenitor supernova's type and progenitor star.

3.5.6 Radio

Radio observations of supernova remnants have been made since the late 1940s. The first discrete radio source was found in Cygnus ("Cygnus A") in 1946. Ryle & Smith (1948) discovered a powerful discrete radio source in Cassiopeia in 1948 (using an interferometer). Minkowski and Baade later identified it as a supernova remnant from a Type II supernova and it was labelled "Cassiopeia A," (Cas A) as the most powerful radio source in Cassiopeia. Ryle et al. (1965) produced a high resolution map of Cas A at $\lambda = 21.3$ cm.

The early radio observations of the Crab Nebula (M 1) are discussed extensively in Shklovsky (1968) and Mitton (1978). Although some radio emissions are thermal, these are generally at a low level and the main mechanism for radio emissions is synchrotron radiation. The source of energy for the synchrotron radiation emissions is either the pulsar at the centre of the supernova remnant (particularly for plerions) or the collision

of the supernova remnant with the circumstellar matter or interstellar matter (particularly for shell type). The supernova itself does not create any radio emissions (except, see Sramek & Weiler, 1990).

A model for radio emission from young and middle aged supernova remnants using the "diffusive shock acceleration" was published by Asvarov (2000). Diffusive shock acceleration is related to first order Fermi acceleration. It is an acceleration that charged particles experience when repeatedly reflected, usually by a magnetic mirror. (A magnetic mirror is a magnetic field structure where the field strength changes as charged particles move along the field lines. The charged particles tend to bounce back from the greater strength field region.) This may be the primary mechanism for particles to gain non-thermal energies in supernova remnant shock fronts. For the mechanism to be effective the particle environment must be collisionless because Fermi acceleration applies only to particles with energies greater than the thermal energies and frequent collisions causes energy loss resulting in no such acceleration.

By the 1970s radio telescope technology had evolved to enough sensitivity and resolution to undeniably detect direct supernova remnant radio emission and telescope sensitivity and resolution have increased drastically since then. Radio emission may appear perhaps one year after the supernova as the supernova remnant interacts with the circumstellar matter, or decades after the supernova when the ejecta becomes transparent enough to detect the radio emissions of the enclosed pulsar or the emissions caused by the interaction of the pulsar's magnetic field with the supernova remnant material. According to one model for supernova radio emissions (focused on shell type supernova remnants) the delay in radio emissions is caused by free-free absorption (see Section 4.3) of radio by the (ionised and thus, radio thick) circumstellar matter, the main source of which was the progenitor star's stellar wind (Sramek & Weiler, 1990).

The biggest problem for observing with high resolution radio interferometers is the loss of flux on the large scale. In order to accurately measure flux from the remnant the telescope needs to see the entire remnant, but doing so loses resolution and thus structural detail. A possible solution to the problem of obtaining detail and accurate flux measurement was suggested by Dyer et al. (2005) by combining high resolution (interferometer) and low resolution (single dish) observations.

There is a relationship between the radio surface brightness (Σ) and the diameter (D) of supernova remnants (the Σ D relation). A formulation of the relationship based on 36 Galactic supernova remnants of known distance was published by Case & Bhattacharya (1998). This relation takes the form of

$$\Sigma = AD^{-\beta}, \tag{3.1}$$

where the parameter A and the slope β are obtained by fitting the observational data for a sample of supernova remnants. It has been argued by some that this relationship doesn't work very well for estimating distances to Galactic supernova remnants because it needs to have known distances to be calibrated. However, recent work shows it can be used (with caution) for extragalactic supernova remnants where the supernova remnant distances are equal to the galaxy's distance (Urošević et al., 2010).

The number of GeV electrons is much greater than the number of TeV electrons in a supernova remnant. GeV electrons create powerful synchrotron radiation emissions in the radio electromagnetic region. This is the dominant source of radio emissions in supernova remnants. All supernova remnants emit radio and most supernova remnants (Galactic and extragalactic) are discovered by their radio emissions. Because of the high absorption of optical and X-ray wavelengths by the interstellar matter, the majority of the Galactic supernova remnants are known only from their radio emissions (Strom, 1996) with at least 170 known while only a few are visible in optical light (Fesen, 1996).

Non-thermal radio emissions from supernova remnants can be described by a power law,

$$I_\nu \propto \nu^{-\alpha}, \tag{3.2}$$

where I_ν is the integrated flux density in janskys, ν is frequency and α is the spectral index (see Section 4.4). For Galactic supernova remnants the spectral index falls between 0.2 and 0.8. A spectral index in this range is used to identify extragalactic supernova remnants from radio surveys. If a break (sudden change) is found in the spectral index at some frequency, the frequency of the break may be used to determine the magnetic field strength within the supernova remnant (Strom, 1996).

Radio emissions should be observed at all stages in the evolution of a supernova remnant. They are generally more intense in the younger stages but they are observed even in the oldest supernova remnants. However there is evidence to show that radio emission from supernova remnants is dependent on the density of the ambient medium (Duric, 2000a, and references therein).

Chapter 4

Supernova Remnant Emission Mechanisms

The central principle of multi-wavelength astronomy is to collect spectral data of the radiation from multiple bands of the electromagnetic spectrum and then use concurrent analysis of these data to determine the nature of the object creating the emissions. There are a number of physical mechanisms causing the emission of electromagnetic radiation from supernova remnants. Because this thesis is concerned with extragalactic supernova remnants only those mechanisms associated with the observable emissions from extragalactic supernova remnants – X-ray, optical and radio – are discussed. This chapter is intended as an overview only – not as an in-depth discussion. The main intention of this chapter is to introduce concepts, terms and symbols used in this thesis. The material in this chapter is adapted from a few of the many books covering the subjects – Aller (1991), Carroll & Ostlie (1996), Harwit (1988), Lang (1980), Osterbrock & Ferland (2006) and Smith (1995). Some statements or conclusions are given specific references.

Isaac Newton introduced the term "spectrum" while studying the dispersion of sunlight through prisms. William Wollaston[1] was the first to observe a few dark lines in the solar spectrum but failed to see any significance in their presence. Joseph Fraunhofer[2], while working to improve the performance of prisms, found over 570 dark lines in the solar spectrum and wrote an analysis of their wavelengths. These dark lines have since been known as the Fraunhofer lines.

[1] William Hyde Wollaston (1766–1828), English chemist. He thought the dark lines were the "edges" of the primary colours.

[2] Joseph von Fraunhofer (1787–1826), German optician. Fraunhofer labelled the lines with letters. Hence, the "sodium D lines."

Modern spectroscopy began with the light emitted by burning substances. Physicists and chemists like Ångström[3], Alter[4], Kirchhoff, Bunsen[5] and others observed the emission and absorption of optical wavelengths in various experiments in their laboratories in the early and mid-1800s. They discovered how to determine the chemical composition of substances from the spectra they produce. In 1859, Kirchhoff published his three laws of radiation (known as Kirchhoff's radiation laws):

1. A hot solid, liquid, or gas under high pressure, gives of a continuous spectrum. (This was the first observation of what became known as black body radiation.)

2. A hot gas under low pressure produces a bright-line or emission line spectrum.

3. A dark-line or absorption spectrum is seen when a continuous source to viewed through a cool gas under pressure.

The second and third laws are related by the critically important observation that the wavelengths of the emitted lines from the hot gas and the absorbed lines in the cool gas are the same. The modern concepts of the atom were not introduced until more than 60 years after Kirchhoff's radiation laws and so he could not have truly understood the origin of these laws – the conservation and quantisation of energy, and atomic theory.

4.1 Basic Definitions

Before describing these important process of emission, some basic definitions of physical quantities and mathematical symbols are needed. The fundamental basis of all electromagnetic radiation is in Maxwell's equations, which also define the fundamental quantities of electricity and magnetism. Written in terms of free charge and

[3]Anders Ångström (1814–1874) Swedish physicist and one of the founders of spectroscopy. He was also keeper of the Uppsala Astronomical Observatory.

[4]David Alter (1807–1881), American inventor and scientist, was the first to propose that every element may have its own emission spectrum (1854).

[5]Robert Bunsen (1811–1899), German chemist was a major contributor to the study of emission spectra of burning elements. The Bunsen burner is named for him. He (and Kirchhoff) discovered the elements caesium and rubidium by solar spectroscopy (1861).

currents (as found in plasmas and supernova remnants) the equations are (modified from Lang, 1980),

$$\begin{aligned} \nabla \times \mathbf{H} - \frac{1}{c}\frac{\partial \mathbf{D}}{\partial t} &= \frac{4\pi}{c}\mathbf{J} \\ \nabla \cdot \mathbf{B} &= 0 \\ \nabla \times \mathbf{E} + \frac{1}{c}\frac{\partial \mathbf{B}}{\partial t} &= 0 \\ \nabla \cdot \mathbf{D} &= 4\pi\rho, \end{aligned} \tag{4.1}$$

where $\mathbf{H}$ is the magnetising force, $\mathbf{B}$ is the magnetic field intensity, $\mathbf{E}$ is the electric field intensity, $\mathbf{D}$ is the electric displacement field, $\mathbf{J}$ is the free electric current density and ρ is the free (unbound) electric charge. We also have,

$$\begin{aligned} \mathbf{B} &= \mu\mathbf{H} \\ \mathbf{D} &= \varepsilon\mathbf{E} \\ \mathbf{J} &= \rho\mathbf{v}, \end{aligned} \tag{4.2}$$

where μ is the magnetic permeability, ε is the electric permittivity and $\mathbf{v}$ is the velocity of the free moving charge. The energy density (U) of the electromagnetic field is,

$$U = U_E + U_H = \frac{\varepsilon}{8\pi}E^2 + \frac{\mu}{8\pi}H^2 = \frac{1}{8\pi}\left[\mathbf{E}\cdot\mathbf{D} + \mathbf{B}\cdot\mathbf{H}\right]. \tag{4.3}$$

For time-varying electromagnetic fields the amount of energy passing through a unit surface (normal to $\mathbf{E}$ and $\mathbf{H}$) per unit time is given by the magnitude of the Poynting vector,

$$\mathbf{S} = \frac{c}{4\pi}\left(\mathbf{E}\times\mathbf{H}\right). \tag{4.4}$$

Planar electromagnetic waves are governed by the wave equation which is derived from Maxwell's equations:

$$\nabla^2 E - \frac{\mu\varepsilon}{c^2}\frac{\partial^2 E}{\partial t^2} = 0 \quad \text{and} \quad \nabla^2 H - \frac{\mu\varepsilon}{c^2}\frac{\partial^2 H}{\partial t^2} = 0. \tag{4.5}$$

The energy flux in the direction of the plane wave is,

$$S = \frac{c}{4\pi}\sqrt{\frac{\varepsilon}{\mu}}E^2 = \frac{c}{4\pi}\sqrt{\frac{\mu}{\varepsilon}}H^2. \tag{4.6}$$

The energy density in the plane wave is,

$$U = \frac{\varepsilon E^2}{4\pi} = \frac{\mu H^2}{4\pi}. \tag{4.7}$$

4.2 Black Body Radiation

Thermal radiation or black body radiation[6] from supernova remnants is the result of collisional heating of gas and dust particles. Black body radiation was one of the two foundation experiments (the other was the photoelectric effect) of quantum mechanics. Explained by Max Planck in 1900, black body radiation assumes that electromagnetic radiation is released in discrete packages of energy called "quanta." These quanta have since become known as photons. The energy carried by a photon is given by

$$E = h\nu = \frac{hc}{\lambda}, \tag{4.8}$$

where h is Planck's constant. The energy is linear with frequency and inverse with wavelength. The momentum carried by a photon is given by

$$p = \frac{h}{\lambda} = \frac{h\nu}{c}. \tag{4.9}$$

Any body or material with a temperature above 0 K emits photons as black body radiation. Black body radiation has three general characteristics, with specific characteristics given by the temperature of the object. The three general characteristics defining the properties of black body radiation are:

1. The intensity of the radiation as a function of frequency has a particular shape. As frequency decreases, there is a steep rise in the intensity until it reaches a maximum value, then a slower decline in intensity as the frequency continues to decrease (Figure 4.1).

2. The wavelength of the radiation at maximum intensity is proportional to the inverse of the body's temperature, T. This is Wien's displacement law[7]. In terms of frequency the law is written as,

$$\nu_{max} \approx \frac{3kT}{h} \approx 6 \times 10^{10} T \tag{4.10}$$

or in terms of wavelength as,

$$\lambda_{max} \approx \frac{0.51}{T}. \tag{4.11}$$

Wien's displacement law shows the relationship between the colour of a glowing object and its temperature. The colour of the glow moves from red to orange, to yellow, to white and then to blue as the object's temperature is increased. As the temperature increases to the point where ν_{max} lies in the ultraviolet or X-ray regions, there is still enough blue light emitted to make the object visible. At much lower

[6] A term coined by Gustav Kirchhoff in 1862.

[7] Wilhelm Carl Wien (1864-1928) German physicist. He proposed this law in 1893.

temperatures, the object may not emit optical photons but it will emit infrared or microwave radiation, so it can be detected with the proper telescope.

3. The total energy emitted per unit area of surface, E_A (summed over the entire electromagnetic spectrum) is proportional to the body's temperature raised to the fourth power (Stefan-Boltzmann Law). Thus,

$$E_A \propto \sigma T^4, \tag{4.12}$$

where $\sigma = 5.6704 \times 10^{-5}$ erg s^{-1} cm^{-2} K^{-4} is known as the Stefan-Boltzmann constant[8]. This is equivalent to finding the area under the curve shown in Figure 4.1. This gives the relationship between the temperature of a body and its luminosity.

The total energy emitted from the surface of the object, E, is then

$$E = E_A A \propto \sigma T^4 A, \tag{4.13}$$

where A is the body's surface area. However, A may be difficult to determine for supernova remnants.

Max Planck combined these features into one formulation, now called Planck's Law (of black body radiation).

$$\mathcal{F}_\nu(T) = \frac{2h\nu^3}{c^2}\left[\frac{1}{\exp\left(\frac{h\nu}{kT}\right)-1}\right] \qquad \text{(Planck's law)} \tag{4.14}$$

$$= \frac{2h\nu^3 n_\nu^2}{c^2}\exp(-\frac{h\nu}{kT}) \qquad (h\nu \gg kT, \text{ Wien's law}) \tag{4.15}$$

$$= \frac{2n_\nu^2\nu^2 kT}{c^2} \qquad (h\nu \ll kT, \text{ Rayleigh-Jeans law}), \tag{4.16}$$

where $\mathcal{F}_\nu(T)$ is the energy emitted per unit area (flux density) per unit frequency, (ν), as a function of temperature (T, in kelvins), h is Planck's constant, k is Boltzmann's constant and n_ν is the index of refraction of the material at frequency ν. Wien's law and the Rayleigh-Jeans law are empirical, and are both derivable from Planck's law. Planck's law creates the curves shown in Figure 4.1.

The total black body radiation intensity is given by

$$I = \frac{\sigma n_\nu^2}{\pi} T^4 \tag{4.17}$$

and the radiated energy density is

$$U = aT^4 n_\nu^3, \tag{4.18}$$

where $a = 4\sigma/c$ is the radiation density constant.

[8]Sigma is not a fundamental constant. $\sigma = \frac{2\pi^5 k^4}{15c^2h^3}$

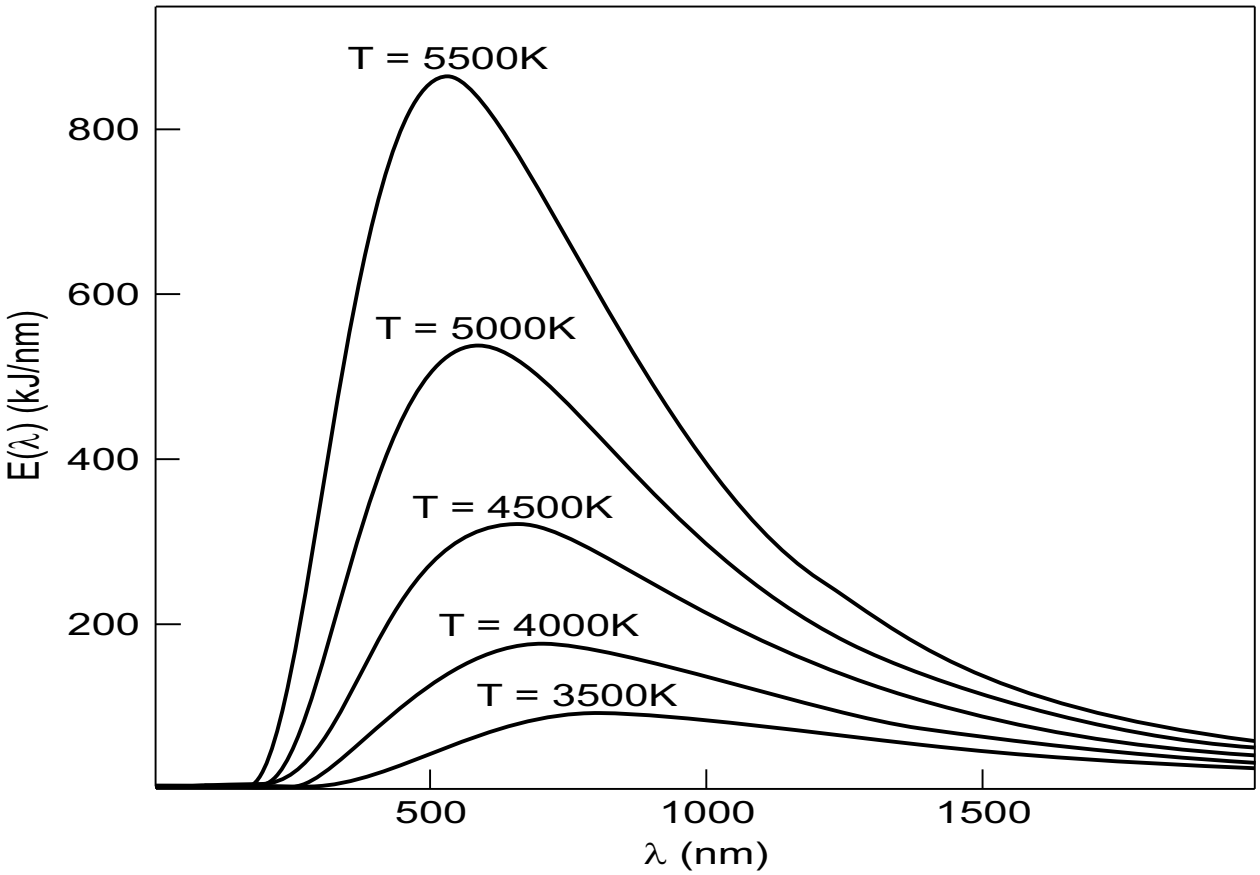

Figure 4.1: The relationship between temperature and energy emission, as discovered by Wien and explained by Max Planck. The total energy emitted for a given temperature is proportional to the area under the curve for that temperature.

Real objects never behave as true black body radiators. At any given frequency, their emission is always a fraction of the intensity predicted by Planck's law. The emissivity, ϵ, of the body's material describes how well the body emits as compared to a true black body. Emissivity depends on factors such as frequency, temperature, emission angle and chemical composition. It is equal to the ratio of the intensity of emissions from a surface to the intensity of the emissions of a true black body at the same temperature. Equation 4.13 becomes (Lang, 1980),

$$E = \epsilon E_A A = \epsilon \sigma T^4 A. \tag{4.19}$$

To determine the energy emitted over the entire electromagnetic spectrum from the entire surface we have

$$E = \int_0^\infty \epsilon(\nu, \ldots)\Phi_\nu(T)\,\mathrm{d}\,\nu \int \mathrm{d}\,A. \tag{4.20}$$

The grey body approximation is the case where the emission spectrum of the body follows a black body emission except it is independent of frequency and has lower level emissivity related to black body emissivity by a constant. An object in thermal equilibrium which does not absorb all incident radiation will emit less energy than a black body radiator at the same temperature.

While stars can only be poorly modelled as black body radiators, gas and dust clouds (e.g. supernova remnants) come reasonably close to emitting a black body spectrum. If the λ_{max} for a supernova remnant is in infrared, black body radiation provides the temperature of the dust in the supernova remnant.

4.3 Thermal Bremsstrahlung Radiation

Bremsstrahlung comes from combining the German words for braking and radiation – "braking radiation." It is created when a charged particle such as an electron is decelerated by interacting with another charged particle such as an atomic nucleus. The electron loses kinetic energy which is converted into a photon. Bremsstrahlung emitted by a plasma can be referred to as free-free radiation because the electrons producing the photons are free both before and after the interaction causing the emission. Thermal bremsstrahlung is the dominant emission mechanism for H II regions at radio wavelengths (Brown, 1987). Additionally, thermal bremsstrahlung radiation should be expected from supernova remnants (Straka & Lada, 1975) and has been used to study the Σ D relationship for supernova remnants (Urosevic et al., 2003a,b). Thermal bremsstrahlung emissions have been used to study discrepancies between theoretical derived and measured values of the Σ D relationship for supernova remnants. These discrepancies may be caused in part by supernova remnants being is various stages

of evolution while contained within various environments (Urošević & Pannuti, 2005).

The inverse of bremsstrahlung is called free-free absorption. In this case the electron's kinetic energy is increased by absorbing a photon. This can only happen if the electron absorbs the photon while it is near an ion (nucleus) because the ion must be used to conserve energy and momentum. This is a major contributor to the opacity (optical thickness) of the plasma.

4.4 Synchrotron Radiation

This section is adapted from sections 6.18 and 6.19 of Harwit (1988). When a charged particle moves across the lines of a magnetic field, the Lorentz force requires it to follow a spiral path. At each instant of the motion the axis of the spiral is tangent to the magnetic field lines and the acceleration experienced by the particle is perpendicular to the field lines. Thus, as the particle moves the direction of acceleration continually changes and the corresponding change in velocity of the particle causes the emission of electromagnetic radiation. If the charge (usually an electron) is moving at relativistic speed, this acceleration of the charge produces electromagnetic radiation called synchrotron radiation (if the circular motion around the field line dominates) or curvature radiation (if the motion is primarily along the field lines). In either case the radiation is strongly linearly polarised, in the plane of the circular motion for synchrotron radiation and in the plane of the curved magnetic field line for curvature radiation (Carroll & Ostlie, 1996).

Analysis of the (simplified as non-relativistic, planar) motion of the charge allows the calculation of the radius of gyration (the Lamor radius, R_L) and the frequency of gyration (the gyrofrequency, ω_c, sometimes called the cyclotron frequency). These are,

$$R_L = \frac{p_c c}{qB} \tag{4.21}$$

and

$$\omega_c = \frac{v_c}{R_L} = \frac{qBv_c}{p_c c} \tag{4.22}$$

respectively, where B is the magnetic field strength, and p_c is the transverse momentum, q is the charge and v_c is the circular velocity of the particle. When the particle is a relativistic electron, the gyrofrequency becomes

$$\omega_c = \frac{eB}{m_0 \gamma c}, \tag{4.23}$$

where γ is the usual relativistic Lorenz factor, e is the charge and m_0 the rest mass of an electron. However, because of the relativistic effect of concentrating the emitted radiation into a narrow beam in the direction

of the electron's motion, the emitted radiation has frequencies many orders of magnitude greater than this gyrofrequency. This means the observer is properly orientated to receive the radiation during only a small time interval for each orbit of the electron. Analysis of this condition leads to an actual radiated frequency of

$$\omega_m \sim \gamma^2 \omega_c = \frac{eB}{m_0 c} \left(\frac{E}{m_0 c^2} \right)^2, \tag{4.24}$$

where E is the total energy of the particle ($E \gg m_0 c^2$). When the analysis is done with rigour on mono-energetic electrons the spectrum of the radiation is a set of finely spaced lines at high harmonics of ω_m. The envelope of those lines is shown in Figure 4.2. The energy radiated per unit time per unit frequency interval ($\mathrm{d}\nu$) by a particle with energy $\mathcal{E}$ is

$$P(\nu, \mathcal{E}) = 2\pi \, P(\omega, \mathcal{E}) = \frac{16 e^3 B}{m_0 c^2} p(\omega/\omega_m). \tag{4.25}$$

The function $p(\omega/\omega_m)$ has as limits at high and low frequencies,

$$p(\omega/\omega_m) = 0.256 \left(\frac{\omega}{\omega_m} \right)^{1/3} \qquad (\omega \ll \omega_m), \tag{4.26}$$

$$p(\omega/\omega_m) = \frac{1}{16} \left(\frac{\pi \omega}{\omega_m} \right)^{1/2} \exp\left(-\frac{2\omega}{3\omega_m} \right) \qquad (\omega \gg \omega_m). \tag{4.27}$$

The exact form of the spectrum (Figure 4.2) depends on the energy spectrum of the radiating particles and the function $P(\nu, \mathcal{E})$. The spectral intensity at frequency ν (I_ν) is found by integrating at different distances r along the line of sight out to some distance R. The result is

$$I_\nu \, \mathrm{d}\nu = \int_0^{\mathcal{E}_{max}} \int_0^R P(\nu, \mathcal{E}) n(\mathcal{E}, r) \, \mathrm{d}r \, \mathrm{d}\mathcal{E} \, \mathrm{d}\nu, \tag{4.28}$$

where $n(\mathcal{E}, r)$ is the number density of particles of energy $\mathcal{E}$ at distance r. Observations of synchrotron sources frequently encounter the situation where $n(\mathcal{E}, r) \propto \mathcal{E}^{-\varphi}$, so the number density of electrons with energy $\mathcal{E}$ is proportional to the energy raised to a constant exponent. In this situation the spectral intensity obeys the relation $I_\nu \propto \nu^{-\alpha}$, where $\alpha = (\varphi - 1)/2$. If every electron's radiated power is at ω_m, then equation 4.24 shows that $\mathcal{E}^{-\varphi} \propto \omega_m^{-\varphi/2}$ and so $\Delta\mathcal{E} \propto \Delta\omega/\omega_m^{1/2}$. Then for a constant spectrum along the path of integration, the total radiated power (eq. 4.28) obeys the proportional relation

$$I(\nu)\Delta\nu \; \propto \; \omega_m \mathcal{E}^{-\varphi} \Delta\mathcal{E} \; \propto \; \omega_m^{(1-\varphi)/2} \Delta\omega. \tag{4.29}$$

This then gives

$$I(\nu) \; \propto \; \nu^{-\alpha} \qquad \text{with} \qquad \alpha = \frac{\varphi - 1}{2}, \tag{4.30}$$

where α is the spectral index. This equation is equivalent to equation 3.2.

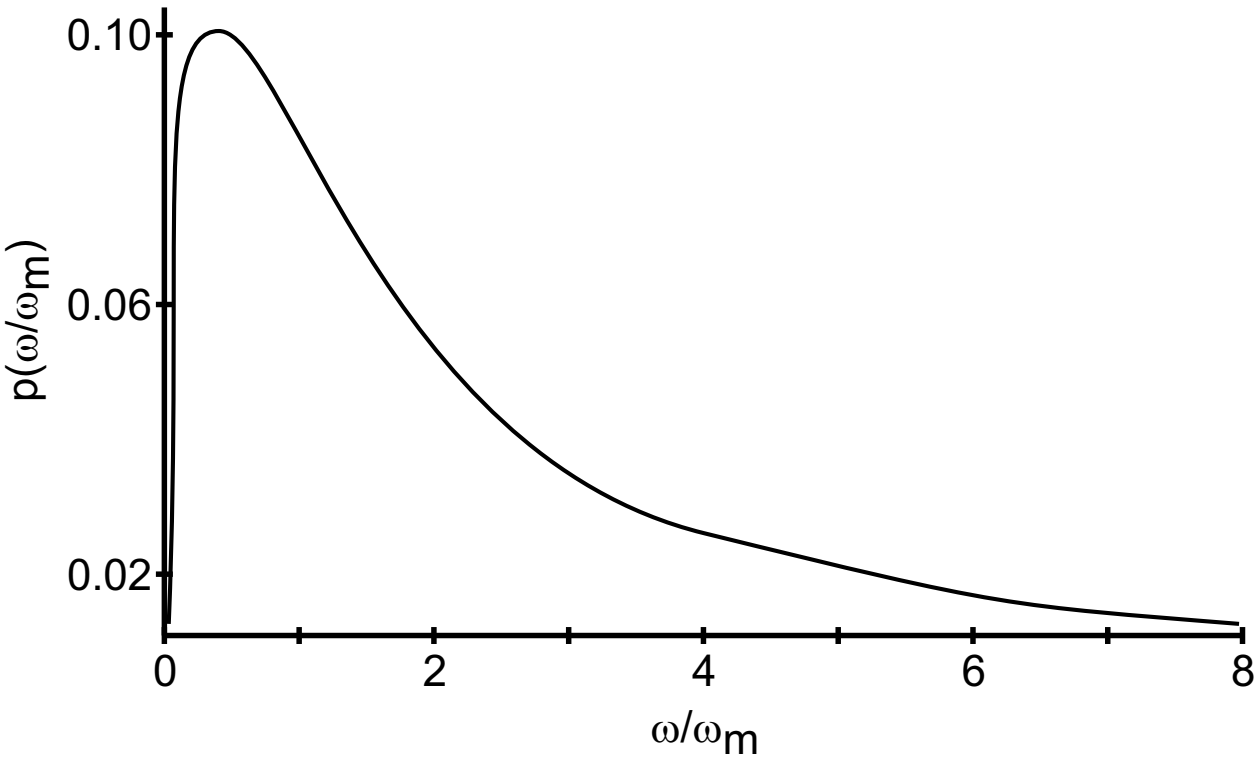

Figure 4.2: The envelope of the narrowly spaced spectral lines of synchrotron radiation. (From Harwit, 1988, after Shklovskii (1960).)

For this relationship between the electron energy and the radiation spectrum to hold, the emission source must be optically thin (not self absorbing). For most non-thermal sources, $0.2 \lesssim \alpha \lesssim 1.2$ (Harwit, 1988). Equations 3.2 and 4.30 are important because they allow us to estimate the relativistic electron energy spectrum by observing the synchrotron radiation. If $I(\nu)$ is related to black body radiation then $\mathcal{E} \sim kT$. The electron energy (which determines the temperature of the body) can be related to the magnetic field $\mathbf{B}$ in the source (see Harwit, 1988, section 6.18). It can be shown from the Rayleigh-Jeans law that the spectral index for a black body radiator is

$$I(\nu) \propto \nu^{-\alpha} T, \tag{4.31}$$

Like all emission processes there is an equivalent absorption process for synchrotron radiation. For some sources where synchrotron emission are expected, no emissions are seen, presumably because the source's material is dense enough to absorb the emitted radiation.

4.5 The Compton and Inverse Compton Effects

If a plasma of relativistic electrons (the supernova remnant material) is immersed in a radiation field (photons) and if the temperature of the plasma (T_e) is very different from the temperature of the photons (T_{rad}), energy will be transferred between them. If $T_e \ll T_{rad}$ then the photons will be cooled by transferring energy to the electrons. This is the Compton effect. If $T_e \gg T_{rad}$ then the electrons will be cooled by transferring energy to the photons. This is the inverse Compton effect.

Compton[9] scattering is the reduction in energy of a photon which collides with a free electron. Analysis of the effect starts with an electron at rest (or in the electron's rest frame). The increase in wavelength is then given by (Lang, 1980, section 1.38)

$$\Delta\lambda = \frac{2h}{mc} \sin^2 \frac{\phi}{2}, \tag{4.32}$$

where ϕ is the photon's deflection angle. If the electron is moving with velocity v and total energy $E = \gamma mc^2$ where $\beta = v/c$ and $\gamma = \sqrt{1-\beta^2}$ then when β is large we have for the scattered frequency

$$\nu_2 \approx \gamma^2 v \quad (\gamma h\nu \ll mc^2). \tag{4.33}$$

In this case the scattering cross-section is

$$\sigma_s \approx \gamma^2 \sigma_T \quad (\gamma h\nu \ll mc^2), \tag{4.34}$$

[9] Arthur Holly Compton (1892–1962), American physicist who first observed and explained this effect in 1923.

where $\sigma_T = 6.65 \times 10^{-25}$ cm is the Thomson cross-section. The total energy radiated per unit time P by an electron passing through radiation of energy density U is then (Lang, 1980)

$$P = \gamma^2 \sigma_T c U \quad (\gamma h\nu \ll mc^2). \tag{4.35}$$

In the classical limit (non-relativistic electrons) Compton scattering is Thomson scattering.

For a source to maintain synchrotron emissions against inverse Compton losses the magnetic field energy density must dominate the local radiation energy density in the region where the electrons are emitting. Thus for a homogeneous isotropic source (Lang, 1980) the magnetic field intensity **H** must have

$$H^2 > \frac{8L}{R^2 c}, \tag{4.36}$$

where R is the radius of the source. The luminosity L is given by

$$L \approx 4\pi R^2 \nu \frac{S}{\theta^2}, \tag{4.37}$$

where ν is the frequency, S is the flux density and θ is the angular size of the source. For a synchrotron radiation source which would have a maximum flux density at ν_{max} the Compton effect dominates at

$$\nu_{max} \geq 10^{13} H \ \text{(Hz)}. \tag{4.38}$$

If a radio source has an upper cutoff frequency of ν_c and a maximum brightness temperature of T_{max} then the Rayleigh-Jeans law (eq. 4.14) gives $B \approx 2\nu_c^2 kT/c^2$. Using [critical frequency of synchrotron radiation] $E \approx kT$, we have $H \approx 10^{-19} \nu_c (kT)^{-2}$. Using these B and H in eq. 4.36 gives (Lang, 1980),

$$10^{-72} T_{max}^5 < 1. \tag{4.39}$$

Assuming $\nu_c \approx 10^{11}$ Hz then $T_{max} < 10^{12}$ K for incoherent synchrotron emission.

The inverse Compton effect can also be used to understand X-ray emissions. Relativistic electrons may be produced by the magnetic field within a supernova remnant. These electrons may then lose energy by the inverse Compton effect (low frequency photons are given energy by the relativistic electron which changes the photon to a higher frequency and slows the electron) producing X-ray photons in the process (Harwit, 1988).

4.6 Electron and Nucleon Energy Transitions

Whenever an electrically charged particle is accelerated by any means, it emits a photon. The energy carried away by the photon is equal to the energy lost by the charged particle. If the particle is an atomically bound electron, the emitted photon's energy is equal to the difference in the energy levels transitioned by the electron.

One of the fundamental principles of quantum mechanics is that the energy of a bound particle is quantised. Electrons bound to an atom are allowed to occupy only specific energy levels. When this principle is applied to the electrons bound to an atomic nucleus the electrons can have only certain allowed energies. The value of these energies depend on the electric charge of the nucleus. The electrons are allowed to move between the energy levels and in doing so absorb or emit photons with a frequency corresponding to the difference in the transited energy levels. Most of these energies correspond to infrared through ultraviolet wavelengths, allowing us to identify the species (chemical element) of the atom.

The nucleons (protons and neutrons) also have specific energy levels and are allowed to move between those levels. However, because of the higher energy levels involved, most of the photons associated with nuclear transitions are in the gamma-ray region of the spectrum.

4.7 The Hydrogen Atom

The hydrogen atom is the simplest of the atoms, consisting of a single proton and a single electron. It is therefore a two-body problem and the equations governing the interaction of the two particles can be solved in closed form. One of the first to investigate the spectrum of hydrogen was the Swiss mathematician Johann Balmer[10] who published a mathematical relationship between the wavelengths of the hydrogen lines:

$$\frac{1}{\lambda} = R_H \left[\frac{1}{2^2} - \frac{1}{n^2} \right], \tag{4.40}$$

where n (now known as the principal quantum number, representing the electron's energy level) is an integer greater than 2 and $R_H = 10\,967\,758.314 \pm 0.001\ \text{m}^{-1}$ is a Rydberg constant (known as the hydrogen Rydberg[11] constant). The lines associated with this set of wavelengths are known as the Balmer lines – over 30 have been observed. These are the only hydrogen lines in the optical region of the electromagnetic spectrum.

Equation 4.40 allows the calculation of the Balmer line wavelengths. Some of these wavelengths are shown in Table 4.1. The $n = 2$ to $n = 3$ transition ($2 \rightarrow 3$) is labelled Hα (hydrogen-alpha). The $2 \rightarrow 4$ transition is Hβ (hydrogen-beta), etc. The Greek letter designation for the transition's symbol is used only for the first

[10] Johann Jakob Balmer (1825–1898).

[11] Johannes Robert Rydberg (1854–1919) Swedish physicist. Namesake of the Rydberg constant and the Rydberg unit. Excited atoms with the electrons in very high values of the principal quantum number are called Rydberg atoms. The infinite Rydberg constant can be related to fundamental constants, $R_\infty = \frac{m_e e^4}{8\epsilon_0^2 h^2}$. The Rydberg constant for hydrogen and other hydrogenic atoms can be derived from the infinite Rydberg constant.

few transitions, then the transitions are numbered. For example, Ly15 is the transition between $n_1 = 1$ and $n_2 = 15$. Equation 4.40 can be generalised as

$$\frac{1}{\lambda} = R_H \left[\frac{1}{n_1^2} - \frac{1}{n_2^2} \right], \tag{4.41}$$

where $n_1 = 1, 2, 3, ...$ is the lower energy level and $n_2 > n_1$ is the upper energy level. This equation can be used to calculate all the possible wavelengths of electron transitions in hydrogen. Many of the n_1 values have associated names for their series (Table 4.1).

Niels Bohr was able to demonstrate the link between the Rydberg constant and the electron's binding energy, the energy with which the electron is bound to the proton at the ground (first) energy level. If W is that binding energy (for hydrogen, 13.6 eV) then

$$R = \frac{W}{hc}. \tag{4.42}$$

Ground state hydrogen can be ionised by any photon with energy greater the 13.6 eV, or wavelength less than 912 Å. This is the major contributor to the gap in observable wavelengths between ultraviolet and X-ray making the observation of the intensity of hydrogen Lyman lines from a celestial object very difficult because the interstellar matter is composed mostly of cold (ground state) hydrogen.

The electron can jump up in energy levels by absorbing a photon of the appropriate energy (creating an absorption spectrum line) or by thermal agitation (collisions with other atoms). While the electron is in a higher energy level, the atom is said to be excited. An emission spectrum is created when the electron drops down in energy levels. The emitted photons carry away the energy lost by the electron. Conservation of energy requires the emitted photons to have the same energy as the absorbed photons for each transition (the origin of Kirchhoff's second and third laws). The electron may drop to its lowest possible energy level in one step, emitting one photon, or it may make multiple transitions creating multiple photons.

An atom (or ion) may also be de-excited by collision with a free electron. In this case no photon is emitted because the free electron carries away the energy released by the bound electron dropping to the atom's (or ion's) lower energy level. In high-density particle environment (such as a lab) these collisions happen in shorter time intervals than the time for the electron to drop down an emit a photon. This leads to the creation of "forbidden transition" lines (Section 4.9) in lower particle density environments such as those found in cosmic plasmas.

Table 4.1: Some frequencies and wavelengths of spectral series for hydrogen (created from eq. 4.41).

Series	**Trans.**	ν **(THz)**	λ **(nm)**	**Region**	**Symbol**
Lyman[a]	$1 \rightarrow 2$	2467	121.6	ultraviolet	Lyα
	$1 \rightarrow 3$	2923	102.6	ultraviolet	Lyβ
	$1 \rightarrow 4$	3085	97.25	ultraviolet	Lyγ
	$1 \rightarrow 5$	3159	94.97	ultraviolet	Lyδ
	$1 \rightarrow 6$	3199	93.78	ultraviolet	Lyϵ
Balmer	$2 \rightarrow 3$	456	656.5	Optical	Hα
	$2 \rightarrow 4$	617	486.3	Optical	Hβ
	$2 \rightarrow 5$	690	434.2	Optical	Hγ
	$2 \rightarrow 6$	731	410.3	Optical	Hδ
	$2 \rightarrow 7$	755	397.1	Optical	Hϵ
Paschen[b]	$3 \rightarrow 4$	160	1876	Infrared	Pα
	$3 \rightarrow 5$	234	1282	Infrared	Pβ
	$3 \rightarrow 6$	274	1094	Infrared	Pγ
	$3 \rightarrow 7$	296	1005	Infrared	Pδ
	$3 \rightarrow 8$	314	954.9	Infrared	Pϵ
Brackett[c]	$4 \rightarrow 5$	74.0	4052	Infrared	Brα
	$4 \rightarrow 6$	114	2626	Infrared	Brβ
	$4 \rightarrow 7$	139	2166	Infrared	Brγ
	$4 \rightarrow 8$	154	1945	Infrared	Brδ
	$4 \rightarrow 9$	165	1818	Infrared	Brϵ
Pfund[d]	$5 \rightarrow 6$	40.2	7460	Infrared	Pfα
	$5 \rightarrow 7$	64.5	4654	Infrared	Pfβ
	$5 \rightarrow 8$	80.2	3740	Infrared	Pfγ
	$5 \rightarrow 9$	91.0	3297	Infrared	Pfδ
	$5 \rightarrow 10$	98.7	3039	Infrared	Pfϵ
Humphreys[e]	$6 \rightarrow 7$	24.2	12 370	Infrared	Huα
	$6 \rightarrow 8$	40.0	7503	Infrared	Huβ
	$6 \rightarrow 9$	50.8	5908	Infrared	Huγ
	$6 \rightarrow 10$	58.5	5129	Infrared	Huδ
	$6 \rightarrow 11$	64.2	4673	Infrared	Huϵ

[a]Theodore Lyman (1874–1954), American physicist.

[b]Friedrich Paschen (1865–1947), German physicist.

[c]Frederick Brackett (1896–1988), American physicist.

[d]August Pfund (1879–1949), German-American physicist.

[e]Curtis Judson Humphreys (1898–1986), American physicist.

4.8 Complex Atoms

The atomic number is equal to the number of protons in the nucleus which also determines the species (chemical element) of the atom. In a neutral atom the number of orbital electrons equals the number of protons – if not, the atom is ionised. If a photon with energy greater than the binding energy of the electron is absorbed by the electron, the electron is freed from the atom. When there is more than one electron, the quantum mechanical equations describing the energy states of the electrons become a many-body problem and are not solvable in closed form. This defines a complex atom. The more electrons, the more possible energy level combinations.

Each principal energy level or shell, is allowed to hold a certain maximum number of electrons. That number is related to the principal quantum number (the shell number) n, as $2n^2$ ($n = 1, 2, ...$). The first shell may have 2, the second 8, and so on. When a shell is filled, the electrons in that shell are bound very tightly to the nucleus. If the atom has only filled shells, the atom becomes chemically inert. These are the elements in the right column of the chemical periodic table.[12] When an atom has one electron in its outermost shell, such as the elements in the leftmost column of the element chart, the electrons in the filled, tightly bound shells play little role in the production of spectra and the outermost electron is principal. Such atoms display spectral line series with wavelength ratios similar to the spectral series of hydrogen. These atoms are then called hydrogenic atoms.

The electrons in each shell are in turn, held in subshells. This corresponds to the second quantum number or the azimuthal quantum number, l. The range of values for l is $0...n-1$. The subshells are also denoted by letters: s (spherical, $l = 0$), p (perfect, $l = 1$), d (diffuse, $l = 2$) and f (fine, $l = 3$). The "shape" of an orbital is determined from mathematics. This shape, along with the character of the spectral lines associated with the subshell, lead to the subshell's naming and lettering. The p subshell is shaped like two balloons tied together at the nucleus. The d subshell (usually, one of them is different) looks like four balloons tied together at the nucleus.

The third quantum number or the magnetic quantum number m_l describes the spatial orientation of the subshell. Its values are in the range $-l$ to $+l$. These are called orbitals. There are three p orbitals ($m_l = -1, 0, +1$), each at right angles to the other (remember the double-balloon shape). They are arbitrarily labelled p_x, p_y, p_z, but they have no relation to those directions in a coordinate system. The p orbitals all have the same energy and are thus called degenerate orbitals. All shells except the first one have p orbitals – the first shell has

[12] They are usually called the "noble elements" because they do not mix with the "common elements."

only the s subshell (1s, 2s, $2p_x, 2p_y, 2p_z$, etc.). There are five d ($m_l = -2, -1, 0, +1, +2$) and seven f orbitals.

The fourth quantum number or the electron spin quantum number m_s is the result of the Pauli exclusion principle[13]. It states that no two electrons can have the same set of quantum numbers. This means that each orbital can hold only two electrons, one with "spin-up" and one with "spin-down." Thus, m_s has only the values $-\frac{1}{2}$ and $+\frac{1}{2}$. Table 4.2 shows the possible values of the quantum numbers. For the ground energy state of helium, the two electrons would have the quantum numbers $[1, 0, 0, -\frac{1}{2}]$ and $[1, 0, 0, +\frac{1}{2}]$. A shorthand for this is, $1s^2$.

[13]Named for Wolfgang Pauli (1900–1958).

Table 4.2: Possible values of the quantum numbers.

Shell $n =$	**Subshell** l	**Subshell Designation**	**Magnetic** m_l	**Total Orbitals**	**Total Electrons**
1	0	1s	0	1	**2**
2	0	2s	0	1	2
	1	2p	$-1, 0, +1$	4	**8**
3	0	3s	0	1	2
	1	3p	$-1, 0, +1$	4	8
	2	3d	$-2, -1, 0, +1, +2$	9	**18**
4	0	4s	0	1	2
	1	4p	$-1, 0, +1$	4	8
	2	4d	$-2, -1, 0, +1, +2$	9	18
	3	4f	$-3, -2, -1, 0, +1, +2, +3$	16	**32**

While the shells continue to higher numbers, the subshells usually do not go beyond f, or $l = 3$ (the possible subshells following f are simply in alphabetical order). The shells, subshells and orbitals are filled by lowest energy first. In the case of degenerate orbitals, Hund's rules[14] are used. Hund's rules state (basically) that for degenerate orbitals, the lowest energy is attained when the greatest number of electron spins are aligned. Hund's rules are the result of electron spin-spin and spin-orbit interactions. When filling the p orbitals, one electron is put into each p orbital before a second electron is added to any p orbital. The periodic table is built on the order of electron placement in the ground energy state (Figure 4.3). A description of the symbology of spectroscopy is shown in Table 4.3.

[14]Named for Friedrich Hund (1896–1997) a German physicist who worked on interpreting atomic and molecular spectra.

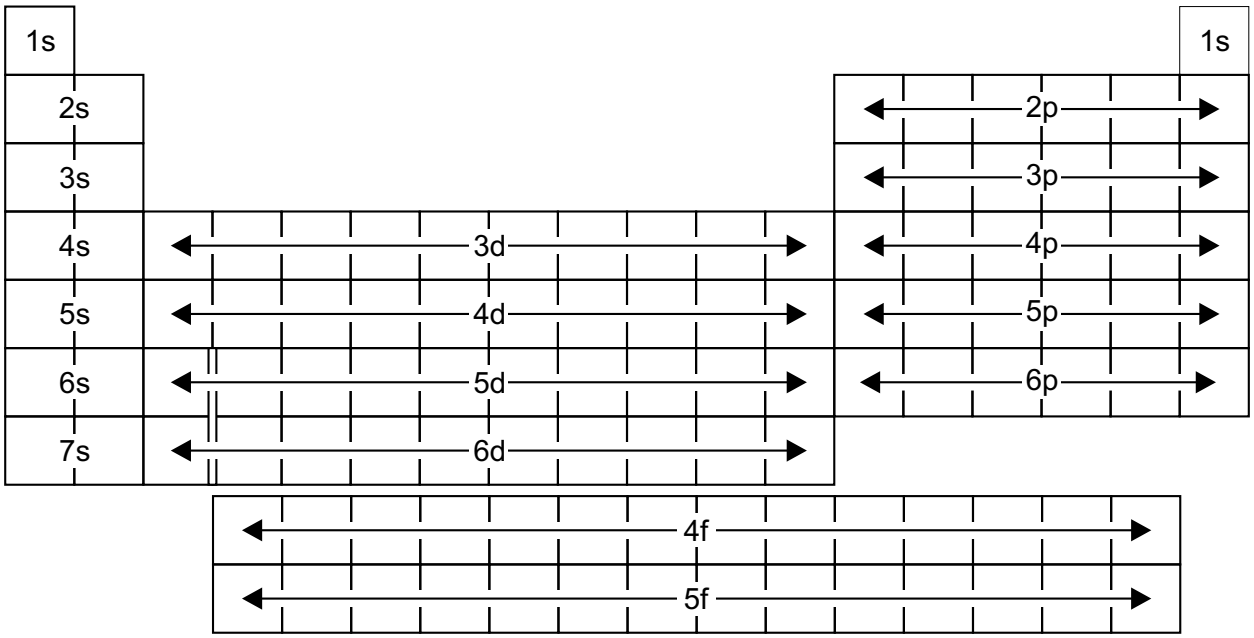

Figure 4.3: The filling of electron shells and orbitals as plotted against the periodic table.

Table 4.3: Nomenclature and symbols used in spectroscopy.

Symbol	**Meaning**
n	principal quantum number
	$n =$ 1 2 3 4 5 6 ...
	shell K L M N O P ...
l	orbital angular momentum of individual electron
	$l =$ 0 1 2 3 4 5 ...
	subshell s p d f g h ...
L	total orbital angular momentum
$L = \sum l$	$L =$ 0 1 2 3 4 5 ...
	S P D F G H ...
s	angular momentum of an individual electron
$S = \sum s$	total spin angular momentum
$j = l + s$	spin-orbit coupling for single electron
$J = \sum j$	(jj coupling) total angular momentum, atoms above iron
$J = L + S$	(LS coupling) total angular momentum, atoms below iron
M	magnetic quantum number, or the z-components of J along an external magnetic field.

The set of values, $[n, l, S, L, J]$ define an energy level for the atom, which includes terms with $2J + 1$ states. Each energy level can be represented in the form: $\mathrm{nl}^{\mathrm{valency}\ 2\mathrm{S}+1}\mathrm{L}_{\mathrm{J}}^{(\pi)}$. For atoms lighter than iron, relativistic effects are weak and $J = L + S$ (LS-coupling or Russell-Saunders coupling) works fine. For atoms above iron, relativistic effects become stronger, so L and S (because they are not conserved quantities) do not work well for finding the total angular momentum. (In atoms with higher nuclear charge, the spin-orbit interactions are generally greater than the spin-spin or orbit-orbit interactions.) For these atoms we must use jj-coupling ($J = \sum j$). For most astronomical cases, we are working with light atoms and so LS-coupling may be used.

The term's parity (π), is determined by reflecting the electron wave function through the nucleus. This is found most easily by summing the orbital angular momentum quantum numbers (m) of the electrons:

$$\pi = (-1)^{\sum m_i}. \tag{4.43}$$

Table 4.4 shows a breakdown for interpreting an energy level written in this format. A spectral line is created by a electron transition between two energy levels. A set of transitions between terms within the same energy level is called a multiplet.

The higher energy shells and orbitals are spatially larger than the lower energy shells and orbitals. This makes the electrons in the higher shells (generally) farther from the nucleus than those in the lower shells. When a shell is filled, its electrons tend to shield the higher energy electrons from the nucleus, decreasing the electrical potential in which those electrons move. This is called the screening effect and it causes the outer electrons to see a lower effective nuclear charge. The outer electrons (in the shells above the shell corresponding to the next lowest noble element) are called the valence electrons. The inner (filled shell) electrons are called the core electrons. It is the valence electrons that produce the majority of the spectral lines of a chemical species. If there is a single valence electron, we have a hydrogenic atom. Because the spectral lines of different hydrogenic atoms may lie very close to each other in wavelength, high resolution spectroscopy may be needed to separate and identify these chemical species. If an atom has two valence electrons, it will behave with some helium characteristics, with a corresponding helium-like spectrum.

With an understanding of the process of filling electron energy shells, the rules for allowed electron transitions between the energy levels can be written. While the transition probabilities can in theory be calculated from the electron wave functions, such calculations must include concerns like conservation of energy, momentum and spin. Thus, these calculations are not trivial and in practise the transition probabilities are measured by careful observation of the laboratory-based spectrum of an element. However, the shell filling rules can

Table 4.4: Interpreting the spectroscopic notation of an atomic energy level.

Example energy state: $2p^3\ {}^4S^o_{3/2}$	
Part :	**Meaning**
2 :	The shell, $n = 2 \rightarrow$ L shell.
p^3 :	The subshell, $l = 1 \rightarrow$ p subshell, with three outer (valence) electrons.
	The term:
4 :	The multiplicity, or the degeneracy of the orbital. With spin $S = 3/2$, (the sum of the spins of the three outer electrons) multiplicity $= 2S + 1 = 4$.
S :	The total angular momentum of the state, $L = 0 \rightarrow$ S orbital.
3/2 :	The total angular momentum, $J = L + S = 0 + 3/2 = 3/2$. This part is included to account for relativistic effects.
o :	Odd parity. There is usually no superscript for even-parity terms.

The inclusion of M (the Zeeman effect) will split terms into states, with $M = -J, \ldots, +J$.

be used to predict the possible energy-level pairs for these transitions and thus predict the possible spectral line wavelengths. When a wavelength corresponding to a particular transition is not seen in the laboratory spectrum, that electron energy-level jump is labelled as a forbidden transition or a forbidden line. However, under certain physical conditions that are not similar to laboratory conditions (very low particle density) these forbidden spectral wavelengths are often seen.

4.9 Permitted and Forbidden Lines

The strength, intensity or depth of spectral lines created by atoms depends on the probability of the electron's transition between the energy levels involved in the production of that line. The greater the probability, the stronger the lines. The rules that govern the transitions are based on conservation laws and are fairly simple but very restrictive. Thus, the number of possible spectral lines is less than the number of possible energy level combinations.

The transitions most likely to occur, according to the selection rules, are called permitted transitions and their corresponding spectral lines are permitted lines. The radiation emitted by these transitions is electric-dipole (the electron and the nucleus form an electric dipole). When an atom has been put into an excited state, either by photon absorption or by collision, the electron may drop down through a permitted transition in mere nanoseconds after the excitation event.

It is also possible for the electron to be put into a metastable excited energy level. In this case, the electron may stay in the higher energy level for a time interval in the range of 1 to 100 seconds. If the atom is left undisturbed, the electron may drop down via a forbidden transition. Spectral lines corresponding to transitions which are not seen in the laboratory are labelled forbidden lines with corresponding forbidden transitions. However, that does not mean they cannot happen. Forbidden transitions create magnetic dipole (M2) or quadrupole (M3), or electric quadrupole (E2) radiation. Table 4.5 shows the transition selection rules. Each column to the right has a factor of about 10^{-3} lower probability from its immediate predecessor to the left.

Ultra-high vacuum pumps used in laboratories start at pressures of 10^{-9} torr[15] or better. At sea-level (one standard atmosphere pressure at 25°C), the atmospheric density is about 2.5×10^{25} particles (molecules) m^{-3}. The ultra-high vacuum pump drops this to about 3.2×10^{13} particles m^{-3}. Even at this low density the atom

[15]The torr (named for Evangelista Torricelli) is the unit of pressure defined as 1/760 of an atmosphere, or in barometric terms, 1 mmHg.

Table 4.5: The selection rules for atomic electron transitions.

Rule	**E1, E Dipole**	**M2, M Dipole**	**E2, E Quadrupole**	**M3, M Quadrupole**
	"Permitted"	**"Forbidden"**	**"Forbidden"**	**"Forbidden"**
1	$\Delta J = 0, \pm 1$ $(0 \nleftrightarrow 0)$	$\Delta J = 0, \pm 1$ $(0 \nleftrightarrow 0)$	$\Delta J = 0, \pm 1, \pm 2$	$\Delta J = 0, \pm 1, \pm 2$
			$(0 \nleftrightarrow 0, 1; \frac{1}{2} \nleftrightarrow \frac{1}{2})$	$(0 \nleftrightarrow 0, 1; \frac{1}{2} \nleftrightarrow \frac{1}{2})$
2	$\Delta M_J = 0, \pm 1$	$\Delta M_J = 0, \pm 1$	$\Delta M_J = 0, \pm 1, \pm 2$	$\Delta M_J = 0, \pm 1, \pm 2$
	If $\Delta J = 0$,	If $\Delta J = 0$,		
	$0 \nleftrightarrow 0$	$0 \nleftrightarrow 0$		
3	$\pi_f = -\pi_i$	$\pi_f = \pi_i$	$\pi_f = \pi_i$	$\pi_f = -\pi_i$
4	If $\Delta S = \pm 1$	If $\Delta S = \pm 1$	If $\Delta S = \pm 1$	If $\Delta S = \pm 1$
	$\Delta L = 0, \pm 1, \pm 2$	$\Delta L = 0, \pm 1, \pm 2$	$\Delta L = 0, \pm 1, \pm 2, \pm 3 (0 \nleftrightarrow 0)$	$\Delta L = 0, \pm 1 (0 \nleftrightarrow 0)$
5	One e^- jump.	No e^- jump.	No or one e^- jump.	One e^- jump.
	$\Delta l = \pm 1$	$\Delta l = 0, \Delta n = 0$	$\Delta l = 0, \pm 2$	$\Delta l = \pm 1$
6	If $\Delta S = 0$	If $\Delta S = 0$	If $\Delta S = 0$	If $\Delta S = 0$
	$\Delta L = 0, \pm 1$	$\Delta L = 0$	$\Delta L = 0, \pm 1, \pm 2,$	$\Delta L = 0, \pm 1, \pm 2,$
	$(0 \nleftrightarrow 0)$		$(0 \nleftrightarrow 0, 1)$	$(0 \nleftrightarrow 0, 1)$

Rules 1, 2 and 3 are rigorous – they must always be followed. Rule 4 applies when there is negligible configuration interaction, rules 5 and 6 apply when LS-coupling is valid.

is much more likely to be de-excited by collision rather than by emitting a "forbidden photon."

Physical conditions in the laboratory cannot simulate some of the extreme conditions found in astronomical objects such as nebulae. Typical nebulae have densities approaching 10^8 atoms m^{-3}. Here, the atom is more likely to be left undisturbed, and the forbidden lines become prominent in the spectra of nebulae.

4.10 Ionised Atoms

Atoms that have gained or lost one or more electrons are called ions. The loss of an electron can happen by thermal collisions between particles in a gas or by the absorption of a photon with sufficient energy that the electron is completely freed from the atom. The last process is known as photoionisation. Hydrogen is the most abundant element in the universe. Most hydrogen nuclei are just single protons and in situations where the hydrogen is ionised, we can view these single protons as ionised hydrogen. In those environments where the electrons are just as abundant as the protons, but not bound to the protons (H II regions) we tend to speak of the protons *and* the electrons as ions. Also, in such environments of balanced positive and negative ions, we can speak about ion pairs.

When an atom has been ionised the interactions between its electrons change, which change (slightly) the allowed electron energy levels. If there are many electrons and only one is lost (or gained) the changes in the energy levels are small. However in those atoms where there are few electrons, the changes may be larger and so more noticeable. In either case, we can detect these changes and therefore detect the ionisation state of the atom.

Astronomers use Roman numerals to designate the ionisation state of an atom. I is used for neutral atoms. As the atom loses electrons[16], the Roman numeral is increased. H I is neutral hydrogen, H II is ionised hydrogen. As an atom loses electrons it is possible for it to reach hydrogenic states, as is the case with He II. He II is the hydrogenic atom first described theoretically by Bohr. His analysis described the spectrum of He II as being much like hydrogen's, except the corresponding lines of a series are one-quarter of the hydrogen wavelength, leading him to conclude that the energy of an electron depends on the square of the nuclear charge. This relationship was later confirmed by stellar spectroscopy.

Strictly speaking, the Roman numerals label the spectrum produced by the atom with a particular ionisation

[16] In the case where an atom becomes a negative ion by gaining an extra electron, it is simply labelled with a superscript minus sign as in, H^- (hydrogen with a closed 1s shell).

state. However, astronomers generally use the Roman numerals to denote the ion state as well. H I (neutral hydrogen) regions generally produce no optical spectra (Balmer lines) because they are too cold for very many electrons to be in the higher energy levels needed to produce the transitions down to the second energy level, thus producing Balmer photons. However, we often see the H I recombination spectrum coming from H II (ionised hydrogen) regions. H II regions have many free protons and free electrons. When these free particles recombine to reform a neutral hydrogen atom, the electron can drop through the energy levels in multiple steps, producing multiple photons, including the Balmer lines.

With further analysis of atoms and ions, a general rule appears between ionised atoms and neutral atoms with the same number of electrons: the spectra of ionised and neutral atoms with the same number of electrons are qualitatively similar, with the ionised atom's lines shifted toward the ultraviolet. High-resolution spectroscopy is used to separate out the hydrogenic ions.

4.11 Electron Transitions in Supernova Remnants

Shock fronts in the expanding supernova remnant are created when the supernova remnant material collides with the interstellar matter. The collisions can cause the ionisation of atoms into one of their metastable states. The excited state can be de-excited by the emission of photons. In the laboratory ionic metastable states are usually de-excited by collisions. However in the low density of the interstellar matter there is a high probability for de-excitation by photon emission because of the lower collision rate. Transitions of particular interest to supernova remnant observations are shown in Table 4.6. Note, not all of the possible Hα electron transitions at the λ 6562 Å wavelength are shown in this table.

The collisionally ionised gas has a temperature corresponding to the ionisation potential of the atomic species comprising the gas. For a region emitting [O III] lines this approximately 0.5–1.0 $\times 10^5$ K. Spectral lines from atomic species with lower ionisation potentials such as [O I] $\lambda\lambda$ 6300, 6363 Å and [S II] $\lambda\lambda$ 6716, 6731 Å are significantly stronger than Hα in shocked material compared to hydrogen cloud regions. When a gas of these atoms is shocked the atoms are instantly heated and ionised and then the gas cools by radiation. The gas is not in thermal or ionisation equilibrium (Osterbrock & Ferland, 2006). Recombination of the ions with free electrons is slower than cooling by emission. "Within H II regions oxygen is completely ionised to O^+ or higher and S^+ is mostly ionised to S^{++} while outside the H II region boundary oxygen is entirely O^0, sulphur is entirely S^+ but there are almost no free electrons and the temperature is too low for appreciable excitation of [S II]

$\lambda\lambda$ 6813, 6731 Å" (Osterbrock & Ferland, 2006).

Table 4.6: The electron transitions associated with the atoms and ions used for identifying supernova remnants in optical spectra (Ralchenko et al., 2012).

Atom/Ion	**Wavelength (Å)**	**Configuration**	**Term**	$J_i - J_k$	**Type**
Hα	6562	2p – 3d	^{2}P° – ^{2}D	$\frac{1}{2} - \frac{3}{2}$	E1
Hα	6562	2s – 3p	^{2}S – ^{2}P°	$\frac{1}{2} - \frac{3}{2}$	E1
Hα	6562	2s – 3p	^{2}S – ^{2}P°	$\frac{1}{2} - \frac{1}{2}$	E1
Hα	6562	2 – 3			E1
Hα	6562	2p – 3d	^{2}P° – ^{2}D	$\frac{3}{2} - \frac{5}{2}$	E1
[O I]	6300	$2s^2 2p^4 - 2s^2 2p^4$	^{3}P – ^{1}D	2 – 2	M1
[O I]	6300	$2s^2 2p^4 - 2s^2 2p^4$	^{3}P – ^{1}D	2 – 2	E2
[O III]	5007	$2s^2 2p^2 - 2s^2 2p^2$	^{3}P – ^{1}D	2 – 2	M1
[O III]	5007	$2s^2 2p^2 - 2s^2 2p^2$	^{3}P – ^{1}D	2 – 2	E2
[S II]	6716	$3s^2 3p^3 - 3s^2 3p^3$	^{4}S° – ^{2}D°	$\frac{3}{2} - \frac{5}{2}$	M1
[S II]	6716	$3s^2 3p^3 - 3s^2 3p^3$	^{4}S° – ^{2}D°	$\frac{3}{2} - \frac{5}{2}$	E2
[S II]	6730	$3s^2 3p^3 - 3s^2 3p^3$	^{4}S° – ^{2}D°	$\frac{3}{2} - \frac{3}{2}$	E2
[S II]	6730	$3s^2 3p^3 - 3s^2 3p^3$	^{4}S° – ^{2}D°	$\frac{3}{2} - \frac{3}{2}$	M1

Chapter 5

Extragalactic Supernova Remnants and NGC 300

The contents of this chapter were originally published in MWF11 and MWF12.

The Solar System is located in the dusty disk of the Galaxy, so the study of Galactic supernova remnants is hampered by the extinction and reddening effects of the interstellar matter. Most Galactic supernova remnants can only be observed at radio or infrared wavelengths. However, observing supernova remnants in nearby galaxies – particularly in face-on galaxies at high Galactic latitude (e.g. NGC 300) – reduces absorption by both the host galaxy and our own (Matonick & Fesen, 1997; Pannuti et al., 2000). Surveys of supernova remnants in the Local Group galaxies and galaxies within some nearby clusters have resulted in better samples that are almost free from biases. "Nearby" means those galaxies that are far enough away that filamentary structure within the supernova remnant cannot be observed but close enough to make reasonable measurement of constituent nebulae diameters – generally galaxies within about 3–4 Mpc. A list of over 450 optical supernova remnants found in nearby galaxies is given by Matonick & Fesen (1997).

There are no Galactic supernova remnants within the Solar Neighbourhood where trigonometric parallax can be used to determine their distance. Other distance measurement techniques have been devised but their measurement uncertainty is large. This affects supernova remnant age determination, an important characteristic of supernova remnants for understanding their evolution. Observations of supernova remnants in nearby galaxies reduces the distance problem to one of determining the distance to the nearby galaxy, which is usually done with Cepheid variables.

5.1 Observations of Extragalactic Supernova Remnants

Finding and confirming extragalactic supernova remnants is a task best carried out using multi-wavelength surveys (mainly X-ray, optical and radio) rather than any single wavelength or electromagnetic region survey (see Filipović et al., 1998; Lacey & Duric, 2001; Payne et al., 2006; Filipović et al., 2008). Radio observations using one frequency cannot uniquely identify supernova remnant candidates, clearly differentiate supernova remnants from other nebulous objects, or contend with the confusion that arises due to the presence of background sources (distant active galactic nuclei). Multiple radio observations at various frequencies must be made. Optical and X-ray surveys also suffer from source confusion and selection effects. Only by combining observations across all these electromagnetic regions can the extragalactic supernova remnant survey success rate be increased. An example of recent work in multiple wavelength observations of extragalactic supernova remnants (M 33) is presented by Long et al. (2010).

The spectral identification of supernova remnants was pioneered in a series of papers by Mathewson & Clarke (1972, 1973a,b,c) where narrow-band optical interference filters, centred on Hα and the [S II] doublet, were used to differentiate between primordial hydrogen and the heavy metal contaminated ejecta of a supernova remnant. This technique depended on the strength of the [S II] lines in supernova remnants being about the same strength as the Hα, probably due to shock fronts in the expanding supernova remnant shell, which should not exist in H II regions. The [S II] lines should be at least an order of magnitude weaker than the Hα in H II regions as compared to supernova remnants (Mathewson & Clarke, 1972). The Hα filters are not able to remove the [N II] $\lambda\lambda$ 6548, 6584 Å doublet which shoulder the Hα line. In some supernova remnants this doublet can be as strong as the Hα itself. An emission region was classified as a supernova remnant if it contained a (non-thermal) radio source and the Hα + [N II] to [S II] ratio was less than two (Mathewson & Clarke, 1972).

Supernova remnant surveys target nearby galaxies with high inclination and Galactic latitude, such as M 33, M 31 and M 83. Source confusion and selection effects make such surveys very incomplete. Shearer et al. (2006) points out that Blair & Long (2004) detected 71 supernova remnants in M 83, while the historical record shows 6 supernovae in M 83 since 1923. This gives a supernova rate of 1 every 15 years. Assuming a 10 000-year visible supernova remnant lifetime, this rate implies that M 83 contains more than 500 supernova remnants. There should be many more supernova remnants to find in any of these galaxies. Section 5.1 of Braun & Walterbos (1993) contains a well considered discussion of the survey completeness problem. Shearer et al. (2006) is arguing for the use of extra-large telescopes for finding extragalactic supernova remnants, even beyond the 30-meter

class, to increase completeness.

Type II supernova occur in or near H II regions and so their remnants may be difficult to separate from the H II region. This is a prime example of source confusion in optical surveys. OB associations can create multiple supernova events creating superbubbles (interstellar matter voids ∼200 pc in diameter) which can mask individual older supernova remnants. D'Odorico et al. (1978) pointed out the possibility of confusion between possible supernova remnants and H II regions as well as between supernova remnants and shells of ionised gas caused by supersonic stellar winds. Arguments were presented based on observations of supernova remnants and H II regions within the Galaxy and within the Large Magellanic Cloud to show how supernova remnants can be identified within M 33 when [S II]:H$\alpha \leq 0.4$. Fesen et al. (1985) found that [O I] $\lambda\lambda$ 6300, 6364 Å, [O II] λ 3727 Å and [O III] $\lambda\lambda$ 4959, 5007 Å are often all simultaneously strong in supernova remnants and this can be used to differentiate supernova remnants from H II regions in cases where the [S II]:Hα is borderline. This list of problems is itself incomplete and exactly what percentage of extragalactic supernova remnant candidates may fall into each of the source confusion scenarios is unknown.

Of the galaxy morphological classes, spiral type galaxies generally have the greatest rate of star formation (outside of starburst galaxies). Members of the Local Group of galaxies (54 galaxies, mostly dwarf ellipticals with the large spirals, M 31 and M 33) with known supernova remnants include M 31, M 33, IC 10, NGC 185. Some spiral galaxies outside the Local group, for instance NGC 2403, NGC 3077, NGC 4214, NGC 4395, NGC 4449, and NGC 5204 are good candidates for extragalactic supernova remnant surveys. The Sculptor group contains 19 galaxies and is the next closest group of galaxies to the Local group. Of this group, supernova remnant surveys include: NGC 45, NGC 55, NGC 247, NGC 253, NGC 300, and NGC 7793, all of which are spiral galaxies.

5.2 The Properties of NGC 300

NGC 300 was chosen for this research because the optical supernova remnants discovered in NGC 300 (BL97) have not been observed since their discovery and recent radio and X-ray surveys of this galaxy found new supernova remnant candidates (PF04) for which optical spectra were needed (see Section 5.4).

NGC 300 is a spiral galaxy and a member of the Sculptor group. The similarity of angular size between NGC 300 and other nearby spiral galaxies that have been studied (e.g. M 33 and other members of the Sculptor Group) lead to the conclusion that NGC 300 is a fairly typical, normal spiral galaxy (BL97). Because it has characteristics similar to other nearby galaxies (see Table 5.1 and references therein), it is a prime object of

investigation in many areas of current research. Many of the properties of NGC 300 (apparent magnitude, disk to bulge ratio, Holmberg radius, the rotational velocity curve, total mass, surface and space density distribution, mass to luminosity ratio) are discussed by Rhee & Chun (1992).

Table 5.1 provides a brief list of the characteristics of NGC 300 following PF04; a more complete list is provided by Kim et al. (2004). NGC 300 is a type SA(s)d[1] galaxy with an angular extent of $21\farcm9 \times 15\farcm5$ (based on ultraviolet isophotes, Gil de Paz et al., 2007). An image of NGC 300 is presented in Figure 5.1. This galaxy has been classified as flocculent – that is, its arms are poorly defined with a "woolly disk structure." It features many giant H II regions which are evidence of many star formation episodes (Read & Pietsch, 2001, here after RP01).

Dynamical observations conclude that NGC 300 has a massive halo. While direct studies of the halo of NGC 300 are few, it has been demonstrated that there are interactions between the disk and the multi-phase halo[2] structures of late type spirals (like NGC 300) that is dependent on the star formation and supernovae rate (Tüllmann et al., 2006a,b,c). These disk-halo interactions include a substantial diffuse ionised gas layer between the disk and halo. The existence of a multi-phase halo surrounding a galaxy is determined by multi-wavelength observations of the halo structure. It is yet to be determined if NGC 300 has a multi-phase halo but it does have a substantial diffuse ionised gas layer with concentration around the H II regions (Hoopes et al., 1996).

Because of its low inclination angle (measured to be between 43° and 46°; Tully & Fisher (1988) and Puche et al. (1990)) and its high Galactic latitude ($-77\fdg17$, Table 5.1), observations of NGC 300 entail very low internal extinction (Butler et al., 2004) and foreground reddening ($E(B-V) = 0.013$ mag, Bland-Hawthorn et al., 2005). For studies of this galaxy, most authors have adopted distances of 2.0-2.1 Mpc (BL97; Freedman et al., 1992, 2001) though recent distance measurements based on observations of Cepheid variables have favoured a closer distance of 1.88 Mpc with an error of 3% (Bresolin et al., 2005b; Gieren et al., 2005). For the research conducted in this thesis the distance of 2.1 Mpc was adopted to stay consistent with previous observations (BL97, PF04). The corresponding linear scale is 10.2 pc arcsecond^{-1}.

Appendix B contains a discussion of observations of objects other than supernova remnants or supernova remnant candidates in NGC 300 and how those observations relate to supernova remnant observations.

---

[1] Some papers have listed NGC 300 as an Sc or Scd type galaxy.

[2] Halos with matter in both gaseous and plasma (in multiple ionisation levels) phase states. See Heald (2006) for a full discussion of multiphase halos, diffuse ionised gas, star formation, supernovae and the interaction of the galactic disk with the halo.

Table 5.1: Gross properties of NGC 300.

Property	**Value**	**Reference**
Hubble Type	SA(s)d	Tully & Fisher (1988)
		de Vaucouleurs et al. (1991)
Right Ascension (J2000.0)	$00^{\rm H}54^{\rm M}53\overset{\rm S}{.}48$	NED
Declination (J2000.0)	$-37^\circ\ 41'\ 03\overset{''}{.}8$	NED
Galactic Latitude	$-77\overset{\circ}{.}17$	NED
Radial Velocity	144 km/s (Solar)	Puche et al. (1990)
		Karachentsev et al. (2003)
Inclination	46°	Tully & Fisher (1988)
	$42\overset{\circ}{.}6$	Puche et al. (1990)
Distance	2.1 Mpc	Freedman et al. (1992)
	2.02 Mpc	Freedman et al. (2001)
	1.88 Mpc	Bresolin et al. (2005b);
		Gieren et al. (2005)
Observed Diameter (D_{25})	$20'.2$	Tully & Fisher (1988)
Observed Diameter (ultraviolet isophotes)	$21'.9 \times 15'.5$	Gil de Paz et al. (2007)
Galaxy Diameter	22.6 kpc, at 2.1 Mpc	Based on Gil de Paz et al. (2007)
Mass (H I)	2.4×10^9 $M_\odot$	Tully & Fisher (1988)
N_H Column Density	2.97×10^{20} cm^{-2}	Read et al. (1997)

Note: NED = NASA/IPAC Extragalactic Database (`http://nedwww.ipac.caltech.edu/`).

Figure 5.1: Composite photograph of NGC 300 made at European Southern Observatory's La Silla Observatory. The total exposure time is over 50 hours. NGC 300 is a flocculent (woolly) galaxy as opposed to a grand design (distinctly two-armed) spiral galaxy. This implies a thick disk structure. (Credit: ESO)

5.3 Observations of Supernova Remnants and Supernova Remnant Candidates in NGC 300

NGC 300 is an Sd type galaxy so supernova remnants from all types of supernovae should be expected. (See page 8 for the correlation between Hubble galaxy types and expected supernova types.) The first paper to present candidate supernova remnants in NGC 300 was D'Odorico et al. (1980) and contains a list of (candidate) supernova remnants in a few nearby galaxies with seven candidates from NGC 300 which are listed here in Table 5.2. In Table 5.2, column 1 is the candidate number where "DDB" was added to differentiate these sources from other sources discussed in this thesis. Columns 2 and 3 are the published right ascension (α) and declination (δ) of the sources precessed from their original B1950 to J2000.0 coordinates. Column 4 is the proposed diameter of the supernova remnant. The identification of these supernova remnants was based on UK Schmidt plates[3] (Russell, 1989) with positions accurate to about $10''$ in δ and 1^s in α.

The next search for supernova remnants in NGC 300 in optical wavelengths was published in BL97. These objects are listed here in Table 5.3. Five of the seven supernova remnants from D'Odorico et al. (1980) were within the survey images of BL97 but only two (DDB2 = N300-S10 and DDB5 = N300-S26) were identified as supernova remnants with DDB1, DDB4 and DDB7 being dominated by continuum emissions (Long, 1996). The candidates in BL97 were first located by using optical filters centred on Hα and [S II] lines. The candidates were then observed with long-slit spectroscopy to verify a [S II]:Hα greater than 0.4. Some of the candidates were not observable in the spectrograph used for that observation. BL97 also measured the flux of [O I] and [O III] (total) relative to the Hα flux. All but a few of the flux levels were on the order of 10^{-15} erg cm^{-2} s^{-1} with substantial uncertainty in the [O I] flux.

Radio supernova remnant surveys of NGC 300 have been published by Harnett (1986), Pannuti et al. (2000, here after, PD00), Pannuti et al. (2001, 2002, 2007), PF04, Payne et al. (2005) and others. Some radio observations of supernova remnant candidates are shown in Tables 5.4 and 5.5. In these tables column 1 is the source designation according to the referenced paper. Columns 2 and 3 are the J2000.0 coordinates of the source. Column 4 is the proposed or known object type. The codes for the objects are as follows (from PF04): SNR/snr = high/low confidence supernova remnant, HII/hii = high/low confidence H II region, BKG/bkg = high/low confidence background source.

[3]The UK Schmidt telescope at Siding Spring Observatory, now operated by the Australian Astronomical Observatory.

Table 5.2: NGC 300 supernova remnant candidates from D'Odorico et al. (1980).

1	**2**	**3**	**4**
	α **(h m s)**	δ ($^\circ$ $'$ $''$)	
Number	**(J2000)**	**(J2000)**	**Diameter (pc)**
DDB1	00 54 21	−37 35 00	< 24
DDB2[a]	00 54 40	−37 40 44	48
DDB3	00 54 47	−37 39 06	< 24
DDB4	00 55 01	−37 36 11	< 24
DDB5	00 55 19	−38 44 39	< 24
DDB6	00 55 32	−37 41 55	< 24
DDB7	00 55 48	−37 39 19	< 24

[a]Associated with an H II region.

Table 5.3: Positions of the optical survey supernova remnants in NGC 300 from BL97.

1	**2**	**3**
Object Name	**Position (J2000.0)**	
	α **(h m s)**	δ ($^\circ$ $'$ $''$)
N300-S1	00 54 19.21	−37 37 23.96
N300-S2	00 54 21.85	−37 40 27.11
N300-S3	00 54 28.86	−37 41 53.32
N300-S4	00 54 30.62	−37 40 53.75
N300-S5	00 54 30.99	−37 37 33.96
N300-S6	00 54 31.91	−37 38 25.68
N300-S7	00 54 33.17	−37 40 16.90
N300-S8	00 54 38.17	−37 41 14.88
N300-S9	00 54 40.20	−37 41 02.12
N300-S10 (DDB2)	00 54 40.87	−37 40 48.73
N300-S11	00 54 42.54	−37 43 14.16
N300-S12	00 54 43.86	−37 43 39.08
N300-S13	00 54 46.60	−37 39 44.32
N300-S14	00 54 47.15	−37 41 07.63
N300-S15	00 54 53.32	−37 38 48.24
N300-S16	00 54 54.46	−37 40 35.46
N300-S17	00 54 56.68	−37 43 57.70
N300-S18	00 55 01.39	−37 39 18.17
N300-S19	00 55 05.41	−37 41 21.04
N300-S20	00 55 05.68	−37 46 13.35
N300-S21	00 55 07.15	−37 39 15.17
N300-S22	00 55 07.50	−37 40 43.20
N300-S23	00 55 09.10	−37 39 32.61
N300-S24	00 55 09.48	−37 40 46.21
N300-S25	00 55 10.68	−37 41 27.13
N300-S26 (DDB5)	00 55 15.46	−37 44 39.11
N300-S27	00 55 17.54	−37 44 36.65
N300-S28	00 55 33.76	−37 43 13.13

Table 5.4: Radio supernova remnants and supernova remnant candidates in NGC 300 from PD00.

1	**2**	**3**	**4**
	α **(h m s)**	δ $(^\circ\ '\ '')$	
Designation	**(J2000.0)**	**(J2000.0)**	**Object Type**
R1	00 54 38.2	−37 41 47	SNR/HII
R2	00 54 38.4	−37 42 42	SNR/HII
R3	00 54 43.4	−37 43 11	SNR/HII
R4	00 54 44.9	−37 41 10	SNR/HII
R5	00 54 45.1	−37 41 49	SNR/HII
R6	00 54 50.3	−37 40 31	SNR/HII
R7	00 54 51.1	−37 40 59	SNR/HII
R8	00 54 51.1	−37 41 45	SNR/HII
R9	00 54 51.3	−37 46 22	SNR/HII
R10	00 54 51.8	−37 39 39	SNR/HII
R11	00 55 03.6	−37 42 49	SNR/HII
R12	00 55 03.7	−37 43 21	SNR/HII
R13	00 55 12.6	−37 41 38	SNR/HII
R14	00 55 30.1	−37 39 20	SNR/HII

Table 5.5: Radio supernova remnants and supernova remnant candidates in NGC 300 from PF04.

1	2	3	4
Designation	α (h m s) (J2000.0)	δ (° ′ ″) (J2000.0)	Object Type
J005408.6–373804	00 54 08.69	−37 38 04.7	?
J005422.5–373615	00 54 22.53	−37 36 15.1	?
J005423.4–373741	00 54 23.48	−37 37 41.4	hii/bkg
J005423.8–373648	00 54 23.84	−37 36 48.4	snr†
J005423.8–373621	00 54 23.88	−37 36 21.1	?
J005431.2–374554	00 54 31.28	−37 45 54.6	hii/bkg
J005431.9–373825	00 54 31.91	−37 38 25.9	SNR
J005437.9–374559	00 54 37.99	−37 45 59.5	bkg
J005438.1–374144	00 54 38.16	−37 41 44.2	SNR/HII
J005438.4–374240	00 54 38.49	−37 42 40.5	snr/HII
J005439.6–373543	00 54 39.61	−37 35 43.4	snr†
J005440.6–374049	00 54 40.68	−37 40 49.7	SNR/HII
J005441.0–373348	00 54 41.05	−37 33 48.9	bkg/snr
J005442.7–374313	00 54 42.70	−37 43 13.3	SNR/HII
J005443.1–374311	00 54 43.11	−37 43 11.0	SNR/HII
J005445.3–373847	00 54 45.39	−37 38 47.1	SNR/HII
J005448.0–373323	00 54 48.01	−37 33 23.7	?
J005450.2–374030	00 54 50.28	−37 40 30.0	SNR/HII
J005450.3–373822	00 54 50.30	−37 38 22.4	SNR/HII
J005450.5–374123	00 54 50.52	−37 41 23.0	hii/bkg
J005450.7–374022	00 54 50.73	−37 40 22.2	SNR/HII
J005451.1–373826	00 54 51.16	−37 38 26.1	SNR/HII
J005451.7–373939	00 54 51.79	−37 39 39.6	SNR/HII
J005455.3–373557	00 54 55.32	−37 35 57.5	bkg
J005456.7–373413	00 54 56.77	−37 34 13.8	hii/bkg
J005500.5–374037	00 55 00.58	−37 40 37.4	SNR/HII
J005500.9–373720	00 55 00.93	−37 37 20.1	hii/bkg
J005501.4–373829	00 55 01.49	−37 38 29.9	SNR
J005502.1–373952	00 55 02.13	−37 39 52.4	?
J005502.2–374731	00 55 02.25	−37 47 31.0	hii/bkg
J005503.5–374246	00 55 03.50	−37 42 46.0	SNR/HII
J005503.6–374320	00 55 03.66	−37 43 20.1	SNR/HII
J005512.7–374140	00 55 12.70	−37 41 40.3	SNR/HII
J005515.4–374439	00 55 15.40	−37 44 39.2	SNR/HII
J005516.4–374653	00 55 16.45	−37 46 53.7	?
J005521.3–374609	00 55 21.35	−37 46 09.6	bkg/snr
J005523.9–374632	00 55 23.95	−37 46 32.4	bkg/snr
J005525.8–373653	00 55 25.82	−37 36 53.8	bkg/snr
J005527.6–374546	00 55 27.66	−37 45 46.4	hii/bkg
J005528.2–374903	00 55 28.25	−37 49 03.3	snr†
J005533.8–374314	00 55 33.87	−37 43 14.6	SNR/HII
J005541.9–374033	00 55 41.94	−37 40 33.5	snr

X-ray observations or surveys of NGC 300 have been done by Zang et al. (1997), PD00, RP01, Pannuti et al. (2001), PF04, Payne et al. (2005), Carpano et al. (2005, here after, C05), Carpano et al. (2004, 2006a,b). Zang et al. (1997) studied the overall X-ray luminosity of NGC 300 and found this and any point source (probably associated with NGC 300) emission levels to be consistent with stellar sources. An extensive list of X-ray point sources has been produced through these studies. Table 5.6 shows those point sources that are known to be associated with supernova remnants or are candidate supernova remnants. This table uses the same format as Tables 5.4 and 5.5.

PF04 includes 10 X-ray sources. C05 contains a list of 162 X-ray point sources found with the XMM-Newton X-ray observatory. This list has no clear indication of the object type and is therefore not included in Table 5.6. However, Section 6.3.5 contains a discussion of possible links between some of C05's point sources and the supernova remnant candidates observed for this thesis.

Table 5.6: X-ray supernova remnants and supernova remnant candidates in NGC 300 from RP01.

1	**2**	**3**	**4**
	α **(h m s)**	δ ($^\circ$ $'$ $''$)	
Designation	**(J2000.0)**	**(J2000.0)**	**Object Type**
P29	00 54 31.90	−37 38 26.4	SNR
P35	00 54 49.82	−37 40 01.0	snr
P36	00 55 42.08	−37 40 29.5	snr
P38	00 54 41.10	−37 40 48.9	SNR
P41	00 54 45.41	−37 41 43.6	snr
P44	00 54 37.82	−37 42 51.5	snr
P49	00 55 16.01	−37 44 39.3	SNR
P56	00 55 20.89	−37 48 14.0	SNR
P59	00 55 11.51	−37 49 44.2	snr

5.4 The Selection of Objects

Radio, optical, and X-ray surveys of NGC 300 have provided supernova remnant candidates in these respective wavelengths. The objects chosen for observation in this thesis are listed in Table 5.7. The BL97 optical candidates have been observed in radio and X-ray regions with a few of them showing emissions at these wavelengths (see Section 5.5). Because these objects have been observed in non-optical wavelengths and the optical data published by BL97 were made with interference filters and a moderate-resolution ($\simeq$5 Å) spectrometer with some candidates undetected, these candidates were chosen for further optical study. Optical spectra have never been taken of the remaining PF04 radio sources.

For Table 5.7, the left half is the radio source supernova remnant candidates as given in PF04 and the right half is the optical supernova remnant candidates as given in BL97. Column 1 is the designation of the object as given in the respective paper, column 2 is the α and column 3 is the δ in J2000.0 coordinates. The table shows a total of 55 objects, however there is some positional overlap between the radio sources and the optical objects bringing the observed total down to 51 (Table 5.8 shows the overlap between sources). The positions of the 51 objects are shown in Figure 5.2. The observed optical spectra of these objects are described and discussed in Chapter 6.

Table 5.7: Positions (J2000.0) of the selected 51 supernova remnants and supernova remnant candidates in NGC 300.

1	2	3	1	2	3
Object Name	**Position (J2000.0)**		**Object Name**	**Position (J2000.0)**	
	α **(h m s)**	δ (° ′ ″)		α **(h m s)**	δ (° ′ ″)
J005423–373648	00 54 23.84	−37 36 48.4	N300-S1	00 54 19.21	−37 37 23.96
J005431–373825	00 54 31.91	−37 38 25.9	N300-S2	00 54 21.85	−37 40 27.11
J005438–374144	00 54 38.16	−37 41 44.2	N300-S3	00 54 28.86	−37 41 53.32
J005438–374240	00 54 38.49	−37 42 40.5	N300-S4	00 54 30.62	−37 40 53.75
J005439–373543	00 54 39.61	−37 35 43.4	N300-S5	00 54 30.99	−37 37 33.96
J005440–374049	00 54 40.68	−37 40 49.7	N300-S6	00 54 31.91	−37 38 25.68
J005441–373348	00 54 41.05	−37 33 48.9	N300-S7	00 54 33.17	−37 40 16.90
J005442–374313	00 54 42.70	−37 43 13.3	N300-S8	00 54 38.17	−37 41 14.88
J005443–374311	00 54 43.11	−37 43 11.0	N300-S9	00 54 40.20	−37 41 02.12
J005445–373847	00 54 45.39	−37 38 47.1	N300-S10	00 54 40.87	−37 40 48.73
J005450–374030	00 54 50.28	−37 40 30.0	N300-S11	00 54 42.54	−37 43 14.16
J005450–373822	00 54 50.30	−37 38 22.4	N300-S12	00 54 43.86	−37 43 39.08
J005450–374022	00 54 50.73	−37 40 22.2	N300-S13	00 54 46.60	−37 39 44.32
J005451–373826	00 54 51.16	−37 38 26.1	N300-S14	00 54 47.15	−37 41 07.63
J005451–373939	00 54 51.79	−37 39 39.6	N300-S15	00 54 53.32	−37 38 48.24
J005500–374037	00 55 00.58	−37 40 37.4	N300-S16	00 54 54.46	−37 40 35.46
J005501–373829	00 55 01.49	−37 38 29.9	N300-S17	00 54 56.68	−37 43 57.70
J005503–374246	00 55 03.50	−37 42 46.0	N300-S18	00 55 01.39	−37 39 18.17
J005503–374320	00 55 03.66	−37 43 20.1	N300-S19	00 55 05.41	−37 41 21.04
J005512–374140	00 55 12.70	−37 41 40.3	N300-S20	00 55 05.68	−37 46 13.35
J005515–374439	00 55 15.40	−37 44 39.2	N300-S21	00 55 07.15	−37 39 15.17
J005521–374609	00 55 21.35	−37 46 09.6	N300-S22	00 55 07.50	−37 40 43.20
J005523–374632	00 55 23.95	−37 46 32.4	N300-S23	00 55 09.10	−37 39 32.61
J005525–373653	00 55 25.82	−37 36 53.8	N300-S24	00 55 09.48	−37 40 46.21
J005528–374903	00 55 28.25	−37 49 03.3	N300-S25	00 55 10.68	−37 41 27.13
J005533–374314	00 55 33.87	−37 43 14.6	N300-S26	00 55 15.46	−37 44 39.11
J005541–374033	00 55 41.94	−37 40 33.5	N300-S27	00 55 17.54	−37 44 36.65
			N300-S28	00 55 33.76	−37 43 13.13

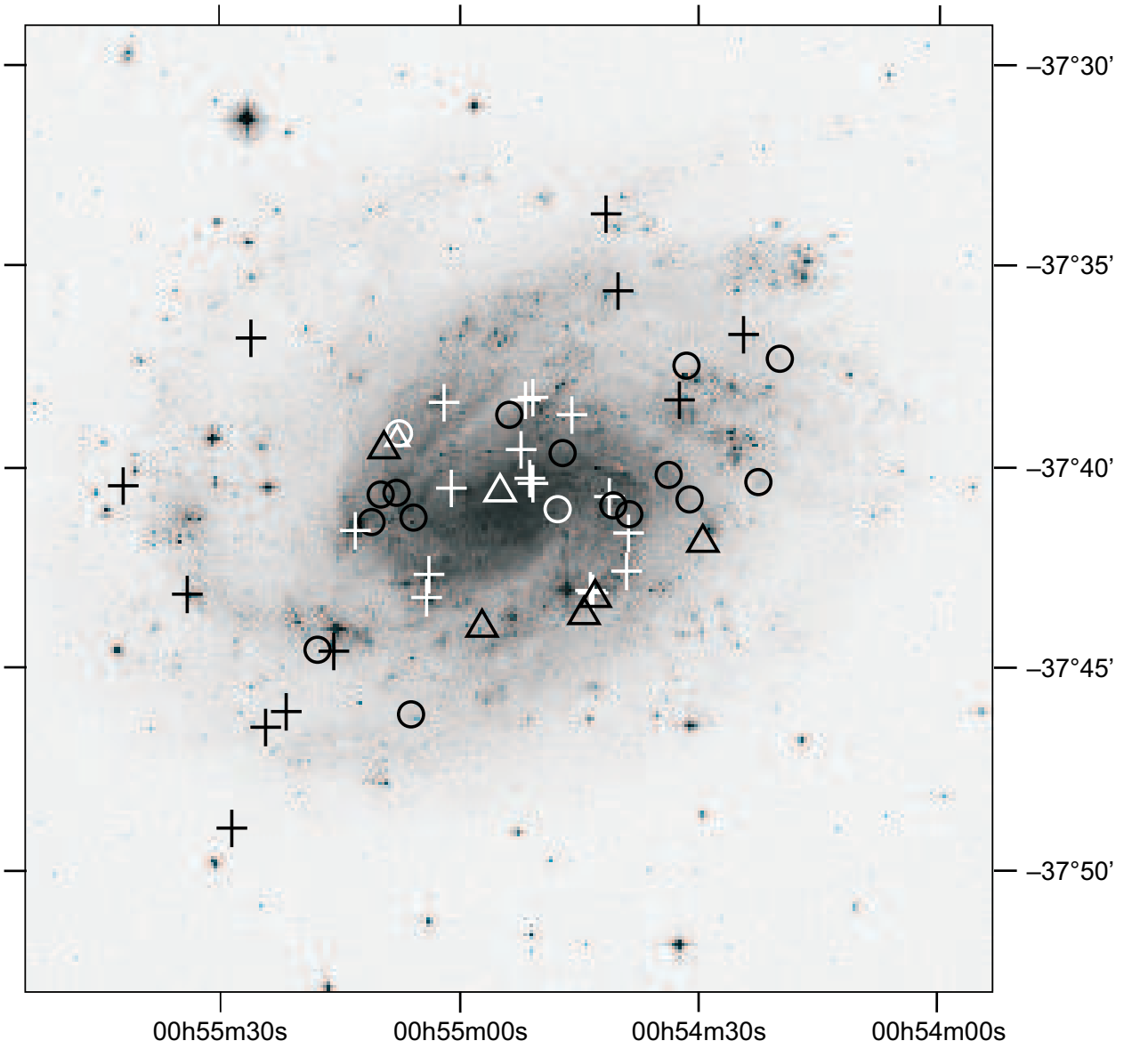

Figure 5.2: A DSS image of NGC 300 indicating the positions (in J2000.0 coordinates) of the 51 supernova remnants and candidate supernova remnants considered in the present study. Selected radio sources from PF04 are shown with crosses. Optical candidates with line ratios measured with long-slit spectra (BL97) are shown as circles and optical candidates with line ratios measured by interference filters (BL97) are shown with triangles. Symbols are black or white only for increased contrast. (Southern sky DSS image, Royal Observatory Edinburgh, Anglo-Australian Observatory, California Institute of Technology.)

5.5 Previous Observations of the Selected Objects

The objects observed for this thesis have a history of observation in electromagnetic regions other than optical. A summary of those observations is presented in Table 5.8. Table 5.8 is divided into three sections according to the results of the observations in Chapter 6. The first section is "SNRs" which are those objects for which the observations resulted in a [S II]:H$\alpha \geq 0.4$. The second section is those objects which did not meet this requirement and the third section is those objects for which no spectrum was obtained.

In Table 5.8, column 1 is the source name used in BL97 and column 2 is the radio source name used in PF04. Column 3 gives the radio spectral index (α, see equation 3.2) from Very Large Array (VLA) observations at 1465 and 4885 MHz as reported in PD00. Column 4 shows the radio spectral index as reported in PF04 and is based on flux densities obtained at 1347, 1448, 2496 and 4860 MHz at ATCA (PF04) or the VLA (PD00).

Column 5 gives the object type proposed by PF04 based on the radio spectral index of column 4. Sources are classified as candidate radio supernova remnants if the spectral index is in the range $-0.8 \leq \alpha \leq -0.2$ and if it is co-identified with an X-ray source. This range is based on a statistical average of the spectral indexes of over 270 Galactic supernova remnants (Trushkin, 1998). PF04 also classified radio supernova remnants taking in account their association with known optical supernova remnants, OB associations or H II regions. For this table, one more object type must be added to the list given on page 73: snr† – is a supernova remnant based on spectral index only.

All supernova remnants emit soft X-rays resulting from heated gas inside the expanding shock front (Aller, 1991; Osterbrock & Ferland, 2006). The identification of potential supernova remnants at X-ray wavelengths is based on spectral fits to the observed emission using thermal bremsstrahlung models. The observed X-ray emission is usually fitted to models (temperature and particle density) to verify the candidacy. X-ray emission can also occur from supernova remnants by virtue of an embedded pulsar or neutron star (e.g. Gaensler et al., 2003).

Columns 6 through 9 show data reported by four papers observing X-ray point sources in positional agreement with the objects observed in this paper. The data come from Read et al. (1997, here after RPS97), RP01, PF04 and C05, respectively.

The data in columns 6 and 7 are from results obtained from observations made with the ROSAT X-ray observatory while data in column 8 are from observations made with the XMM-Newton observatory. A further investigation of putative associations between X-ray sources and supernova remnants through the analysis of

an archival Chandra Observatory HRC-I observation of NGC 300 was performed (see Section 6.2.2).

Column 10 indicates if the source is visible as a nebulous object on the DSS2-Red survey. Column 11 gives the [S II]:Hα as reported by BL97. The values in parenthesis are from Table 3A of BL97 and are based on interference filter images, otherwise they are from Table 4A of BL97 and are based on long-slit spectra.

Table 5.8: Previous observations of the selected objects.

1	2	3	4	5	6	7	8	9	10	11
Object Designation		Radio Observations			X-ray Observations				Optical Observation (BL97)	
Optical	Radio	Spectral Index (PD00)	Spectral Index (PF04)	Proposed Object (PF04)	RPS97 Label Data	RP01 Label Data	PF04 Label Data	C05 Label Data	DSS2-Red	[S II]:Hα
N300-S1									No	0.68
N300-S2								#79	Yes	0.77
N300-S4									Yes	0.99
N300-S5									Yes	0.68
N300-S6	J005431–373825			SNR	#1	P29	XMM2		Yes	0.96
N300-S7									Yes	0.72
N300-S8									Yes	0.61
N300-S9									Yes	0.67
N300-S12									Yes	(0.52)
N300-S13									Yes	0.98
N300-S14									Yes	0.83
N300-S15									Yes	0.74
N300-S16									Yes	(0.70)
N300-S17									Yes	(0.69)
N300-S19								#123	Yes	0.90
N300-S20									Yes	1.00
N300-S22									Yes	0.57
N300-S24									No	0.83
N300-S26 (DDB5)	J005515–374439			SNR/HII	#10	P49	XMM9	#34	Yes	1.03
N300-S25									Yes	0.80
N300-S27									Yes	1.05
N300-S28	J005533–374314			SNR/HII				#151	Yes	0.72
Other Objects (H II Regions?)										
	J005438–374144	< 1.1	-0.8	SNR/HII					Yes	
	J005438–374240	< 1.5		snr/HII					Yes	
	J005439–373543		-0.4	snr†					No	
					36.66, 82.8, 0.10	0.87, -0.33	1.27, -0.63, -0.99	-0.17, -0.58		
						4.8, 25.4	1.63, -0.58, -1.00	1.03, 5.03		
	J005441–373348			bkg/snr			XMM4		Yes	
							1.39, $+0.84$, $+0.94$		Yes	
							0.72, $+0.31$, $+0.62$		Yes	
	J005442–374313		-0.9	SNR/HII					Yes	(0.66)
	J005443–374311	-0.6	-0.6	SNR/HII					Yes	
	J005445–373847		-0.3	SNR/HII					Yes	
	J005450–374030	-0.6	-0.5	SNR/HII					Yes	
	J005450–373822		-0.2	SNR/HII					Yes	
	J005450–374022		-0.3	SNR/HII					Yes	
	J005451–373826		-1.2	SNR/HII					Yes	
	J005451–373939	-0.4	-0.1	SNR/HII					Yes	
	J005500–374037		-0.4	SNR/HII					Yes	
	J005501–373829		-0.9	SNR					Yes	
	J005503–374246	-0.2	-0.4	SNR/HII					Yes	
	J005503–374320	-1.0	-0.7	SNR/HII					Yes	
	J005512–374140	-0.4	-0.7	SNR/HII					Yes	
N300-S3									No	(0.40)
N300-S10(DDB2)	J005440–374049		-0.5	SNR	#4	P38	XMM3	#12	Yes	0.47
N300-S11[a]	J005442–374313?		-0.9	SNR/HII					Yes	(0.66)
N300-S18									Yes	0.71
N300-S21									Yes	(0.59)
N300-S23									Yes	(0.46)
No Signal										
	J005423–373648		-0.7	snr†					No	
	J005521–374609		-1.0	bkg/snr					No	
	J005523–374632		-0.9	bkg/snr					No	
	J005525–373653		-1.0	bkg/snr					No	
	J005528–374903		-0.6	snr†					No	
	J005541–374033			snr			XMM10		No	
							2.35, -0.76, -0.88		No	
							1.08, -0.88, -0.93		No	

Chapter 6

Optical Spectra of Supernova Remnant Candidates in NGC 300

The observations presented in this chapter were originally published in the journal *Astrophysics and Space Sciences* (MWF11). This chapter is an expanded version of that paper. Most of the introductory material from MWF11 is included in Chapter 5.

6.1 Introduction

This chapter presents moderate-resolution (< 5 Å) long-slit optical spectra for 51 nebular objects in the nearby Sculptor Group galaxy NGC 300. The long accepted [S II]:Hα line flux density ratio to distinguish between a supernova remnant and an H II region or planetary nebula is adopted. This criterion – if the [S II]:Hα ratio is ≥ 0.4 the object is assumed to be a supernova remnant, if it is less than 0.2 the object is more likely to be an H II region or a planetary nebula – has been used many times for galaxies in the Local Group and other nearby galaxies (for example, BL97; Matonick & Fesen, 1997; McNeil & Winkler, 2006; Payne et al., 2007, 2008a,c).

The physical processes thought to create this criterion are well understood (BL97 and references therein). Optical emission from a supernova remnant is due mostly to radiative shocks in relatively dense material. Short impulses heat and ionise the gas which recombines over a period of time. Thus supernova remnants have the spectrum of a recombining plasma with strong forbidden-line emission from a variety of ionisation states, including singly ionised sulphur (S^+). In H II regions the ionisation state of the plasma is maintained by hot

stars and most of the sulphur is doubly ionised (S^{++}). Therefore the [S II] lines in H II regions are weak.

The observations and data reduction are presented in Section 6.2. The results of analysis are presented in Section 6.3 including notes on individual objects. Twenty-two objects are confirmed as supernova remnants while the nature of the remaining 29 objects remains uncertain. The main results are summarised in Section 6.4.

6.2 Observations and Data Reduction

6.2.1 Optical Data

The positions (J2000.0) of all 51 supernova remnants and supernova remnant candidates are given in Table 5.7 and are shown in Figure 5.2. Optical spectra of all the sources were obtained in August of 2006 using the 2.3 m ($f/17.9$) Advanced Technology Telescope at Siding Spring Observatory, Australia, and the Dual-Beam Spectrograph (DBS, Rodgers et al., 1988). The slit width was $1''$ and a $4'$ decker[1] was adopted. The observed wavelength domain was 5400 to 9000 Å (from which data were extracted between 6300 and 6800 Å).

Most objects were observed twice, once with the DBS slit aligned in δ (position angle, PA = 0°) and again with the slit aligned in α (PA = 90°). A few objects were surrounded by interesting structure (in DSS2-Red) and further observations were made with the slit positioned at the appropriate angle to include that structure. Fine telescope pointing was done manually by comparing the DBS slit camera image with pointing charts prepared from DSS2-Red images (problems with this technique are discussed in Section 7.7).

The observations reported here used only the red arm of the DBS. The grating used was the 316R (316 lines/mm) which is blazed at $6°\ 48'$. This grating gives a resolution of 4.1 Å (170 km s^{-1}). Used here at a Grating Angle of $3°\ 49'$, the 316R grating gives a central wavelength $\lambda_{\rm cent}$ of 7200 Å. The DBS's SiTE CCD camera has dimensions (1752×532 pixels, with pixels of 15μm). All spectra were 600 second exposures returning a typical background (sky) level of ∼30 – 60 counts per pixel and a centre of spectra level of ∼400 – 600 counts per pixel.

Data reduction and analysis was performed using the Image Reduction and Analysis Facility (IRAF) software package, with Starlink's Figaro cosmic ray cleaner, and Brent Miszalski's "Planetary Nebula Extraction" package for IRAF. All line flux densities were measured with the DEBLEND function of IRAF's SPLOT task. Data reduction included bias subtraction, flat-field correction and wavelengths calibration using standard NeAr arc-

[1] In long-slit spectroscopy, the "decker" is the length of the spectrograph's slit.

lamp lines. The star EG274 was the photometric standard for flux density calibration (Stone & Baldwin, 1983; Baldwin & Stone, 1984; Hamuy et al., 1994).

6.2.2 X-ray Data

To complement the optical spectroscopic observation of supernova remnants in NGC 300, an archival X-ray observation made of this galaxy with the Chandra X-ray Observatory (Weisskopf et al., 2002) was also analysed. This observation made use of the High Resolution Camera (HRC-I, Murray et al., 2000) which can attain an angular resolution of approximately $0\farcs4$. The data from this observation (ObsID 7072 – centred at (J2000.0) $\alpha = 00^{\rm H}55^{\rm M}10^{\rm S}$, $\delta = -37^\circ\ 38'\ 55''$) were downloaded and reduced using standard tools available in the Chandra Interactive Analysis of Observations (CIAO) package (Fruscione et al., 2006) Version 4.0.1. The CIAO tool "acis_process_events" was run to apply the latest calibration files: in addition, the data set was filtered based on grade and status to create a new level = 2 event file (that is, events were removed that did not have a good grade or had one or more of the STATUS bits set to 1). The good time intervals and a light curve was generated to search for background light flares during the observation. The effective exposure time of the final image after processing was 15.19 kiloseconds and the corresponding energy range was 0.3 – 10.0 keV. To detect sources in this field of view, the tool "wavdetect,"[2] was used: a total of 31 sources were detected to a limiting unabsorbed luminosity of approximately 10^{37} ergs sec^{-1} (assuming a distance of 2.1 Mpc to NGC 300; a column density of $N_{\rm H} = 3.08 \times 10^{20}$ cm^{-2}; a Raymond-Smith thermal plasma emission model with a temperature $kT = 0.5$ keV; and solar abundance ratios).

From these 31 sources, only two discrete X-ray sources were found to match the positions (to within $2''$ or less) of known supernova remnants in NGC 300. These particular supernova remnants are the optically-identified supernova remnants N300-S10 and N300-S26. The associations between the X-ray sources and these optically-identified supernova remnants have been presented in previous works (PD00, PF04). The estimated absorbed (unabsorbed) luminosities (over the energy range of 0.3 – 10.0 keV) for the HRC-detected X-ray counterparts to S10 and S26 are 2.7×10^{37} (3.5×10^{37}) and 1.1×10^{37} (1.5×10^{37}), respectively. These luminosities were calculated using the tool PIMMS[3] Version 3.9i assuming a Galactic column density $\rm N_H = 3.08\times10^{20}$ cm^{-2} toward NGC 300 and a thermal bremsstrahlung model with a temperature of $kT = 0.5$ keV. Unfortunately, because of the short

[2] A wavelet-based algorithm used for source detection (Freeman et al., 2002).

[3] http://cxc.harvard.edu/toolkit/pimms.jsp

exposure time of the observation, the limiting unabsorbed luminosity of approximately 1×10^{37} ergs sec^{-1} is too high to detect X-ray emission from the large majority of supernova remnants associated with NGC 300.

6.3 Analysis and Results

For approximately half of the spectra collected the length along the decker of the Hα and the [N II] and [S II] lines were essentially the same, indicating that the emission regions for these lines were of approximately the same physical size. Reduction of these spectra followed standard procedures.

For spectral lines where the Hα, [N II] and [S II] emissions differ in length across the decker (indicating a possible different physical size for the emitting regions) extraction was done so as to ensure that the line ratio was not dominated by Hα emission from the background. In these cases the Hα channels (CCD rows) were a higher count than the [S II] channels and data were extracted only from the channels containing the [S II] emission.

Table 6.1 gives the (measured) integrated line flux densities for all objects in Table 5.8. The first two columns are the designation of the supernova remnant or supernova remnant candidate in PF04 (column 1) or BL97 (column 2). Also listed is the integrated Hα flux density (column 3); the total, integrated [N II] doublet (λ 6548 Å + λ 6583 Å) flux density (column 4); the total, integrated [S II] doublet (λ 6716 Å + λ 6731 Å) flux density (column 5); the ratio of [S II]:Hα (column 6); the total, integrated [O I] lines (λ 6300 Å + λ 6364 Å) flux density (column 7); and the Hα diameter of the object (column 8).

With a few exceptions, each object was observed at least twice and these multiple observations allow the direct computation of the uncertainties in flux densities of each line. Figure 6.1 shows the standard errors (expressed as a percentage) in the means (SEMs) of the individual flux densities for each spectral line in Table 6.1 as a function of flux density of that line. Here, the noise independent uncertainty (of about 22%) and the noise dependent component are clearly delineated. The envelope of uncertainties in Figure 6.1 is defined by:

$$\Delta \mathrm{L} = \sqrt{0.15\mathrm{L} + 0.05\mathrm{L}}, \tag{6.1}$$

where ΔL is the uncertainty in the flux density of each individual line and L is the flux density of that line in units of 10^{-15} erg cm^{-2} s^{-1}. The envelopes for the Hα, [N II] and [S II] data were consistent. The formal uncertainties in the line flux density values of columns 3, 4 and 5 of Table 6.1 are defined by this relationship.

The uncertainty in the [S II]:Hα (column 6 of Table 6.1) is governed by the uncertainties in the flux densities

Table 6.1: The integrated line flux density measurements.

1	2	3	4	5	6	7	8
Designation		Hα	[N II] total	[S II] total		[O I] total	Diameter
Radio	Optical	(10^{-15} erg cm^{-2} s^{-1})	(10^{-15} erg cm^{-2} s^{-1})	(10^{-15} erg cm^{-2} s^{-1})	[S II]:Hα	(10^{-15} erg cm^{-2} s^{-1})	(pc)
SNRs							
	N300-S1[a]	1.3	0.25	0.57	0.46±0.29	2.1	38
	N300-S2	11	3.7	8.1	0.72±0.39	3.3	69
	N300-S4	7.0	3.0	6.5	0.93±0.04	5.1	150
	N300-S5	8.4	2.4	4.7	0.56±0.47	2.2	...[b]
J005431–373825	N300-S6	4.2	1.2	2.9	0.69	0.22	44
	N300-S7	5.2	2.1	3.0	0.57±0.41	2.7	31
	N300-S8	5.0	1.9	2.9	0.58±0.06	2.6	49
	N300-S9	37	12	20	0.53±0.23	4.0	83
	N300-S12	2.3	1.2	1.7	0.73±0.27	2.4	22
	N300-S13	1.9	1.1	1.8	0.91±0.05	1.0	35
	N300-S14	2.3	1.8	2.5	1.08±0.24	1.5	41
	N300-S15	3.0	1.0	1.7	0.57±0.39	0.90	12
	N300-S16	2.2	2.0	2.1	0.94±0.06	1.1	57
	N300-S17	4.2	1.6	4.1	0.96±0.15	1.4	65
	N300-S19	9.4	3.8	6.6	0.70±0.42	0.90	30
	N300-S20	2.3	0.71	1.8	0.79±0.11	0.28	48
	N300-S22	2.9	1.1	1.3	0.46±0.38	1.0	75
	N300-S24	2.7	0.86	1.7	0.64±0.13	0.66	100
	N300-S25	16	4.7	8.7	0.54±0.40	1.8	80
J005515–374439	N300-S26[a]	26	11	23	0.86±0.67	11	31
	N300-S27	6.5	1.7	4.2	0.64±0.48	1.1	66
J005533–374314	N300-S28[a]	69	13	31	0.45±0.15	6.5	63
Other Objects (H II Regions?)							
J005438–374144		80	15	13	0.17±0.07	3.2	
J005438–374240		39	8.5	10	0.25±0.02	3.4	
J005439–373543		5.9	1.4	1.6	0.27	5.2	
J005440–374049	N300-S10	105	32	36	0.35±0.15	4.9	
J005441–373348[a]		1.7	0.34	0.62	0.36	1.5	
J005442–374313		250	48	49	0.19±0.07		
J005443–374311		290	58	53	0.18±0.09		
J005445–373847		130	20	14	0.11±0.03		
J005450–374030		140	46	43	0.32±0.12	8.1	24
J005450–373822		200	40	44	0.22±0.14	7.9	
J005450–374022		84	28	32	0.38±0.31	4.5	130
J005451–373826		140	30	36	0.26±0.16	2.2	
J005451–373939[a]		100	16	10	0.10±0.18	0.51	
J005500–374037		53	17	13	0.25±0.09	2.1	
J005501–373829		6.4	1.5	2.3	0.35±0.12	1.1	31
J005503–374246		150	24	20	0.14±0.04	1.3	
J005503–374320		270	53	41	0.15±0.08	1.6	
J005512–374140		240	27	19	0.08±0.02	0.95	
	N300-S3	51	10	12	0.24±0.31	4.2	26
	N300-S11	1670	39	50	0.30±0.12	6.9	150
	N300-S18[a]	5.0	1.5	1.6	0.32±0.32	0.44	69
	N300-S21	2.1	0.72	0.78	0.37±0.30	0.35	41
	N300-S23	29	7.2	9.1	0.31±0.08	1.3	43
No Signal[c]							
J005423–373648							
J005521–374609							
J005523–374632							
J005525–373653							
J005528–374903							
J005541–374033							

[a] Very low faint spectrum recorded.

[b] Gaussian fit returned value too small to be deconvolved with reference star.

[c] No observed spectral lines.

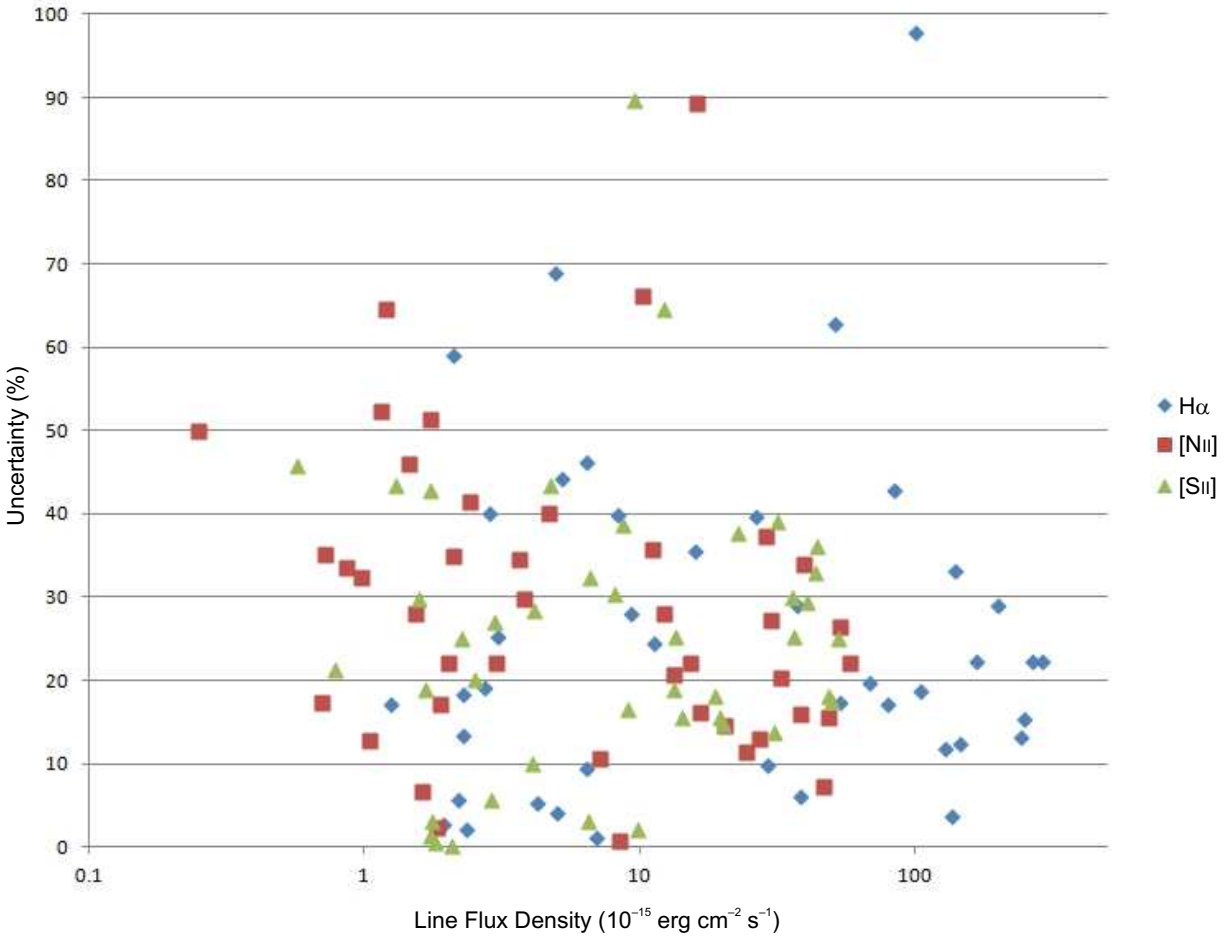

Figure 6.1: The standard errors (expressed as a percentage) in the means (SEMs) of the multiple flux density measurements in the individual spectral lines as a function of flux density of that line. The domain is logarithmic from 0.1 to 500. The noise independent uncertainty is about 22%. Details are given in the text. (Modified from MWF11.)

of the individual lines and is about 8% for ratios close to unity and about 20% for ratios tending towards zero. For the smaller values of [S II]:Hα the uncertainty is made larger by the increased uncertainty in the weaker [S II] lines.

A comparison of the line ratios reported here with those of BL97 (Figure 6.1) shows consistency between these results and the results presented by BL97, but with a small (of order 10%) bias (with BL97 greater than this work) and an indication that this bias is induced by the size of the source as well as the selection of the type of extraction used (see above). As one would expect, the bias is also dependent on the strength of the lines, caused by the rising noise component in the line flux density for very weak lines. Low signal levels (or high background noise) increase the likelihood of not finding a supernova remnant (due to increased measurement errors) and thus increases the bias in the overall results.

6.3.1 Measurement of the Supernova Remnant Diameter

The estimated linear diameter of the supernova remnant candidates was made by fitting a Gaussian profile to the Hα, [N II] and [S II] lines along the decker. The image scale of the SiTE detector is $0\farcs78$ channel^{-1} which corresponds to 7.7 pc channel^{-1} at the adopted distance of NGC 300 (2.1 Mpc). Each spectral line was then deconvolved with the standard star for that night to give a diameter of the candidate in parsecs. The full-width half-maximum (FWHM) diameters are given in column 8 of Table 6.1.

For the optical candidates published in BL97, a comparison of these diameter measurements with those in BL97 does not show good correlation ($r^2 = 0.02$). This, it is believed, was not the result of any problem with these data or that of BL97, rather that the data sets are limited by the seeing ($\sim 2''$), which is of approximately the same size as the object itself. These measured diameters indicate an average size of 54 ± 22 pc, and on this basis, it was noted that there are only three objects (N300-S4, N300-S11 and N300-S24; where N300-S4 and N300-S24 are confirmed supernova remnants) that are worthy of being noted as large objects at 150 pc, 150 pc and 100 pc respectively. Sources of this size may be superbubbles rather than a single supernova remnant.

In addition, a search was made for large Hα diameters relative to smaller [N II], [S II] or [N II] + [S II] diameters, as indications of an embedded supernova remnant in H II regions. There is only one object that might stand a solid statistical analysis – N300-S6 – where the Hα is larger than the [S II] by a factor of 2.6 and the combined [N II] + [S II] is larger by 2.2. However, BL97 reported the same diameter, therefore, either the [S II] diameter reported by BL97 or Hα diameter measurement here is an overestimate. Further work at higher

angular resolution is required to better determine the diameters of these objects.

6.3.2 Overall Results

The supernova remnant candidates published in BL97 were originally found using Hα and [S II] interference filters on the 2.5 m du Pont Telescope at Las Campanas. Surveys of this type preferentially find objects with large [S II]:Hα ratios. As confirmation, moderate-resolution long-slit spectra were obtained by BL97 for 21 of their 28 candidates using the Modular Spectrograph and the line flux density measurements are presented in BL97 as Table 4A. Satisfactory spectra for all 28 candidates were obtained from these observations and 22 (78%) objects were confirmed as optical supernova remnants, based on [S II]:Hα.

Figure 6.2 shows example spectra (from MWF11) of objects meeting the [S II]:H$\alpha \geq$ 0.4 criterion and are therefore labelled as supernova remnants in these results. Figure 6.3 shows example spectra for objects which do not meet the criterion. A summary of these results is given in Table 6.2. Of the 27 radio objects suggested as supernova remnants by PF04, only three are confirmed (11%). These three radio sources are positionally linked to three of the supernova remnants listed in BL97 and are included in the 22 confirmed supernova remnants.

Figure 6.4 shows a plot of the [S II]:Hα values for all objects which returned data. A trend can be seen for objects below 0.4 to have greater Hα emissions, lending support to these objects appearing as H II regions rather than supernova remnants at optical wavelengths. Figure 6.5 shows a plot of [N II] flux against Hα flux. This plot shows a fairly consistent ratio of $[\mathrm{N\,II}]_{Total}$:Hα of 0.3 across both groups of objects. Figure 6.6 shows a plot of [O I] flux against Hα flux. The plot shows a consistent value of [O I] emission from both object groups, with greater Hα emission from the "other" objects. Because [O I] flux is associated with supernova remnant shock fronts it may be possible that the emission from the "other sources" is caused by shock fronts created by supernova remnants buried within H II regions and are visible only in radio.

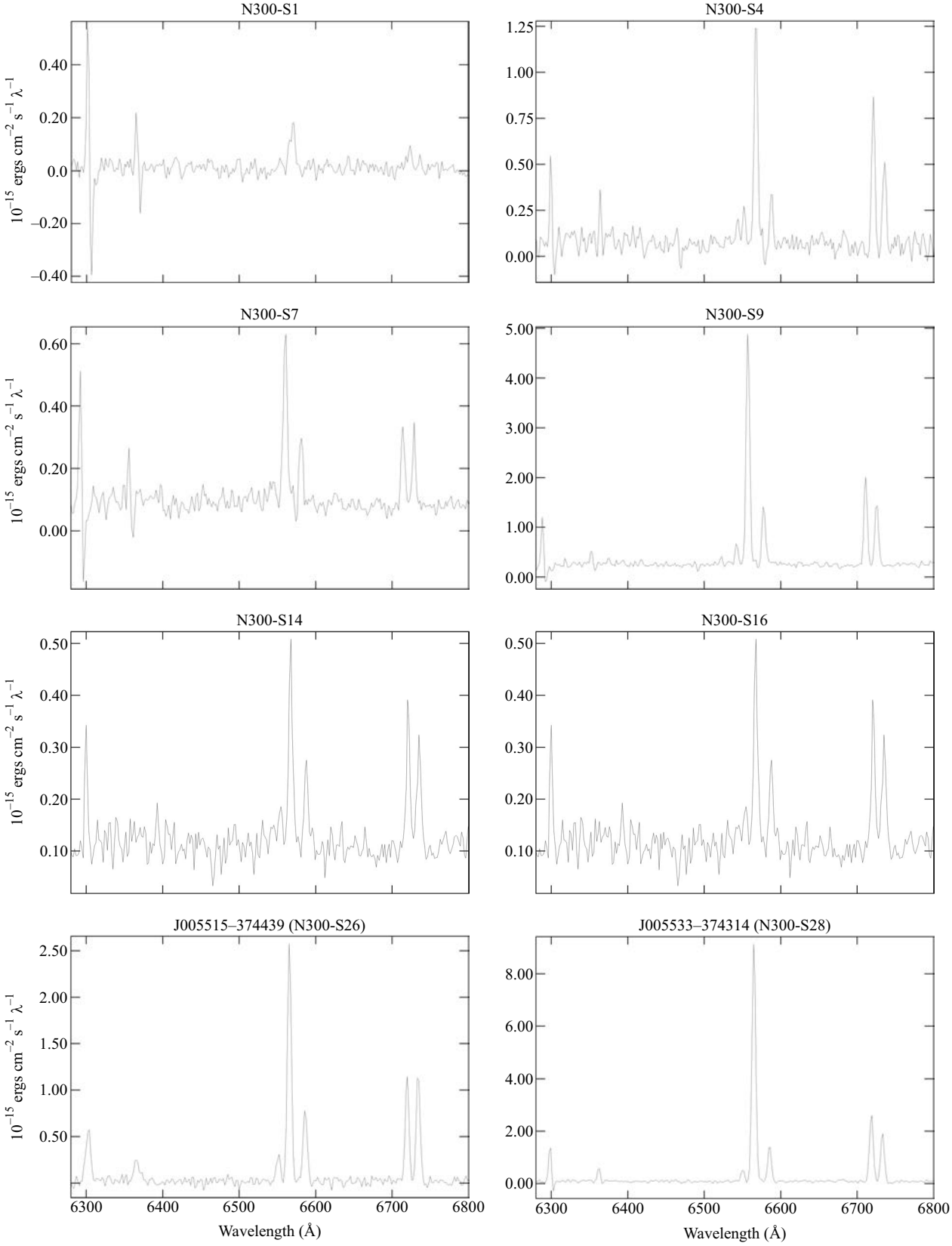

Figure 6.2: Example spectra of objects meeting the [S II]:Hα > 0.4 criterion and are therefore labelled as supernova remnants in these results. (Credit: MWF11)

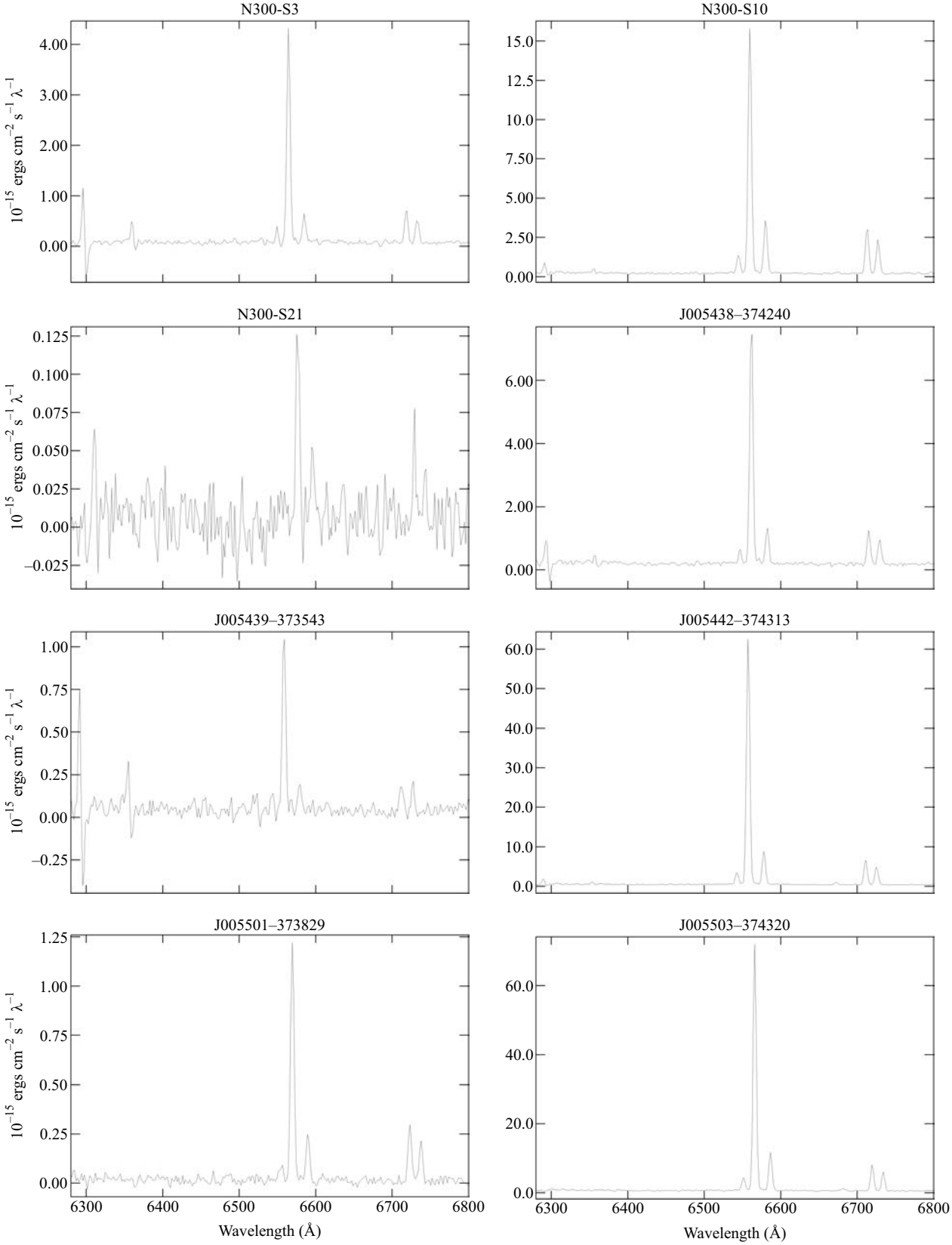

Figure 6.3: Example spectra of objects which did not meet the [S II]:H$\alpha > 0.4$ criterion and are therefore labelled as "other objects" in these results. (Credit: MWF11)

Table 6.2: Summary of results.

1 Optical object	2 Radio object	3 Object type (PF04)	4 Object type (BL97)	5 [S II]:Hα	6 Diameter (pc)
SNRs					
N300-S1			SNR	0.46±0.29	38
N300-S2			SNR	0.72±0.39	69
N300-S4			SNR	0.93±0.04	150
N300-S5			SNR	0.56±0.47	...[a]
N300-S6	J005431–373825	SNR	SNR	0.69	44
N300-S7			SNR	0.57±0.41	31
N300-S8			SNR	0.58±0.06	49
N300-S9			SNR	0.53±0.23	83
N300-S12			SNR	0.73±0.27	22
N300-S13			SNR	0.91±0.05	35
N300-S14			SNR	1.08±0.24	41
N300-S15			SNR	0.57±0.39	12
N300-S16			SNR	0.94±0.06	57
N300-S17			SNR	0.96±0.15	65
N300-S19			SNR	0.70±0.42	30
N300-S20			SNR	0.79±0.11	48
N300-S22			SNR	0.46±0.38	75
N300-S24			SNR	0.64±0.13	100
N300-S25			SNR	0.54±0.40	80
N300-S26	J005515–374439	SNR/HII	SNR	0.86±0.67	31
N300-S27			SNR	0.64±0.48	66
N300-S28	J005533–374314	SNR/HII	SNR	0.45±0.15	63
Other Objects (H II Regions?)					
	J005438–374144	SNR/HII		0.17±0.07	
	J005438–374240	snr/HII		0.25±0.02	
	J005439–373543	snr†		0.27	
	J005441–373348	bkg/snr		0.36	
	J005442–374313	SNR/HII		0.19±0.07	
	J005443–374311	SNR/HII		0.18±0.09	
	J005445–373847	SNR/HII		0.11±0.03	
	J005450–374030	SNR/HII		0.32±0.12	
	J005450–373822	SNR/HII		0.22±0.14	
	J005450–374022	SNR/HII		0.38±0.31	130
	J005451–373826	SNR/HII		0.26±0.16	
	J005451–373939	SNR/HII		0.10±0.18	
	J005500–374037	SNR/HII		0.25±0.09	
	J005501–373829	SNR		0.35±0.12	31
	J005503–374246	SNR/HII		0.14±0.04	
	J005503–374320	SNR/HII		0.15±0.08	
	J005512–374140	SNR/HII		0.08±0.02	
N300-S3			SNR	0.24±0.31	26
N300-S10	J005440–374049	SNR	SNR	0.35±0.15	63
N300-S11			SNR	0.30±0.12	150
N300-S18			SNR	0.32±0.32	69
N300-S21			SNR	0.37±0.30	41
N300-S23			SNR	0.31±0.08	43
No Signal					
	J005423–373648	snr†			
	J005521–374609	bkg/snr			
	J005523–374632	bkg/snr			
	J005525–373653	bkg/snr			
	J005528–374903	snr†			
	J005541–374033	snr			

[a]Gaussian fit returned a value too small to be deconvolved.

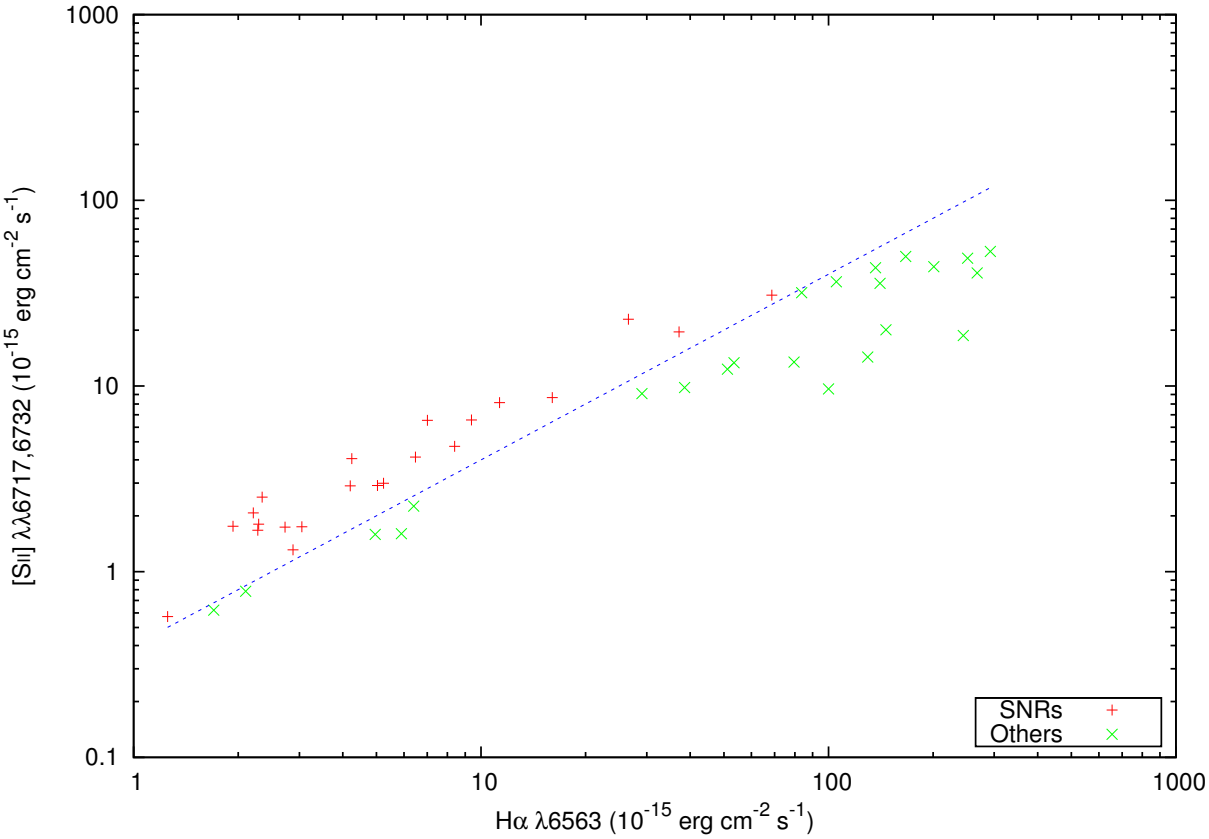

Figure 6.4: A plot of [S II]:Hα values for the objects labelled as supernova remnants and "other objects." The scales were made logarithmic to make the data points more visible. The dashed line represents the [S II]:Hα of 0.4. (Credit: MWF11)

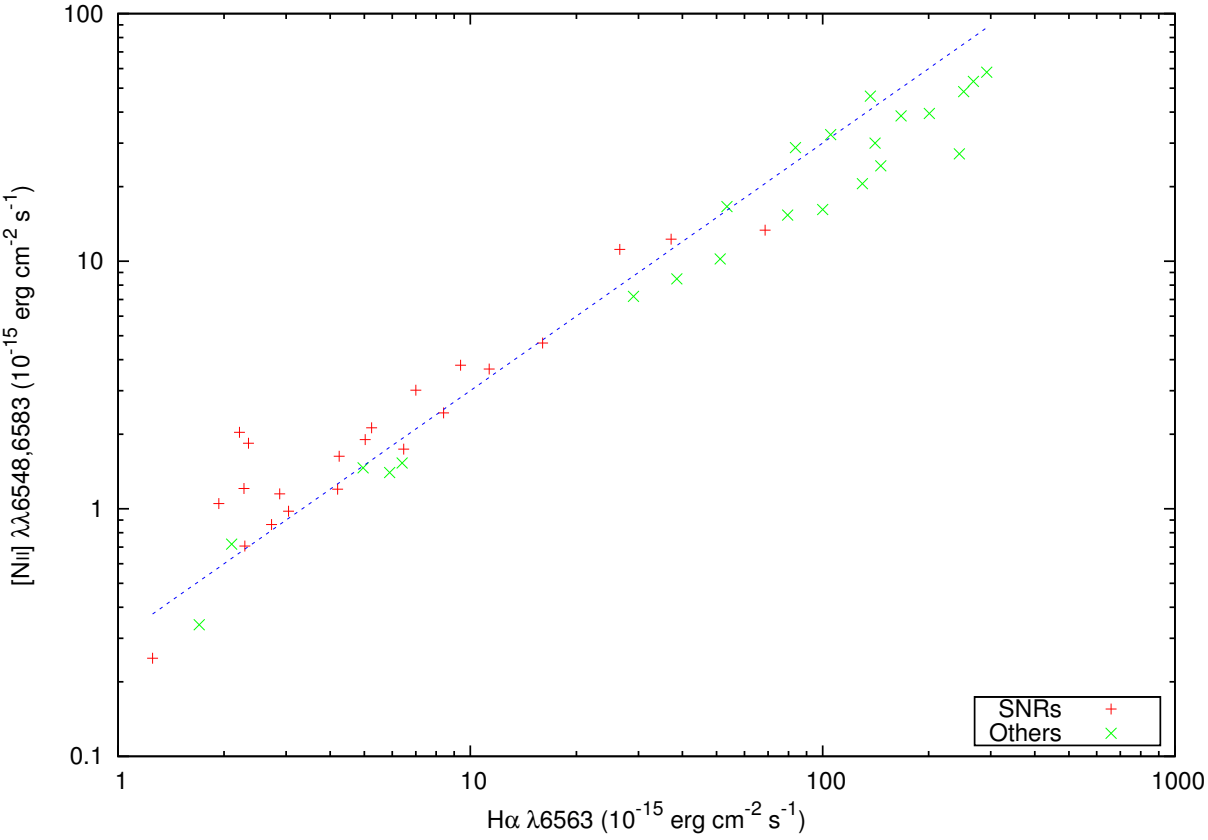

Figure 6.5: A plot of [N II] vs. Hα flux values for the objects labelled as supernova remnants and "other objects." The scales were made logarithmic to make the data points more visible. The plot shows a consistent nitrogen-hydrogen ratio of roughly 0.3 (indicated by the dashed line) across both groups of objects. (Credit: MWF11)

6.3.3 Notes on Individual Radio Objects

These radio sources are point sources. That is, there is no measured (surface) size for these sources. The optical-spectral observations of these radio sources attempted to place the coordinates of these sources in the spectrograph's slit by guiding on visible objects in the slit image camera and printed finding maps. Seeing was estimated as two arcseconds. Later analysis showed the success or failure to place the source's coordinates within the slit. See Section 7.7 for examples of this analysis.

J005431-373825

The radio source J005431-373825 is associated with the optical object N300-S6 and thus has both radio and optical emission. The line ratio of 0.69 confirms this object as a supernova remnant but for unknown reasons it has very weak [O I] lines (0.22). This supernova remnant also shows hard X-ray emission (C05).

J005438-374144

There is a faint optical object at the position of this radio source which was previously classified as a supernova remnant by PF04. The spectrum shows a [S II]:Hα ratio of 0.17 with an error of 0.07. [S II]:Hα does not confirm this object as a supernova remnant although on the basis of the [O I] flux of 3.2, this radio source may be a supernova remnant hidden within an H II region.

J005440-374049

The radio source J005440-374049 (N300-S10) was observed three times (once more after the main runs, with PA = 45°) because of the interesting structure seen on the DSS2-Red. All three observations return a line ratio of < 0.4. The diameter measurement for this object is 63 pc, significantly larger than BL97 which describes it as very compact (16 pc). Based on the proposed radio and optical identification from PF04 and BL97, the X-ray identification (also see Section 6.2.2), the [S II]:Hα of < 0.4 but the [O I] flux of 4.9, this object is classified as a supernova remnant.

J005441-373348

Optical emission from this source was very weak and so the flux measurements are unreliable. However it was observed in X-rays as XMM4 by PF04 and as source #54 in C05. As these papers have noted, this object is probably a background source.

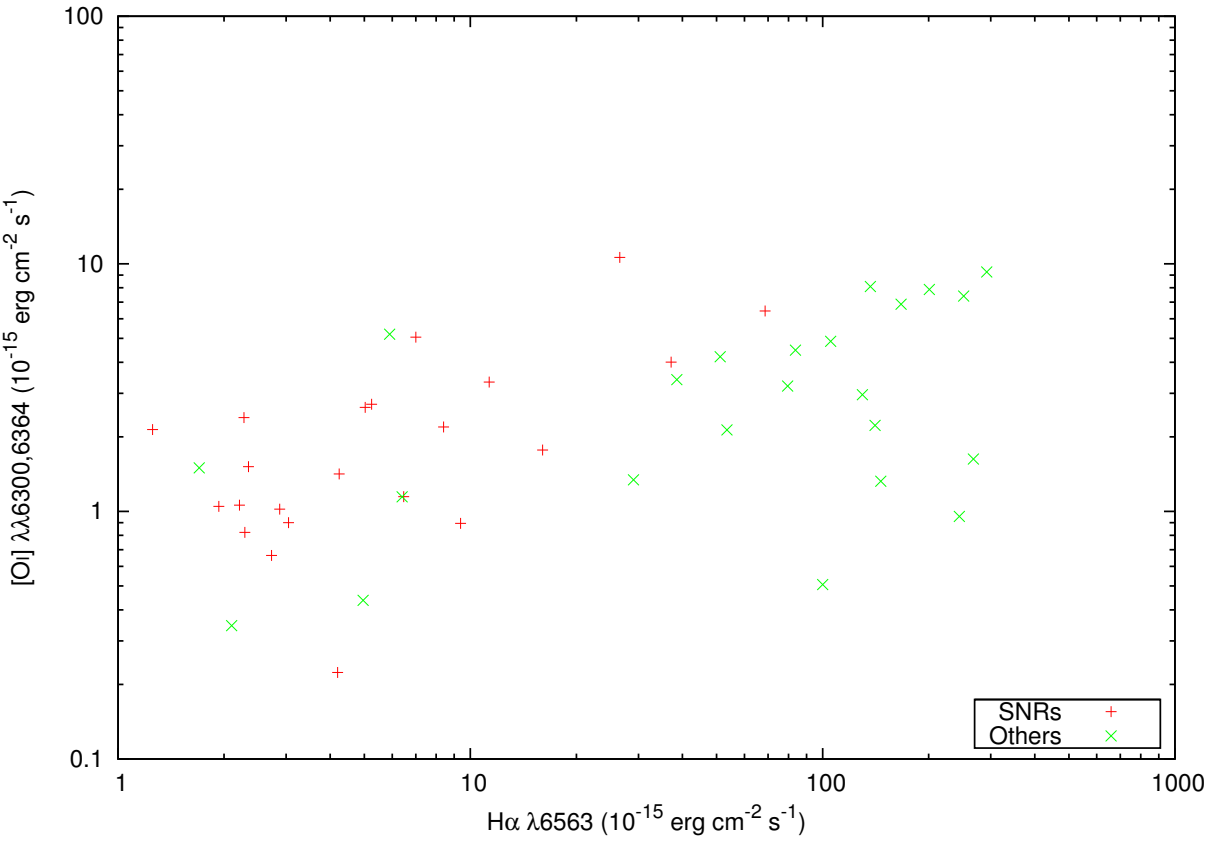

Figure 6.6: A plot of [O I] vs. Hα flux values for the objects labelled as supernova remnants and "other objects." The scales were made logarithmic to make the data points more visible. The plot shows a consistent value of [O I] emission from both object groups, with greater Hα emission form the "other" objects. Because [O I] flux is associated with supernova remnant shock fronts it may be possible that the emission from the "other objects" is caused by shock fronts created by supernova remnants that are visible only in radio, being buried within H II regions. (Credit: MWF11)

J005442-374313 and J005443-374311

The sources J005442–374313, J005443–374311 and N300-S11, are in the same line of sight and may be located near to each other. They also have similar optical spectra and [S II]:Hα ratios (Table 6.3) with no measurable [O I] emission. This is most likely due to the inability to separate these source under the seeing conditions. N300-S11 was observed in both PD00 and BL97 and identified as a supernova remnant in BL97. PD00 searched for X-ray and radio emissions from this source but no definitive counterparts could be identified. X-ray source #161 in the catalogue given by C05 is nearby, but not within the positional uncertainties given in the respective papers. With these data, these objects remain candidate "radio" or "optical" supernova remnants and their physical association is still questionable. Table 6.3 gives the positional agreement between these sources and source #161 from the C05 X-ray point source catalogue.

J005450-374030 and J005450-374022

Radio sources J005450-374030 and J005450-374022 are 10.″3 ($\simeq$100 pc) from each other. The [S II]:Hα for these objects are 0.32$\pm$0.12 and 0.38$\pm$0.31 respectively. However the [O I] flux of the later (4.5) is about half that of the former (8.1). They may be two radio emission regions within the same (perhaps older and larger) supernova remnant or simply two neighbouring candidate radio supernova remnants. Also note that the rather large errors in these flux ratio measurements overlap the supernova remnant criterion value, 0.4.

J005501-373829

J005501-373829 is on the western edge of a large region of optical emission (dim in DSS2-Red but bright in DSS; perhaps indicating a strong component of reflected emission). This object has radio (PF04) emission but its optical emission has [S II]:Hα of 0.35 ± 0.12 with relatively weak [O I] of 1.1. Note the proximity of the OB association AS_082 (Pietrzyński et al., 2001a) which is cross-referenced by those authors to H II region 115 in the Deharveng et al. (1988) catalogue.

J005515-374439

The radio source J005515-374439 is associated with N300-S26 and has [S II]:Hα of 0.86$\pm$0.67 with a very strong [O I] emission of 11. This source is confirmed as a supernova remnant although the ratio measurement error is quite large. It is on the edge of a small, circular, faint object visible in both DSS2-Red and DSS images. This supernova remnant has proximity to OB association AS_107, H II region 141 and also to PF04's XMM9 X-ray

Table 6.3: Three neighbouring sources.

1	**2**	**3**	**4**	**5**	**6**
Source	**J005442–374313**	**J005443–374311**	**N300-S11**	**Carpano #161**	**[S II]:Hα**
J005442–374313		6.57, 66.3	2.73, 27.6	20.3, 205	0.282±0.003
J005443–374311	6.57, 66.3		9.23, 93.2	25.2, 254	0.237±0.002
N300-S11	2.73, 27.6	9.23, 93.2		18.9, 191	0.317±0.003

Note: The distance between each pair of sources is given in arcseconds and then in parsecs.

source. Also, C05 lists N300-S26 as a soft X-ray source (#34). The complementary HRC X-ray observations of this object confirm a discrete X-ray source within 2″ of the radio position. For more details see Section 6.2.2.

J005533-374314

J005533-374314 (associated with N300-S28) has a measured [S II]:Hα of 0.45±0.15, a moderate [O I] emission of 6.5 and an optical counterpart with an estimated size of 63 pc, which in both DSS2-Red and DSS has a two-lobed shape. The radio emission is southeast of the centre of the lobes. J005533–374314 may be linked to the OB association AS_113 and H II region 159. C05 found an X-ray source at this location (#151). Better optical imaging and further X-ray observations of this supernova remnant will prove beneficial.

6.3.4 Sources with No Measured Spectrum

No measurable level of Hα and/or [S II] flux against the background noise was detected from the following sources: J005423–373648, J005521–374609, J005523–374632, J005525–373653, J005528–374903, and J005541–374033. The nature of these sources is thus uncertain.

PF04 suggests the two radio sources J005423–373648 and J005528–374903 as low confidence supernova remnant candidates. The other PF04 sources in the above list have radio emission which would not exclude them as possible supernova remnants. Given the data and discussion in PF04, failure to detect an optical emission spectrum typical of supernova remnants is consistent with the PF04 expectations.

6.3.5 The Multi-Wavelength Properties of the Supernova Remnants

In PD00, PF04, Pannuti et al. (2007), Long et al. (2010) and Pannuti et al. (2011), Venn diagrams were used to show the number of "radio," "optical," and "X-ray" supernova remnants in NGC 300, M 33 and NGC 7793. Figure 6.7 shows a new diagram using results from these data and PD00, PF04, C05, and Carpano et al. (2006a). The supernova remnants included within each region are listed in Table 6.4.

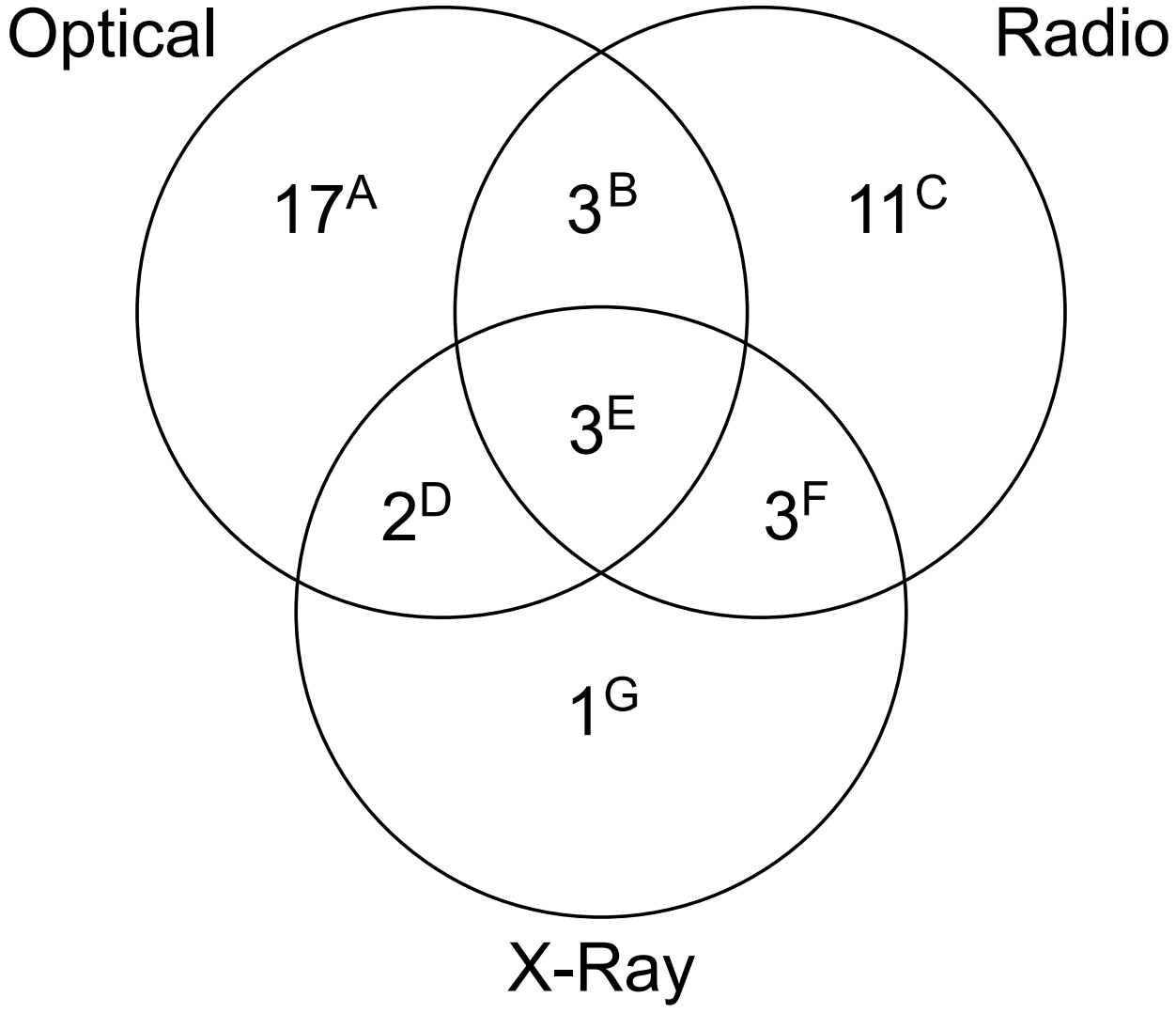

Figure 6.7: A Venn diagram showing the intersection of selected sets of supernova remnants for NGC 300. The letter superscript on each value corresponds to the "Venn Region" column of Table 6.4. (Credit: MWF11)

The majority of the supernova remnants (29 out of 40) are identified with emission in only one wavelength region. Note also the low numbers of multiple-frequency and high-energy supernova remnants; there are only six supernova remnants detected in both radio and optical wavelengths and only three detected in all three wavelength regions. One supernova remnant was detected in X-ray wavelengths only, and nine supernova remnants detected in X-ray wavelengths.

These results are somewhat similar to the M 33 findings of Long et al. (2010) and in NGC 7793 (Pannuti et al., 2011) where a large number of optical-only supernova remnants are identified. This may imply a possible observational bias towards the optical techniques of supernova remnant detection in external galaxies where the resolution (and sensitivity) may play a dominant role in supernova remnant identification. To further this argument, Dopita et al. (2010a,b) showed that the [S II]:Hα is a very "sharp" tool in the case of two other nearby galaxies (M 83 and NGC 4214) where they used advanced Hubble Space Telescope imaging and spectroscopy. Therefore, the population in the Venn cells is probably of little astrophysical consequence as it is determined mostly by selection effects and the sensitivity limits of the present radio, optical and X-ray survey technologies. Details of these limits are given in PF04, Pannuti et al. (2007), BL97, and by C05 for the X-ray observations reported here.

It is accepted (Filipović et al., 1998) that all supernova remnants will emit some thermal radiation at all of these wavelengths. In addition, most supernova remnants exhibit non-thermal properties in radio and a handful of supernova remnants in X-ray. However, the amount of emission at each band is the subject of numerous studies, and it is generally understood that the emission is determined by the supernova event itself and the interstellar matter in which it occurs. These two variables lead to a wide range of observed structural and emission properties when supernova remnants are studied over the full electromagnetic spectrum, and no standard spectrum over all wavelengths exists for supernova remnants.

Compounding these variations are the selection effects that have been introduced. The radio observations of PF04 have preferentially selected all sources with spectral index below +0.2 (a safer spectral index selection cut-off value would be +0.5), which probably excludes half of the supernova remnants available at these wavelengths, and selects preferentially the non-thermal objects. Similarly, the filter-based optical selection of BL97 preferentially selects objects with strong [S II]. This again is a safe choice for locating supernova remnants, but will miss older objects or the [O III] dominated objects that are perhaps present at the 10 to 15% level (Stupar et al., 2008). It is clear that further studies conducted with instruments featuring improved sensitivity will result

Table 6.4: Sources placed in the Venn diagram of Figure 6.7.

Venn region	**Source count**	**Designations**
A	17	N300-S1, S4, S5, S7 – S9, S12 – S17, S20, S22, S24, S25, S27
B	3	J005450–374030, J005450–374022, J005501–373829
C	11	J005438–374144, J005442–374313 (N300-S11?)
		J005443–374311, J005445–373847, J005450–373822
		J005451–373826, J005451–373939, J005500–374037
		J005503–374246, J005503–374320, J005512–374140
D	2	N300-S2 (C79), N300-S19 (C123)
E	3	N300-S6 (J005431–373825, C69)
		N300-S26 (J005515–374439, C34)
		N300-S28 (J005533–374314, C151)
F	3	C60 (SNR5-R4), C72 (SNR3-R3)
		N300-S10 (J005440–374049, C12)
G	1	C20 (SNR15-X11)

Note: N300-S (or just S) refers to BL97 optically selected supernova remnants.

Note: SNR refers to PD00 radio (-R) and X-ray (-X) supernova remnants.

Note: J refers to PF04 (ATCA) radio supernova remnants.

Note: C refers to C05 X-ray supernova remnants.

in the detection of more supernova remnants within each wavelength region thus increasing the populations of individual cells of the Venn diagram.

To complete this study the dependence of the [S II]:Hα with distance from the galactic nucleus was investigated. No statistically-significant dependence was found.

6.4 Summary

It is not surprising that only a few radio supernova remnant candidates exhibiting the established [S II]:Hα were found. At the distance to this galaxy (2.1 Mpc), with this slit width (1″) and the seeing spread along the decker, the sampling is about 100 square parsecs per "line." Thus, each spectral line contains the light from ∼50 000 field stars as well as the emission from the nebula. Although [S II]:H$\alpha \geq 0.4$ may be fine for galaxies of the Local Group, it may not be the best tool for detecting more distant extragalactic supernova remnants unless the highest resolution telescopes such as the Hubble Space Telescope are used. The findings are summarised as follows:

1. Moderate resolution optical spectra of 51 nebular objects in the Sculptor Group galaxy NGC 300 were obtained. Of the 51 objects, 4 were proposed as supernova remnant candidates in both optical and radio observations, 24 are proposed supernova remnant candidates from optical spectra and 23 are supernova remnant candidates from radio spectra.

2. Twenty-two objects meeting the accepted [S II]:Hα criterion were confirmed as supernova remnants, with the nature of the remaining 29 objects either unclear or unknown. A slight bias (of order 10%) appears between the [S II]:Hα for the optical candidates compared to a previous observation of these same objects (BL97).

3. A Gaussian fit of the image of the nebular object across the spectroscope's slit was created to estimate the diameter of the candidate supernova remnants. Comparison of these new diameter measurements does not show good correlation with previous size estimates (from BL97).

4. Thirty-one X-ray sources in this galaxy were found, two of which are positionally linked to nebulae meeting the accepted [S II]:Hα ratio as supernova remnants.

Chapter 7

Optical Observing Techniques: NGC 300

The observing techniques, equipment used and seeing conditions for extragalactic supernova remnant surveys and spectroscopy may have a negative influence on the reliability of spectroscopic extragalactic supernova remnant identification. This possibility is examined here. Most of the content of this chapter was originally published in the *Serbian Astronomical Journal* (MWF12). This chapter is an expanded version of that paper. Most of the introductory material from MWF12 is included in Chapter 5.

7.1 Introduction

The resolving power (or seeing) of the two-meter class, ground-based telescopes usually used for supernova remnant observations is generally from $0\farcs5$ (Chilé) up to $2''$ (Siding Spring, Australia or Sutherland, South Africa). These seeing conditions do not allow the direct imaging of extragalactic supernova remnants (to any useful resolution) and therefore, spectral line intensity ratios are used for identification of these objects.

The spectra of 51 extragalactic supernova remnants in NGC 300 were examined in Chapter 6 and the results of the observations are shown in Table 6.2. A new summary of the results of all previous observations (BL97, PF04, MWF11) is given in Table 7.1. Column 1 is the optical designation as given in BL97. Column 2 is the radio designation as given in PF04. Columns 3 and 4 are the α and δ coordinates. Column 5 is the [S II]:Hα as reported in (or derived from) BL97. Column 6 is the [S II]:Hα as reported in MWF11 (including

the measurement error discussed in MWF11). Column 7 is the spectral index (α) as reported in PF04 and column 8 is the measured diameter as reported in MWF11. The radio sources which do not reach the [S II]:Hα threshold value (0.4) to be labelled as optical supernova remnants may still be supernova remnants if they are actually being obscured by the emissions from neighbouring H II regions. This possibility is further supported by the investigation of the radio observations' astrometry (Section 7.3.1).

To investigate the reliability of using [S II]:H$\alpha \geq 0.4$ as a defining criterion for the detection and identification of extragalactic supernova remnants, and the effectiveness of the observing techniques used for extragalactic supernova remnant surveys and spectrographs, a study of comparisons of the observations of these supernova remnant candidates between BL97, PF04, MWF11 and images containing the candidates found in the archives of the Hubble Space Telescope was made. For reasons given below, this study included an analysis of the astrometry of the original CCD images from BL97, a discussion of the astrometry of the radio observations from PF04, and an analysis of the pointing errors inherent in the ground-based telescopes generally used for extragalactic supernova remnant observations.

Five sources which were comparable between the observation sets – four radio sources and one optical source – were found. An apparent systematic error in the radio observation astrometry was also observed. Unfortunately, with only four radio sources to work with in the current Hubble Space Telescope data, testing this possible error any further requires more high-resolution (Hubble Space Telescope) optical images which are currently unavailable. Only one source was in both the BL97 and Hubble Space Telescope observations. However this one source demonstrated a need for further investigation into the reliability of using the [S II]:Hα line ratio for the identification of extragalactic supernova remnants in optical surveys and spectral observations.

Table 7.1: Summary of observational results for the selected objects (from BL97, PF04, and MWF11). The cut-in headers are from MWF11.

1	2	3	4	5	6	7	8
Optical	**Radio**	α	δ	**[S II]:Hα**	**[S II]:Hα**	$\alpha \pm \Delta\alpha$	**Diameter**
Object	**Object**	**(h m s)**	**(° ′ ″)**	**(BL97)**	**(MWF11)**	**(PF04)**	**(pc, MWF11)**
SNRs (MWF11)							
N300-S1		00 54 19.21	−37 37 23.96	0.44	0.46 ± 0.29		38
N300-S2		00 54 21.85	−37 40 27.11	0.49	0.72 ± 0.39		69
N300-S4		00 54 30.62	−37 40 53.75	0.71	0.93 ± 0.04		150
N300-S5		00 54 30.99	−37 37 33.96	0.46	0.56 ± 0.47		
N300-S6	J005431–373825	00 54 31.91	−37 38 25.68	0.60	0.69[a]	–[b]	44
N300-S7		00 54 33.17	−37 40 16.90	0.57	0.57 ± 0.41		31
N300-S8		00 54 38.17	−37 41 14.88	0.61	0.58 ± 0.06		49
N300-S9		00 54 40.20	−37 41 02.12	0.44	0.53 ± 0.23		83
N300-S12		00 54 43.86	−37 43 39.08	0.52	0.73 ± 0.27		22
N300-S13		00 54 46.60	−37 39 44.32	0.59	0.91 ± 0.05		35
N300-S14		00 54 47.15	−37 41 07.63	0.63	1.08 ± 0.24		41
N300-S15		00 54 53.32	−37 38 48.24	0.65	0.57 ± 0.39		12
N300-S16		00 54 54.46	−37 40 35.46	0.70	0.94 ± 0.06		57
N300-S17		00 54 56.68	−37 43 57.70	0.69	0.96 ± 0.15		65
N300-S19		00 55 05.41	−37 41 21.04	0.53	0.70 ± 0.42		30
N300-S20		00 55 05.68	−37 46 13.35	0.75	0.79 ± 0.11		48
N300-S22		00 55 07.50	−37 40 43.20	0.27	0.46 ± 0.38		75
N300-S24		00 55 09.48	−37 40 46.21	0.80	0.64 ± 0.13		100
N300-S25		00 55 10.68	−37 41 27.13	0.64	0.54 ± 0.40		80
N300-S26	J005515–374439	00 55 15.46	−37 44 39.11	0.57	0.86 ± 0.67	–	31
N300-S27		00 55 17.54	−37 44 36.65	0.70	0.64 ± 0.48		66
N300-S28	J005533–374314	00 55 33.76	−37 43 13.13	0.61	0.45 ± 0.15	–	63
Other Objects (H II Regions? MWF11)							
	J005438–374144	00 54 38.16	−37 41 44.2		0.17 ± 0.07	-0.8 ± 0.2	
	J005438–374240	00 54 38.49	−37 42 40.5		0.25 ± 0.02	–	
	J005439–373543	00 54 39.61	−37 35 43.4		0.27	-0.4 ± 0.1	
	J005441–373348	00 54 41.05	−37 33 48.9		0.36	–	
	J005442–374313	00 54 42.70	−37 43 13.3		0.19 ± 0.07	-0.9 ± 0.3	
	J005443–374311	00 54 43.11	−37 43 11.0		0.18 ± 0.09	-0.6 ± 0.2	
	J005445–373847	00 54 45.39	−37 38 47.1		0.11 ± 0.03	-0.3 ± 0.1	
	J005450–374030	00 54 50.28	−37 40 30.0		0.32 ± 0.12	-0.5 ± 0.2	
	J005450–373822	00 54 50.30	−37 38 22.4		0.22 ± 0.14	-0.2 ± 0.2	
	J005450–374022	00 54 50.73	−37 40 22.2		0.38 ± 0.31	-0.3 ± 0.1	130
	J005451–373826	00 54 51.16	−37 38 26.1		0.26 ± 0.16	-1.2 ± 0.7	
	J005451–373939	00 54 51.79	−37 39 39.6		0.10 ± 0.18	-0.1 ± 0.2	
	J005500–374037	00 55 00.58	−37 40 37.4		0.25 ± 0.09	-0.4 ± 0.4	
	J005501–373829	00 55 01.49	−37 38 29.9		0.35 ± 0.12	-0.9 ± 0.1	31
	J005503–374246	00 55 03.50	−37 42 46.0		0.14 ± 0.04	-0.4 ± 0.1	
	J005503–374320	00 55 03.66	−37 43 20.1		0.15 ± 0.08	-0.7 ± 0.3	
	J005512–374140	00 55 12.70	−37 41 40.3		0.08 ± 0.02	-0.7 ± 0.1	
N300-S3		00 54 28.86	−37 41 53.32	0.40	0.24 ± 0.31		26
N300-S10	J005440–374049	00 54 40.87	−37 40 48.73	0.67	0.35 ± 0.15	-0.5 ± 0.3	63
N300-S11		00 54 42.54	−37 43 14.16	0.66	0.30 ± 0.12		150
N300-S18		00 55 01.39	−37 39 18.17	0.53	0.32 ± 0.32		69
N300-S21		00 55 07.15	−37 39 15.17	0.59	0.37 ± 0.30		41
N300-S23		00 55 09.10	−37 39 32.61	0.64	0.31 ± 0.08		43
No Signal (MWF11)							
	J005423–373648	00 54 23.84	−37 36 48.4			-0.7 ± 0.1	
	J005521–374609	00 55 21.35	−37 46 09.6			-1.0 ± 0.3	
	J005523–374632	00 55 23.95	−37 46 32.4			-0.9 ± 0.1	
	J005525–373653	00 55 25.82	−37 36 53.8			-1.0 ± 0.1	
	J005528–374903	00 55 28.25	−37 49 03.3			-0.6 ± 0.3	
	J005541–374033	00 55 41.94	−37 40 33.5			–	

[a] For some objects only one spectrum was obtained so the error could not be determined.

[b] The spectral index was not determined for some radio sources (PF04).

7.2 NGC 300 Supernova Remnants in the HST Archival Data

A request for all archival data from the Hubble Space Telescope which contained any data related to NGC 300 was submitted through the Space Telescope Science Institute (STScI) Multimission Archive at the STScI (MAST) website[1]. The request was fulfilled on three DVD disks containing about 11 GB of data held in 553 text and flexible image transport system (FITS) files. Of these, 96 FITS files contained telescope images. Of these 96 files, 56 contained images with usable information for this project. These 56 images were made with various Hubble Space Telescope camera filters and each FITS file header specified the image's filter's centre wavelength and bandwidth.

The "HST Key Descriptions"[2] document was very helpful in determining the contents of the files. Files with the `_drz` extension are "geometrically corrected, dither-combined image" files. Files with the `_flt` extension are "individual exposure (not produced if `CR_split`)." All 56 files containing a usable image had one of these two extensions.

Table C.1 (page 215) shows the file names associated with the central wavelengths sorted by wavelength along with the original proposal identification and any publications based on the data. Table C.2 shows the bandwidths for each of the Hubble Space Telescope filters used for these images. These data were taken from the images' FITS file header[3]. These atoms/ions are known to be within (Galactic) supernova remnants (Fesen & Hurford, 1996).

Based on Tables C.1 and C.2, Table 7.2 lists the files with filter central wavelength and bandpass containing atomic or ionic spectral lines which are diagnostic to the identification of supernova remnants (see Section 3.5.4). Column 1 is the filter central wavelength and column 2 is the filter bandwidth. Column 3 are the atoms/ions with emission lines within the filter bandwidth. The atoms/ions of most interest are: Hα, [S II], [O I] λ 6300 Å, and [O III] λ 5007 Å. Only the files containing these wavelengths were searched for candidates from Table 5.7.

A computer program was written to read the Hubble Space Telescope FITS file headers and to look for candidates from Table 5.7 within the image, based on each file's FITS world coordinate system (WCS). The results of the search are found in Table C.3. Here is a simplified list of the objects from Table 5.7 that were found in one or

[1] `http://archive.stsci.edu/`

[2] `http://archive.stsci.edu/hst/manifestkeywords.html`

[3] They are also available on the Hubble Space Telescope's Wide-Field Planetary Camera 2 (WFPC2) instrument website. `http://www.stsci.edu/hst/wfpc2/documents/IHB_17.html`

Table 7.2: HST filters containing atom/ion species important for supernova remnant identification.

1	**2**	**3**
Wavelength (Å)	**RMS Bandwidth (Å)**	**SNR Diagnostic Atoms/Ions with Wavelengths (Å)**
5741	1836	H I: 4861.36 (Hβ), 6562.85 (Hα)
		[N II]: 5754.59, 6548.05, 6583.45
		[O I]: 5577.34, 6300.30, 6363.78
		[O III]: 4958.91, 5006.84
6001	638	[O I]: 6300.30
6564	54	H I: 6562.85 (Hα)
		[N II]: 6548.05, 6583.45

more of the images files: J005438–374144, J005440–374049, J005445–373847, J005450–374030, J005450–373822, J005450–374022, J005451–373826, J005451–373939, J005500–374037, J005501–373829, J005503–374246, J005503–374320, N300-S8, N300-S9, N300-S10, N300-S13, N300-S14, N300-S15, N300-S16, N300-S18. As can be seen from Table C.1, only one image file group contains data with Hα (`u671370#r_drz`, where `#` is one of the digits, 5 to 9). There were no files containing the [S II] doublet wavelengths. The images centred on $\lambda = 5741$ Å and $\lambda = 6001$ Å contain wavelengths of interest but none of these images contain objects from Table 5.7. Thus, only the Hα images were of use for this study.

Only 5 of the 51 objects were found within the Hα images. All of the Hα images have the same field of view. The final results of the search are shown in Table 7.3. Column 1 is the optical supernova remnant candidate from BL97 and column 2 is the radio source supernova remnant candidate from PF04. Columns 3 and 4 are the (J2000.0) α and δ of the object respectively. Column 5 is the spectral index of the radio source as published in PF04. Column 6 is the [S II]:Hα with measurement error and column 7 is the measured nebular diameter, both from Table 6.2.

Table 7.3: Five candidates found in the Hα Hubble Space Telescope image `u6713709r_drz.fits`. The positions are the J2000.0 coordinates reported by PF04 (radio sources) and BL97 (optical candidates).

1	**2**	**3**	**4**	**5**	**6**	**7**
Optical	**Radio**	α **(J2000.0)**	δ **(J2000.0)**	**Spectral**		**Diameter**
Candidate	**Candidate**	**(h m s)**	$(^\circ\ '\ '')$	**Index**[a]	[S II]:Hα[b]	**(pc)**[b]
	J005450–374030	00 54 50.279	−37 40 30.01	-0.5 ± 0.2	0.32 ± 0.12	
	J005450–374022	00 54 50.730	−37 40 22.25	-0.3 ± 0.1	0.38 ± 0.31	130
	J005451–373939	00 54 51.790	−37 39 39.55	-0.1 ± 0.2	0.10 ± 0.18	
	J005500–374037	00 55 00.579	−37 40 37.44	-0.4 ± 0.4	0.25 ± 0.09	
N300-S16		00 54 54.462	−37 40 35.46		0.94 ± 0.06	57

[a]From PF04.

[b]From Table 6.2.

The Hubble Space Telescope Hα images are centred on ($\alpha = 00^{\mathrm{H}}54^{\mathrm{M}}54\overset{\mathrm{S}}{.}54$, $\delta = -37^{\circ}\ 40'\ 35\overset{''}{.}9$). They are 400 second exposures taken in May of 2001 with the Wide-Field Planetary Camera 2 (WFPC2) instrument using its (default) PC1 aperture. The filter used in these images (F656N) was centred on $\lambda = 6563.76$ Å with a RMS bandwidth of $\Delta\lambda = 53.77$ Å. The bandpass characteristics of this filter are shown in Figure 7.1. The data were originally collected as part of the Hubble Space Telescope proposal 8591 by, Douglas Richstone (Richstone, 2000, the proposal abstract is reprinted in the appendix, page 245). The file `u6713709r_drz.fits` appeared to provide the cleanest image for analysis of the supernova remnant candidates' environment.

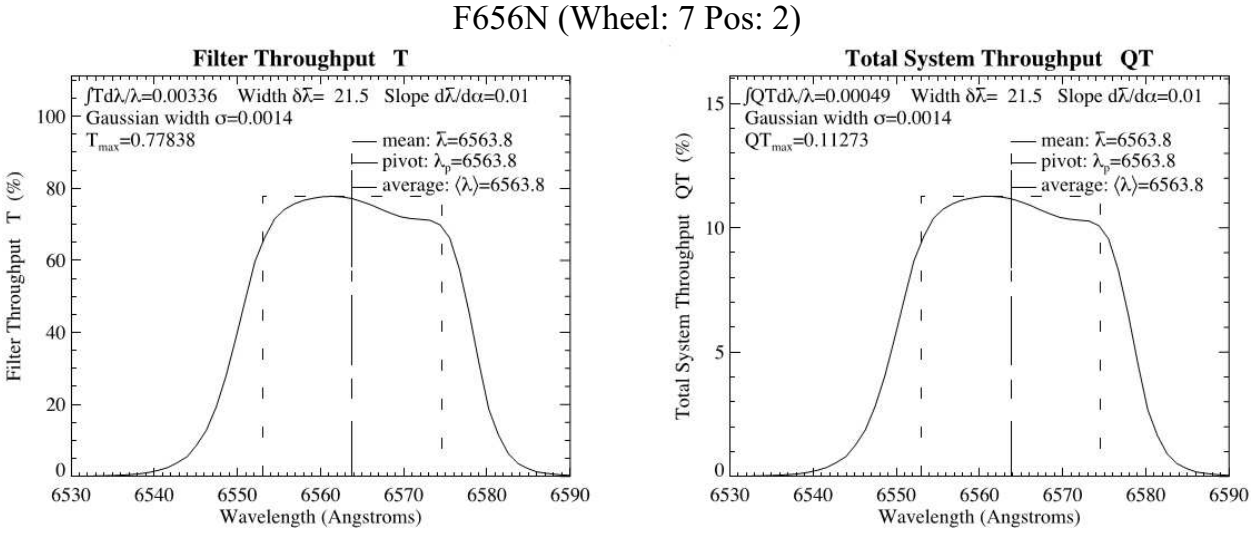

Figure 7.1: The pass band characteristics of the N565 filter used on the WFPC2 of the Hubble Space Telescope. (STScI Institute, WFPC2 Observer's Handbook.)

Figure 7.2 shows the image contained in this file as a negative grey-scale. The five supernova remnant candidates (Table 7.3) in the field of view are labelled. For comparison, Figure 7.3 shows an image with the same position, size and rotation using DSS2-Red data from SkyView[4]. There is a slight difference in plate scale between the two images. Figure 7.3 was modified to appear with the same shape as the Hubble Space Telescope's CCD array, which contains a high-resolution CCD chip in the first quadrant. The centre of NGC 300 is within the high-resolution chip. There are some differences in the apparent distribution of gas in the DSS2-Red image compared to the Hubble Space Telescope image, probably due to the wider pass band of the DSS2-Red image. There is a triangular shaped optical artifact located to the north of the very bright star near the bottom of the DSS2-Red image. The four radio supernova remnant candidates from PF04 were not optically confirmed, the optical supernova remnant candidate from BL97 was confirmed (MWF11).

[4]http://skyview.gsfc.nasa.gov/

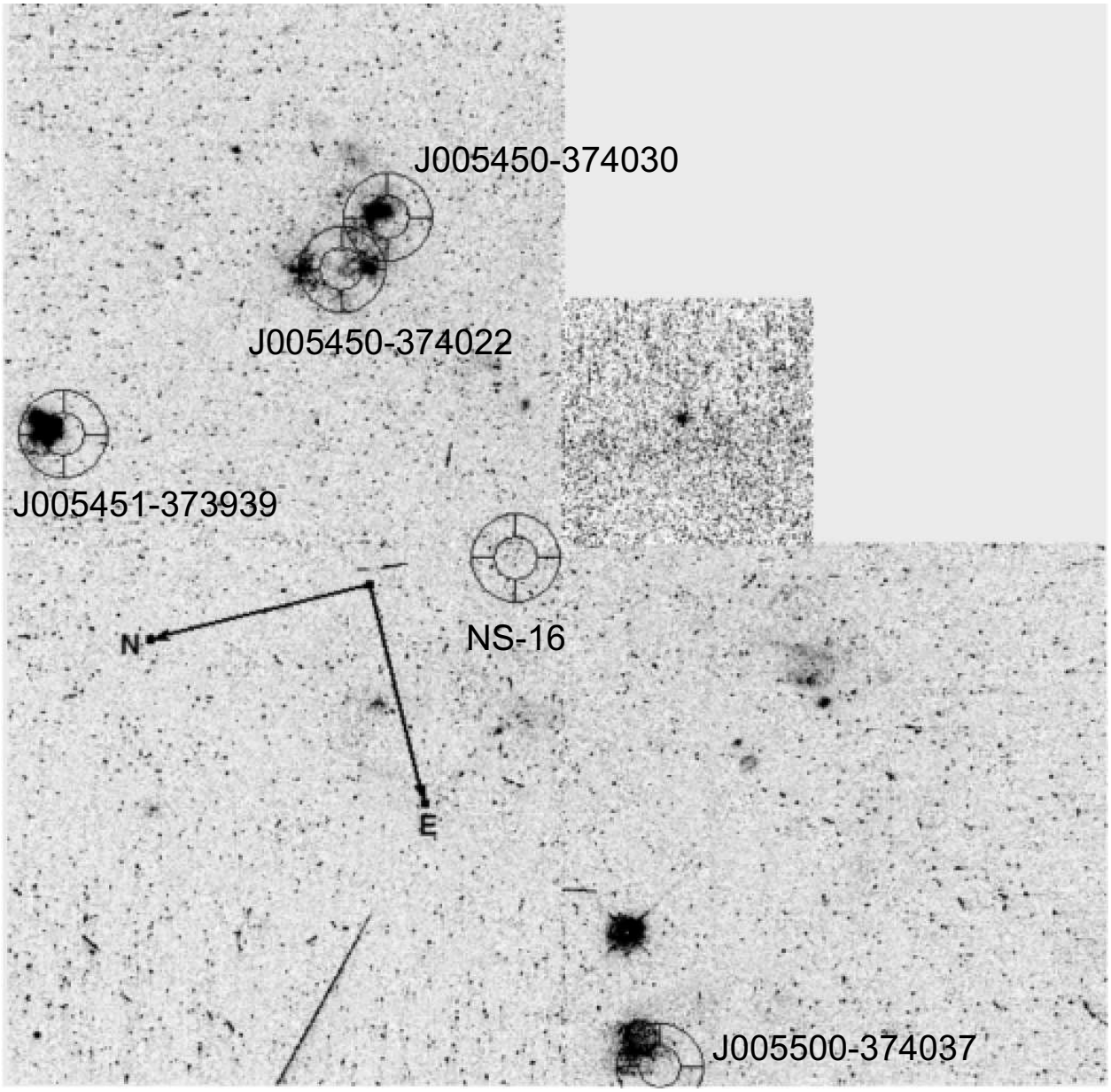

Figure 7.2: This image is contained in the file `u6713709r_drz.fits` and is here modified using the SAO's DS9 software. The image is a 400 second exposure centred on $\alpha = 00^{\rm H}54^{\rm M}54\overset{\rm S}{.}54$, $\delta = -37^\circ\ 40'\ 35\overset{''}{.}9$ and rotated $\simeq$104° east of north. The high-resolution CCD (first quadrant) is centred on the nucleus of NGC 300. The five supernova remnant candidates in this image are described in Table 7.3. The pandas are centred on each candidate with an inner circle diameter of $6''$ (61.2 pc). (Courtesy of STScI MAST.)

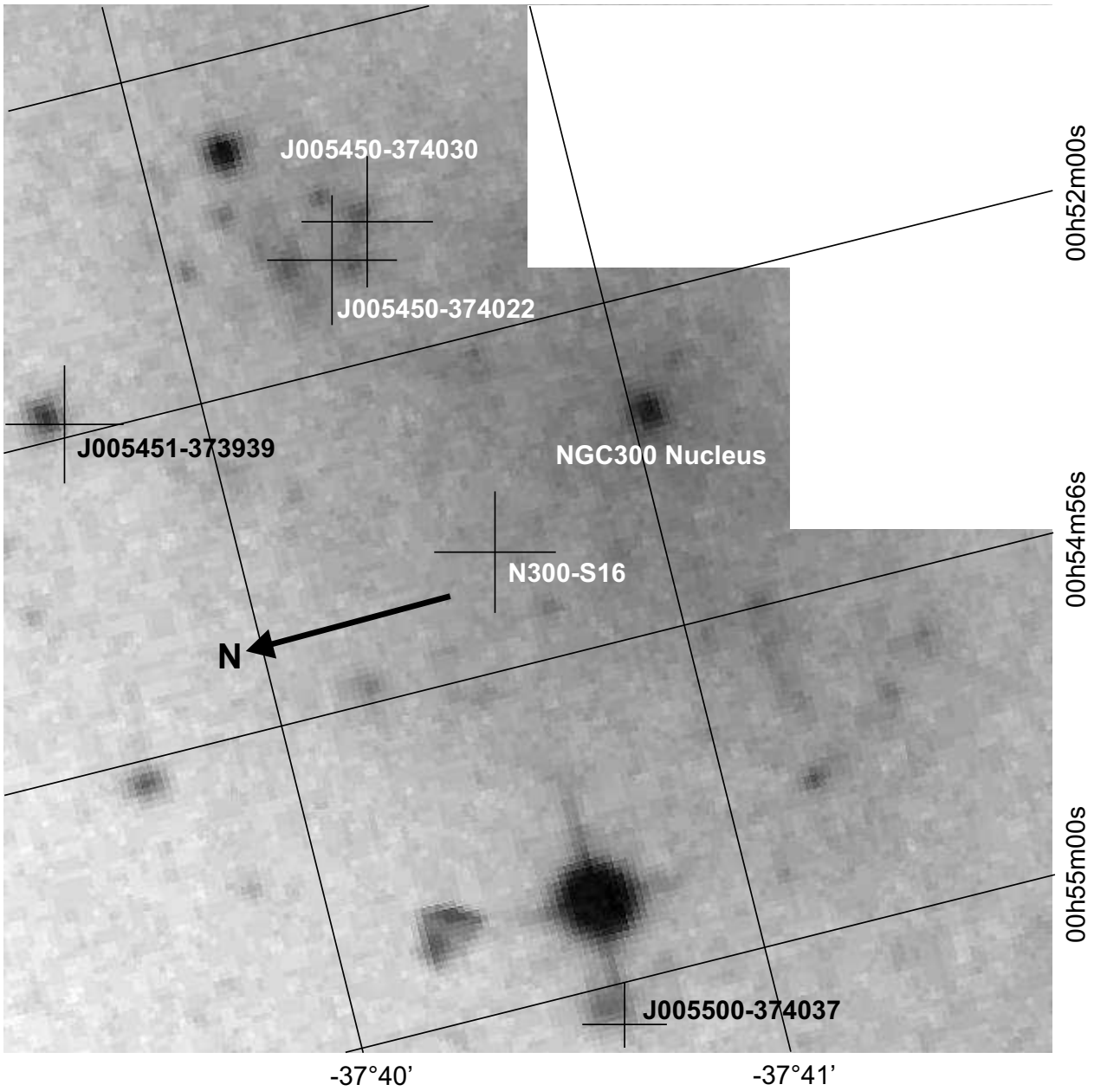

Figure 7.3: This is the approximate equivalent to the Hubble Space Telescope image of Figure 7.2 created with SkyView using DSS2-Red data. Black or white labelling is simply for best contrast. (Southern sky DSS image, Royal Observatory Edinburgh, Anglo-Australian Observatory, California Institute of Technology.)

7.3 Analysis of the Radio Sources

When the Hubble Space Telescope image was displayed in false colour[5] to show emission intensity (Figures 7.4 through 7.7) a number of small sized, high-intensity objects appeared in the image. Most likely these are stars but that is difficult to determine from the available data. Here after these objects are referred to simply as "hot spots."

The four radio sources are found next to hydrogen cloud structures visible in the Hα images from the Hubble Space Telescope. Based on the general condition that radio supernova remnants with no detectable optical emission are found in such locations, these four radio sources can be labelled as (imaged) Hubble Space Telescope supernova remnants.

7.3.1 Radio Observations Astrometry

The majority of the supernova remnants found in the Galaxy and the Magellanic clouds are 50 pc or less in diameter (Strom, 1996). If the same is assumed for NGC 300, then the supernova remnants in NGC 300 should be less than 5″ in diameter at the assumed distance (page 70). The radio observations published in PF04 used a circular beam width of 6″. Thus the typical supernova remnant would not fill the beam of the radio telescope increasing random error that may have added in the same direction to any systematic error already present in the telescope's pointing. In Figures 7.2 through 7.7 the images (particularly the Hubble Space Telescope Hα images) appear to show that there is such a systematic error in the astrometry of the radio candidates. The candidates show a consistent displacement to the southwest from the neighbouring H II region.

Multi-wavelength observations of extragalactic supernova remnants are limited by current technologies to radio, optical and X-ray emissions. Supernova remnants expanding in a denser medium tend to be brighter in radio and X-ray than those expanding in a lower density medium and optically detected supernova remnants are generally found in optically thin, lower density media (Duric, 2000a). This also explains why most optically identified supernova remnants are not detected in X-ray. Therefore, to account for radio emissions typical of a supernova remnant without corresponding optical emissions (particularly when the candidate is ∼50 pc in diameter) the radio source should be located within or adjacent to the hydrogen cloud region so the candidate supernova remnant's optical emissions could be masked while the radio emission is strong. Thus, the proximity of the supernova remnant to an H II region is the most likely explanation for such candidate supernova remnant

[5] Using the Smithsonian Astrophysical Observatory's DS9 software package `http://hea-www.harvard.edu/RD/ds9/`.

radio/optical observations as seen in this research (PD00; PF04; Duric, 2000a,b).

None of the four radio sources in this image (all of which are close to H II regions) are known to have emissions in other wavelengths. No ground-based telescope should be able to separate these candidates from their respective H II region – this would require a space-based telescope or adaptive optics. Radio observations with a higher resolving power and very high-resolution optical observations (Hubble Space Telescope) are needed to resolve this possible astrometric error. N300-S16 (which is away from any visible H II region) is observed only in the optical.

7.3.2 Supernova Remnant Candidate J005450–374030

This radio supernova remnant candidate has a spectral index of -0.5 ± 0.2. It has a [S II]:Hα of 0.32 ± 0.12 (MWF11, Table 7.1). Because the threshold value of the [S II]:Hα is 0.4 this candidate could not be classified as an optical supernova remnant (MWF11). Note however that the threshold value is within the error of the line ratio measurement. Figure 7.4 shows the detail in the Hubble Space Telescope image at the location of this radio source. The candidate is located very near the edge of an H II region (H II C29, Soffner et al., 1996, $8\farcs33$, 85 pc away from centre) showing no special structural properties.

A single image in Hα does not allow us to determine the nature of the emissions from the region. An Hubble Space Telescope [S II] image would be very helpful. If there is a systematic error in the astrometry of the radio source (see Section 7.3.1), it is possible that the radio source is actually inside the H II region and the H II region would then interfere with the optical line ratio measurement, as discussed above.

7.3.3 Supernova Remnant Candidate J005450–374022

Figure 7.5 shows detail in the Hubble Space Telescope Hα emissions surrounding the radio source J005450–374022 which was classified as being either a supernova remnant or an H II region in PF04. The radio source is located on the edge of a large bubble in the H II region (76C, Deharveng et al., 1988, $2\farcs36$, 24 pc away from centre). The small magenta ($1''$) circle pointed out by the red arrow shows the position of the candidate. The larger magenta ellipse (at the edge of which the radio candidate is located) outlines one possible border to the large bubble. A smaller region within the ellipse which can be seen at the green emission level may also be a supernova remnant shock front within this H II region. Without proper [S II] data these remain simply possibilities of shock fronts.

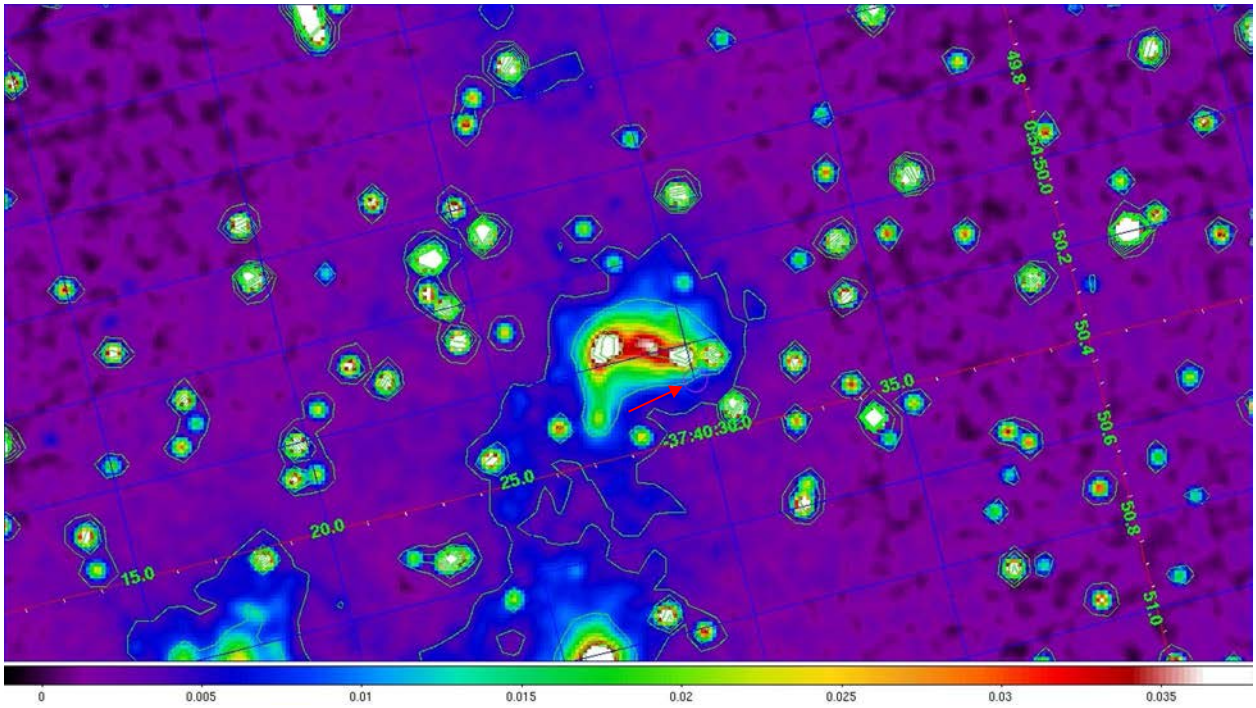

Figure 7.4: The region surrounding the PF04 candidate J005450–374030. The candidate location is shown by the magenta circle (red arrow pointing to it) just to the lower right of centre of the intense H II emission. The circle is 1″ (10.2 pc) in diameter – about twice the 1σ positional error (see Section 7.6.2). This false colour image and contour plot was created with DS9 (See Appendix E for details). (Courtesy of STScI MAST.)

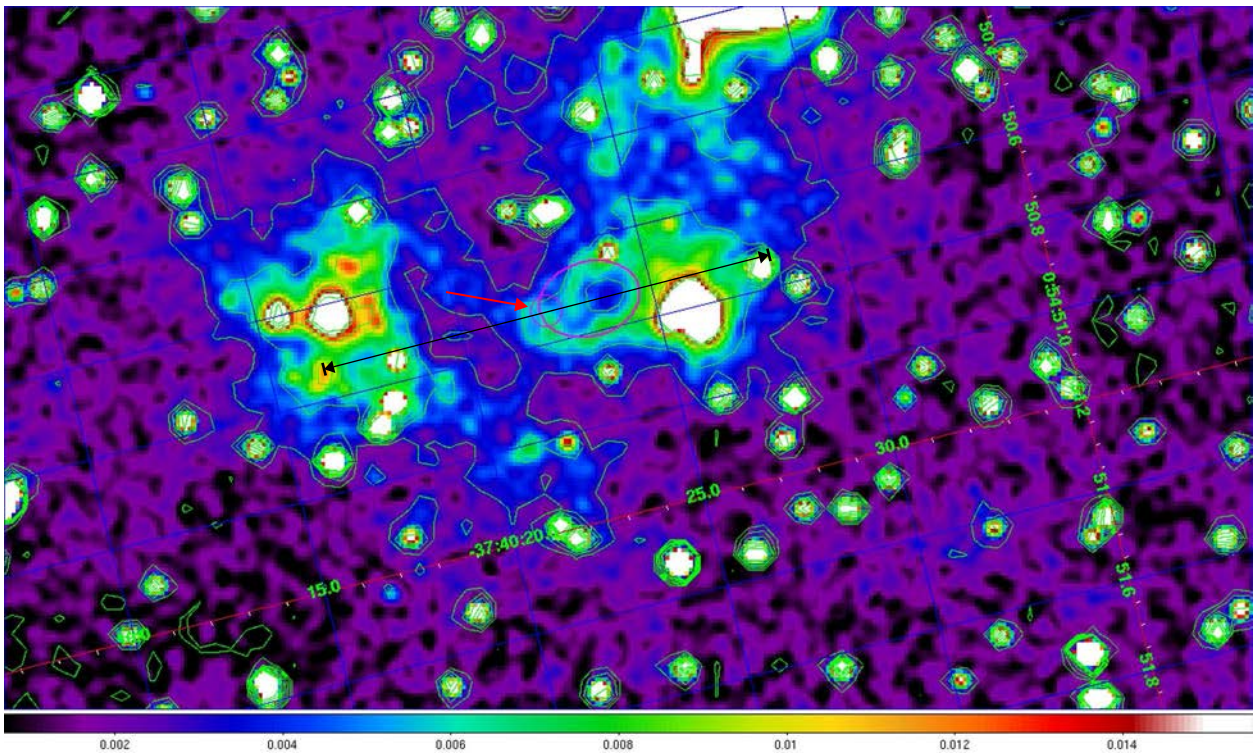

Figure 7.5: The region surrounding the PF04 candidate J005450–374022. The radio source location is shown by the magenta circle (red arrow pointing to it). The circle is 1″ in diameter ($\simeq 2\sigma$ positional error, see Section 7.6.2). This false colour image and contour plot was created with DS9 (See Appendix E for details). (Courtesy of STScI MAST.)

The magenta ellipse is $2\farcs54 \times 2\farcs38$ or 25.9×24.8 pc with its semi-major axis aligned in δ. This is approximately the size of a supernova remnant of about 10 000 to 20 000 years in age (Section 3.1, Cioffi, 1990). Supernova remnants of this age are typically (depending on interstellar matter density) in the radiative, pressure-driven snowplow stage which likely presents a bubble shaped appearance such as the one seen in this image. The [S II]:Hα for this candidate is 0.38 ± 0.31 (MWF11, Table 7.1). While the ratio is just below the critical value of 0.40, the large noise error in this measurement combined with the apparent structure next to the radio candidate raises serious concern about denying its classification as an optical supernova remnant.

Also shown in Figure 7.5 is a black line corresponding to the diameter measurement of this candidate (130 pc) as published in MWF11 (Table 7.1). This allows comparison of the poorer seeing conditions during those observations with the resolution of the Hubble Space Telescope image. This 130 pc ($\simeq 12\farcs7$) line is drawn centred on the published position of the radio source. Given this diameter comparison, the seeing conditions of the above [S II]:Hα measurement is clearly including the H II region. Given the confusion of sources, no firm conclusion about the optical emissions of this radio source can be drawn from these data.

7.3.4 Supernova Remnant Candidate J005451–373939

Figure 7.6 shows the location of J005451–373939, next to an H II region (#20, Bresolin et al., 2009, $3\farcs80$, 39 pc away from centre). This H II region has a bright emission source off to one side at the same location as the radio source. It is not likely this "hot spot" could be the supernova remnant but it could be the known Wolf-Reyet star from Schild et al. (#18, 2003a). There is also a known star association in this region (AS 57, Pietrzyński et al., 2001b). Emissions from these stars (the association or the Wolf-Rayet) cannot be separated from the supernova remnant candidate in the spectrographic slit and the Wolf-Rayet star may also contribute to the radio emissions (note the discussion of excessive radio emissions and the spectral index of Galactic Wolf-Rayet stars in Montes et al., 2009).

This radio source could be a supernova remnant within the H II region or it could be a coincidence with a combination of stars. Observations with the Hubble Space Telescope's WFPC2 instrument using the F673N filter to indicate the presence of any [S II] emission could be very helpful here. The spectroscopic measurements from MWF11 do not support this object as a supernova remnant.

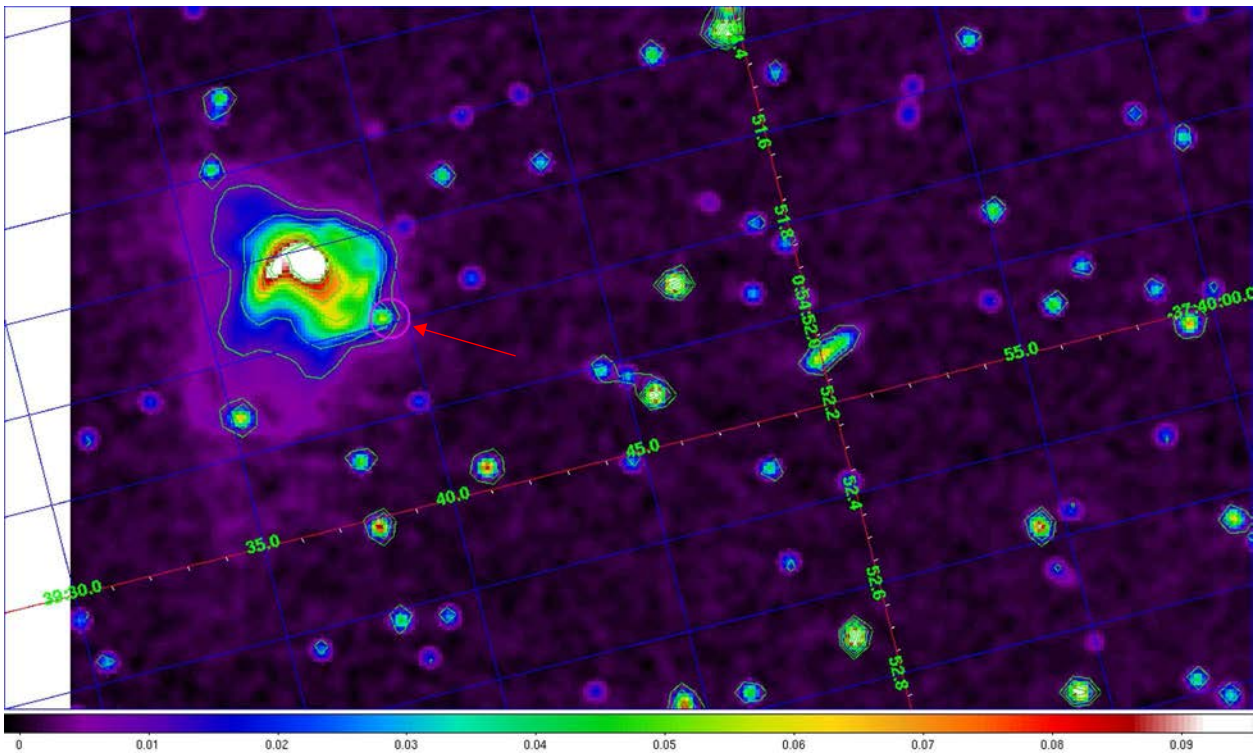

Figure 7.6: The region surrounding the PF04 candidate J005451–373939. The radio source location is shown by the magenta circle (red arrow pointing to it) 1^{s} (10.2 pc) in diameter ($\simeq 2\sigma$ positional error, see Section 7.6.2). This false colour image and contour plot was created with DS9 (See Appendix E for details). (Courtesy of STScI MAST.)

7.3.5 Supernova Remnant Candidate J005500–374037

Figure 7.7 shows the location of the supernova remnant candidate J005500–374037. The radio source is outside of any notable Hα emission. There is a large inset into the H II region (H II E18, Soffner et al., 1996, 4.″45, 45 pc away) on the side nearest the radio source. However, if this inset were due to a supernova event the supernova remnant would definitely be in the pressure-driven snowplow (page 22) stage and both radio and optical emissions should be coming from the shock front, not from the centre of, or outside of the expanding shock. There are at least four known H II regions, a planetary nebula and a star association in the vicinity of this radio source but they are far enough from the source that they should be separable in the spectrometer slit – given the correct source astrometry and telescope pointing. There is a possibility that this radio source is a background object (e.g. a quasar) which happens to lie very near an H II region within NGC 300 although this source was classified as a supernova remnant as opposed to SNR/H II region in PF04. As has been mentioned previously, this could also be a supernova remnant without optical emissions.

If the apparent systemic radio astrometry error is real, it may be a supernova remnant with its optical emissions masked by the H II region emissions. Given their proximity and the typical seeing conditions of ground-based observations, the emissions from the supernova remnant and the H II region would be impossible to distinguish.

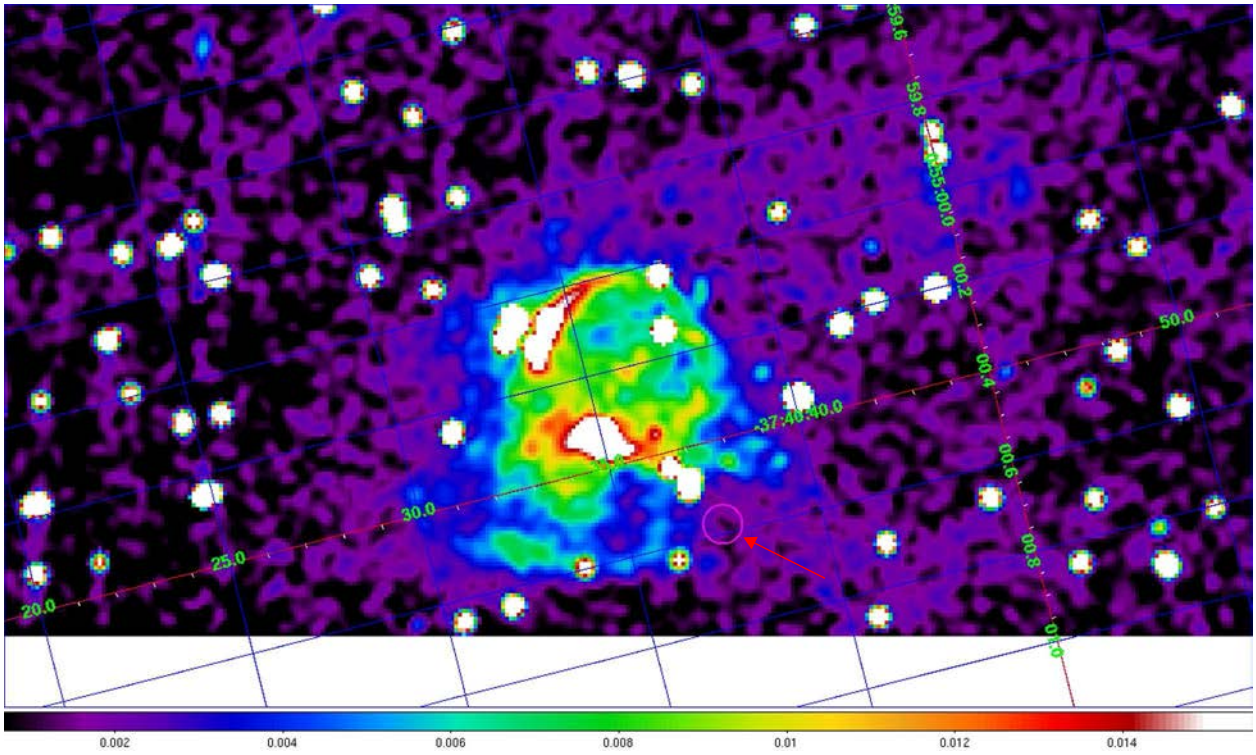

Figure 7.7: The region surrounding the PF04 candidate J005500–374037. The radio source location is shown by the magenta circle (red arrow pointing to it) 1″ in diameter ($\simeq 2\sigma$ positional error, see Section 7.6.2). This false colour image was created with DS9 (See Appendix E for details). (Courtesy of STScI MAST.)

7.4 Analysis of the Optical Candidate, N300-S16

The N300-S16 [S II]:Hα ratio was not measured from spectra in BL97 but Table 3A of that paper shows N300-S16 with a [S II]:Hα of 0.70, based on the BL97 survey CCD images. BL97 also reports a (Hα) diameter of 52 pc. From MWF11, N300-S16 has an observed [S II]:Hα of 0.94 ± 0.06 and a measured diameter of 57 pc. This large measured ratio is based on fairly low flux levels[6]: Hα = 2.2 and [S II] = $2.1(10^{-15}$ erg cm^{-2} s^{-1}). Hoopes et al. (1996) have demonstrated that a [S II]:Hα of up to 0.5 can be created by the diffuse ionised gas of NGC 300. Because this candidate is not near any known H II region this "background ratio" could be subtracted from the MWF11 ratio and the result still exceeds the 0.4 critical [S II]:Hα ratio for indication of a supernova remnant. However, the critical value is then within the small noise error.

Figure 7.8 shows the BL97 images (set G) of N300-S16 zoomed and cropped. On the left is the Hα filter image and on the right is the [S II] filter image. In both images only a faint increase from the background is seen at N300-S16's given position. The inner panda circle is centred on the N300-S16 coordinates with an apparent $8''$ (81.6 pc) diameter – somewhat larger than the measured diameter. The outer panda circle is twice as big.

Figure 7.9 zooms in to the Hubble Space Telescope Hα image at N300-S16. In this figure there is no evidence of any structure in the Hα emissions. It is possible that the [S II]:Hα test for supernova remnant character has failed. No satisfactory explanation of the apparent contradiction between the two observations has been found.

[6] The BL97 candidates' spectral flux density was consistently weaker by an order of magnitude compared to the PF04 candidates. Lower flux levels can cause larger measurement error. See MWF11.

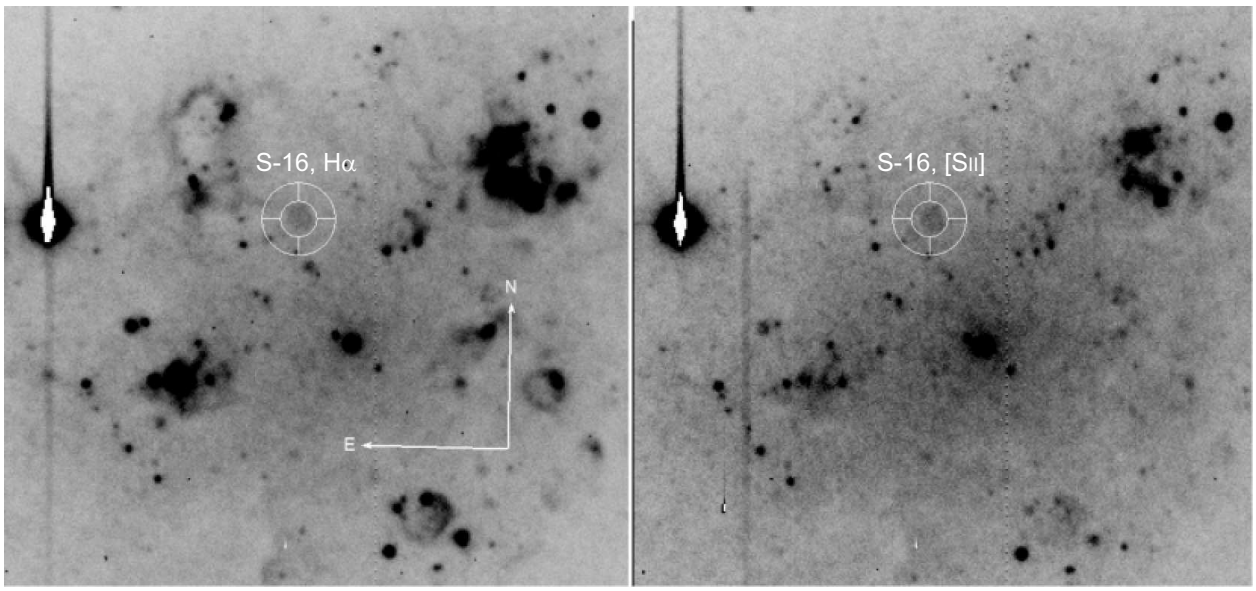

Figure 7.8: These are original CCD images from set G of the BL97 survey (see Section 7.5). On the left is the Hα filter image. On the right is the [S II] filter image. An object which could be N300-S16 is visible as a faint smudge in these images. The inner circle of the panda is $8''$ (81.6 pc) in diameter. (Image courtesy of William Blair.)

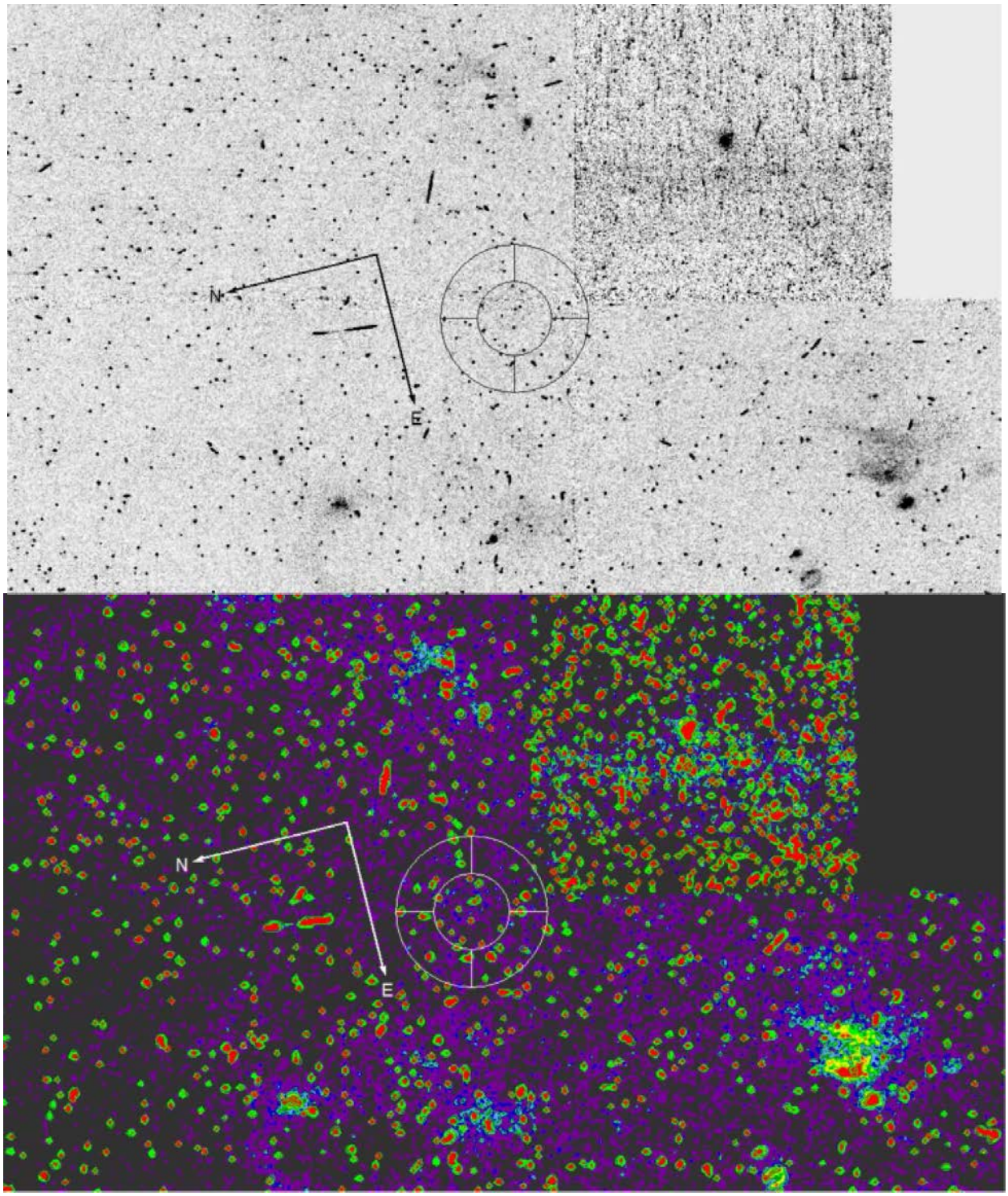

Figure 7.9: The Hubble Space Telescope Hα image of N300-S16 from shown in inverted grey-scale on top and in false colour on the bottom. In either case no discernible structure is seen in the hydrogen gas at the reported location of this candidate supernova remnant. The panda inner circle is 8″ (81.6 pc) in diameter. (Courtesy of STScI MAST.)

The N300-S16 Hα emission is just above and barely discernible from the background level. It may be possible that the Hubble Space Telescope's CCD chips may require a longer exposure time to detect the low level emission. To examine this possibility a comparison between the BL97 and Hubble Space Telescope CCDs' sensitivity was made. DS9 was used to extract tables of pixel values from locations within the BL97 G-Hα image and the Hubble Space Telescope Hα image for the comparison. Three regions were chosen: The location of N300-S16, a nearby H II region and an average looking background region not far from N300-S16. Table 7.4 lists the image locations $(x, y; \alpha, \delta)$ used for the extractions. Column 1 is the source of the pixel data, column 2 is the character of the region, column 3 is the central pixel location and column 4 is the α and δ coordinates of the selected region.

The Hubble Space Telescope Hα images were flux calibrated and thus the FITS array contained floating point values. The BL97 images were raw pixel counts, not flux calibrated, and the FITS array contained integers. The pixel table data were transferred into a spreadsheet for calculations. A linear conversion equation was derived to convert the Hubble Space Telescope pixels to equivalent pixel counts, such that the average value of the pixels from the background tables were as equal as possible.

Tables 7.5 through 7.7 show the pixel tables for the three locations with the average value of the pixels for each table. Figure 7.10 shows a surface plot for each extracted region. In these tables the pixel data are arranged in x, y as row-column. The pixel table for the Hubble Space Telescope image region from N300-S16 contained a bad pixel (the empty table entry). This table entry was removed from all pixel tables to keep the comparison as fair as possible. A total of 80 pixels were used from each region. Table 7.8 shows the comparison of the regional pixel tables' average value. In this table column 2 is the ratio of the array average for the H II region with the average of the background region array for each image. For the BL97 image, the H II region average was 5.113 times higher than the background region average. The same ratio for the Hubble Space Telescope image was 5.796 which is 12.5%[7] higher than the BL97 image. The Hubble Space Telescope image is a 400 second exposure. The BL97 image is a 1500 second exposure. The Hubble Space Telescope camera therefore appears to be more sensitive. This was not surprising but the comparison should be made for completeness of the discussion.

[7] Percent difference calculated as the difference in the values divided by the average of the values.

Table 7.4: Three pixel regions selected from the BL97 and Hubble Space Telescope Hα images for CCD sensitivity comparison.

1	**2**	**3**	**4**
		(x, y)	α, δ
Image	**Region**	**(pixels)**	**(h m s $^\circ$ $'$ $''$)**
HST	Background	(649, 780)	00 54 53.928, −37 40 31.60
BL97	Background	(207, 452)	00 54 53.931, −37 40 31.60
HST	H II	(512, 1204)	00 54 50.182, −37 40 28.75
BL97	H II	(318, 456)	00 54 50.188, −37 40 28.91
HST	N300-S16	(702, 728)	00 54 54.462, −37 40 35.46
BL97	N300-S16	(191, 443)	00 54 54.462, −37 40 35.46

Table 7.5: Background pixel (value) arrays extracted from the BL97 and Hubble Space Telescope Hα images. A surface plot of these pixel values is shown in Figure 7.10a (BL97) and b (Hubble Space Telescope).

BL97 (Figure 7.10a)								
379	410	394	422	407	451	399	406	390
441	451	430	438	419	423	435	425	410
397	419	413	416	432	453	416	429	456
422	436	395	418	415	449	439	410	404
452	426	443	442	447	435	408	432	447
435	418	408	422	407	433	432	445	440
437	448	430	435	430	456	419	410	435
405	459	443	465		398	444	415	454
441	444	442	459	442	465	430	475	438
Average = 429.25								
HST (Figure 7.10b)								
476	525	406	437	584	247	262	292	230
365	446	503	464	479	413	508	525	283
530	366	389	340	579	475	647	429	389
381	186	508	547	523	471	515	535	444
545	248	609	403	451	465	339	395	472
518	431	498	414	219	453	275	532	483
616	481	208	315	243	328	423	530	355
245	454	379	422		405	468	474	562
396	762	630	332	300	460	168	468	468
Average = 429.26								

Table 7.6: H II pixel (value) arrays extracted from the BL97 and Hubble Space Telescope Hα images. A surface plot of these pixel values is shown in Figure 7.10c (BL97) and d (Hubble Space Telescope).

BL97 (Figure 7.10c)								
2113	2357	2512	2403	1982	1533	1186	973	921
2395	2812	3294	3150	2520	1848	1356	1029	928
2602	3266	3801	3754	2875	2078	1422	1139	910
2635	3466	3977	3883	3123	2207	1526	1170	971
2788	3546	3975	3668	2932	2128	1475	1154	983
2916	3647	3894	3350	2605	2009	1482	1142	942
2824	3563	3565	2894	2332	1787	1407	1154	943
2550	3005	2878	2419		1523	1333	1094	911
2062	2346	2243	1985	1620	1340	1135	1030	892
Average = 2195								
HST (Figure 7.10d)								
2252	1984	1766	1935	2293	2627	2521	2256	2218
2742	2541	2000	2223	2706	2888	2862	2641	2704
2472	2384	2021	2580	3134	2979	2714	2895	3153
2404	2491	2750	2860	3038	2917	2739	2790	2864
2854	2635	2584	2685	2594	2540	2567	2958	3156
3224	2904	2735	2789	2893	2693	2489	2802	3230
2418	2338	2498	2641	2467	2109	2275	2439	2808
1935	2082	2129	1990		1985	2262	2191	2417
1861	1667	1734	1786	1928	2147	2215	2048	1983
Average = 2488								

Table 7.7: N300-S16 pixel (value) arrays extracted from the BL97 and Hubble Space Telescope Hα images. A surface plot of these pixel values is shown in Figure 7.10e (BL97) and f (Hubble Space Telescope).

BL97 (Figure 7.10e)								
514	555	515	503	499	519	508	526	518
509	498	498	510	525	547	478	493	510
511	515	528	492	554	523	520	511	509
503	500	521	498	519	512	490	511	496
488	462	506	500	511	527	496	500	475
498	500	503	530	535	523	505	510	512
505	527	478	503	519	486	539	522	517
455	501	463	483		541	522	526	486
448	477	496	548	513	527	480	530	505
Average = 508								
HST (Figure 7.10f)								
307	458	447	655	840	765	530	450	492
686	471	424	295	665	241	417	436	432
302	483	588	425	299	411	338	465	464
444	483	488	586	424	374	651	563	445
444	647	578	615	501	587	561	261	316
383	609	371	768	665	281	484	383	149
638	604	575	613	418	495	608	501	587
580	496	306	562		470	440	441	540
418	614	441	458	530	435	457	323	378
Average = 485								

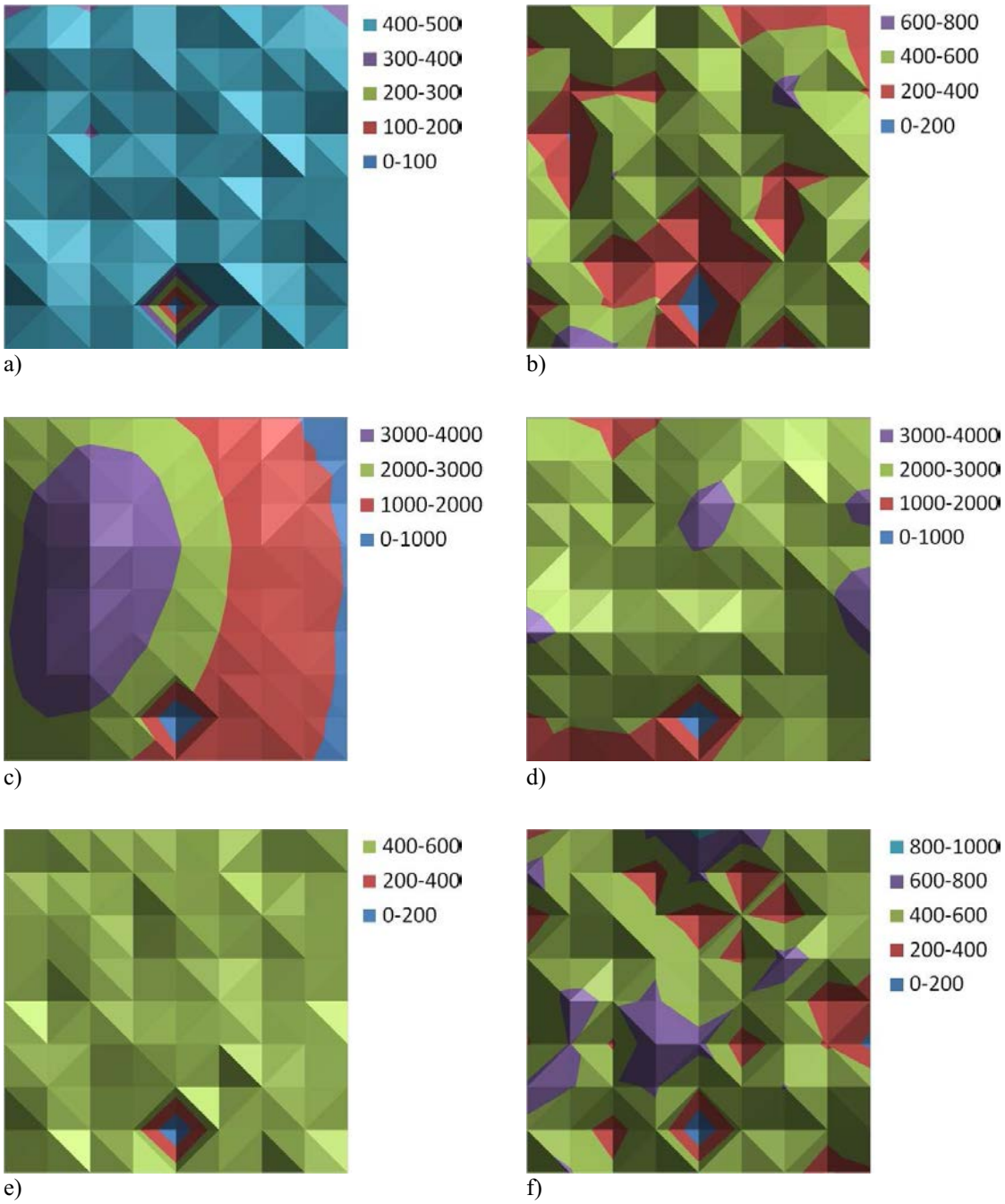

Figure 7.10: A surface plot of the pixel values from tables 7.5, 7.6 and 7.7. Plot a) is from the top half (BL97) of Table 7.5. Plot b) is from the bottom half (Hubble Space Telescope) of Table 7.5. Plot c) is from the top half (BL97) of Table 7.6. Plot d) is from the bottom half (Hubble Space Telescope) of Table 7.6. Plot e) is from the top half (BL97) of Table 7.7. Plot f) is from the bottom half (Hubble Space Telescope) of Table 7.7.

The same comparison for the N300-S16 region pixel array shows the Hubble Space Telescope average is 4.6% lower than the BL97 average. If N300-S16 is a valid supernova remnant its region's pixel average percent difference should be nearly the same as the H II region's. The difference in these percent differences is significant: 17.1%. The FWHM bandwidth of the BL97 Hα filter was 52 Å and the Hubble Space Telescope Hα filter bandwidth was 54 Å (difference of 3.8%). The filter characteristics are probably not a significant concern for the possible cause of this difference. Both filters allow the passage of [N II] flux. It may be possible that this extra flux could be a problem if the two regions have significantly different [N II] flux levels. There was no way to test this possibility with the given data.

Table 7.8: Results of BL97:HST CCD sensitivity comparison.

1	**2**	**3**
	H II	**N300-S16**
BL97	5.113	1.183
HST	5.796	1.129
% Diff	12.5	-4.6

7.5 The Astrometry of BL97

There is contradictory evidence for the existence of a supernova remnant at the location labelled as N300-S16. BL97 and MWF11 have high [S II]:Hα values but the Hubble Space Telescope Hα image shows no indication of any structure in the vicinity. In an attempt to find a resolution the astrometry of the BL97 CCD images was checked. The CCD images used for the BL97 optical survey were provided by William Blair. These images were sets and each set was labelled with the letters 'C' through 'J.' Each lettered image set contained a continuum image, an Hα filter image and an [S II] filter image with the same centre, plate scale and rotation (see BL97). The files did not include the 'I' image (which was used in BL97) but did include a 'K' image which was not used in BL97. The 'I' image contained supernova remnant candidates N300-S12 and N300-S17. The 'C' and 'K' images contained no supernova remnant candidates and thus were not considered in this analysis.

The images are in the flexible image transport system (FITS) format, 800 pixels on a side, with a field of view of approximately $0\overset{\circ}{.}087$. The central coordinate (J2000.0 α and δ) are given in Table 2 of BL97 and included for comparison in Table 7.11. The image files did not have a FITS WCS and the x-axis needed to be inverted to obtain the correct orientation (north up and east to the left). A WCS was created for each of the FITS files (see below).

BL97 used known H II regions for the astrometry in determining the location of the supernova remnant candidates. A mosaic of the Hα images identifying the supernova remnant candidates is shown in Figure 1a of BL97. Figure 1b of that paper shows the same image mosaic with the identified H II regions. H II regions are not point sources and are thus prone to astrometric error. The first step was to create a process to build a WCS for each image and insert the relevant data into each image's FITS file header. This then allowed the study of the position (astrometry) and environment of the supernova remnant candidates (as was done in the previous sections) in a FITS file viewer such as DS9. For this astrometry analysis, point sources were chosen from a searchable, online, Two-Micron All Sky Survey (2MASS) J-Band (1.25 μm) catalogue[8]. The 2MASS point source catalogue has a position error of less than $0\overset{''}{.}2$ (Skrutskie et al., 2006).

This is the general outline for building the WCS: The x, y pixel coordinates and the estimated (α, δ) coordinates of three 2MASS J-Band point sources found within each image's field of view were determined by inspection and entered into a text file. A computer program was created which read this text file and a text file containing a list of 2MASS point source coordinates around NGC 300. The estimated 2MASS source coordinates

[8] http://www.cfa.harvard.edu/catalogue/search

were then matched to catalogue source coordinates. Then the program determined the CCD image centre and WCS coordinate differentials (plate scale and rotation) using the equations shown in the next section. The resulting values were linked to the appropriate FITS header keywords and added to each image's FITS header.

7.5.1 The Astrometry Equations

Figure 7.11 shows the concept behind the astrometry equations used to build the WCS. The WCS requires a reference pixel with known (α, δ) which is usually the central pixel[9] of the array and the rate of change of α and δ with respect to the x and y CCD pixel axes – six quantities. The reference pixel is designated here by (x_c, y_c) $\rightarrow$ (α_c, δ_c). The following notation is used for the coordinate values with respect to the pixel axes:

$$\partial_{\alpha x} \equiv \frac{\partial \alpha}{\partial x}, \quad \partial_{\alpha y} \equiv \frac{\partial \alpha}{\partial y}, \quad \partial_{\delta x} \equiv \frac{\partial \delta}{\partial x}, \quad \partial_{\delta y} \equiv \frac{\partial \delta}{\partial y}, \tag{7.1}$$

which are considered constant. These four quantities describe both plate scale (degrees per pixel) and plate rotation (degrees from north). There are six unknown quantities:

$$\alpha_c, \delta_c, \partial_{\alpha x}, \partial_{\alpha y}, \partial_{\delta x}, \partial_{\delta y}. \tag{7.2}$$

Because the image pixel array is 800×800 we have the two known quantities,

$$(x_c, y_c) = (400.5, 400.5). \tag{7.3}$$

The other known quantities are the CCD pixel coordinates and the 2MASS catalogue J2000.0 equatorial coordinates of three chosen point sources within the image. So the known quantities are:

$$(x_c, y_c);\ (x_1, y_1), (\alpha_1, \delta_1);\ (x_2, y_2), (\alpha_2, \delta_2);\ (x_3, y_3), (\alpha_3, \delta_3). \tag{7.4}$$

The known and unknown quantities are related by the transformation equations which is a system of six

[9] Using the central pixel allows for minimum error in calculated α and δ at the edges of the image.

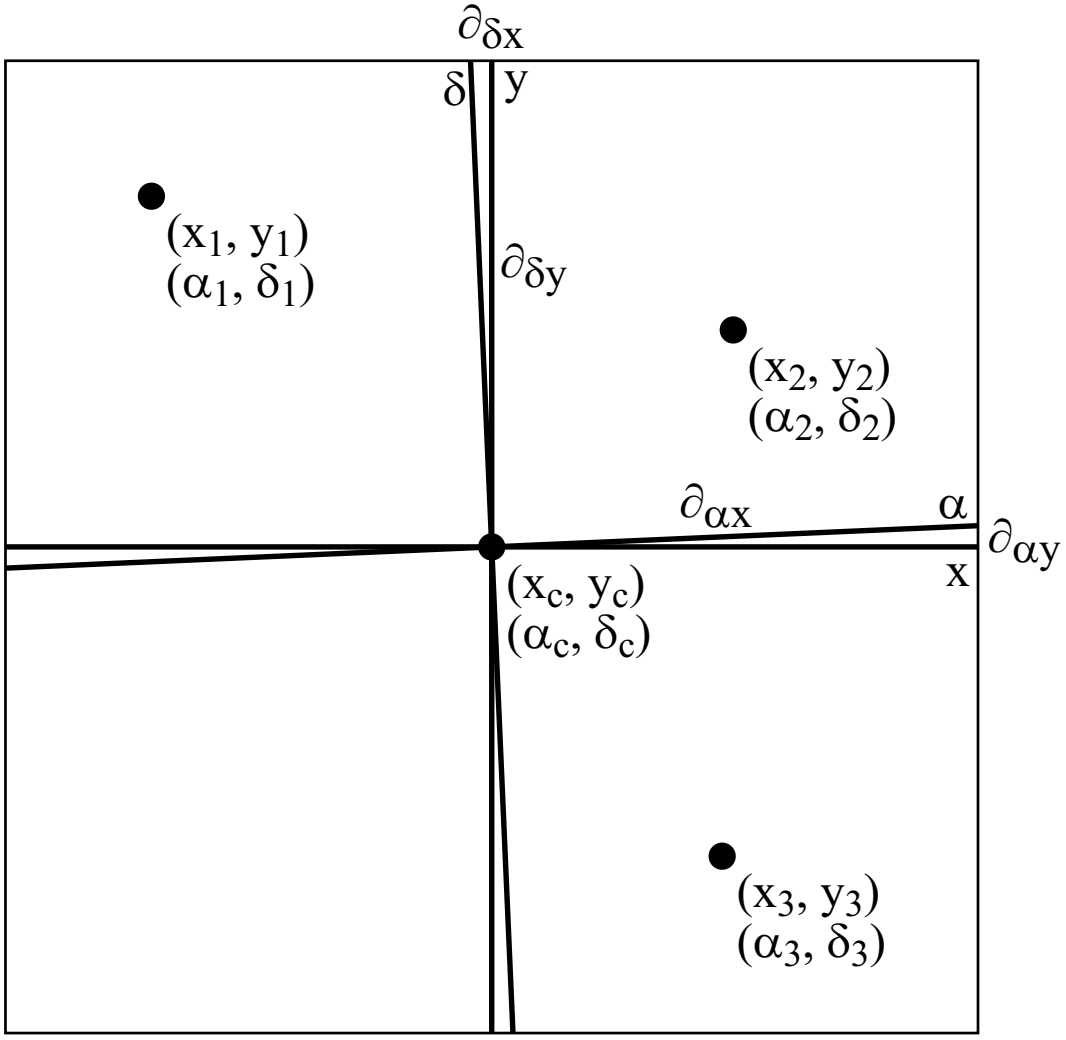

Figure 7.11: Three point sources are chosen because their known coordinate pairs solve the general coordinate transformation equations 7.5. If there is no rotation then $\partial_{\alpha y}$ and $\partial_{\delta x}$ are zero.

equations for the six unknowns:

$$\begin{aligned}
\delta_1 &= \delta_c + (x_1 - x_c)\,\partial_{\delta x} + (y_1 - y_c)\,\partial_{\delta y},\\
\delta_2 &= \delta_c + (x_2 - x_c)\,\partial_{\delta x} + (y_2 - y_c)\,\partial_{\delta y},\\
\delta_3 &= \delta_c + (x_3 - x_c)\,\partial_{\delta x} + (y_3 - y_c)\,\partial_{\delta y},\\
\alpha_1 &= \alpha_c + (x_1 - x_c)\cos\delta_1\;\partial_{\alpha x} + (y_1 - y_c)\cos\delta_1\;\partial_{\alpha y},\\
\alpha_2 &= \alpha_c + (x_2 - x_c)\cos\delta_2\;\partial_{\alpha x} + (y_2 - y_c)\cos\delta_2\;\partial_{\alpha y},\\
\alpha_3 &= \alpha_c + (x_3 - x_c)\cos\delta_3\;\partial_{\alpha x} + (y_3 - y_c)\cos\delta_3\;\partial_{\alpha y}.
\end{aligned} \tag{7.5}$$

These equations provide the following solutions:

$$\begin{aligned}
\delta_c &= \delta_3 - (x_3 - x_c)\,\partial_{\delta x} - (y_3 - y_c)\,\partial_{\delta y},\\
\partial_{\delta x} &= \frac{(y_2 - y_3)\,(\delta_1 - \delta_3) - (y_1 - y_3)\,(\delta_2 - \delta_3)}{(y_2 - y_3)\,(x_1 - x_3) - (y_1 - y_3)\,(x_2 - x_3)},\\
\partial_{\delta y} &= \frac{(x_2 - x_3)\,(\delta_1 - \delta_3) - (x_1 - x_3)\,(\delta_2 - \delta_3)}{(x_2 - x_3)\,(y_1 - y_3) - (x_1 - x_3)\,(y_2 - y_3)},\\
\alpha_c &= \alpha_3 - \frac{x_3 - x_c}{\cos\delta_3}\partial_{\alpha x} - \frac{y_3 - y_c}{\cos\delta_3}\partial_{\alpha y},\\
\partial_{\alpha x} &= \frac{\left[\frac{y_2-y_c}{\cos\delta_2} - \frac{y_3-y_c}{\cos\delta_3}\right](\alpha_1 - \alpha_3) - \left[\frac{y_1-y_c}{\cos\delta_1} - \frac{y_3-y_c}{\cos\delta_3}\right](\alpha_2 - \alpha_3)}{\left[\frac{y_2-y_c}{\cos\delta_2} - \frac{y_3-y_c}{\cos\delta_3}\right]\left[\frac{x_1-x_c}{\cos\delta_1} - \frac{x_3-x_c}{\cos\delta_3}\right] - \left[\frac{y_1-y_c}{\cos\delta_1} - \frac{y_3-y_c}{\cos\delta_3}\right]\left[\frac{x_2-x_c}{\cos\delta_2} - \frac{x_3-x_c}{\cos\delta_3}\right]},\\
\partial_{\alpha y} &= \frac{\left[\frac{x_2-x_c}{\cos\delta_2} - \frac{x_3-x_c}{\cos\delta_3}\right](\alpha_1 - \alpha_3) - \left[\frac{x_1-x_c}{\cos\delta_1} - \frac{x_3-x_c}{\cos\delta_3}\right](\alpha_2 - \alpha_3)}{\left[\frac{x_2-x_c}{\cos\delta_2} - \frac{x_3-x_c}{\cos\delta_3}\right]\left[\frac{y_1-y_c}{\cos\delta_1} - \frac{y_3-y_c}{\cos\delta_3}\right] - \left[\frac{x_1-x_c}{\cos\delta_1} - \frac{x_3-x_c}{\cos\delta_3}\right]\left[\frac{y_2-y_c}{\cos\delta_2} - \frac{y_3-y_c}{\cos\delta_3}\right]}.
\end{aligned} \tag{7.6}$$

The quantities 7.4 and the equations 7.6 were used by the computer program to find the quantities 7.2 which were the values used for the WCS keywords in the FITS file header.

7.5.2 Finding Known Objects Within the Images

A list of 2MASS point sources from the online catalogue was created from of a search for all sources within a radius of 1.°0 of the centre of NGC 300. The list contained about 4040 sources. It was formatted in degrees, minutes and seconds for both the (J2000.0) α and δ coordinates. The computer program created for this analysis converted these to decimal radians[10] as the file was read. The program used a dynamic array of a record structure to store the coordinates of each 2MASS point source along with a "distance" data field, which is discussed below.

NASA's SkyView was used to create DSS and DSS2-Red FITS file images which appeared equivalent to the BL97 images. The published central coordinates of each BL97 image were used, requesting an 800 square

[10] The program's source language required trigonometric function arguments to be in radians.

pixel image, a field of view of ($0^\circ.087$) and rotation of ($\simeq 0^\circ.5$) producing a DSS image very similar to the BL97 (continuum wavelength) images. Based on the parameters which produced the equivalent DSS images, 2MASS J-Band images were also created with SkyView. The SkyView 2MASS images were used as a visual aid in associating bright, easy to locate 2MASS point sources with optical counterparts in each BL97 image. To reduce errors in calculating the image scale the chosen sources were always closer to (but not at) the edge of the image.

As an example, Figure 7.12 shows the selected point sources for image G, which is the set containing N300-S16. For each image an estimated (α, δ) of the 2MASS point source was taken from the SkyView image and the pixel (x, y) coordinates were taken from the BL97 image. Using the DS9 FITS file viewer the BL97 (x, y) and 2MASS image (α, δ) values were found by carefully positioning the cursor over the point source image and selecting the pixel with the maximum value compared to its surrounding pixels. When two neighbouring pixels had the same or nearly the same value, or when the centre of the source image was saturated, the positioning pixel was chosen by placing the source image in the centre of the DS9 magnifying box. Table 7.9 lists the rectangular (column 1, x, y from BL97 images) and equatorial coordinates (columns 2 and 3, estimated from the SkyView 2MASS J-Band images) for the three point sources used for each image.

The BL97 (x, y) coordinates and 2MASS (α, δ) coordinates of each of the three sources from each image were put into a text file read by the computer program. Once read – with (α, δ) both converted to decimal radians – the estimated coordinates were compared to the previously read list of catalogue coordinates. The comparison created a distance measurement[11] between the estimated and the list of 2MASS catalogue coordinates which was stored in the "distance" data field of each point source data record structure. The source list was then sorted on the distance field with the smallest distance put at the top of the list. This was done for each 2MASS source on each image. The catalogue coordinates at the top of the just sorted list were the (α, δ) coordinates actually used for calculating the BL97 image centre, plate scale and rotation. Table 7.10 shows the estimated and actual 2MASS coordinates used for the astrometry and the distance between the two positions. It also shows the distance between the estimated position and the next nearest source. This was done as an indicator of any possible source confusion. Column 1 is the estimated position of the source, column 2 is the selected actual position from the sorted catalogue list, column 3 is the distance between them in arcseconds and column 4 is the distance between the estimated position and the second closest catalogue source in the sorted list, in arcseconds.

[11] Using the usual technique for calculating the distance between two points on the celestial sphere.

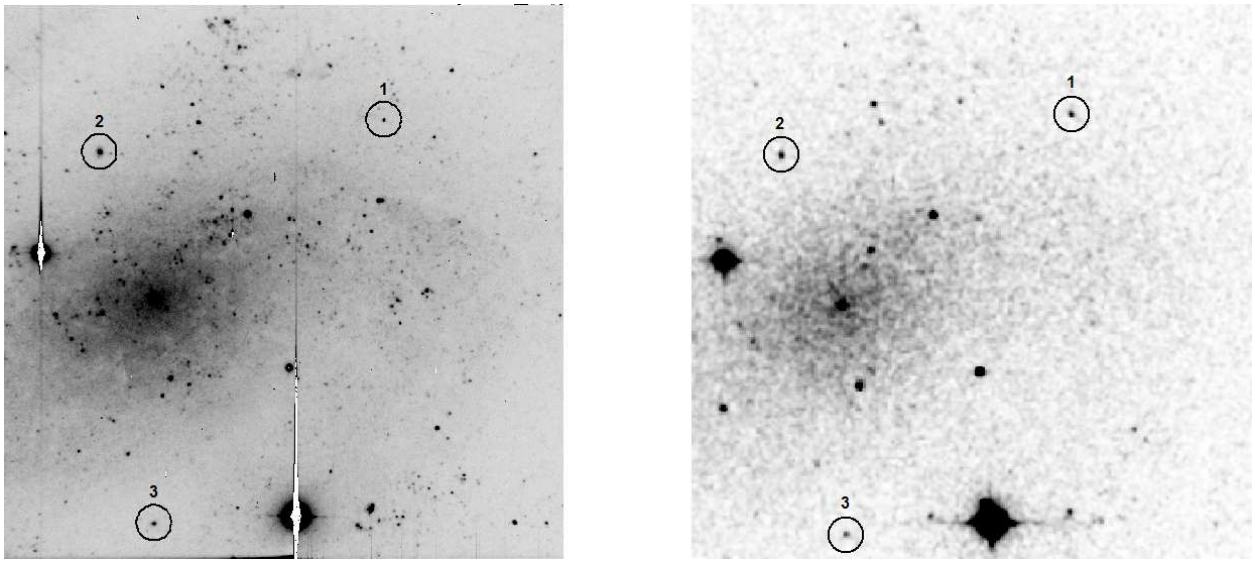

Figure 7.12: The 2MASS point sources chosen for image set G, which contains the supernova remnant candidate N300-S16 discussed in Section 7.8. On the left is the BL97 image in continuous wavelengths. The x-axis must be reversed in the BL97 FITS file to obtain the correct orientation. North is up and east to the left. On the right is the SkyView 2MASS J-Band image of the equivalent field of view. The chosen point sources are circled and numbered, and correspond to the information given in Table 7.9. (Left: Courtesy of William Blair. Right: 2MASS (See Acknowledgements).)

Table 7.9: The coordinates of the selected 2MASS point sources for each of the BL97 image sets.

	1	**2**	**3**
	BL97 Pixel	**2MASS α (J2000.0)**	**2MASS δ (J2000.0)**
	(x, y)	**(est. h m s)**	**(est. $^\circ$ $'$ $''$)**
Image D			
Source 1	314, 671	00 54 20.266	−37 34 02.08
Source 2	096, 439	00 54 12.729	−37 35 33.31
Source 3	356, 071	00 54 21.259	−37 38 03.74
Image E			
Source 1	163, 611	00 55 30.907	−37 39 21.56
Source 2	563, 607	00 55 44.457	−37 39 27.05
Source 3	296, 232	00 55 35.125	−37 41 54.65
Image F			
Source 1	707, 455	00 55 23.930	−37 40 32.88
Source 2	512, 748	00 55 17.597	−37 38 33.50
Source 3	199, 081	00 55 06.449	−37 42 58.15
Image G			
Source 1	256, 631	00 54 42.662	−37 39 17.02
Source 2	391, 278	00 54 46.981	−37 41 40.71
Source 3	662, 586	00 54 56.344	−37 39 39.71
Image H			
Source 1	223, 687	00 54 17.055	−37 38 54.61
Source 2	679, 555	00 54 32.451	−37 39 52.54
Source 3	398, 051	00 54 22.494	−37 43 12.62
Image J			
Source 1	153, 551	00 55 05.699	−37 44 47.45
Source 2	755, 457	00 55 26.000	−37 45 31.67
Source 3	594, 064	00 55 20.326	−37 48 07.51

Table 7.10: Estimated and catalogue matched 2MASS point source coordinates.

	1	**2**	**3**	**4**
	Estimate	**Actual**	**Distance**	**Next**
	(h m s ° ′ ″)	**(h m s ° ′ ″)**	**(″)**	**(″)**
Image: D				
Source 1	00 54 20.313 −37 34 02.380	00 54 20.277 −37 34 02.179	00.469	64.41
Source 2	00 54 12.737 −37 35 33.150	00 54 12.734 −37 35 33.173	00.039	38.17
Source 3	00 54 28.254 −37 37 54.890	00 54 28.262 −37 37 54.196	00.700	13.83
Image: E				
Source 1	00 55 30.609 −37 40 28.110	00 55 30.548 −37 40 27.829	00.772	09.26
Source 2	00 55 44.457 −37 39 27.050	00 55 44.443 −37 39 27.223	00.242	60.52
Source 3	00 55 44.591 −37 41 15.100	00 55 44.555 −37 41 14.960	00.449	11.02
Image: F				
Source 1	00 55 18.356 −37 39 52.190	00 55 18.329 −37 39 52.574	00.500	78.09
Source 2	00 55 06.449 −37 42 58.150	00 55 06.465 −37 42 58.216	00.197	21.17
Source 3	00 55 17.597 −37 38 33.500	00 55 17.600 −37 38 34.145	00.646	42.72
Image: G				
Source 1	00 54 42.662 −37 39 16.630	00 54 42.670 −37 39 17.226	00.604	62.76
Source 2	00 54 56.344 −37 39 39.320	00 54 56.330 −37 39 39.733	00.447	39.18
Source 3	00 54 53.283 −37 43 11.530	00 54 53.276 −37 43 11.593	00.101	48.73
Image: H				
Source 1	00 54 32.418 −37 39 52.930	00 54 32.428 −37 39 52.988	00.128	75.62
Source 2	00 54 17.055 −37 38 54.610	00 54 17.082 −37 38 55.144	00.626	60.48
Source 3	00 54 22.494 −37 43 12.620	00 54 22.496 −37 43 12.554	00.069	10.31
Image: J				
Source 1	00 55 05.699 −37 44 47.450	00 55 05.706 −37 44 47.544	00.123	46.69
Source 2	00 55 26.033 −37 45 31.670	00 55 26.025 −37 45 31.586	00.130	42.00
Source 3	00 55 20.821 −37 48 11.030	00 55 20.826 −37 48 11.491	00.466	07.09

7.5.3 Program Results and Astrometry of the Supernova Remnants

Table 7.11 shows the results for the calculation of the image centres. Column 1 is the centre as given in BL97's Table 2. Column 2 is the calculated centre from the program and Column 3 is the distance (or offset) between them, in arcseconds.

After studying the continuous, Hα filter and [S II] filter images for each lettered image set, any difference in the centre coordinates between the image filter types appeared to be negligible. Because the filters used to make the Hα and [S II] images were narrow band it was impossible to locate 2MASS point sources within those images with any level of confidence. Thus, centre coordinates and plate scale values were calculated only for the continuous images and then applied to all image filter types for the image field (lettered set). Figure 7.13 shows example data added to the headers of the BL97 image files to create a WCS. Based on the calculated WCS for each image, Table 7.12 shows the reported equatorial and calculated pixel coordinates for each of the BL97 supernova remnant candidates. Column 1 is the candidate designation, column 2 is the reported position, column 3 is the BL97 image set in which the candidate was found and column 4 is the $x - y$ pixel coordinates of the source within that image group.

Table 7.11: Image centre coordinates from BL97 and 2MASS calibrated.

1	**2**	**3**	**4**
	BL97 Centre	**Calculated Centre**	**Difference**
Image	**(h m s ° ′ ″)**	**(h m s ° ′ ″)**	**(″)**
D	00 54 23.030 −37 35 50.600	00 54 22.966 −37 35 51.374	1.081
E	00 55 38.770 −37 40 47.900	00 55 38.793 −37 40 48.215	0.420
F	00 55 13.460 −37 40 51.900	00 55 13.550 −37 40 52.086	1.082
G	00 54 47.360 −37 40 50.400	00 54 47.359 −37 40 51.305	0.905
H	00 54 22.840 −37 40 50.700	00 54 22.856 −37 40 52.042	1.356
J	00 55 14.000 −37 45 50.300	00 55 13.987 −37 45 50.463	0.227

```
WCSAXES =                    2
CRPIX1  =                400.5
CRPIX2  =                400.5
CRVAL1  =     13.593612874752
CRVAL2  =    -37.597688400505
CTYPE1  = 'RA---TAN'
CTYPE2  = 'DEC--TAN'
CD1_1   =  1.77559332940E-004
CD1_2   =  4.13476861646E-006
CD2_1   = -2.77629148958E-006
CD2_2   =  1.11557511448E-004
ORIENTAT=      1.333987793755
EQUINOX =               2000.0
```

Figure 7.13: Example header data added to BL97 image FITS files to create the WCS.

N300-S16 is the only BL97 supernova remnant candidate to appear in an Hubble Space Telescope Hα image. Figure 7.14 shows the BL97 Hα filter and [S II] filter images of N300-S1 (image set D). The pandas[12] mark the coordinates given for N300-S1 in BL97 as calibrated by 2MASS point sources. The BL97 astrometry is good – certainly within the seeing conditions reported in BL97 ($\sim$1″). Figure 7.15 shows a comparison of the reported position (BL97, on left) of N300-S16 with the apparent centre of the assumed image of the candidate (Hubble Space Telescope, on right). The offset in these positions (0.″7) is again within the reported seeing conditions. The logical next step would be to calibrate the Hubble Space Telescope images to 2MASS and study the Hubble Space Telescope Hα image of N300-S16 in comparison to the BL97 images.

[12] "Panda" is the term used in the SAO, DS9 software for this style (inner and outer circles connected by a cross) of marking positions on images.

Table 7.12: Calculated pixel positions of BL97 candidate supernova remnants.

1	**2**	**3**	**4**
	BL97 Coordinates		(x, y) **Location**
Object	**(h m s ° ′ ″)**	**Image**	**(pixel position)**
N300-S1	00 54 19.21 −37 37 23.96	D	508, 165
N300-S2	00 54 21.85 −37 40 27.11	H	431, 458
N300-S3	00 54 28.86 −37 41 51.32	H	219, 254
N300-S4	00 54 30.62 −37 40 53.75	H	170, 398
N300-S5	00 54 30.99 −37 37 33.96	D	158, 149
N300-S6	00 54 31.91 −37 38 25.68	D	128, 020
		H	141, 767
N300-S7	00 54 33.17 −37 40 16.90	H	097, 492
N300-S8	00 54 38.17 −37 41 14.88	G	671, 333
N300-S9	00 54 40.20 −37 41 02.12	G	612, 366
N300-S10	00 54 40.87 −37 40 48.73	G	593, 400
N300-S11	00 54 42.54 −37 43 14.16	G	535, 040
N300-S12	00 54 43.86 −37 43 39.08	(I)	
N300-S13	00 54 46.60 −37 39 44.32	G	427, 564
N300-S14	00 54 47.15 −37 41 07.63	G	406, 357
N300-S15	00 54 53.32 −37 38 48.24	G	231, 709
N300-S16	00 54 54.46 −37 40 35.46	G	191, 443
N300-S17	00 54 56.68 −37 43 57.70	(I)	
N300-S18	00 55 01.39 −37 39 18.17	F	762, 629
N300-S19	00 55 05.41 −37 41 21.04	F	636, 323
N300-S20	00 55 05.68 −37 46 13.35	J	645, 336
N300-S21	00 55 07.15 −37 39 15.17	F	592, 639
N300-S22	00 55 07.50 −37 40 43.18	F	577, 419
N300-S23	00 55 09.10 −37 39 32.61	F	535, 597
N300-S24	00 55 09.48 −37 40 46.21	F	518, 413
N300-S25	00 55 10.68 −37 41 27.13	F	482, 311
N300-S26	00 55 15.46 −37 44 39.31	J	361, 579
N300-S27	00 55 17.54 −37 44 36.65	J	299, 587
N300-S28	00 55 33.76 −37 43 13.33	E	541, 034

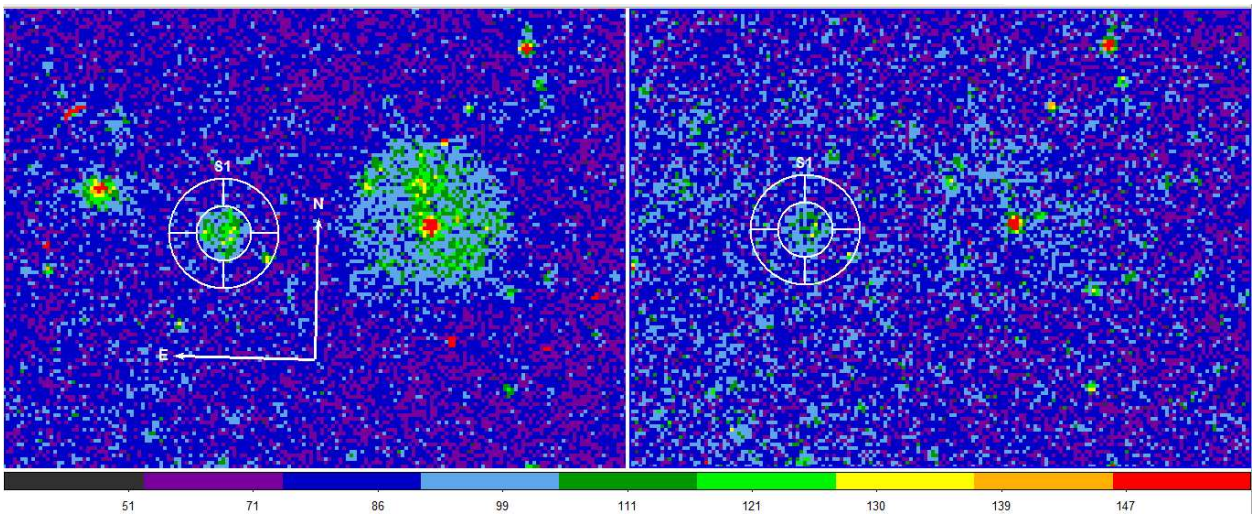

Figure 7.14: This is the BL97 published location of N300-S1 ($\alpha = 00^{\rm H}54^{\rm M}19\overset{\rm S}{.}21$, $\delta = -37^\circ\ 37'\ 23\overset{''}{.}96$) as found on the BL97 images (Image D) with 2MASS calibrated astrometry. The Hα image is on the left and the [S II] image is on the right. The pandas on both images are centred on the published coordinates for N300-S1, as guided by the 2MASS calibrated WCS for these images. The inner circle of the panda is $5\overset{''}{.}1$ in diameter (52 pc) and the outer circle is $10\overset{''}{.}2$ in diameter (104 pc). (Original images courtesy of William Blair.)

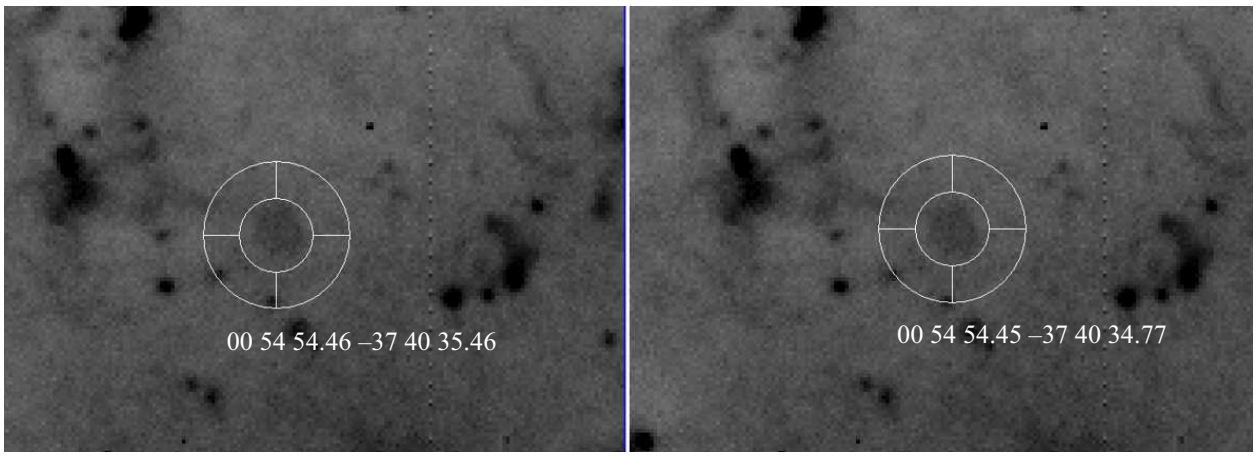

Figure 7.15: This is the BL97 location of N300-S16. The G-Hα image is shown on both the left and right with north up and east to the left. The inner circle of the pandas is $4''$. On the left is the reported position of N300-S16 (BL97) and on the right is the apparent centre of the assumed (probable) image of the supernova remnant candidate on the image. The astrometry error is within the reported seeing conditions for the observations. (Original images courtesy of William Blair.)

7.6 HST Image Astrometry

The Hubble Space Telescope FITS file headers indicated that the Hubble Space Telescope Guide Star Catalogue (GSC) version 1.x was used for the image astrometry. According to the Astrometry Department of the United States Naval Observatory (USNO)[13] the accuracy of this catalogue is approximately 500 mas ($0\farcs5$). The biggest problem with the GSC is that it does not provide for the proper motion of the stars.

The attempt to calibrate the Hubble Space Telescope images to the 2MASS catalogue using the procedure and software from above (Section 7.5) proved to be impractical because of the high-resolution of the Hubble Space Telescope images. The difference in resolution between the SkyView 2MASS images and Hubble Space Telescope images made it impossible to correctly identify 2MASS point sources in the Hubble Space Telescope images with reasonable confidence. Therefore an alternative method to check the astrometry was used.

7.6.1 Alternative Analysis

An analysis of the Hubble Space Telescope and DSS2-Red files' WCS accuracy against the BL97 2MASS-calibrated images was made by comparing the position of a bright star which could be identified in all image sets. The first comparison, between BL97 and the Hubble Space Telescope images, is shown in Figure 7.16. On the left is the BL97 G-Hα image containing N300-S16 and on the right is the Hubble Space Telescope Hα image containing N300-S16. The position of the selected star within these images is listed in Table 7.13. In this table column 1 is the image used for the observation (BL97, Hubble Space Telescope, DSS2-Red), columns 2 and 4 are the J2000.0 α and δ coordinates of the centre of the image of the star as found using DS9. The centre of the star was determined using the same process as described in Section 7.5.2. Table 7.13 columns 3 and 5 are the difference between the positions (with BL97 as the reference) in arcseconds. Column 6 is then the difference in position (offset) between the two images, measured in arcseconds. Between the BL97 and Hubble Space Telescope images there is an offset of $0\farcs15$.

[13] http://ad.usno.navy.mil/star/star_cats_rec.shtml

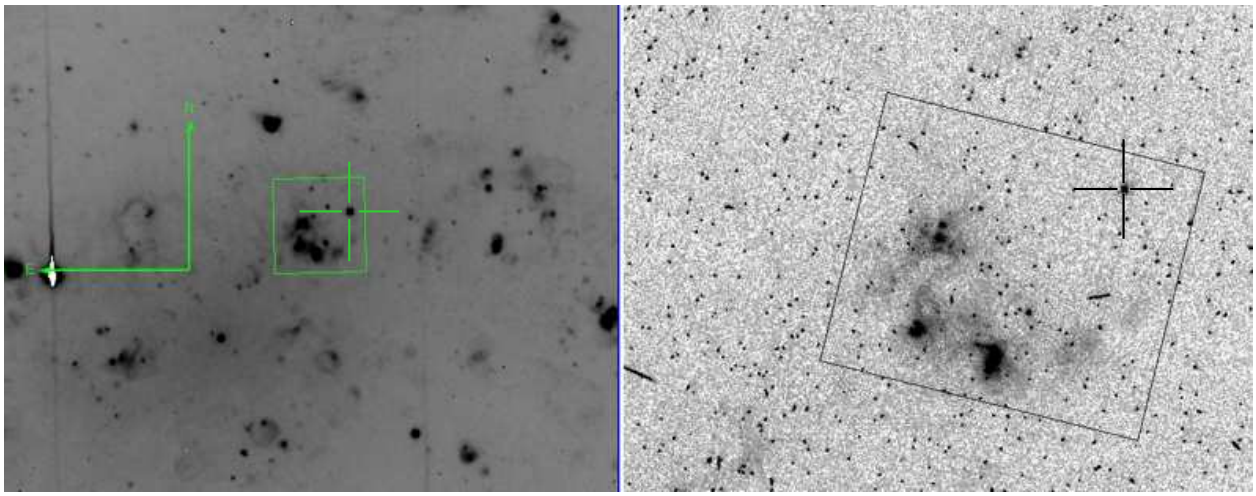

Figure 7.16: A comparison of the position of a bright star in BL97 G-Hα image and the Hubble Space Telescope image `u6713709r_drz.fits`. The images are both rotated to show north as up and east to the left. The boxes show a set of H II regions used to help identify the star and the selected star is marked with a cross. The measured difference in position is shown in Table 7.13. (Left image courtesy of William Blair. Right image courtesy of STScI MAST.)

Table 7.13: A comparison of positions of a bright star in the image sets. Because the BL97 images were calibrated to 2MASS those star coordinates are used as the standard.

1	**2**	**3**	**4**	**5**	**6**
Image Set	α **(J2000.0)**	Δ ($''$)	δ **(J2000.0)**	Δ ($''$)	**Distance** ($''$)
BL97 (Image G)	00 54 49.146	—	−37 40 11.99	—	—
HST File (`u6713709r_drz.fits`)	00 54 49.085	−0.061	−37 40 12.13	0.14	0.15
DSS2-Red	00 54 49.099	−0.047	−37 40 12.11	0.12	0.13

The second comparison was made between BL97 and the DSS2-Red images used for the finding maps for the observations in MWF11 and is shown in Figure 7.17. Between the BL97 and DSS2-Red images there was an offset of $0\farcs13$. Mickaelian (2004) measured the astrometry of the DSS2-Red images based on active galactic nuclei positions and found an accuracy of $0\farcs33$. These comparisons demonstrate that any error in the astrometry of the images used was within the reported seeing conditions.

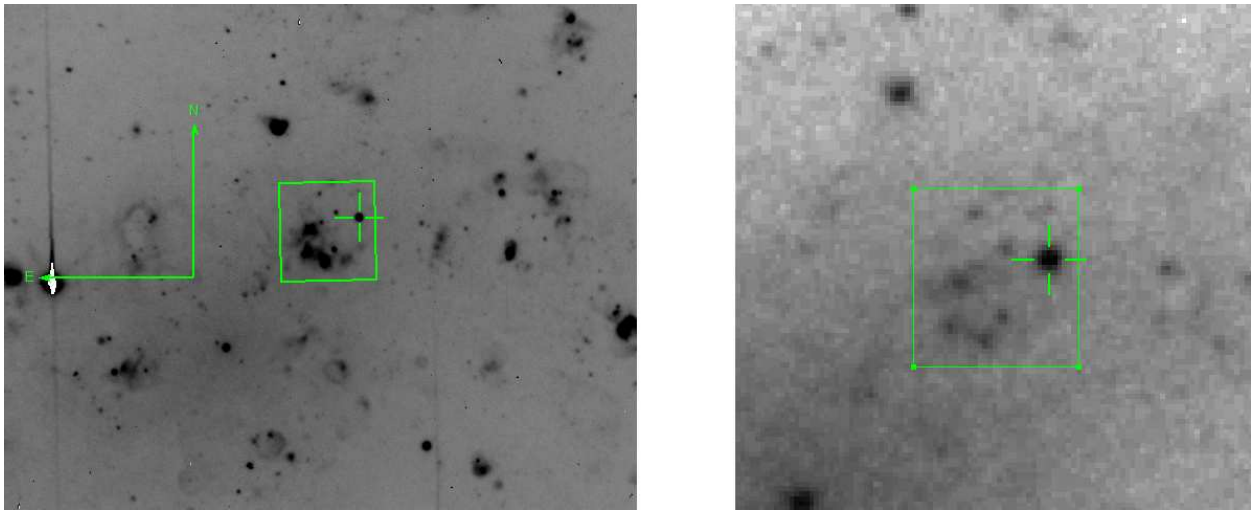

Figure 7.17: A comparison of the position of a bright star in BL97 G-Hα image and a DSS2-Red image containing the same H II regions. The image frames are both rotated to show north as up and east to the left. The boxes show a set of H II regions used to help identify the star and the selected star is marked with a cross. The measured difference in position is shown in Table 7.13. (Left image courtesy of William Blair. Right image courtesy of SkyView, Southern sky DSS image, Royal Observatory Edinburgh, Anglo-Australian Observatory, California Institute of Technology.)

7.6.2 Estimating Positional Error

Because of the difficulty in recalibrating the Hubble Space Telescope image WCS the alternative procedure of convolving the position errors was used. In Section 7.5.3 it was found that the position error in the BL97 images was $\sim 1''$. This was convolved with the approximate position error of the Hubble Space Telescope images from Table 7.13 to find a positioning error of the BL97 supernova remnants on the Hubble Space Telescope images:

$$Err_{candidate} = \sqrt{Err_{BL97}^2 + Err_{HST}^2} = \sqrt{1^2 + 0.15^2} = 1.0 \text{ arcsec}, \tag{7.7}$$

which is essentially the reported seeing conditions of BL97. The same was done with the radio supernova remnants from PF04. According to Table 2 of PF04 these candidates were observed with a circular beam width of $6''$. Using 10% of that as a 1σ positioning error for the candidates gives,

$$Err_{candidate} = \sqrt{Err_{PF04}^2 + Err_{HST}^2} = \sqrt{0.6^2 + 0.15^2} = 0.62 \text{ arcsec} \simeq 0.6 \text{ arcsec}. \tag{7.8}$$

These values were used as the 1σ positioning error for finding the supernova remnant candidates within the Hubble Space Telescope images.

7.7 Seeing and Telescope Pointing

Some of the candidates from BL97 which were observed in MWF11 returned no signal. In an attempt to determine the cause, the telescope pointing accuracy was analysed by superimposing the slit camera images on top of the observation finding maps. Figures 7.18 and 7.19 show examples of the results. Figure 7.18 shows a very good alignment with N300-S2. In Figure 7.19 there is a confusion of sources surrounding N300-S11. Both N300-S11 and J005442–374313 were clearly within the slit and the seeing conditions ($\sim 2''$) were undoubtedly allowing J005443–374311 ($<1''$ from the slit) to also flow through. Exactly what was being measured here is uncertain but it was labelled as N300-S11 (MWF11) because it was the principal candidate for that observation. This observation also included emission from the neighbouring H II region.

For N300-S11, BL97 reports [S II]:Hα = 0.66 (based on CCD images, not spectra) and MWF11 reports [S II]:Hα = 0.30 ± 0.12. Because of source confusion, neither of these measurements can be trusted. BL97 claimed seeing of $1''$, but these sources would be confused in any spectrometer's slit. To make the observations for MWF11, finding maps were created from SkyView DSS2-Red images using the KARMA software package. The image from the spectrograph's slit camera was compared to the finding map and the telescope was manually positioned to place the target object on the slit. Seeing conditions will affect the precision of this process.

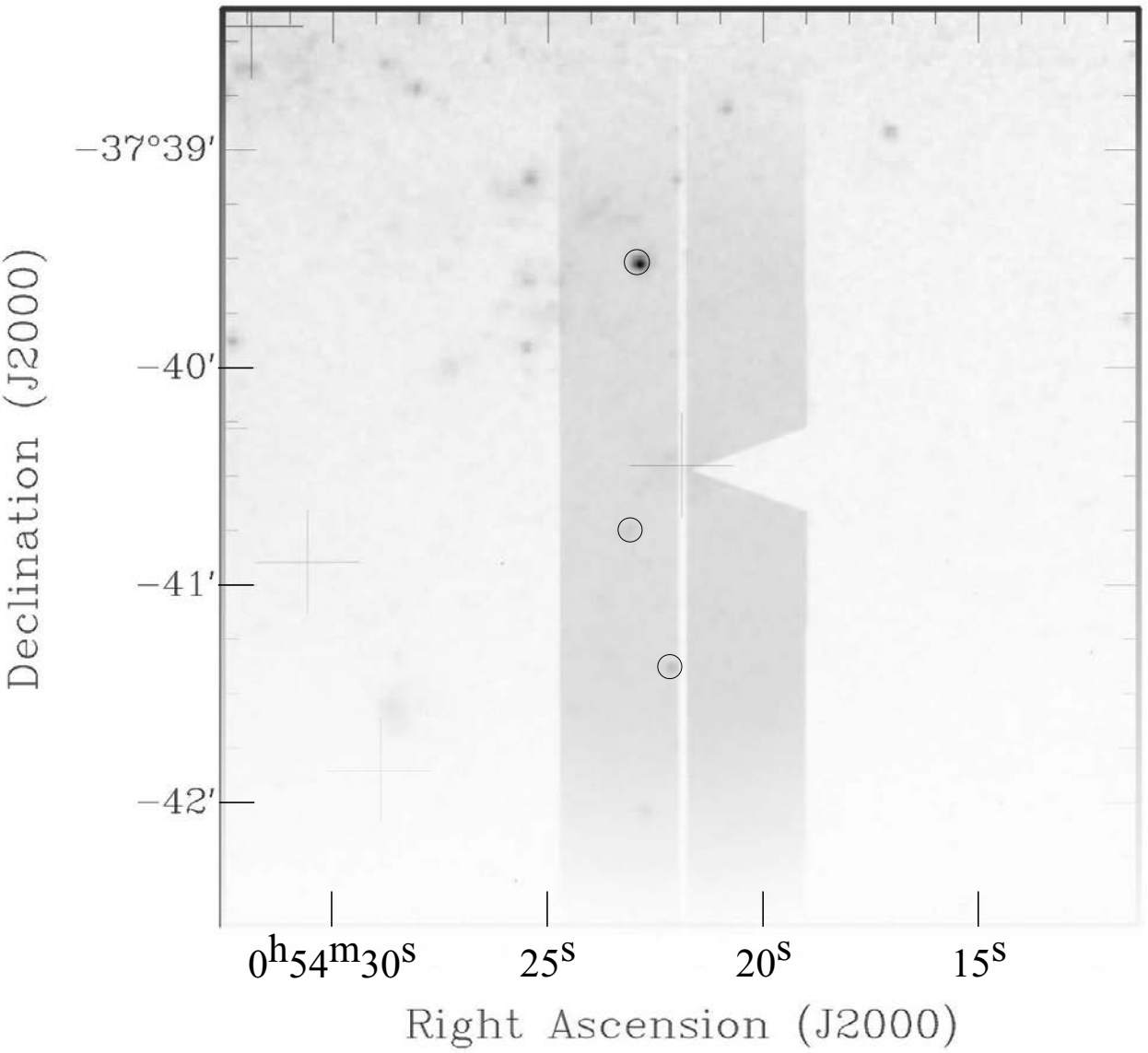

Figure 7.18: The DBS slit camera image (taken during the MWF11 observations) laid on top of the MWF11 finding map for BL97 candidate N300-S2. The circled objects are those which were used for the alignment of the two images. The pointing was exact but there is a significant difference between the measured [S II]:Hα: BL97 = 0.49 and MWF11 = 0.72 ± 0.39. The large error in the flux measurement also allows this object to be below the [S II]:Hα critical value. (Sky image courtesy of SkyView, Southern sky DSS image, Royal Observatory Edinburgh, Anglo-Australian Observatory, California Institute of Technology. Slit image: Author.)

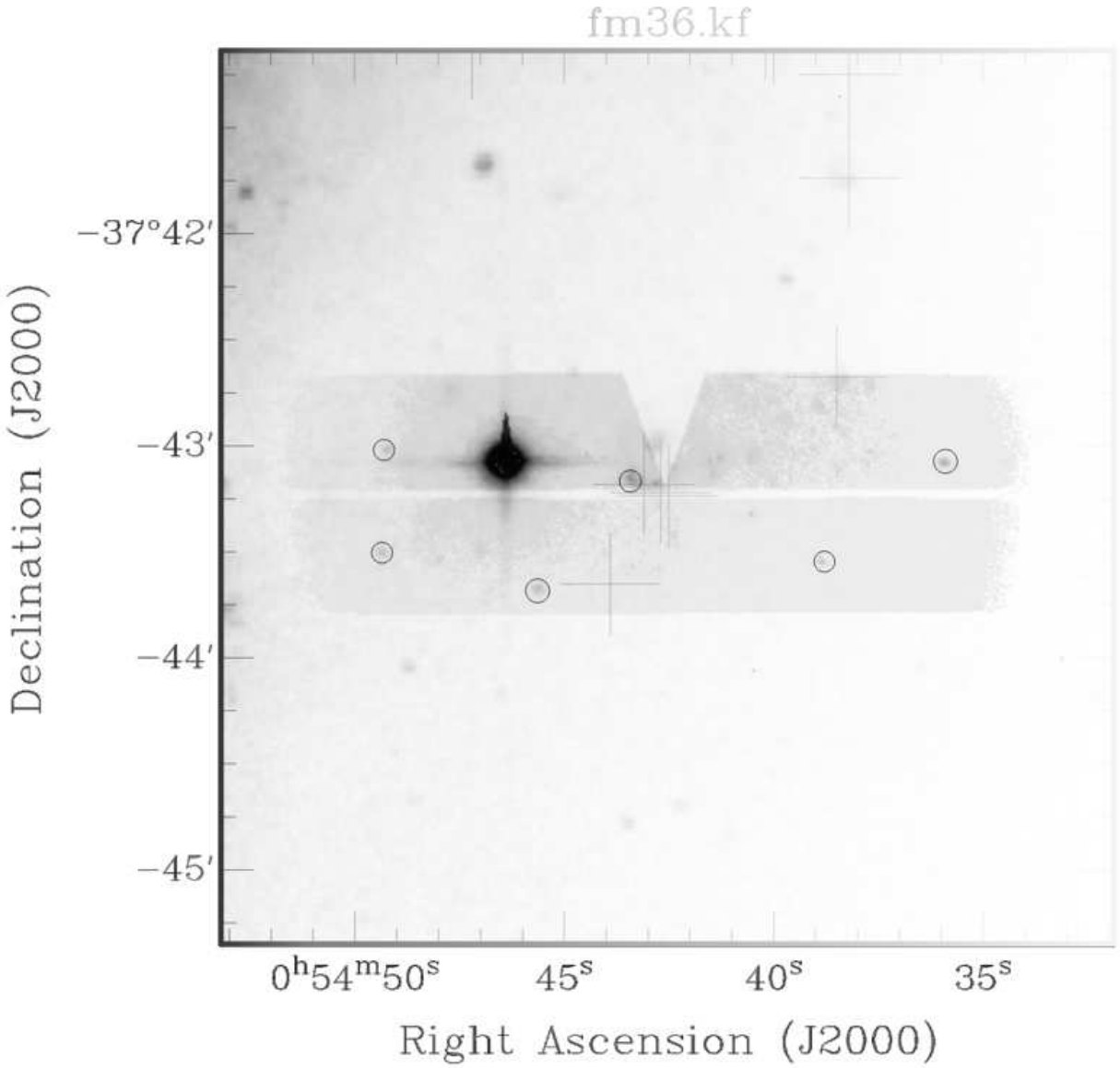

Figure 7.19: The DBS slit camera image (taken during the MWF11 observations) laid on top of the MWF11 finding map for BL97 candidate N300-S11 (lower right cross). The circled objects are those which were used for the alignment of the two images. In this case there is significant source confusion. (Sky image courtesy of SkyView, Southern sky DSS image, Royal Observatory Edinburgh, Anglo-Australian Observatory, California Institute of Technology. Slit image: Author.)

Due to seeing conditions creating telescope positioning error and confusion between objects, and the possible astrometry error in the radio observations, it is not possible to determine if J005442–374313 and N300-S11 are actually the same object. Measurements of the diameter of N300-S11 (BL97, MWF11) are greater than 100 pc. This large diameter may be caused by source confusion with the H II region or it may be a multiple supernovae site. Multiple supernova remnant sites are usually linked to OB associations and there are no known OB associations in this region. The only way to resolve this problem is with a higher-resolution telescope with no seeing problems – the Hubble Space Telescope. Unfortunately no archival Hubble Space Telescope file contained an image of these candidates.

Figure 7.20 shows the slit camera image on the finding map of N300-S16 used for the observations for MWF11. For this candidate the telescope pointing was erroneous (by 1″ to 2″, or 10 to 20 pc) and yet a [S II]:Hα 0.94 ± 0.06 was measured. The cause of the poor alignment is difficult to determine – equipment or seeing conditions. It is most likely due to seeing conditions which were on the order of 2″ to 3″ for most nights of the observing run. The seeing conditions may have allowed most of the flux from N300-S16 through the slit but it is then difficult to account for the higher ratio compared to the BL97 results (0.70).

However, we still have the real problem with this observation – the Hubble Space Telescope image containing N300-S16 shows no evidence of the candidate's existence (Figure 7.9).

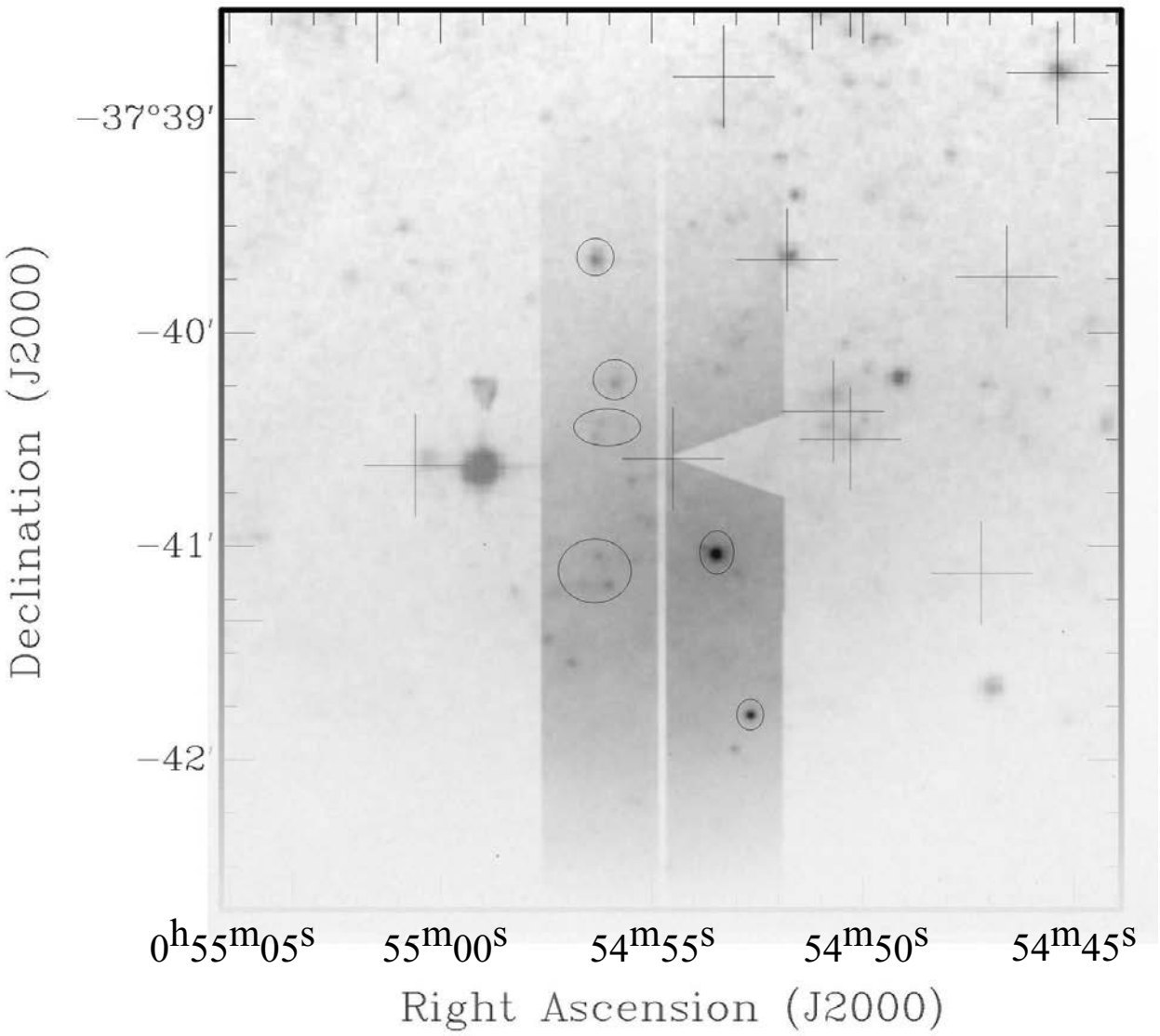

Figure 7.20: The DBS slit camera image (taken during the MWF11 observations) laid on top of the MWF11 finding map for BL97 candidate N300-S16. The circled objects are those which were used for the alignment of the two images. Due to pointing error the slit was not well aligned with the reported position of the source but a [S II]:Hα of 0.70 (BL97) or 0.94 ± 0.06 (MWF11) was measured. (Sky image courtesy of SkyView, Southern sky DSS image, Royal Observatory Edinburgh, Anglo-Australian Observatory, California Institute of Technology. Slit image: Author.)

7.8 Analysis of the BL97 Images

BL97 obtained long slit spectra for ∼2/3 of the candidates found in the previous optical filter survey for that paper. With 100% confirmation ([S II]:H$\alpha > 0.4$) of this 2/3 sample, there was confidence in all 28 candidates being confirmed as supernova remnants (Long, 1996). N300-S16 was not a member of that 2/3 subset.

7.8.1 Candidate Image Profiles

Optical emissions are expected to be greatest during the pressure-driven snowplow stage (Cioffi, 1990, page 22). This stage is typically 50 pc at maximum diameter. At the distance to NGC 300 50 pc is equivalent to $4\farcs9$. The images for BL97 are 800×800 pixels at $5\farcm3$ square (BL97; Long, 1996) and the pixel size is then $0\farcs4$. At the distance to NGC 300 this is about 4 pc. The maximum theoretical size of a pressure-driven snowplow stage supernova remnant on a BL97 image would be about 12 pixels in diameter or an area of about 110 pixels squared.

The Hα and [S II] images used for BL97 were analysed for candidate image profiles with the intention of investigating the actual number of CCD pixels used to determine the [S II]:Hα ratio of the candidate supernova remnants. Using the "Co-Add" command of SBIG's CCDOps program[14] the image of each supernova remnant candidate was stacked to form a composite image. This was done with both the Hα and [S II] images. The x and y-axis profiles of these composite images are shown in Figures 7.21 and 7.22.

Figure 7.21 shows two renditions of the stacked Hα candidate images. These two renditions differ by the display intensity scale and the number of plotted contour lines. The images were stacked so all supernova remnant candidates were located (the pixel corresponding to their equatorial coordinates) at the same resultant pixel. The rendition on the right has the crosshairs and profiles centred on the emissions peak which happens to be the same as the coordinate pixel. As an example of the data, Table 7.14 shows a 9×9 grid of the CCD pixel values from Figure 7.21 where the rows and columns are the $x - y$ pixel coordinates respectively. Figure 7.23 shows a surface plot of these values which clear shows a high signal level against the background. Figure 7.24 shows a line plot of the values along the x-axis (east-west) at y-axis (north-south) row number 165. The full-width half maximum is about 10×12 pixels ($\simeq 41 \times 49$ pc) which is about the same as the expected 12 pixel diameter area and the most expected diameter for candidates at this stage of their evolution.

[14] Available from Santa Barbara Instruments Group, `http://www.sbig.com/sbwhtmls/ccdopsv5.html`

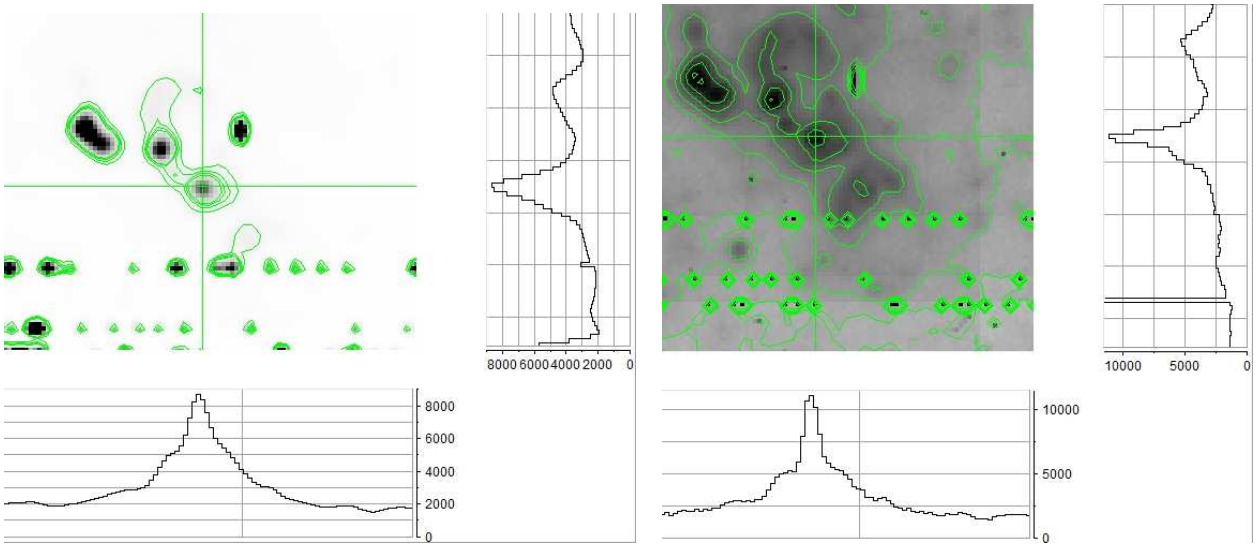

Figure 7.21: Stacked BL97 Hα images of the supernova remnant candidates. The left and right renditions differ in intensity scale, zoom level and contour line count. The profiles of the image stack for x (east-west) and y (north-south) axes are shown below and to the right, respectively. The lines across the rendition (crosshairs) indicate which CCD row (x) and column (y) are displayed in the profiles. These renditions were created with DS9 after stacking the supernova remnant images with SBIG's CCDOps software. (Original images courtesy of William Blair.)

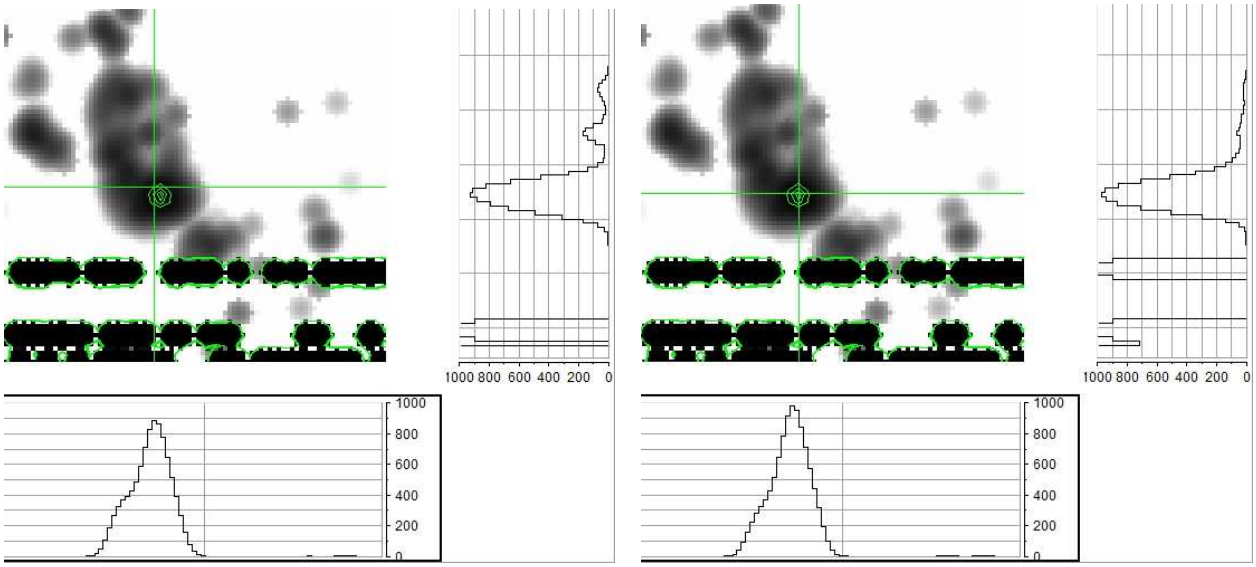

Figure 7.22: Stacked [S II] images of the BL97 supernova remnant candidates. Because of their noise level, this stack does not include the candidates found on the H and J images. The left and right renditions differ in the takeoff location of the profiles. The left rendition's profiles are based on the position of the supernova remnant candidate. The right rendition's profiles are based on the pixel with the maximum count. In each rendition, the profiles of the image stack for x (east-west) and y (north-south) axes are shown below and to the right, respectively. The lines (crosshairs) across the rendition indicate which CCD row (x) and column (y) are displayed in the profiles. These renditions were created with DS9 after stacking the supernova remnant images with SBIG's CCDOps software. (Original images courtesy of William Blair.)

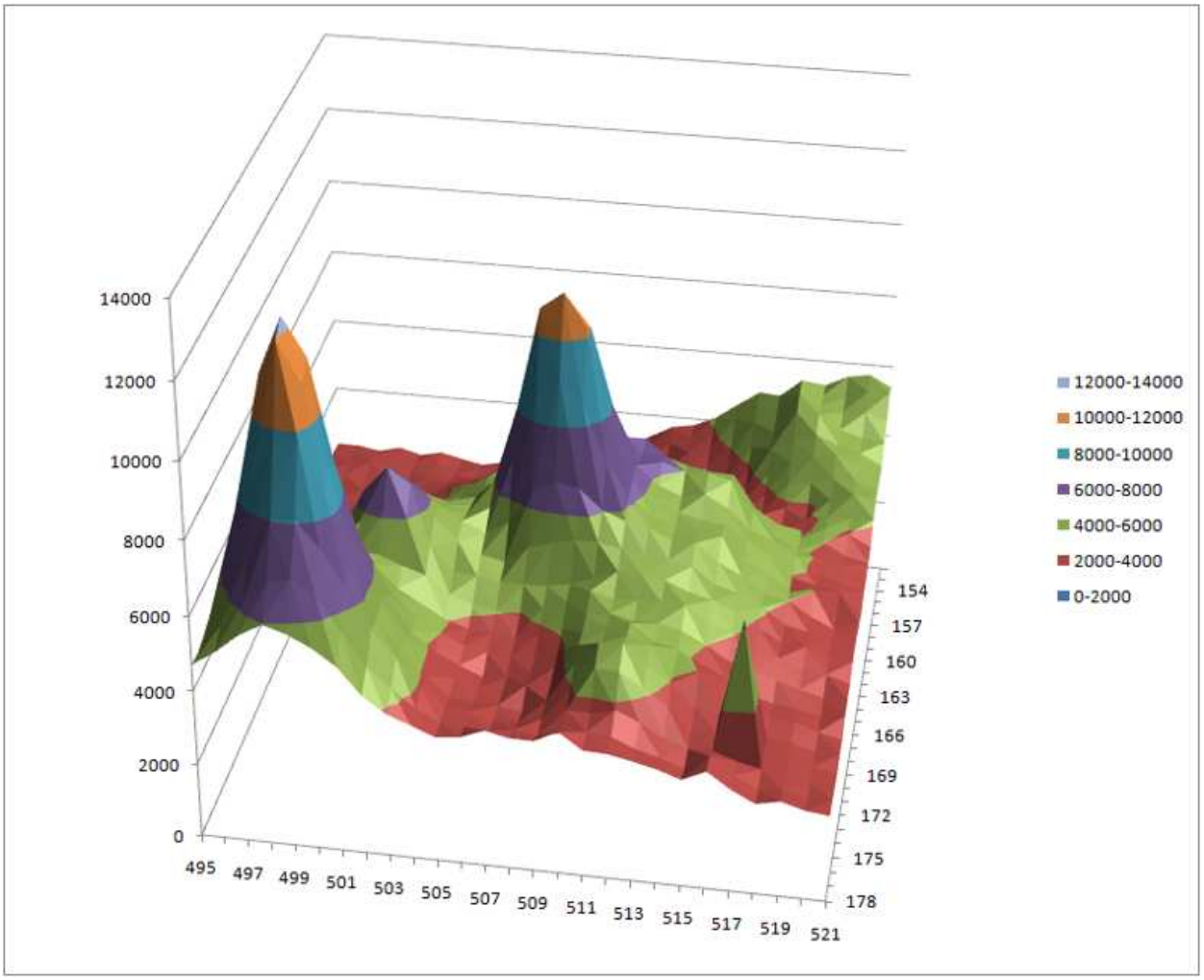

Figure 7.23: This is a 27×27 pixel (110×110 pc) surface plot the central supernova remnant location of the stacked Hα images shown in Figure 7.21. The data values of the central 9×9 region is shown in Table 7.14. A plot of the peak along the x-axis (east-west) at y-axis (north-south) pixel row 165 is shown in Figure 7.24.

Table 7.14: A 9×9 pixel (37×37 pc) region of CCD pixel values surrounding the central Hα peak in Figure 7.21. The x-axis (east-west) pixel numbers are across the top and the y-axis (north-south) pixel numbers are along the left side of the table. A surface plot of these data is shown in Figure 7.23 and a line plot of the peak is shown in Figure 7.24.

	504	**505**	**506**	**507**	**508**	**509**	**510**	**511**	**512**
169	4664	4606	4489	4482	4507	4610	4842	5088	5071
168	5168	4856	4704	5165	5357	5485	5495	5369	5272
167	5400	5122	5478	6374	6677	6588	6046	5802	5665
166	5270	5494	6869	8522	9109	8479	7062	6104	5669
165	5182	5889	7939	10668	11117	10225	8087	6320	5801
164	5088	5611	7712	9893	10624	9952	7889	6366	5851
163	4897	5182	6255	7615	7955	7798	7071	6165	6185
162	4775	4922	5444	5919	6285	6397	6471	6066	6040
161	4709	4740	5362	5681	6046	6129	6120	6164	5652

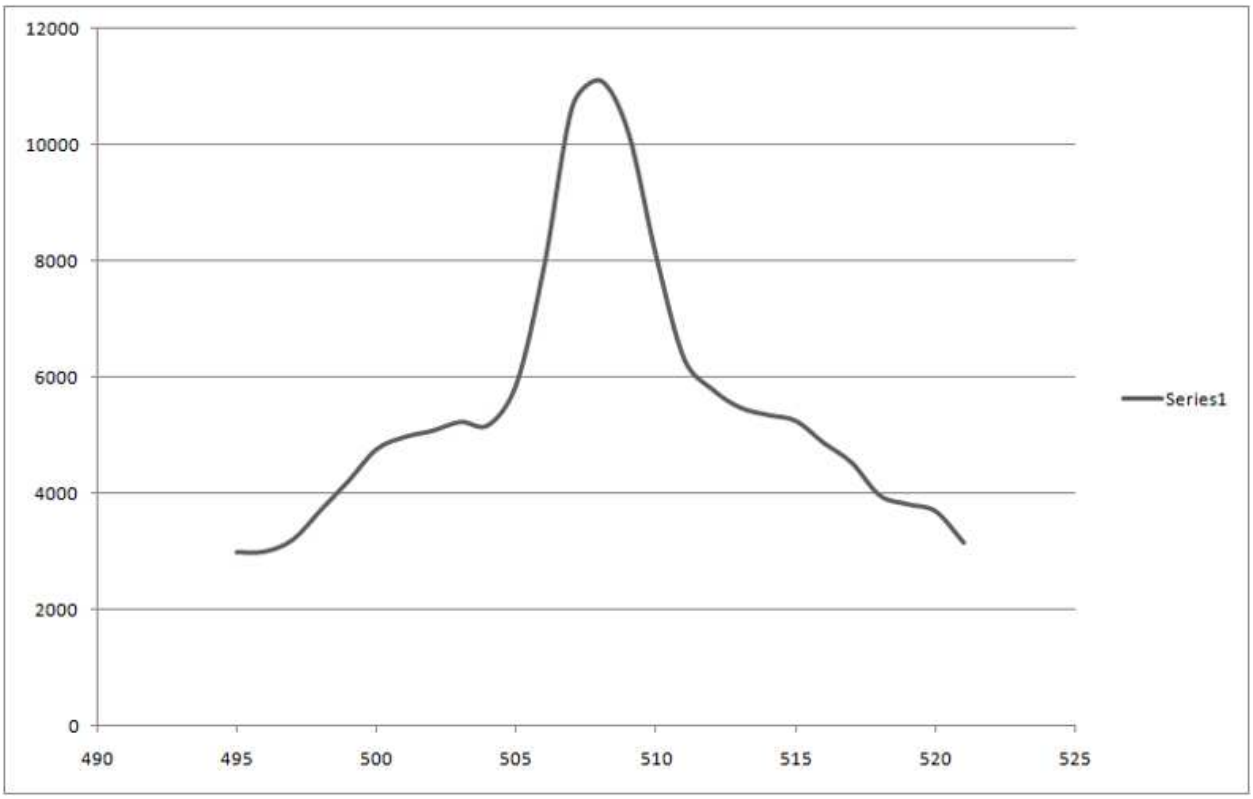

Figure 7.24: This is a plot of the stacked Hα images x-axis (east-west) values in y-axis (north-south) row 165 shown in Figure 7.21 and Table 7.14.

In Figure 7.22 the [S II] frames were stacked but did not include the H and J images as these were too noisy for this procedure. Various techniques were used to remove the noise. CCDOps has some noise treatment routines such as, "Kill Hot Pixels," "Kill Cold Pixels," "Smooth Pixels," all of which were tried. The problem was that the [S II] signal on these images was too close to the noise floor so none of the noise reduction techniques were successful. The H and J images were therefore not included in the stacked image of Figure 7.22. The H and J images contained candidates: N300-S2, S3, S4, S7 (H image); S20, S26, S27 (J image). Figure 7.22 shows two renditions of the stacked [S II] images. On the left the crosshairs (and the profiles) are centred on the supernova remnant coordinate pixel (508, 164). On the right, the crosshairs (and profiles) are centred on the pixel with maximum value (509, 162). This difference in pixel position corresponds to about 4 (α) and 8 pc (δ) in physical distance, respectively. The supernova remnant positions were determined from the Hα images based on H II regions but this also implies that the maximum Hα and the maximum [S II] emissions are on the opposite side of the supernova remnant. A surface plot of the image shown in Figure 7.22 is shown in Figure 7.25. The x-axis profile is shown in Figure 7.26. The FWHM (centred on the greatest peak) is about 7×7 pixels ($\simeq 28 \times 28$ pc).

The estimated FWHM of Hα and [S II] profiles were deconvolved with the FWHM of a small star from the J-[S II] image. The profile of the star is shown in Figure 7.27. When the FWHM of the stacked [S II] image profile (Figure 7.26) was deconvolved with the small star image profile (Figure 7.27) the resulting apparent size of the stacked [S II] regions was,

$$\sqrt{(28 \text{ pc})^2 - (15 \text{ pc})^2} = 23 \text{ pc} = 6 \text{ pixels} \tag{7.9}$$

This was taken as the average supernova remnant candidate diameter, so the extant image area of the [S II] emissions was approximately 28 pixels squared. Because the images could not be flux calibrated, the number of pixels actually contributing to the [S II]:Hα could not be estimated with reasonable confidence. The theoretically expected maximum number of pixel was about 110. With only 28 pixels (in a stacked image of all sources) contributing to the flux measurement of spectra, flux measurements of BL97 may well have large errors. Weak signals may lead to large flux measurement error (as an overestimate) an effect noted in other extragalactic supernova remnant observations by Blair et al. (1981).

7.8.2 Images of N300-S16

Figure 7.14 shows the BL97 [S II] and Hα images zoomed in on N300-S16. As measured in MWF11 the Hα and [S II] flux levels for N300-S16 were about 2×10^{-15} erg cm^{-2} s^{-1} which was only about 100 CCD pixel counts

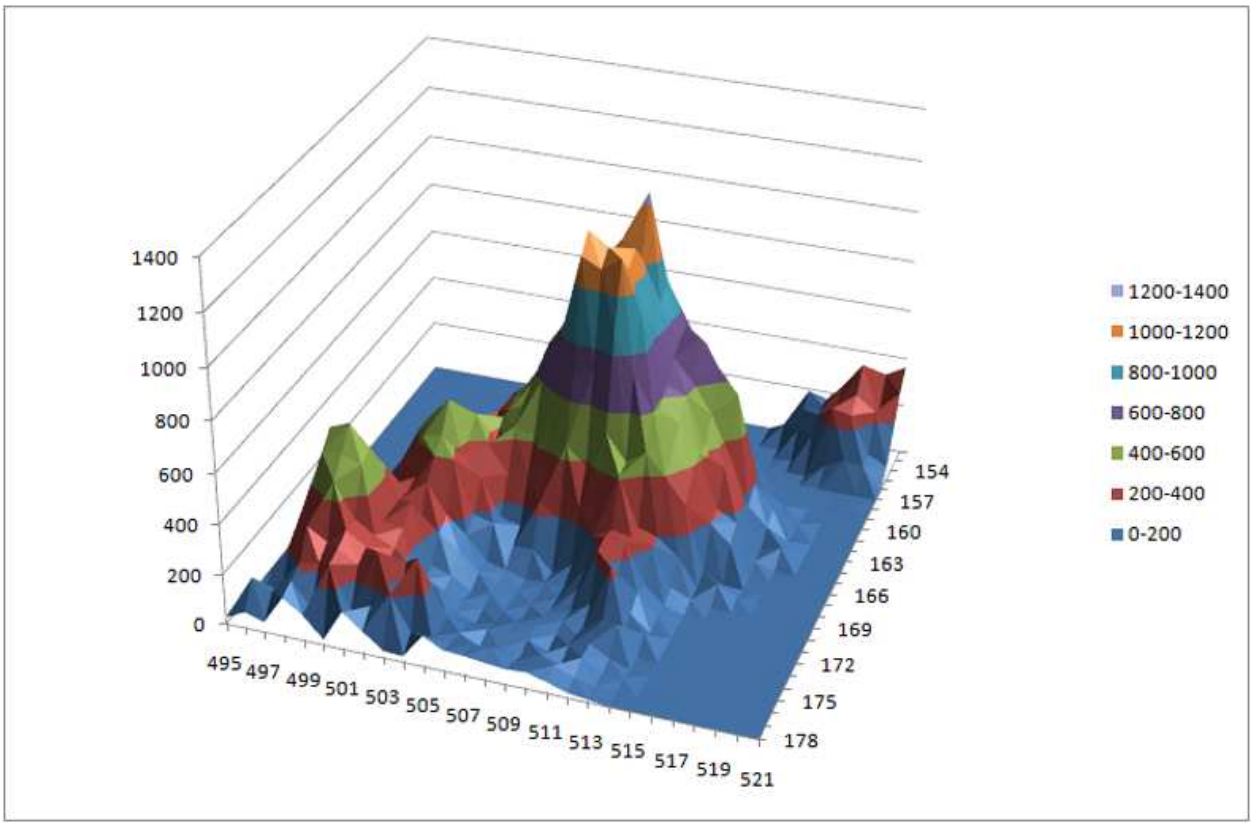

Figure 7.25: This is a 27×27 pixel (110×110 pc) surface plot the central supernova remnant location of the stacked [S II] images shown in Figure 7.22. A plot of the peak along the x-axis (east-west) at y-axis (north-south) pixel row 165 is shown in Figure 7.26.

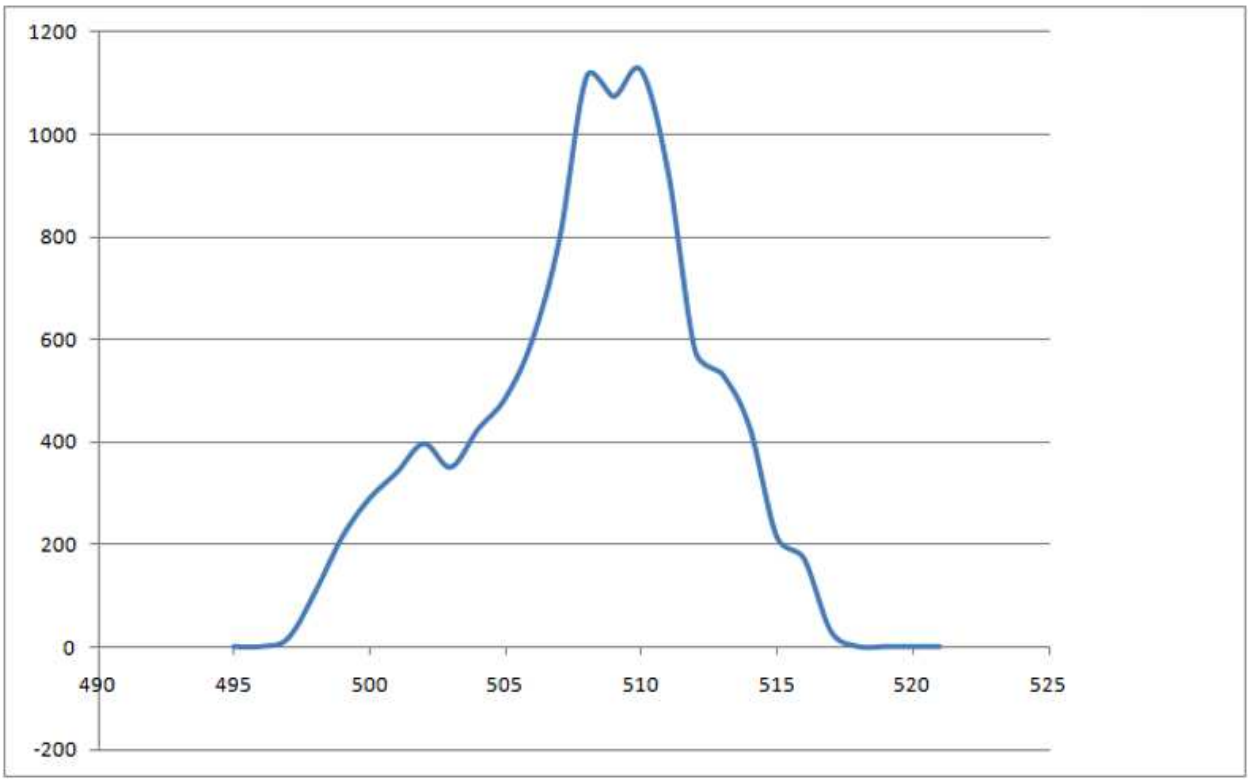

Figure 7.26: This is a profile of the stacked [S II] images x-axis (east-west) values in y-axis (north-south) row 165 shown in Figure 7.25. The FWHM is taken at 550 count as 7 pixels (28 pc).

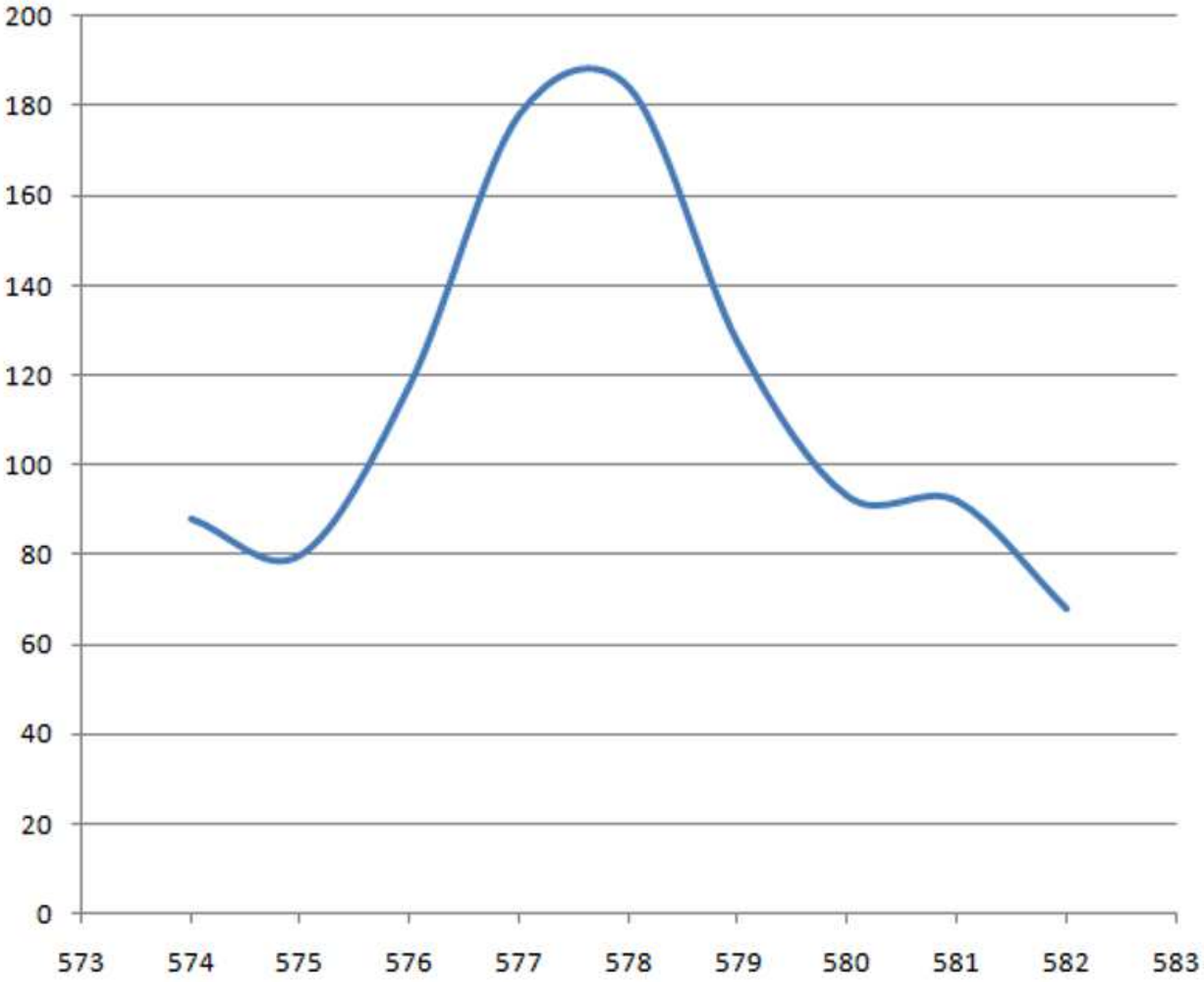

Figure 7.27: This is the x-axis (east-west) emission profile of a small star from the [S II] J image. The FWHM is taken at 130 count with a pixel width of 3.7 (15 pc).

above the background. The spectrum shows a high level background along the slit. Figure 7.20 shows the telescope was at least 1″ away from the reported coordinates of the candidate. The spectrum from MWF11 of N300-S16 is shown in Figure 7.29. There is a strong λ 6300 Å line from [O I] which is an indicator of shocked material, but there is no visual indication of such. See further comments below.

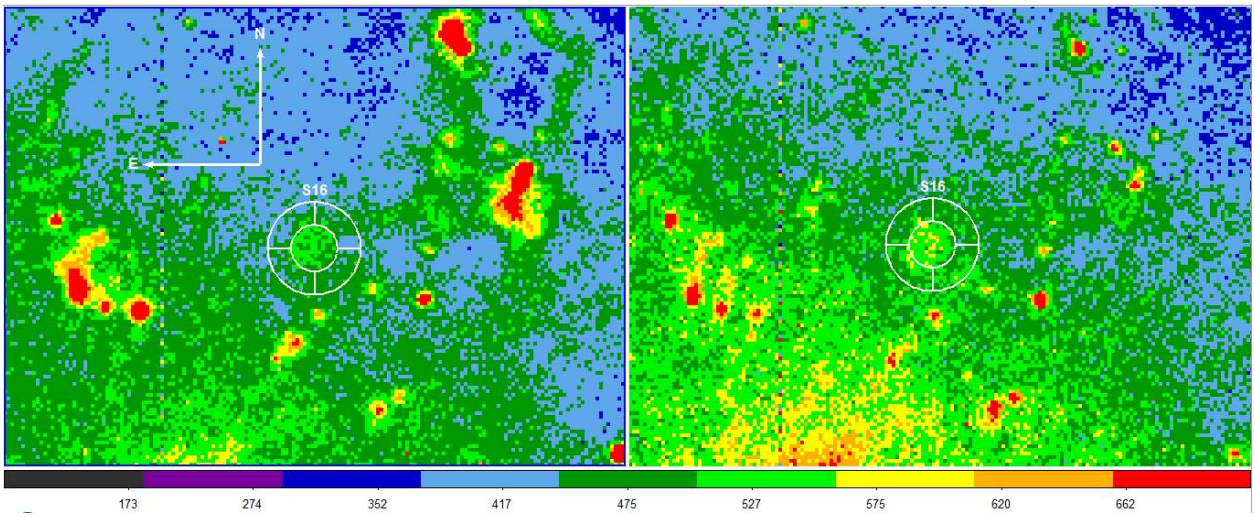

Figure 7.28: This is the BL97 location of N300-S16 ($\alpha = 00^{\rm H}54^{\rm M}54\overset{\rm S}{.}46$, $\delta = -37^\circ\ 40'\ 35\overset{''}{.}46$) as found on the BL97 images (G) with 2MASS calibrated astrometry. The Hα image is on the left and the [S II] image is on the right. The inner circle of the panda is $5\overset{''}{.}1$ in diameter (52 pc). (Original images courtesy of William Blair.)

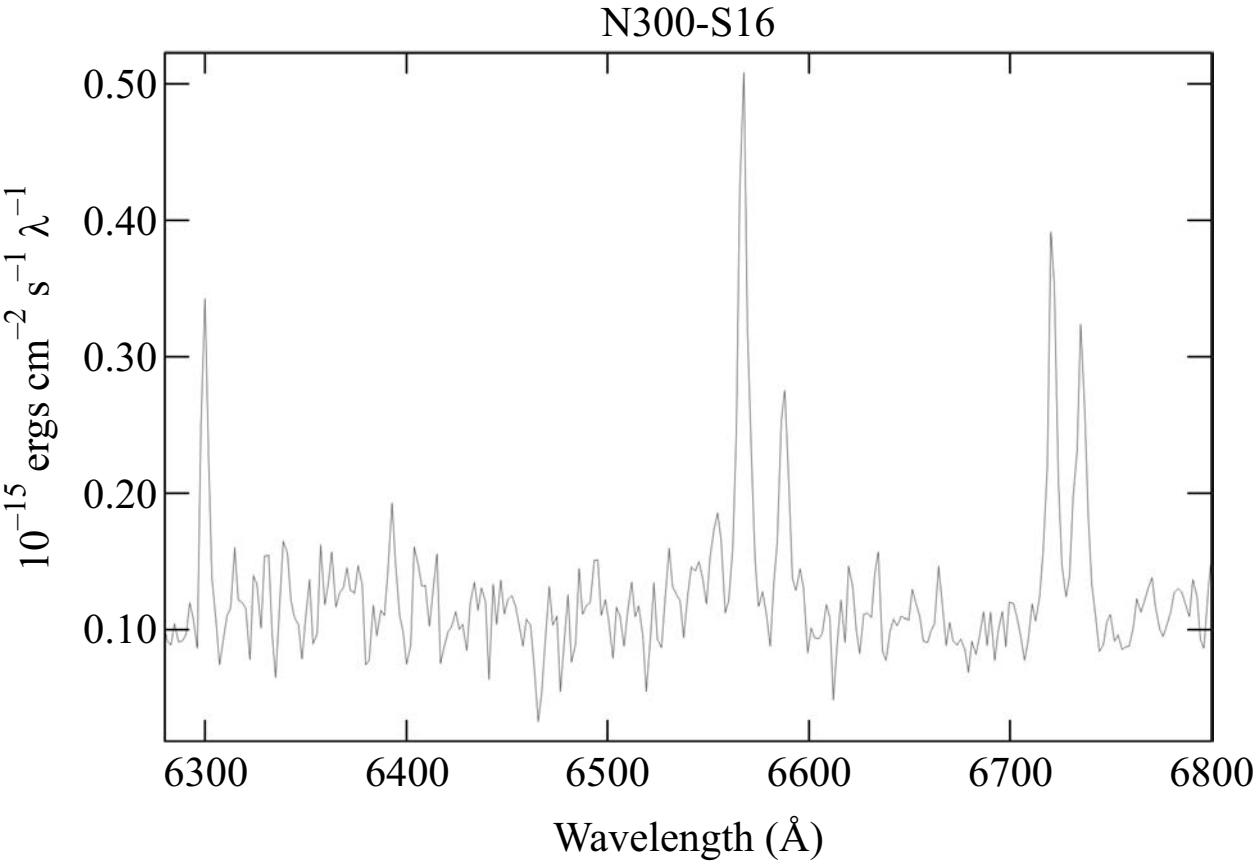

Figure 7.29: The spectrum of N300-S16 from MWF11. The spectrum also contains a prominent [O I] line at 6300 Å which is an indicator of shock fronts typical of supernova remnants. Note the broad band noise level in the spectrum and the low flux density.

In the Hubble Space Telescope Hα image of N300-S16 (Figure 7.9) there was little if any evidence of a disturbance in the hydrogen gas in the region of the location of N300-S16. While the equivalent images of the radio supernova remnant candidates (see Figures 7.4, 7.5, 7.6 and 7.7) show strong evidence of such, even though the measured [S II]:Hα ratio does not confirm them as optical supernova remnants. There are no known X-ray emissions associated with N300-S16.

Figure 7.30 shows a 3-D plot of the BL97 CCD Hα (top) and [S II] (middle) image pixel counts of N300-S16. The pixels plotted (a 27×27 array (110×110 pc) centred on the candidate's coordinates) are shown by the green box in the image tile on the left. The plot is shown on the right. In both cases the emissions are only slightly above the background but clearly discernible. The size of the candidate (50 pc) implies it to be at the end of its pressure-driven snowplow stage, if it is in a denser (than average) environment. The 3-D plot on the bottom of the figure is a plot of the result of dividing the [S II] pixel value by the Hα pixel value. The apparent supernova remnant disappears in the high-level diffuse ionised gas noise.

There are spectral line characteristics other than [S II]:Hα to support supernova remnant candidacy (e.g. the presence of [O I] in the spectrum) and there is a selection effect biased toward finding supernova remnants away from hydrogen regions in optical surveys (P04). Type Ia supernova which are away from any hydrogen region are then located in less dense interstellar matter. As a result, there is a lower abundance of shocked material to produce the [S II] (and other metallic) spectral lines in the supernova remnant. Such supernova remnant spectra may be dominated by the Balmer lines (e.g. SN 1006, Tycho's and Kepler's supernovae) and are generally missed by optical surveys (PD00). A check of the data from MWF11 shows no Balmer dominance in the spectrum of N300-S16, particularly with a [S II]:Hα of 0.6 and a high level of [O I] usually associated with shocked interstellar matter. High-resolution imaging should be used to confirm the existence of this supernova remnant. This imaging could be done with space-based telescopes (Hubble Space Telescope) or with ground-based telescopes equipped with adaptive optics.

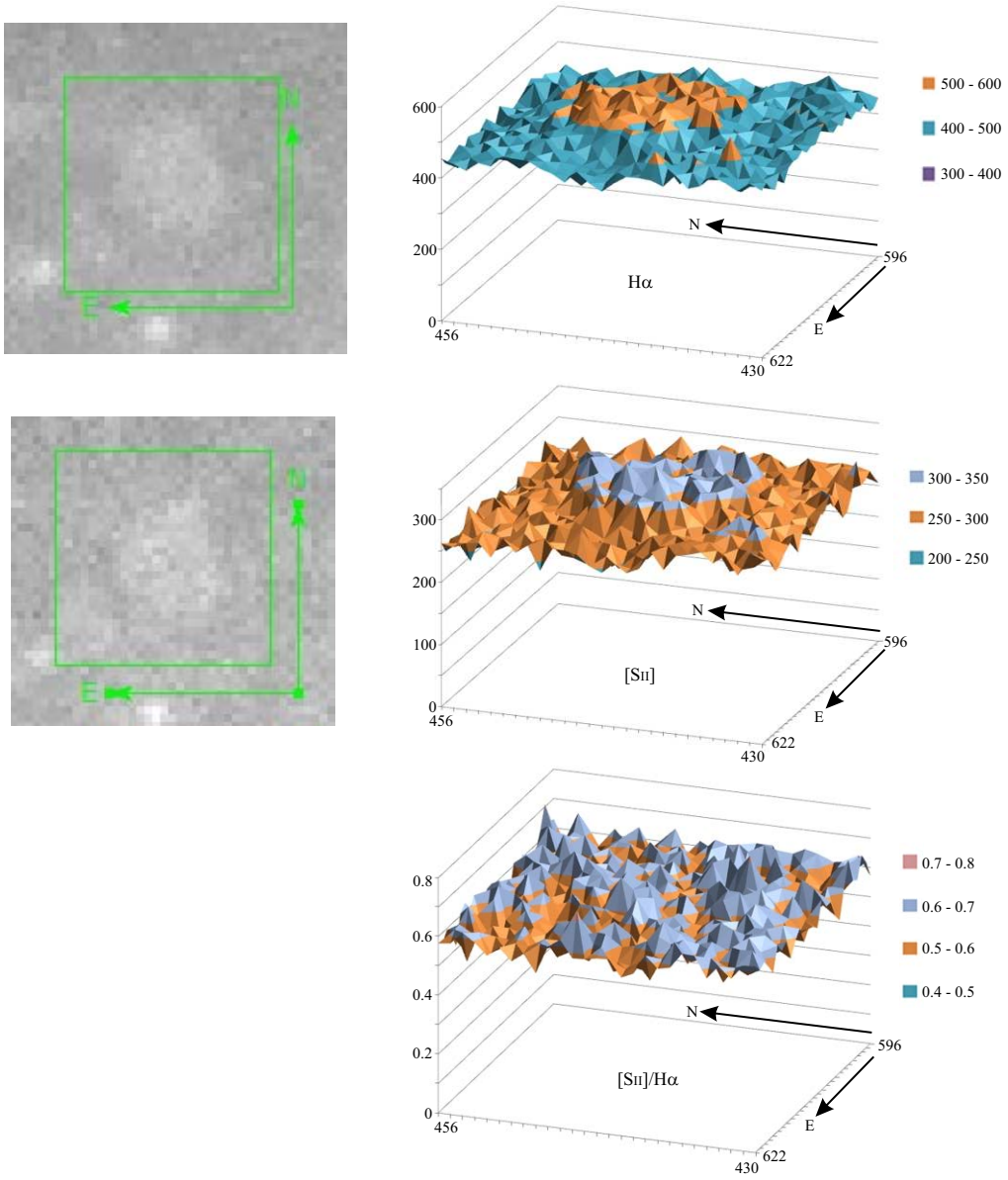

Figure 7.30: These are 3-D plots of the BL97 image CCD pixel counts of N300-S16 in Hα (top) and [S II] (middle). The pixels plotted (27 $\times$ 27 array (110 $\times$ 110 pc) centred on the candidate's coordinates) are shown by the green box in the image tile on the left. The plot is shown on the right. In both cases the emissions are only slightly above the background but clearly discernible. The size of the candidate implies it to be at the end of its pressure-driven snowplow stage. The 3-D plot on the bottom was the result of dividing the [S II] pixel value by the Hα pixel value. The apparent supernova remnant disappears in the high-level noise – possibly the diffuse ionised gas. (Thumb images on left made from CCD images courtesy of William Blair.)

7.9 Conclusion

A careful investigation of the data collected with the telescopes and instruments typically used for the discovery and confirmation of extragalactic supernova remnants reveals that the reliability of these techniques may be questionable. A strict flux density measurement error analysis shows that large errors in the [S II]:Hα ratio occur when the ratio is based on low flux density levels (MWF11). Seeing conditions lead to blurring of the spectrograph's slit image which increases pointing errors in (manual) fine positioning of the telescope which may then impinge in the reliability of the flux measurements and on the confidence of exactly what object is being measured. In cases where the target galaxy has high level emission from its diffuse ionised gas, the spectroscopic data may not be sufficient to confirm the presence of a supernova remnant. This is particularly true if the remnant is the result of a Type Ia event which is not near any H II regions. High resolution optical images from space-based telescopes or from ground-based telescopes using adaptive optics may be necessary for confirming the existence of these supernova remnants.

Chapter 8

Conclusions

The focus of this thesis was on the multi-wavelength study of supernova remnant candidates in NGC 300, with emphasis on optical observation and measurement techniques. A review of the astronomical literature provided a collection of previous surveys and observations of NGC 300 supernova remnants and candidate supernova remnants in the X-ray, optical and radio regions of the electromagnetic spectrum. The results of these surveys and observations have demonstrated the effectiveness of multi-wavelength observation techniques. The previous work of identifying supernova remnants in NGC 300, the archival data available from the Hubble Space Telescope and the new data collected for this thesis (MWF11) have been reviewed. Appendix B contains an overview of general observations of NGC 300 and observations of objects other than supernova remnants which can be confused with supernova remnants or affect the observation and study of extragalactic supernova remnants, particularly within NGC 300. This chapter is a discussion of the findings of these reviews and original research, and conclusions based on the findings.

A radio survey published in PF04 presented a number of new supernova remnant candidates which had never been observed in optical spectra. Some of the candidates found in an optical survey and published in BL97 had no spectral results in BL97 and none of these objects had been observed (as optical spectra) since that survey. For this thesis, long slit optical spectra for all these candidates (see Table 5.7) were obtained with the Advanced Technology Telescope at Siding Spring Observatory with the moderate-resolution (< 5 Å) dual-beam spectrometer. Most of the radio sources of PF04 did not meet the accepted requirement of [S II]:H$\alpha > 0.4$ while most of the optical sources from BL97 did (see Chapter 6, Table 6.1 and MWF11).

The original BL97 Hα and [S II] CCD images were analysed for astrometric accuracy and for the number of

image pixels detecting the emissions used for the [S II]:Hα. Any error in the astrometry was within the seeing conditions for those observations. The candidate supernova remnant images were stacked and the resulting image profiles (along the CCD chip row and column pixels) were examined. The [S II] profile was deconvolved with the profile of a small star from the [S II] image. This allowed an upper estimate to the greatest number of pixels contributing to the [S II] flux used to determine [S II]:Hα for the BL97 candidates. The low number of contributing pixels (BL97) and the low flux density values compared to background noise (BL97 and MWF11) implied that the [S II]:Hα measurements may not be as reliable an indicator of supernova remnant character as has been accepted and should be used with caution.

The ground-based imaging (BL97) and optical spectral observations (MWF11) of the supernova remnant candidate labelled N300-S16 compared with an archival observation from the Hubble Space Telescope (in Hα, Graham et al., 2001) provide conflicting evidence as to the true nature of this object. The [S II]:Hα far exceeds the accepted minimum value for supernova remnant identification and there is a presence of [O I] (see Table 6.1 and Figure 7.29) both of which are accepted indicators of supernova remnants. However, the higher-resolution, higher-sensitivity Hubble Space Telescope image of the object shows no signs of any structure in the interstellar matter at N300-S16's location while clear interstellar matter structure does appear near other supernova remnant candidate sites within the same Hubble Space Telescope image. Also, a demonstrated pointing error in the MWF11 observation (with a greater [S II]:Hα than the BL97 estimate from the CCD images) raises concern about what was actually measured in either observation. The calculated flux density measurement error for N300-S16 as found in MWF11 is at the bottom of the range of errors for the measurements in that paper.

N300-S16 may be a remnant from an isolated (away from an H II region) Type Ia supernova and so there may be only very low levels of metallic emissions. (Type Ia supernova remnants are generally Balmer line dominated.) These levels may be too close to the background emissions of NGC 300 for reliable flux density measurement even though the error analysis in MWF11 returned a very small error value. Although there are known problems with the [S II]:H$\alpha > 0.4$ criterion for identifying supernova remnants and there are reported resolutions to these problems, there appears to be more problems that may as yet be unrecognised. One reasonable method of improving the reliability of these results is to improve the seeing conditions of the observations. This may be accomplished through space-based observations (Hubble Space Telescope, James Webb Space Telescope) or by using larger ground-based telescopes equipped with adaptive optics.

The sulphur/oxygen gradient of NGC 300 has been studied (Christensen et al., 1997). NGC 300 has a high

level of diffuse ionised gas (Hoopes et al., 1996) and this may itself be a large contributor to the [S II]:Hα ratio. In the literature, no study has been done into the relationship between the supernova remnant [S II]:Hα minimum and the metallicity (Z) or chemical evolutionary status of the galaxy containing the supernova remnant. There are papers reporting the chemical composition of the interstellar matter by studying the chemical composition of supernova remnants (e.g., Cioffi, 1990). This approach perhaps needs to be reversed or at least to have the supernova remnants confirmed by means other than or along with optical spectra – preferably by very high-resolution optical imaging.

There are no available studies pertaining to the relationship between the [S II]:Hα and the galaxy morphological class although some has been done into the galaxy class and rate and distribution of supernova remnants (see for example the discussions in Matonick & Fesen, 1997). It is accepted that core-collapse supernovae are more likely to occur near H II regions and Type Ia supernovae may not be near H II regions. N300-S16 is not near any known H II regions and one might thus claim it is the result of a Type Ia explosion. However, Type Ia explosions occur in binary systems with the demise of an helium or carbon/oxygen white dwarf. There should not be a large amount of sulphur in such a system but this object has an unusually large [S II]:Hα ratio.

This investigation of supernova remnant candidates in NGC 300 leads to the conclusion that the long accepted [S II]:H$\alpha > 0.4$ as an indication of an object's supernova remnant character may not be as trustworthy as has been accepted. More work needs to be done to verify that the long accepted [S II]:H$\alpha > 0.4$ is truly an acceptable criterion for the identification of supernova remnants in all galaxies. What roles the host galaxy's chemical evolution, metallicity and diffuse ionised gas play in the measurement of the [S II]:Hα of a supernova remnant candidate must be investigated by observing many supernova remnant candidates in as many galaxies as possible – particularly within our own and the Local Group. There is no convincing evidence that the optical spectra from the objects studied here are those of supernova remnants.

Of the five objects studied in detail in Chapter 7 the [S II]:Hα criterion shows a 100% failure rate. Viewing these 5 as part of the 51 objects studied in Chapter 6 there is a 10% failure rate for the [S II]:Hα criterion. Because there are only these five objects available in the Hubble Space Telescope data for NGC 300, the 10% failure rate can only be described as the minimum [S II]:Hα failure rate for this sample of objects.

To this point in time a literature search returns no observations concerning the dynamics or structure of extragalactic supernova remnants. Such studies are one of the justifications for observing extragalactic supernova remnants. Ground-based telescopes, particularly those of the class currently used for extragalactic supernova

remnant surveys, are not suited for observations of the structure and dynamics of these distant objects. The seeing associated with these telescopes is far too poor. To learn more about supernova remnants, observations of these characteristics of extragalactic supernova remnants should be made. The only telescopes with the resolving power to make these observations are active optics class, or space-based telescopes – both of which are dedicated mainly to other types of observations. The problems with the [S II]:Hα and other spectral line measurements will not be resolved until higher resolution equipment can be used for extragalactic supernova remnant observations. Problems with observing extragalactic supernova remnants appear with multiple observations of supernova remnant candidates. These problems are summarised in Table 8.1.

Table 8.1: Problems with observing extragalactic supernova remnants – summary of conclusions.

1 **Problem**	**2** **Cause**	**3** **Effect**	**4** **Resolution**
Image resolution.	Seeing conditions.	Poor astrometry, creating source confusion and telescope pointing error.	Using ground-based telescopes with adaptive optics or using space-based observatories.
Spectroscopic resolution.	Seeing and low-resolution spectrographs.	Poor signal to noise ratio in flux measurements.	Using higher resolution spectrographs.
Survey resolution.	Seeing conditions and telescope resolution.	Level of emission flux used in finding supernova remnant candidates by using [S II]:Hα.	Using ground-based telescopes with adaptive optics or using space-based observatories.
[S II]:Hα ratio.	Background contamination low signal level measurement and noise error.	Ratio may not be valid in all galaxies.	More thorough study of the relationship between the [S II]:Hα ratio, the interstellar matter, the diffuse ionised gas and the Z for all nearby early and late spiral galaxies.
Radio resolution.	Telescope configuration.	Source confusion and astrometry.	Using telescopes with longer baseline at declinations (altitude) optimised at the telescopes' latitude.
X-ray telescope resolution.	Sensitivity, and spatial and energy resolution of detectors.	X-ray source intensity and astrometry.	Construction of higher-resolution and higher-sensitivity X-ray observatories.

8.1 Summary

Here is a list of the important results of this study of supernova remnants and supernova remnant candidates in the Sculptor Group galaxy, NGC 300:

- A review of the astronomical literature provided a collection of previous surveys and observations of NGC 300 supernova remnants and candidate supernova remnants in the X-ray, optical and radio regions of the electromagnetic spectrum. The results of these surveys and observations have demonstrated the effectiveness of multi-wavelength observation techniques.

- Radio and optical supernova remnant candidates were observed with long slit optical spectra with a moderate resolution dual-beam spectrometer. Most of the radio sources did not meet the accepted requirement of [S II]:H$\alpha > 0.4$ while most of the optical sources did. A few of the source remain unidentified because no spectral signal was obtained.

- The original BL97 CCD images were analysed for astrometric accuracy. Any error in the astrometry in that optical survey was within the seeing conditions for those observations. However, there appears to be a systematic astrometric error in the PF04 radio survey.

- The original BL97 CCD images were analysed for the number of image pixels used for the [S II]:Hα. The object images were stacked and the resulting image profiles were examined. The low number of contributing pixels and the low flux density values compared to background noise implied that the [S II]:Hα measurements may not be as reliable an indicator of supernova remnant character as has been accepted. Also, these measurements are highly biased against H II regions, near which a high number of supernova remnants should be detected.

- Ground-based image and optical spectral observations of N300-S16 were compared with an archival Hubble Space Telescope image. The comparison shows conflicting evidence as to the true nature of this object. The [S II]:Hα far exceeds the accepted minimum value and there is a presence of [O I] both of which are accepted indicators of supernova remnants. However, the Hubble Space Telescope image shows no indication of structure in the interstellar matter at N300-S16's location while other supernova remnant sites in the same image show clear interstellar matter structure.

- A demonstrated pointing error in N300-S16's spectral observation (MWF11) raises concern about what was actually measured. The flux density measurement error was at the bottom of the range for this error in the observation set.

- The sulphur/oxygen gradient of NGC 300 has been studied. NGC 300 has a high level of diffuse ionised gas which may be a large contributor to the [S II]:Hα ratio.

- This investigation of supernova remnant candidates in NGC 300 leads to the conclusion that the long accepted [S II]:H$\alpha > 0.4$ as an indication of an object's supernova remnant character may not be as trustworthy as has been accepted. More work needs to be done to verify that [S II]:H$\alpha > 0.4$ is truly a valid criterion for the identification of supernova remnants in all galaxies. What roles does the host galaxy's chemical evolution, metallicity and diffuse ionised gas play in the measurement of the [S II]:Hα of a supernova remnant candidate? This must be investigated by observing as many supernova remnant candidates in as many nearby galaxies as possible – particularly within the Milky Way and the Local Group. There is no convincing evidence that the optical emissions from the objects studied here are those of supernova remnants.

8.2 Overview of Thesis Research Goals

The stated goals of this research project (Section 1.1) have been reached. Four principal sources of error for observations and analysis of extragalactic supernova remnants have been identified:

1. Flux-density measurement errors: Multiple spectra of the same object should be taken to make actual error estimates. This helps to identify "borderline" candidates needing support of other spectral lines, further observation in the same or other frequency regions, or optical imaging to confirm the existence of a supernova remnant.

2. Telescope pointing errors: Improved telescope pointing techniques are needed. Pointing error should be checked for each candidate to ensure the candidate's spectrum has actually been observed. For objects where visual pointing is difficult or questionable, one possible technique is to take spectra for a set of positions near the source so that at least one of the observations from the set is on target. Pointing error is also affected by the seeing conditions.

3. Astrometry: Astrometry should be checked against the most accurate available catalogue (currently 2MASS). Optical astrometry should be demonstrated consistent with seeing conditions. Radio astrometry may be improved by filled-beam observations.

4. Imaging: High-resolution optical imaging may be needed to confirm the existence of some supernova remnant candidates. Some structure consistent with known supernova remnant effects in the interstellar medium should be visible at the candidate's location. The use of space-based or adaptive optics in larger class ground-based telescopes may be needed for such observations.

Chapter 9

Future Work

The smaller-class telescopes used for extragalactic supernova research to date have very served well for the purpose by virtue of the number of these objects found in nearby galaxies – almost 500. But this research field is more than ready to move beyond the limitations of this equipment. Sub-arcsecond resolving power is needed to identify these objects, let alone to further understand the structure and dynamics of these systems.

More observations of supernova remnants and supernova remnant candidates in the Milky Way and other galaxies need to be made in all frequency bands. This work requires the combining of radio, optical and X-ray observations and if possible, infrared. The James Webb Space Telescope (JWST) should be able to observe these objects in infrared – which can only add to our understanding of supernova remnants and their contribution to the distribution of dust within a galaxy. However, supernova remnant research would be a side-bar project for the JWST because it does not fit into one of the four stated principal science programs for the telescope.

Optical imaging and spectral observations should be made with space-based or ground-based telescopes equipped with adaptive optics to increase the resolution of the object images. The Hubble Space Telescope is leaving service soon and so a space-based optical telescope will not be available, leaving only ground-based telescopes for extragalactic supernova remnant studies. With adaptive optics, these telescopes are now exceeding the Hubble Space Telescope in resolving power. For example, the Large Binocular Telescope should have resolving power as much as five times that of the Hubble Space Telescope. These telescopes should easily be able to resolve the detail needed for extra-galactic supernova remnant studies.

Observations of the *structure and dynamics* of extragalactic supernova remnants need to be made with very-high-resolution telescopes so that the spectral criteria can be verified as a reliable method of identifying

extragalactic supernova remnants – particularly in galaxies with high levels of diffuse ionised gas. The higher-resolution is also needed for the spectra so that there is less confusion about which object is being observed with the spectrograph. Section 5.1 of Braun & Walterbos (1993) contains a well considered discussion of the optical supernova remnant survey completeness problem. Shearer et al. (2006) argues for the use of extra-large telescopes for finding extragalactic supernova remnants, even beyond the 30-meter class, to increase survey completeness. Better understanding of supernova remnant evolution can also be gained through such high-resolution observations. Comparison of these observations with observations of Galactic supernova remnants will also increase the validity and reliability of spectral observations.

A general study of the relationship between metallicity and H II, for planetary nebulae and supernova remnant element abundance ratios is needed. Studies of the relationship between a galaxy's sulphur gradient and [S II]:Hα need to be done on multiple spiral type galaxies (both early and late). The relationship between the diffuse ionised gas and the interstellar matter and [S II]:Hα need to be studied for all types of spiral galaxies. But this needs to be done where the supernova remnants have been verified as supernova remnants by means of spectral measurements *and* high resolution imaging.

All of this work requires time on extra-large-class or space-based telescopes where the imaging is of high enough resolution to see structure in the interstellar matter of these distant galaxies and hopefully the structure of the supernova remnant candidate itself. Only when the supernova remnant can be verified by all these techniques can the study of these relationships be trusted. With these relationships known there can be greater assurance of the validity of the identification of extragalactic supernova remnants by spectroscopy alone. Unfortunately these extra-large telescopes are extremely expensive and thus have science missions with goals well beyond the study of extragalactic supernova remnants. It may be some time before these telescopes will be made available to this field of research.

Without the ability to see structure in these distant objects, extragalactic supernova remnant hunters will remain simple census takers.

Appendix A

Multi-Wavelength Astronomy

The central principle of multi-wavelength astronomy is to collect spectral data from multiple bands of the electromagnetic spectrum and then use concurrent analysis of these data to determine the nature of the object creating the emissions. Modern astronomy begins with the introduction of chemical spectroscopy in the 1850's and the introduction of the theory of electromagnetism in the 1860's. Atomic and molecular theory (1920's) described the interactions of light and matter – explaining spectroscopy – and revolutionised the way the universe is studied.

The human eye can detect less than one percent of the entire electromagnetic spectrum. This narrow band is generally called "visible light" but here after the term "optical light" shall be used. Advancements in technology have effectively made the entire electromagnetic spectrum "visible" and thus celestial objects once hidden by interstellar gas and dust are now observable. The dynamic, physical processes occurring inside and around celestial objects create photons over the entire electromagnetic spectrum. To understand these objects and the processes occurring within them and indeed even to correctly identify celestial objects, observations from multiple regions of the electromagnetic spectrum must be analysed. This is the philosophy behind multi-wavelength astronomy – spectroscopy across multiple wavelength regions of the electromagnetic spectrum. Multi-wavelength astronomy is now considered a fundamental observation technique for distinguishing between the many objects in the universe having similar spectroscopic or structural characteristics in the optical.

Multi-wavelength astronomy is the process of gathering and collectively analysing spectra from celestial objects with telescopes specifically built for each region of the electromagnetic spectrum. Because of the atmospheric window this process must include the use of space-based observing platforms and thus, some

level of international collaboration of astronomers. The multi-wavelength observation technique is applicable (and should be applied) to every celestial object. This thesis is concerned with differentiating between hydrogen nebulae (H I and H II regions), supernova remnants and planetary nebulae by using multi-wavelength techniques, particularly to correctly identify one class of objects – supernova remnants.

Generally, data from sky surveys in one or more bands of the electromagnetic spectrum (usually in radio but also in X-ray or optical) are used to select specific objects for further study. A selected object is then observed in as many electromagnetic regions as possible. Observations in infrared, optical, ultraviolet and gamma-ray regions may be needed to resolve specific difficulties in identification or in understanding the physical processes occurring within the object. Based on the analysis of spectra from multiple electromagnetic regions an object may be first identified or have its identity verified. Then the overall characteristics of the object may be determined. With these results further study of an object's structure or characteristics (particularly by imaging in radio or optical at very high resolution) may be warranted.

In the Sculptor Group galaxies NGC 300 and NGC 7793, very little overlap has been found between electromagnetic region emissions from supernova remnants and supernova remnant candidates (Pannuti et al., 2002). This has been interpreted as support for the necessity for multi-wavelength techniques in finding extragalactic supernova remnants.

A.1 Multi-Wavelength Astronomy and the Electromagnetic Spectrum

The electromagnetic spectrum has been divided into regions and bands. Sub-millimeter, microwave and radio are many times grouped together as radio. The regions are shown in Table A.1.

Table A.1: The regions of the electromagnetic spectrum.

Region	**Frequency (Hz)**	**Wavelength (m)**
Gamma-rays (γ-rays)	$> 3 \times 10^{18}$	10^{-10}
X-ray	$(3,000 \rightarrow 30) \times 10^{15}$	$10^{-10} \rightarrow 10^{-8}$
Ultraviolet	$(30,000 \rightarrow 750) \times 10^{12}$	$10^{-8} \rightarrow 4 \times 10^{-7}$
Optical	$(750 \rightarrow 430) \times 10^{12}$	$4 \times 10^{-7} \rightarrow 7 \times 10^{-7}$
Infrared	$(430 \rightarrow 3) \times 10^{12}$	$7 \times 10^{-7} \rightarrow 10^{-4}$
Sub-millimeter	$(3,000 \rightarrow 300) \times 10^{9}$	$10^{-4} \rightarrow 10^{-3}$
Microwave	$(300 \rightarrow 3) \times 10^{9}$	$10^{-3} \rightarrow 10^{-1}$
Radio	$< 3 \times 10^{9}$	$> 10^{-1}$

A.1.1 Units of Measure

Only occasionally is frequency mentioned in connection with spectral measurement. In the lower regions of the electromagnetic spectrum, from radio through optical, wavelengths are generally measured in meters (or micrometres or nanometres). For those regions above the optical, the photonic energy is used to describe the spectral components. This energy is usually expressed in electron volts (eV). One electron volt is the kinetic energy gained by an electron as it moves through a potential of one volt ($1\ \mathrm{eV} = 1.602 \times 10^{-12}$ erg). Also, in the infrared and radio regions, the black body equivalent temperature,

$$T = \frac{2.89 \times 10^{-3}(\text{ m K})}{\lambda} = \frac{2898\ \mu(\text{ m K})}{\lambda} \tag{A.1}$$

is used to describe the energy of the photons.

A.1.2 Regions and Bands of the Electromagnetic Spectrum

The regions of the electromagnetic spectrum are further divided into bands. Tables A.2 through A.11 list the spectral regions and their bands as used in astronomy. In the higher frequency bands (ultraviolet, X-ray and gamma-ray), the borders separating the sub-bands are not well defined. For example, extreme ultraviolet has some overlap with soft X-rays. The main criteria used to distinguish soft and hard X-rays, and soft and hard gamma-rays, and indeed, to distinguish X-rays from gamma-rays, is the method of detection and the source of the radiation.

Table A.2: The gamma-ray region bands.

Frequency (Hz)	**Wavelength (m)**	**Energy (eV)**	**Designation**	**Comments**
$>$ 24 E	$<$ 12 p	$>$ 100 k		All gamma-rays
$>$ 7.3 Z	$<$ 41 f	$>$ 30 M	Hard gamma-rays	Pair production detectors.
7.3 Z – 24 E	41 f – 12 p	30 M – 100 k	Soft gamma-rays	Scintillation detectors.

Table A.3: The X-ray region bands.

Frequency (Hz)	**Wavelength (m)**	**Energy (eV)**	**Designation**	**Comments**
24 E – 30 P	12 p – 12 n	100 – 0.1 k		All X-rays
24 E – 2.4 E	12 p – 0.12 n	100 – 10 k	Hard X-ray	Scintillation detectors.
2.4 E – 30 P	0.12 n – 12 n	10 – 0.1 k	Soft X-ray	Grazing incidence mirrors.

An electromagnetic band between ultraviolet and X-rays (25 Å – 912 Å, 120 PHz – 3.3 PHz, 496 eV – 13.6 eV) is highly absorbed by the interstellar matter and is practically unobservable.

Table A.4: The ultraviolet region bands.

Frequency (Hz)	**Wavelength (nm)**	**Energy (eV)**	**Designation**	**Comments**
300 P – 749 T	1 – 400	1240 – 3.10		All ultraviolet
300 P – 30 P	1 – 10	1240 – 124	EUV, XUV	Extreme ultraviolet
30 P – 3 P	10 – 100	124 – 12.4	FUV, VUV	Far or vacuum ultraviolet
3 P – 1.07 P	100 – 280	12.4 – 4.43	UVC	Near ultraviolet, “germicidal”
1070 T – 952 T	280 – 315	4.43 – 3.94	UVB	Near ultraviolet
952 T – 749 T	315 – 400	3.94 – 3.10	UVA	Near ultraviolet, “black light”

Near ultraviolet is often included as part of the optical band, but it is hindered by poor reflectivity or transmission of optical elements, and atmospheric opacity. The border for vacuum ultraviolet is established by the opacity of air to ultraviolet. Extreme ultraviolet is characterised by a physical transition between photons interacting mainly with the valence electrons and photons interacting mainly with the core electrons and the nucleus of atoms.

Because infrared radiation is associated with heat energy, this spectral region is described both in terms of wavelength and in terms of the equivalent black body temperature T, for that wavelength (eq. A.1).

Table A.5: The optical region: Spectral lines of interest and filter wavelengths used for apparent magnitude measurement.

Frequency (THz)	**Wavelength (nm)**	**Temperature (K)**	**Designation**	**Comments**
749 – 411	400 – 730	7230 – 3960	All optical.	
730.8	410.2	7045	Balmer Series	Hδ
690.6	434.1	6660		Hγ
616.7	486.1	5950		Hβ
456.8	656.3	4400		Hα
UBV(RI) filter system				
817	367	7870	Ultraviolet (U)	BW = 66 nm
688	436	6630	Blue (B)	BW = 94 nm
550	545	5300	Visible (V)	BW = 88 nm
470	638	4530	Red (R)	BW = 138 nm
376	797	3630	Infrared (I)	BW = 149 nm
uvby filter system				
857	350	8260	Ultraviolet	BW = 30 nm
730	411	7030	Visible	BW = 19 nm
642	467	6190	Blue	BW = 18 nm
548	547	5280	Yellow	BW = 23 nm
Johnson-Cousins-Glass filter system				
246	1220	2370	Infrared (J)	BW = 213 nm
184	1630	1770	Infrared (H)	BW = 307 nm
137	2190	1320	Infrared (K)	BW = 390 nm
87	3450	838	Infrared (L)	BW = 472 nm
63	4750	608	Infrared (M)	BW = 460 nm

Table A.6: The infrared region bands.

Frequency (THz)	**Wavelength (μm)**	**Temperature (K)**	**Designation**	**Comments**
411 – 0.86	0.73 – 350			All infrared.
411 – 60	0.73 – 5.0	3950 – 578	Near infrared	Cooler red stars.
				Red giants.
				Dust is transparent.
60 – 10	5.0 – 30	578 – 96	Mid infrared	Planet, comets, asteroids.
				Dust warmed by starlight.
				Protoplanetary disks.
10 – 0.86	30 – 350	96 – 8.3	Far infrared	Emissions from cold dust.
				Central regions of galaxies.
				Cold molecular clouds.

Infrared wavelengths are mostly in micrometres (μm) or "microns." This is generally abbreviated to just μ within context. Short wavelength, near-infrared can be observed with optical telescopes (using appropriate, cooled detectors). Longer wavelengths require more specialised telescope constructions. The following infrared bands are passed through the atmosphere and thus allow ground-based infrared astronomy (on high mountain tops): 1.1 – 1.4 μ, 1.5 – 1.8 μ, 2.0 – 2.4 μ, 3.0 – 4.0 μ, 4.6 – 5.0 μ, 7.5 – 14.5 μ, 17 – 40 μ, 330 – 370 μ. These narrow bands have varying transparency and trouble with sky brightness worsening with longer wavelength.

Table A.7: The submillimeter bands.

Frequency (THz)	**Wavelength (mm)**	**Designation**	**Comments**
3 – 0.3	0.1 – 1	Submillimeter	Detected by radio telescopes.

The designation of wavelength bands in the microwave region has a long and confused history. Here is at least one version assembled from a variety of sources. At the lower end of these bands, there is an overlap with the radio bands.

Table A.8: The general microwave region bands.

Frequency (GHz)	**Wavelength (cm)**	**Designation**	**Comments**
300 – 3	1 – 10		All microwaves.
300 – 30	0.1 – 1	EHF	Extra High Frequency.
30 – 3	1 – 10	SHF	Super High Frequency.
110 – 75	0.27 – 0.4	W	
75 – 40	0.4 – 0.75	V	
40 – 26	0.75 – 1.2	Ka	
26 – 18	1.2 – 1.7	K	
18 – 12	1.7 – 2.5	Ku	
12 – 8	2.5 – 3.75	X	
8 – 4	3.75 – 7.5	C or Q	
4 – 2	7.5 – 15	S	Microwave / Radio
2 – 0.5	15 – 60	L	Microwave / Radio
0.5 – 0.25	60 – 120	P	Microwave / Radio
0.25 – 0.2	120 – 150	G	Microwave / Radio
< 0.2	> 150	I	Microwave / Radio

Table A.9: The microwave bands allocated to astronomy.

Frequency (GHz)	**Wavelength (mm)**	**Designation**	**Comments**
95.00 – 100.0	3.156 – 2.998	W-Band	
92.00 – 94.00	3.259 – 3.189		
86.00 – 92.00	3.486 – 3.259		
72.77 – 72.91	4.120 – 4.112	V-Band	Formaldehyde line
58.20 – 59.00	5.151 – 5.081		
51.40 – 54.25	5.833 – 5.526		
48.94 – 49.04	6.126 – 6.113	C-Band	Carbon monosulphide
42.50 – 43.50	7.054 – 6.892		Silicon monoxide
36.43 – 36.50	8.229 – 8.214	Ka-Band	Hydrogen-cyanide & Hydroxyl
31.20 – 31.80	9.609 – 9.427		
23.60 – 24.00	12.70 – 12.49		Ammonia line
23.07 – 23.12	12.99 – 12.97		
22.86 – 22.91	13.11 – 13.09		Ammonia
22.01 – 22.50	13.62 – 13.32		Water lines
15.35 – 15.40	19.53 – 19.47	Ku-Band	
15.20 – 15.35	19.72 – 19.53		
14.47 – 14.50	20.72 – 20.68		
10.60 – 10.70	28.28 – 28.02	X-band	
6.6500 – 6.6752	45.082 – 44.911	C-Band	
5.0000 – 5.0300	59.959 – 59.601		
4.9900 – 5.0000	60.079 – 59.959		
4.8000 – 4.9900	62.457 – 60.079		
3.3458 – 3.3525	89.603 – 89.424	S-band	
3.3320 – 3.3390	89.974 – 89.785		
3.2600 – 3.2670	91.961 – 91.764		
2.6900 – 2.7000	111.45 – 111.03		
2.6550 – 2.6900	112.92 – 111.45		
1.7188 – 1.7222	174.42 – 174.08	L-Band	
1.6684 – 1.6700	179.69 – 179.52		
1.6605 – 1.6684	180.54 – 179.69		
1.6600 – 1.6605	180.60 – 180.54		
1.400 – 1.427	214.1 – 210.1		21 cm hydrogen line

Table A.10: These are the recognised bands for general radio transmission.

Frequency (Hz)	**Wavelength (m)**	**Designation**	**Comments**
300 M – 3 G	1 – 10 c	UHF	Ultra High Frequency
30 M – 300 M	10 – 1	VHF	Very High Frequency
3 M – 30 M	100 – 10	HF	High Frequency
300 k – 3 M	1 k – 100	MF	Medium Frequency
30 k – 300 k	10 k – 1 k	LF	Low Frequency
3 k – 30 k	100 k – 10 k	VLF	Very Low Frequency
300 – 3 k	1000 k – 100 k	VF	Voice Frequency
30 – 300	10 000 k – 1000 k	ELF	Extra Low Frequency
< 30	$> 10\,000$ k	ULF	Ultra Low Frequency

Table A.11: These radio bands are protected for astronomical observation.

Frequency (MHz)	**Wavelength (m)**	**Designation**	**Comments**
608.0 – 614.0	0.493 – 0.488		
406.1 – 410.0	0.738 – 0.731		Pulsar observations
322.0 – 328.6	0.931 – 0.912	UHF	
150.05 – 153.00	1.998 – 1.959		Pulsar observations
			Solar observations
73.00 – 74.60	4.11 – 4.02		Solar wind observations
37.50 – 38.25	7.99 – 7.84	VHF	
25.55 – 25.67	11.73 – 11.68		
13.36 – 13.41	22.44 – 22.35	HF	

Appendix B

Other Known Objects in NGC 300

This chapter is an overview of some general observations of NGC 300 to note other observational factors or effects that can affect the results of supernova remnant surveys and observations. The observations of NGC 300 concerned with objects other than supernova remnants are of interest because those objects can be confused with supernova remnant candidates. These observations provide the identification and location of both known and candidate H I and H II regions, planetary nebulae, Wolf-Rayet stars and star clusters. They also provide information about NGC 300's diffuse ionised gas and interstellar matter.

A study of radio continuum emission at 843 MHz was made by Harnett (1986) and NGC 300 was not detected. Only an upper limit to the emission at this frequency (< 2 mJy beam^{-1}) could be determined. This was taken as evidence that radio emissions from this galaxy may be fairly weak.

Optical photographs (Figure 5.1) show that NGC 300 is a flocculent galaxy with a thick disk structure making the spiral arm structure less discernible than in grand design galaxies. With a greater abundance of interstellar matter material there may be greater metallic background-emissions from the interstellar matter and diffuse ionised gas for this galaxy compared to other galaxies. A survey of the history of observations of NGC 300 should discern how the metallicity and composition of the interstellar matter and diffuse ionised gas may affect identification and observation of supernova remnants.

B.1 Hydrogen Nebulae

Figure B.1 shows an ESO photograph of NGC 300 in Hα wavelength. Hydrogen nebulae (H I and H II regions) have been studied and mapped by PF04, Sérsic (1966); Pagel et al. (1979); Deharveng et al. (1988); Puche et al.

(1990); Hoopes et al. (1996); Soffner et al. (1996); Payne et al. (2005); Bresolin et al. (2009) with Deharveng et al. (1988) listing over 170 identified H II regions. The known hydrogen regions of NGC 300 are contained in the SIMBAD[1] object database. The distribution of H I and H II regions within NGC 300 has implications on an expected global distribution of supernova remnants. Because core-collapse supernovae are generally associated with H II regions supernova remnants should be found within or near their locations.

The first observations of H I in NCG 300 were performed by Seielstad & Whiteoak (1965) to study the rotation curve and derive a mass for the galaxy. Further H I (21-cm) observations were made by Shobbrook & Robinson (1967). These observations showed the existence of a large H I cloud possibly associated with NGC 300, located to the south-east of the galaxy and a minimum in emissions around the centre of the galaxy. By observing differences in H I emission intensity and optical luminosity between the east and west side of the galaxy this paper concluded that the centre of mass of the galaxy is essentially the same as the optical centre of the galaxy. Mathewson et al. (1975) later showed the large H I cloud to the south-east is actually associated with the Magellanic Stream and not with NGC 300. An "H I tail" was also found from NGC 300 off to the south-east. Rogstad et al. (1979) found no apparent connection between NGC 300 and this H I tail. However, a mapping of the H I distribution within NGC 300 showed the disk as being warped (see that paper's Figure 6). Whiteoak & Gardner (1977) made higher resolution (H I velocity) observations of NGC 300 and suggested there may be greater detail to be learned about the central regions of NGC 300. Observations by Arp (1985) and Puche et al. (1990) leave the connection between the galaxy and the H I tail to the south-east still unsettled, however the warped shape of the galaxy's disk was further supported.

H II regions were first observed by Sérsic (1966). Eighty-five H II regions were discovered asymmetrically distributed with emissions from the north-side farther from the nucleus. Pagel et al. (1979) used spectroscopic observations of H II regions in NGC 300 to estimate the abundance gradient (in oxygen) of the disk. A gradient similar to M 33 and M 101 was found, with no gradient in nitrogen/oxygen. The abundance of neon, sulphur and argon (Ar) relative to oxygen are close to those of Orion and the Magellanic clouds. Edmunds & Pagel (1984) shows further data on NGC 300 and also some plots of the abundance gradient for this and other galaxies.

[1] http://simbad.u-strasbg.fr/simbad/

Figure B.1: A version of Figure 5.1 (left) is shown with the Hα image (right) with the same size and plate scale. Much of the diffuse light from the galaxy is from ionised hydrogen recombination. The composite photograph of NGC 300 in Hα light by the European Southern Observatory also shows a close association between H II regions and OB associations. This indicates a high star production rate for the past 100 million years with a correlated increased possibility of core collapse supernovae and supernova remnants near these regions. (Photos from the European Space Agency.)

B.2 Planetary Nebulae

Planetary nebulae are important in creating and sustaining the chemical evolution of galaxies, contributing about half of the overall enrichment of the interstellar matter (Aller, 1991). They are the product of the end stage of lower-mass, red giant stars where nuclear reactions create high levels of helium, nitrogen, oxygen and carbon (Millar et al., 2008). They are a greater contributor to the interstellar matter's nitrogen/oxygen abundance than supernova remnants (Torres-Peimbert & Peimbert, 1971). Young supernova remnants and planetary nebulae have a similar optical appearance.

Supernova remnants are differentiated from planetary nebulae by using abundance (line flux) ratios. Generally (see, Reid & Parker, 2006; Payne et al., 2008b), planetary nebulae spectra have an [O III] λ 5007 Å : [O III] λ 4959 Å : Hβ intensity ratio of about 9:3:1. If the intensity of [N II] λ 6583 Å is greater than Hα, then a strong [O III] line with the high excitation of helium λ 4686 Å has been detected, which is rarely seen in H II regions. More importantly, [S II] $\lambda\lambda$ 6717, 6731 Å are usually present in planetary nebulae but are not significant when compared to Hα. This last characteristic is a first step in differentiating planetary nebulae from supernova remnants. These [S II] lines are prominent in supernova remnants. The argument for using line ratios to differentiate planetary nebulae and supernova remnants is based on observations of these object types within the Galaxy, where they can be identified visually.

A study of planetary nebulae in NGC 300 was performed by Soffner et al. (1996, 2003). These papers list 34 known planetary nebulae in NGC 300 (Soffner et al., 1996, as Table 2,) and as an on-line catalogue (Soffner et al., 2003). Peña (2011) performed an optical search for planetary nebulae in NGC 300, finding 69 in the central region and 30 in the outer. All but six (the lowest magnitude) of Soffner et al.'s planetary nebulae where found in this search. None of these planetary nebulae have position in agreement with the supernova remnant candidates studied in this thesis (Chapter 6). Preliminary results from Peña (2010) of the chemical abundance in NGC 300 planetary nebulae suggest these planetary nebulae have a similar composition and abundance gradient to the NGC 300 H II regions. This suggests a better understanding of the metallicity of NGC 300 may be needed in order to rely on abundance ratios for determining the character of the objects observed. Multi-wavelength observations should be a minimum requirement for proper identification of any object.

B.3 Stars and Star Clusters

Wolf-Rayet stars are the probable progenitors of Type Ib/c supernovae (see page 12). The ratios of Wolf-Rayet star subtypes (WC and WN)[2] are strongly linked to a galaxy's Z (see Maeder, 1991, and references therein). Essentially, the Z (of an enclosing H II region) changes the opacity of the Wolf-Rayet star's circumstellar matter and thus the rate of mass loss. This leads to differences in the subtypes of Wolf-Rayet stars observed in galaxies and thus an indication of the galaxy's Z. The WR/WO, WC/WR and WC/WN ratios increase as the Z increases (See Figures 6 and 7 of Maeder, 1991). While this link has been clearly demonstrated there may also be other factors involved in the determining the ratios (such as small influences from the stellar initial mass function and possible larger influences from rapid stellar rotation, Arnault et al., 1989).

D'Odorico et al. (1983) studied the giant H II regions of NGC 300 for enclosed Wolf-Rayet stars. Two H II regions were found with strong indications of the presence of WC and WN type stars with two other regions showing a possibility of containing a WC star. Schild & Testor (1991) discusses three Wolf-Rayet stars and Schild & Testor (1992) is a study of ten (including the previous three and those found by D'Odorico et al.) Wolf-Rayet stars in NGC 300. Breysacher et al. (1997) detected Wolf-Rayet stars in five star associations in NGC 300. Schild et al. (2003b) increased the list to 60 Wolf-Rayet stars by using the Very Large Telescope. Based on these observations and the observations of red giant and asymptotic giant branch stars (Butler et al., 2004) the Z of NGC 300 is between that of the Milky Way and the Large Magellanic Cloud. In the central regions of NGC 300 the metallicity is about solar ($Z_\odot = 0.02$) but in the disk outskirts it drops to roughly 0.3 $Z_\odot$ with a logarithmic gradient of -0.08 dex kpc^{-1} (Kudritzki et al., 2008).

Nantais et al. (2010) measures the Z of the known globular clusters (GCs) of NGC 300 and finds a value equivalent to the GCs of the Milky Way. This paper is also useful for inspecting the possibility that the supernova remnant candidates studied in this thesis (Table 5.7) are contained in a GC rather than in the disk of the galaxy. It also indicates known or possible background galaxies (Table 1 of that paper) which can also be compared to the source list here. No candidate was found within $1''$ of any object in that table. This indicates that each candidate should be part of the disk of NGC 300 or perhaps (in the case of the radio sources) an unknown background source.

[2] Wolf-Rayet stars are divided into three subtypes based on their spectra. WN stars (nitrogen dominant, some carbon), WC stars (carbon dominant, no nitrogen) and the rare WO stars with $C : O < 1$.

B.4 NGC 300's Interstellar Matter and Diffuse Ionised Gas

As can be seen in Figure B.1 many bubble-like structures are visible in the Hα emissions of NGC 300. Some of the giant Hα shells illuminated by ionising star clusters and seen at many locations in the disk may have been created by supernovae (Roussel et al., 2005).

About 50% of the total Hα emission comes from the diffuse ionised gas (Hoopes et al., 1996). A high level of diffuse ionised gas is found in many spiral galaxies (and may be typical for spiral galaxies) and is interpreted to imply a high rate of star formation. This should produce a higher supernovae and supernova remnant count (Pannuti et al., 2002). Just how the interstellar matter and diffuse ionised gas composition may affect supernova remnant line ratios is still unclear.

Appendix C

HST File Search Data and Results

This appendix contains tables used in the discussions of Chapter 7. Table C.1 shows the file names associated with the central wavelengths sorted by wavelength along with the original proposal identification and any publications based on the data. In this table, column 1 is the central wavelength of the Hubble Space Telescope filter, column 2 is the file name (all with `.FITS` extension) containing the image, column 3 is a list of publications associated with the observation. The references are included to provide the original objectives of the observations of NGC 300 at these wavelengths and other publications which have used these observations (all publication data is from the MAST web site).

Table C.1: Archival Hubble Space Telescope files organised by filter centre wavelength. The Hubble Space Telescope proposal abstracts are reprinted in Appendix D.

1	**2**	**3**	**4**
Wavelength (Å)	**Files**	**Proposal ID**	**Associated Publications**
2993	u8hhvp02m_drz	9677	Wadadekar et al. (2006).
4318	j8d702010_drz	9492	Gliozzi et al. (2009); Gogarten et al. (2009a);
	j8d702mcq_flt		Nantais et al. (2010); Gogarten et al. (2010);
	j8d702mjq_flt		Gieren et al. (2004); Bresolin et al. (2005a);
	j8d702mrq_flt		Rizzi et al. (2007); Kudritzki et al. (2008);
	j8d703010_drz		Bond et al. (2009); Barth et al. (2009);
	j8d703viq_flt		Dalcanton et al. (2009); Rizzi et al. (2006);
	j8d703vpq_flt		Tikhonov et al. (2005);
	j8d703vxq_flt		Kuntz & Snowden (2010).
4747	j9ra11010_drz	10915	Berger et al. (2009); Gogarten et al. (2009b);
	j9ra11neq_flt		Holwerda et al. (2009); Lianou et al. (2009);
	j9ra11nfq_flt		Nantais et al. (2010); Williams et al. (2010);
			Melbourne et al. (2010); Gogarten et al. (2010);
			de Mello et al. (2008); Girardi et al. (2008);
			Mould & Sakai (2008); Bond et al. (2009);
			Williams et al. (2009a); Kornei & McCrady (2009);
			Williams et al. (2009b).
5360	j8d702020_drz	9492	See $\lambda = 4318$ Å.
	j8d702mdq_flt		
	j8d702mlq_flt		
	j8d702mtq_flt		
	j8d703020_drz		
	j8d703vjq_flt		
	j8d703vrq_flt		

Continued...

Table C.1, continued.

1	2	3	4
Wavelength (Å)	**Files**	**Proposal ID**	**Associated Publications**
	j8d703vzq_flt		
5484	u6713701m_drz	8591	Graham et al. (2001); Schinnerer et al. (2003);
	u6713702r_drz		Larsen (2004); Lauer et al. (2005);
	u6713703r_drz		Rosolowsky & Blitz (2005); Lauer et al. (2007a);
	u6713704r_drz		Lauer et al. (2007b); González Delgado et al. (2008);
			Dai & Wang (2008); Siopis et al. (2009);
			Beifiori et al. (2009).
5741	o6j3bzkyq_flt	9285	Shaw et al. (2006).
5921	j9ra11020_drz	10915	See $\lambda = 4747$ Å.
	j9ra11nhq_flt		
	j9ra11njq_flt		
6001	u8hhvp01m_drz	9677	Wadadekar et al. (2006).
6001	u8ixhd01m_drz	9676	Tikhonov & Galazutdinova (2009); Van Dyk et al. (2003);
	u8ixhd02m_drz		Larsen (2004); Smartt et al. (2004);
			Tikhonov & Galazutdinova (2005); Sugerman (2005);
			Milone et al. (2006); Wadadekar et al. (2006);
			Sugerman et al. (2006); Shaw et al. (2007);
			Maund & Smartt (2009); Guerrero & Chu (2008).
6564 (Hα)	u6713705r_drz	8591	See $\lambda = 5484$ Å.
	u6713706r_drz		
	u6713707r_drz		
	u6713708r_drz		
	u6713709r_drz		
7996	u65w0201r_drz	8599	Windhorst et al. (2002); Böker et al. (2003a);
	u65w0202r_drz		Larsen (2004); Butler et al. (2004);

Continued...

Table C.1, continued.

1	2	3	4
Wavelength (Å)	**Files**	**Proposal ID**	**Associated Publications**
	u65w0203r_drz		Walcher et al. (2005); de Grijs et al. (2005); Tully et al. (2006); Rossa et al. (2006); Schinnerer et al. (2006); Peeples & Martini (2006); Ganda et al. (2006); Cao & Wu (2007); Seth et al. (2008); Böker et al. (2003b); González Delgado et al. (2008); Ghosh et al. (2009); Böker et al. (2004); Andersen et al. (2008); Böker et al. (2002).
8057	j9ra11030_drz	10915	See $\lambda = 4747$ Å.
	j9ra11nlq_flt		
	j9ra11nnq_flt		
8060	j8d702030_drz	9492	See $\lambda = 4318$ Å.
	j8d702mfq_flt		
	j8d702moq_flt		
	j8d702mvq_flt		
	j8d702n0q_drz		
	j8d702n0q_flt		
	j8d703030_drz		
	j8d703vlq_flt		
	j8d703vuq_flt		
	j8d703w1q_flt		
	j8d703w6q_drz		
	j8d703w6q_flt		

Table C.2 shows the bandwidths for each of the Hubble Space Telescope filters used for these images. These data were taken from the images' FITS file header[1]. Column 1 is the filter central wavelength and column 2 is the filter bandwidth. This table also shows the atoms/ions and associated wavelengths that are found within the bandwidth of the filters (column 3). These ions are known to be within (Galactic) supernova remnants (Fesen & Hurford, 1996).

[1]They are also available on the Hubble Space Telescope WFPC2 instrument website. http://www.stsci.edu/hst/wfpc2/documents/IHB_17.html

Table C.2: Central Wavelengths of Hubble Space Telescope Image File Sequences.

1	**2**	**3**
Filter Centre	**Filter RMS**	**Known SNR Atoms/Ions with Wavelengths**
Wavelength (Å)	**Bandwidth (Å)**	**(Å, Fesen & Hurford, 1996)**
2993	325	Mg I: 2852.13
4318	293	H I: 4340.49 (Hγ)
		C II: 4267.00, 4267.26
		[O III]: 4363.21
		[Fe II]: 4177.21, 4243.98,
		4244.81, 4287.40, 4358.10, 4358.37, 4359.34,
		4413.78, 4414.45, 4416.27, 4452.11, 4457.95
		[Fe V]: 4227.20
4747	420	H I: 4861.36 (Hβ)
		He I: 4713.14, 4713.37, 4921.93
		He II: 4685.68
		[Ne IV]: 4724.17, 4725.60
		Mg I: 4571.10
		[Mg I]: 4562.48
		[Ar IV]: 4711.33, 4740.20
		[Fe II]: 4632.27, 4774.74, 4814.55,
		4889.63, 4889.70, 4905.35
		[Fe III]: 4658.10, 4701.62, 4733.93,
		4754.83, 4769.60, 4777.88, 4813.90, 4881.11,
		4924.50, 4930.50
		[Fe VII]: 4893.40, 4942.50
5360	360	He II: 5411.52
		[N I]: 5197.90, 5200.26

[a]Unable to find these wavelengths for H I in NIST database.

Continued...

Table C.2, continued.

1	2	3
Filter Centre Wavelength (Å)	**Filter RMS Bandwidth (Å)**	**Known SNR Atoms/Ions with Wavelengths (Å, Fesen & Hurford, 1996)**
		[Cl III]: 5517.71
		[Ar III]: 5191.82
		[Ca V]: 5309.18
		[Fe II]: 5184.80, 5220.06, 5261.61,
		5268.88, 5273.38, 5296.84, 5333.65, 5376.47,
		5412.64, 5413.34, 5527.33
		[Fe III]: 5270.30
		[Fe VI]: 5277.80, 5335.20, 5424.20, 5426.60, 5484.80
		[Fe XIV]: 5302.86
5484	206	He II: 5411.52
		[O I]: 5577.34
		[Cl III]: 5517.71
		[Fe II]: 5412.64, 5413.34, 5527.33
		[Fe VI]: 5424.20, 5426.60, 5484.80
5741	1836	H I: 4861.36 (Hβ), 6562.85 (Hα)
		He I: 4921.93, 5015.68, (5876)
		He II: 5411.52
		[N I]: 5197.90, 5200.26
		[N II]: 5754.59, 6548.05, 6583.45
		[O I]: 5577.34, 6300.30, 6363.78
		[O III]: 4958.91, 5006.84
		Na I: 5889.95, 5895.92
		[S III]: 6312.06

[a]Unable to find these wavelengths for H I in NIST database.

Continued...

Table C.2, continued.

1	2	3
Filter Centre	**Filter RMS**	**Known SNR Atoms/Ions with Wavelengths**
Wavelength (Å)	**Bandwidth (Å)**	**(Å, Fesen & Hurford, 1996)**
		[Cl III]: 5517.71
		[Ar III]: 5191.82
		[Ar V]: 6435.10
		[Ca V]: 5309.18
		[Fe II]: 4889.63, 4889.70, 4905.35,
		4973.39, 5039.10, 5043.53, 5072.40, 5107.95,
		5111.63, 5158.00, 5158.81, 5184.80, 5220.06,
		5261.61, 5268.88, 5273.38, 5296.84, 5333.65,
		5376.47, 5412.64, 5413.34, 5527.33
		[Fe III]: 4881.11, 4924.50, 4930.50,
		4985.90, 4987.20, 5270.30
		[Fe VI]: 4972.50, 5145.80, 5176.00,
		5277.80, 5335.20, 5424.20, 5426.60, 5484.80,
		5631.10, 5677.00
		[Fe VII]: 4893.40, 4942.50, 5158.90, 5720.70, 6087.00
		[Fe X]: 6374.51
		[Fe XIV]: 5302.86
5921	672	He I: (5876)
		[N II]: 5754.59
		Na I: 5889.95, 5895.92
		[Fe VI]: 5631.10, 5677.00
		[Fe VII]: 5720.70, 6087.00
6001	638	He I: (5876)

[a]Unable to find these wavelengths for H I in NIST database.

Continued...

Table C.2, continued.

1	**2**	**3**
Filter Centre	**Filter RMS**	**Known SNR Atoms/Ions with Wavelengths**
Wavelength (Å)	**Bandwidth (Å)**	**(Å, Fesen & Hurford, 1996)**
		[N II]: 5754.59
		[O I]: 6300.30
		Na I: 5889.95, 5895.92
		[S III]: 6312.06
		[Fe VII]: 5720.70, 6087.00
6564	54	H I: 6562.85 (Hα)
		[N II]: 6548.05, 6583.45
7996	646	He II: 8236.77
		O I: (7774)
		[Ar III]: 7751.06
		[Cr II]: 7999.85, 8125.22, 8229.55, 8308.39
		[Fe II]: 7686.19, 7686.90
		[Fe XI]: 7891.80
		[Ni II]: 8300.99
8057	652	H I: 8345.55, 8359.00, 8374.48[a]
		He II: 8236.77
		O I: (7774)
		[Ar III]: 7751.06
		[Cr II]: 7999.85, 8125.22, 8229.55, 8308.39, 8357.51
		[Fe XI]: 7891.80
		[Ni II]: 8300.99
8060	653	H I: 8345.55, 8359.00, 8374.48[a]
		He II: 8236.77

[a]Unable to find these wavelengths for H I in NIST database.

Continued...

Table C.2, continued.

1	**2**	**3**
Filter Centre	**Filter RMS**	**Known SNR Atoms/Ions with Wavelengths**
Wavelength (Å)	**Bandwidth (Å)**	**(Å, Fesen & Hurford, 1996)**
		O I: (7774)
		[Ar III]: 7751.06
		[Cr II]: 7999.85, 8125.22, 8229.55, 8308.39, 8357.51
		[Fe XI]: 7891.80
		[Ni II]: 8300.99

[a]Unable to find these wavelengths for H I in NIST database.

Table C.3 groups the files by candidates within the field of view of the Hubble Space Telescope image file. The object locations were found by calculating the x and y pixel coordinates from the α and δ of each candidate, using the FITS file WCS data within the fits file header. The candidate groups are based on candidates found in multiple files. Column 1 is the candidate group, column 2 is the candidates in the group and column 3 is the files containing the candidates. Candidate group A is the list of files containing none of the objects of interest. Candidate group C is a subset of group B. These two groups are listed in the table and then dropped from further use because their objects are also found in various other groups.

Table C.3: Files grouped by candidates within their field of view. The wavelength (Å) of the filter used for the file is shown in parentheses after the file name.

1	**2**	**3**
Candidate Group	**Candidates**	**File Names**
A	None	o6j3bzkyq_flt.fits (5741)
B	J005438–374144, J005440–374049, J005445–373847, J005450–374030, J005450–374022, J005451–373939, N300-S8, N300-S9, N300-S10, N300-S13, N300-S14, N300-S16	j9ra11010_drz.fits (4747), j9ra11020_drz.fits (5921), j9ra11030_drz.fits (8057)
C	J005440–374049, N300-S8, N300-S9, N300-S10, N300-S14	j9ra11neq_flt.fits (4747), j9ra11nfq_flt.fits (4747), j9ra11nhq_flt.fits (5921), j9ra11njq_flt.fits (5921), j9ra11nlq_flt.fits (8057), j9ra11nnq_flt.fits (8057)
D	J005445–373847, J005450–374030, J005450–373822, J005450–374022, J005451–373826, J005451–373939, J005500–374037, J005501–373829, N300-S13, N300-S15, N300-S16, N300-S18	j8d702010_drz.fits (4318), j8d702020_drz.fits (5360), j8d702030_drz.fits (8060), j8d702n0q_drz.fits (8060)
E	J005445–373847, N300-S13	u8hhvp02m_drz.fits (2993), u8hhvp01m_drz.fits (6001), u8ixhd01m_drz.fits (6001), u8ixhd02m_drz.fits (6001)

Continued

Table C.3 continued.

Candidate Group	Candidates	File Names
F	J005450–374030,	u6713701m_drz.fits (5484),
	J005450–374022,	u6713702r_drz.fits (5484),
	J005451–373939,	u6713703r_drz.fits (5484),
	J005500–374037,	u6713704r_drz.fits (5484),
	N300-S16	u6713705r_drz.fits (6564),
		u6713706r_drz.fits (6564),
		u6713707r_drz.fits (6564),
		u6713708r_drz.fits (6564),
		u6713709r_drz.fits (6564),
		u65w0201r_drz.fits (7996),
		u65w0202r_drz.fits (7996),
		u65w0203r_drz.fits (7996)
G	J005450–374030, J005450–374022,	j8d703010_drz.fits (4318),
	J005500–374037, J005503–374246,	j8d703020_drz.fits (5360),
	J005503–374320,	j8d703030_drz.fits (8060),
	N300-S14, N300-S16	j8d703w6q_drz.fits (8060)
H	J005500–374037,	j8d702mcq_flt.fits (4318),
	J005501–373829,	j8d702mdq_flt.fits (5360),
	N300-S15,	j8d702mfq_flt.fits (8060)
	N300-S16	
I	J005501–373829,	j8d702mjq_flt.fits (4318),
	N300-S15,	j8d702mrq_flt.fits (4318),
	N300-S16,	j8d702mlq_flt.fits (5360),
	N300-S18	j8d702mtq_flt.fits (5360),
		j8d702moq_flt.fits (8060),
		j8d702mvq_flt.fits (8060),
		j8d702n0q_flt.fits (8060)

Continued

Table C.3 continued.

Candidate Group	**Candidates**	**File Names**
J	J005503–374246,	j8d703viq_flt.fits (4318),
	J005503–374320	j8d703vpq_flt.fits (4318),
		j8d703vxq_flt.fits (4318),
		j8d703vjq_flt.fits (5360),
		j8d703vrq_flt.fits (5360),
		j8d703vzq_flt.fits (5360),
		j8d703vlq_flt.fits (8060),
		j8d703vuq_flt.fits (8060),
		j8d703w1q_flt.fits (8060),
		j8d703w6q_flt.fits (8060)

Table C.4 now lists the objects from Table 5.7 which are available in any Hubble Space Telescope image. Table C.4 is both a rearrangement and a reduction of Table C.3. Objects which are located off the actual image contained in the file (only the low resolution CCD chips contained useful image data) and files which contain the same objects at the same wavelength have been reduced by subjective selection of image quality. A few objects were entirely lost because they were just off the edge of any image. Table C.4 represents the smallest set of Hubble Space Telescope archival NGC 300 data which must be analysed. Column 1 is the object designation as given in BL97 or PF04. Column 2 is the Hubble Space Telescope file in which the candidate was found. Column 3 is the central wavelength of the observation. Columns 4 and 5 are the central pixel location of the image of the object in the file.

Table C.4: List of objects of interest from Table 5.7 which are found in the Hubble Space Telescope files.

1	2	3	4	5
Object	**File Name**	**Wavelength (Å)**	**X Pixel**	**Y Pixel**
J005438–374144	j9ra11010_drz.fits	4747	3604	71
	j9ra11020_drz.fits	5921	3604	71
	j9ra11030_drz.fits	8060	3604	71
J005440–374049	j9ra11010_drz.fits	4747	3631	1314
	j9ra11neq_flt.fits	4747	3624	1141
	j9ra11nfq_flt.fits	4747	3629	1200
	j9ra11020_drz.fits	5921	3631	1314
	j9ra11nhq_flt.fits	5921	3629	1200
	j9ra11njq_flt.fits	5921	3624	1141
	j9ra11030_drz.fits	8060	3631	1314
	j9ra11nlq_flt.fits	8060	3624	1141
	j9ra11nnq_flt.fits	8060	3629	1200
J005445–373847	u8hhvp02m_drz.fits	2993	850	1132
	j8d702010_drz.fits	4318	1979	3946
	j9ra11010_drz.fits	4747	3889	3997
	j8d702020_drz.fits	5360	1979	3945
	j9ra11020_drz.fits	5921	3889	3997
	u8hhvp01m_drz.fits	6001	838	1123
	u8ixhd01m_drz.fits	6001	826	1114
	u8ixhd02m_drz.fits	6001	826	1114
	j8d702030_drz.fits	8060	1979	3945
	j8d702n0q_drz.fits	8060	1976	3916
	j9ra11030_drz.fits	8060	3889	3997
J005450–374030	j8d702010_drz.fits	4318	3995	2713
	j8d703010_drz.fits	4318	3071	4117

Continued

Table C.4 continued.

Object	File Name	Wavelength (Å)	X Pixel	Y Pixel
	j9ra11010_drz.fits	4747	1854	2795
	j8d702020_drz.fits	5360	3995	2712
	j8d703020_drz.fits	5360	3071	4117
	u6713701m_drz.fits	5484	527	1195
	u6713702r_drz.fits	5484	527	1195
	u6713703r_drz.fits	5484	527	1196
	u6713704r_drz.fits	5484	527	1196
	j9ra11020_drz.fits	5921	1854	2795
	u6713705r_drz.fits	6564	527	1196
	u6713706r_drz.fits	6564	527	1196
	u6713707r_drz.fits	6564	527	1196
	u6713708r_drz.fits	6564	527	1196
	u6713709r_drz.fits	6564	527	1196
	u65w0201r_drz.fits	7996	566	1230
	u65w0202r_drz.fits	7996	566	1230
	u65w0203r_drz.fits	7996	566	1230
	j8d702030_drz.fits	8060	3995	2713
	j8d702n0q_drz.fits	8060	3992	2684
	j8d703030_drz.fits	8060	3071	4117
	j8d703w6q_drz.fits	8060	3067	4088
	j9ra11030_drz.fits	8060	1854	2795
J005450–373822	j8d702010_drz.fits	4318	1445	2797
	j8d702020_drz.fits	5360	1445	2797
	j8d702030_drz.fits	8060	1444	2797
	j8d702n0q_drz.fits	8060	1441	2768
J005450–374022	j8d702010_drz.fits	4318	3836	2612

Continued

Table C.4 continued.

Object	File Name	Wavelength (Å)	X Pixel	Y Pixel
	j8d703010_drz.fits	4318	2943	4256
	j9ra11010_drz.fits	4747	1839	2983
	j8d702020_drz.fits	5360	3836	2611
	j8d703020_drz.fits	5360	2943	4257
	u6713701m_drz.fits	5484	464	1125
	u6713702r_drz.fits	5484	465	1125
	u6713703r_drz.fits	5484	465	1125
	u6713704r_drz.fits	5484	464	1125
	j9ra11020_drz.fits	5921	1839	2984
	u6713705r_drz.fits	6564	464	1125
	u6713706r_drz.fits	6564	464	1125
	u6713707r_drz.fits	6564	465	1125
	u6713708r_drz.fits	6564	465	1125
	u6713709r_drz.fits	6564	464	1125
	u65w0201r_drz.fits	7996	501	1162
	u65w0202r_drz.fits	7996	501	1162
	u65w0203r_drz.fits	7996	501	1162
	j8d702030_drz.fits	8060	3835	2611
	j8d702n0q_drz.fits	8060	3832	2582
	j8d703030_drz.fits	8060	2943	4256
	j8d703w6q_drz.fits	8060	2940	4228
	j9ra11030_drz.fits	8060	1839	2984
J005451–373826	j8d702010_drz.fits	4318	1512	2591
	j8d702020_drz.fits	5360	1512	2590
	j8d702030_drz.fits	8060	1511	2590
	j8d702n0q_drz.fits	8060	1508	2561

Continued

Table C.4 continued.

Object	File Name	Wavelength (Å)	X Pixel	Y Pixel
J005451–373939	j8d702010_drz.fits	4318	2975	2390
	j9ra11010_drz.fits	4747	2047	3847
	j8d702020_drz.fits	5360	2976	2389
	u6713701m_drz.fits	5484	82	898
	u6713702r_drz.fits	5484	83	898
	u6713703r_drz.fits	5484	83	898
	u6713704r_drz.fits	5484	82	898
	j9ra11020_drz.fits	5921	2047	3847
	u6713705r_drz.fits	6564	82	898
	u6713706r_drz.fits	6564	82	898
	u6713707r_drz.fits	6564	83	898
	u6713708r_drz.fits	6564	83	898
	u6713709r_drz.fits	6564	82	898
	u65w0201r_drz.fits	7996	110	951
	u65w0202r_drz.fits	7996	110	951
	u65w0203r_drz.fits	7996	110	951
	j8d702030_drz.fits	8060	2975	2389
	j8d702n0q_drz.fits	8060	2972	2360
	j9ra11030_drz.fits	8060	2047	3847
J005500–374037	j8d702010_drz.fits	4318	4058	264
	j8d702mcq_flt.fits	4318	4094	90
	j8d703010_drz.fits	4318	669	3630
	j8d702020_drz.fits	5360	4058	263
	j8d702mdq_flt.fits	5360	4094	90
	j8d703020_drz.fits	5360	669	3630
	u6713701m_drz.fits	5484	899	28

Continued

Table C.4 continued.

Object	File Name	Wavelength (Å)	X Pixel	Y Pixel
	u6713702r_drz.fits	5484	900	28
	u6713703r_drz.fits	5484	900	29
	u6713704r_drz.fits	5484	899	29
	u6713705r_drz.fits	6564	899	29
	u6713706r_drz.fits	6564	899	29
	u6713707r_drz.fits	6564	900	29
	u6713708r_drz.fits	6564	900	29
	u6713709r_drz.fits	6564	899	29
	u65w0201r_drz.fits	7996	890	49
	u65w0202r_drz.fits	7996	890	49
	u65w0203r_drz.fits	7996	890	49
	j8d702030_drz.fits	8060	4057	263
	j8d702mfq_flt.fits	8060	4094	90
	j8d702n0q_drz.fits	8060	4054	234
	j8d703030_drz.fits	8060	669	3630
	j8d703w6q_drz.fits	8060	666	3601
J005501–373829	j8d702010_drz.fits	4318	1502	136
	j8d702mcq_flt.fits	4318	1532	34
	j8d702mjq_flt.fits	4318	1534	63
	j8d702mrq_flt.fits	4318	1537	93
	j8d702020_drz.fits	5360	1502	135
	j8d702mdq_flt.fits	5360	1532	34
	j8d702mlq_flt.fits	5360	1534	63
	j8d702mtq_flt.fits	5360	1537	93
	j8d702030_drz.fits	8060	1502	135
	j8d702mfq_flt.fits	8060	1532	33

Continued

Table C.4 continued.

Object	File Name	Wavelength (Å)	X Pixel	Y Pixel
	j8d702moq_flt.fits	8060	1534	63
	j8d702mvq_flt.fits	8060	1537	93
	j8d702n0q_drz.fits	8060	1499	106
	j8d702n0q_flt.fits	8060	1534	63
J005503–374246	j8d703010_drz.fits	4318	342	987
	j8d703viq_flt.fits	4318	331	913
	j8d703vpq_flt.fits	4318	334	943
	j8d703vxq_flt.fits	4318	336	973
	j8d703020_drz.fits	5360	342	987
	j8d703vjq_flt.fits	5360	331	913
	j8d703vrq_flt.fits	5360	333	943
	j8d703vzq_flt.fits	5360	336	973
	j8d703030_drz.fits	8060	342	986
	j8d703vlq_flt.fits	8060	331	913
	j8d703vuq_flt.fits	8060	333	943
	j8d703w1q_flt.fits	8060	336	973
	j8d703w6q_drz.fits	8060	338	958
	j8d703w6q_flt.fits	8060	333	943
J005503–374320	j8d703010_drz.fits	4318	399	306
	j8d703viq_flt.fits	4318	417	234
	j8d703vpq_flt.fits	4318	419	264
	j8d703vxq_flt.fits	4318	422	293
	j8d703020_drz.fits	5360	399	306
	j8d703vjq_flt.fits	5360	417	234
	j8d703vrq_flt.fits	5360	419	264
	j8d703vzq_flt.fits	5360	422	293

Continued

Table C.4 continued.

Object	File Name	Wavelength (Å)	X Pixel	Y Pixel
	j8d703030_drz.fits	8060	399	306
	j8d703vlq_flt.fits	8060	417	234
	j8d703vuq_flt.fits	8060	419	264
	j8d703w1q_flt.fits	8060	422	293
	j8d703w6q_drz.fits	8060	396	277
	j8d703w6q_flt.fits	8060	419	264
N300-S8	j9ra11010_drz.fits	4747	3895	580
	j9ra11neq_flt.fits	4747	3918	402
	j9ra11nfq_flt.fits	4747	3923	461
	j9ra11020_drz.fits	5921	3895	580
	j9ra11nhq_flt.fits	5921	3924	461
	j9ra11njq_flt.fits	5921	3918	402
	j9ra11030_drz.fits	8060	3895	580
	j9ra11nlq_flt.fits	8060	3918	402
	j9ra11nnq_flt.fits	8060	3924	461
N300-S9	j9ra11010_drz.fits	4747	3605	1042
	j9ra11neq_flt.fits	4747	3609	871
	j9ra11nfq_flt.fits	4747	3614	930
	j9ra11020_drz.fits	5921	3605	1042
	j9ra11nhq_flt.fits	5921	3614	930
	j9ra11njq_flt.fits	5921	3609	871
	j9ra11030_drz.fits	8060	3605	1042
	j9ra11nlq_flt.fits	8060	3609	871
	j9ra11nnq_flt.fits	8060	3614	930
N300-S10	j9ra11010_drz.fits	4747	3602	1353
	j9ra11neq_flt.fits	4747	3593	1181

Continued

Table C.4 continued.

Object	File Name	Wavelength (Å)	X Pixel	Y Pixel
	j9ra11nfq_flt.fits	4747	3598	1240
	j9ra11020_drz.fits	5921	3602	1353
	j9ra11nhq_flt.fits	5921	3598	1240
	j9ra11njq_flt.fits	5921	3593	1181
	j9ra11030_drz.fits	8060	3602	1353
	j9ra11nlq_flt.fits	8060	3593	1181
	j9ra11nnq_flt.fits	8060	3598	1240
N300-S13	u8hhvp02m_drz.fits	2993	412	737
	j8d702010_drz.fits	4318	3113	3618
	j9ra11010_drz.fits	4747	3068	3149
	j8d702020_drz.fits	5360	3113	3618
	j9ra11020_drz.fits	5921	3068	3149
	u8hhvp01m_drz.fits	6001	400	728
	u8ixhd01m_drz.fits	6001	389	719
	u8ixhd02m_drz.fits	6001	389	719
	j8d702030_drz.fits	8060	3112	3618
	j8d702n0q_drz.fits	8060	3109	3589
	j9ra11030_drz.fits	8060	3068	3149
N300-S14	j8d703010_drz.fits	4318	3911	3475
	j9ra11010_drz.fits	4747	2121	1771
	j9ra11neq_flt.fits	4747	2090	1642
	j9ra11nfq_flt.fits	4747	2095	1700
	j8d703020_drz.fits	5360	3911	3475
	j9ra11020_drz.fits	5921	2121	1772
	j9ra11nhq_flt.fits	5921	2095	1701
	j9ra11njq_flt.fits	5921	2090	1642

Continued

Table C.4 continued.

Object	File Name	Wavelength (Å)	X Pixel	Y Pixel
	j8d703030_drz.fits	8060	3911	3475
	j8d703w6q_drz.fits	8060	3908	3446
	j9ra11030_drz.fits	8060	2121	1772
	j9ra11nlq_flt.fits	8060	2090	1642
	j9ra11nnq_flt.fits	8060	2095	1701
N300-S15	j8d702010_drz.fits	4318	1936	2062
	j8d702mcq_flt.fits	4318	1889	1940
	j8d702mjq_flt.fits	4318	1891	1970
	j8d702mrq_flt.fits	4318	1894	1999
	j8d702020_drz.fits	5360	1936	2062
	j8d702mdq_flt.fits	5360	1889	1940
	j8d702mlq_flt.fits	5360	1891	1970
	j8d702mtq_flt.fits	5360	1894	1999
	j8d702030_drz.fits	8060	1936	2062
	j8d702mfq_flt.fits	8060	1889	1940
	j8d702moq_flt.fits	8060	1891	1970
	j8d702mvq_flt.fits	8060	1894	1999
	j8d702n0q_drz.fits	8060	1933	2033
	j8d702n0q_flt.fits	8060	1891	1970
N300-S16	j8d702010_drz.fits	4318	4070	1717
	j8d702mcq_flt.fits	4318	4046	1537
	j8d702mjq_flt.fits	4318	4049	1566
	j8d702mrq_flt.fits	4318	4051	1596
	j8d703010_drz.fits	4318	2103	3871
	j9ra11010_drz.fits	4747	940	3197
	j8d702020_drz.fits	5360	4070	1717

Continued

Table C.4 continued.

Object	File Name	Wavelength (Å)	X Pixel	Y Pixel
	j8d702mdq_flt.fits	5360	4046	1537
	j8d702mlq_flt.fits	5360	4049	1566
	j8d702mtq_flt.fits	5360	4051	1596
	j8d703020_drz.fits	5360	2103	3871
	u6713701m_drz.fits	5484	702	728
	u6713702r_drz.fits	5484	702	728
	u6713703r_drz.fits	5484	702	728
	u6713704r_drz.fits	5484	702	728
	j9ra11020_drz.fits	5921	940	3197
	u6713705r_drz.fits	6564	702	728
	u6713706r_drz.fits	6564	702	728
	u6713707r_drz.fits	6564	702	728
	u6713708r_drz.fits	6564	702	728
	u6713709r_drz.fits	6564	702	728
	u65w0201r_drz.fits	7996	722	756
	u65w0202r_drz.fits	7996	722	756
	u65w0203r_drz.fits	7996	722	756
	j8d702030_drz.fits	8060	4069	1717
	j8d702mfq_flt.fits	8060	4046	1537
	j8d702moq_flt.fits	8060	4049	1566
	j8d702mvq_flt.fits	8060	4051	1596
	j8d702n0q_drz.fits	8060	4066	1688
	j8d702n0q_flt.fits	8060	4049	1566
	j8d703030_drz.fits	8060	2103	3870
	j8d703w6q_drz.fits	8060	2099	3842
	j9ra11030_drz.fits	8060	940	3197

Continued

Table C.4 continued.

Object	File Name	Wavelength (Å)	X Pixel	Y Pixel
N300-S18	j8d702010_drz.fits	4318	2468	126
	j8d702mjq_flt.fits	4318	2505	27
	j8d702mrq_flt.fits	4318	2507	56
	j8d702020_drz.fits	5360	2468	126
	j8d702mlq_flt.fits	5360	2505	27
	j8d702mtq_flt.fits	5360	2507	56
	j8d702030_drz.fits	8060	2467	126
	j8d702moq_flt.fits	8060	2505	27
	j8d702mvq_flt.fits	8060	2507	56
	j8d702n0q_drz.fits	8060	2464	97
	j8d702n0q_flt.fits	8060	2505	27

Table C.4 can be reduced by removing files of the same wavelength from each source. However, this must be done carefully. Of course, any file which is unique in wavelength for a particular source is not removed. For those sources with multiple files of one wavelength, the file with the greatest number of sources within its field of view is used so that the astrometry task is reduced in overall size. Table C.5 shows this reduced list of files for each source.

Table C.5: List of objects of interest from Table 5.7 with reduced file list from Table C.4.

1	2	3	4	5
Object	**File Name**	**Wavelength (Å)**	**X Pixel**	**Y Pixel**
J005438–374144	j9ra11010_drz.fits	4747	3604	71
	j9ra11020_drz.fits	5921	3604	71
	j9ra11030_drz.fits	8060	3604	71
J005440–374049	j9ra11010_drz.fits	4747	3631	1314
	j9ra11020_drz.fits	5921	3631	1314
	j9ra11030_drz.fits	8060	3631	1314
J005445–373847	u8hhvp02m_drz.fits	2993	850	1132
	j8d702010_drz.fits	4318	1979	3946
	j9ra11010_drz.fits	4747	3889	3997
	j8d702020_drz.fits	5360	1979	3945
	j9ra11020_drz.fits	5921	3889	3997
	u8hhvp01m_drz.fits	6001	838	1123
	j8d702030_drz.fits	8060	1979	3945
J005450–374030	j8d702010_drz.fits	4318	3995	2713
	j9ra11010_drz.fits	4747	1854	2795
	j8d702020_drz.fits	5360	3995	2712
	u6713701m_drz.fits	5484	527	1195
	j9ra11020_drz.fits	5921	1854	2795
	u6713709r_drz.fits	6564	527	1196
	u65w0201r_drz.fits	7996	566	1230
	j8d702030_drz.fits	8060	3995	2713
J005450–373822	j8d702010_drz.fits	4318	1445	2797
	j8d702020_drz.fits	5360	1445	2797
	j8d702030_drz.fits	8060	1444	2797
J005450–374022	j8d702010_drz.fits	4318	3836	2612

Continued

Table C.5 continued.

Object	File Name	Wavelength (Å)	X Pixel	Y Pixel
	j9ra11010_drz.fits	4747	1839	2983
	j8d702020_drz.fits	5360	3836	2611
	u6713701m_drz.fits	5484	464	1125
	j9ra11020_drz.fits	5921	1839	2984
	u6713709r_drz.fits	6564	464	1125
	u65w0201r_drz.fits	7996	501	1162
	j8d702030_drz.fits	8060	3835	2611
J005451–373826	j8d702010_drz.fits	4318	1512	2591
	j8d702020_drz.fits	5360	1512	2590
	j8d702030_drz.fits	8060	1511	2590
J005451–373939	j8d702010_drz.fits	4318	2975	2390
	j9ra11010_drz.fits	4747	2047	3847
	j8d702020_drz.fits	5360	2976	2389
	u6713701m_drz.fits	5484	82	898
	j9ra11020_drz.fits	5921	2047	3847
	u6713709r_drz.fits	6564	82	898
	u65w0201r_drz.fits	7996	110	951
	j8d702030_drz.fits	8060	2975	2389
J005500–374037	j8d702010_drz.fits	4318	4058	264
	j8d702020_drz.fits	5360	4058	263
	u6713701m_drz.fits	5484	899	28
	u6713709r_drz.fits	6564	899	29
	u65w0201r_drz.fits	7996	890	49
	j8d702030_drz.fits	8060	4057	263
J005501–373829	j8d702010_drz.fits	4318	1502	136
	j8d702020_drz.fits	5360	1502	135

Continued

Table C.5 continued.

Object	File Name	Wavelength (Å)	X Pixel	Y Pixel
	j8d702030_drz.fits	8060	1502	135
J005503–374246	j8d703010_drz.fits	4318	342	987
	j8d703020_drz.fits	5360	342	987
	j8d703030_drz.fits	8060	342	986
J005503–374320	j8d703010_drz.fits	4318	399	306
	j8d703020_drz.fits	5360	399	306
	j8d703030_drz.fits	8060	399	306
N300-S8	j9ra11010_drz.fits	4747	3895	580
	j9ra11020_drz.fits	5921	3895	580
	j9ra11030_drz.fits	8060	3895	580
N300-S9	j9ra11010_drz.fits	4747	3605	1042
	j9ra11020_drz.fits	5921	3605	1042
	j9ra11030_drz.fits	8060	3605	1042
N300-S10	j9ra11010_drz.fits	4747	3602	1353
	j9ra11020_drz.fits	5921	3602	1353
	j9ra11030_drz.fits	8060	3602	1353
N300-S13	u8hhvp02m_drz.fits	2993	412	737
	j8d702010_drz.fits	4318	3113	3618
	j9ra11010_drz.fits	4747	3068	3149
	j8d702020_drz.fits	5360	3113	3618
	j9ra11020_drz.fits	5921	3068	3149
	u8hhvp01m_drz.fits	6001	400	728
	j8d702030_drz.fits	8060	3112	3618
N300-S14	j8d703010_drz.fits	4318	3911	3475
	j9ra11010_drz.fits	4747	2121	1771
	j8d703020_drz.fits	5360	3911	3475

Continued

Table C.5 continued.

Object	File Name	Wavelength (Å)	X Pixel	Y Pixel
	j9ra11020_drz.fits	5921	2121	1772
	j9ra11030_drz.fits	8060	2121	1772
N300-S15	j8d702010_drz.fits	4318	1936	2062
	j8d702020_drz.fits	5360	1936	2062
	j8d702030_drz.fits	8060	1936	2062
N300-S16	j8d702010_drz.fits	4318	4070	1717
	j9ra11010_drz.fits	4747	940	3197
	j8d702020_drz.fits	5360	4070	1717
	u6713701m_drz.fits	5484	702	728
	j9ra11020_drz.fits	5921	940	3197
	u6713709r_drz.fits	6564	702	728
	u65w0201r_drz.fits	7996	722	756
	j8d702030_drz.fits	8060	4069	1717
N300-S18	j8d702010_drz.fits	4318	2468	126
	j8d702020_drz.fits	5360	2468	126
	j8d702030_drz.fits	8060	2467	126

Appendix D

HST Proposal Abstracts

This appendix is a reprint of the Hubble Space Telescope proposal abstracts that resulted in the creation of these image files.

D.1 Proposal 8591

"Small nuclear black holes are the last major unexplored part of BH parameter space. We propose to search for the smallest BHs that HST can possibly find. Past studies have concentrated on massive, distant spheroids, overlooking many BH candidates on our own doorstep. The minimum detectable BH mass can be driven down by nearly two orders of magnitude by focusing on the nearest galaxies. We can easily reach down to 10^5 $M_\odot$, the probable mass of the "first born" objects that *in other cases* grow or merge up to the quasar mass range. This strategy also favours disk-like "pseudobulges," which probably formed differently from classical spheroids and which therefore provide a fresh perspective on the relationship between BHs and their embryonic environments. Our complete sample of 20 nearby galaxies includes all unstudied objects within 7.5 Mpc, brighter than $M_B = -17$, with well defined, unobscured centres. STIS long-slit spectra will be used to measure BH masses using both gas and stellar kinematics, comparing the results whenever practical. Emission-line and broad-band images are sought to characterise the central morphology of gas and stars. Of prime importance is the maser galaxy NGC 4258, which provides a unique chance to calibrate both stellar – and gas – dynamical BH masses against the impressively accurate maser BH mass."

This Hubble Space Telescope proposal was submitted by Douglas Richstone of the University of Michigan.

D.2 Proposal 8599

"We conduct a WFPC2 I-band snapshot survey of a well-defined sample of nearby, face-on spiral galaxies of type Scd or later. Given the sizes of known nuclear clusters (R_{eff} approximately $0\farcs2$), HST provides an order of magnitude contrast improvement over ground-based imaging, crucial for an unambiguous identification of the cluster. The data will yield cluster sizes and unblended luminosities, which are impossible to obtain from the ground. This program will be the first systematic census of nuclear star clusters in late-type spirals. As such, it will provide a valuable catalogue for follow-up spectroscopy to study the stellar populations, masses, and ages of these clusters, all of which are important diagnostics for understanding their formation mechanism and possible influence on the surrounding bulge."

This Hubble Space Telescope proposal was submitted by Torsten Boeker of the European Space Agency – ESTEC.

D.3 Proposal 9285

Abstract unavailable.

This Hubble Space Telescope proposal was submitted by Stefi Baum of the Rochester Institute of Technology

.

D.4 Proposal 9677

"The investigation of the Wind Momentum-Luminosity Relationship WLR of blue supergiant stars as an independent extragalactic distance indicator has reached a critical phase. Following our recent discovery and spectroscopic follow-up of several tens of stars outside of the Local Group in NGC 300 and NGC 3621, we can now calibrate the WLR in terms of spectral subtype and Z with a higher accuracy than hitherto possible with the statistically limited samples available in the nearby galaxies studied so far. This, however, requires high-resolution imaging to obtain accurate BVI photometry of a significant fraction of those stars for which we have spectroscopic information. This can be effectively accomplished with eight ACS/WFC fields in these two galaxies. As a further step, we can use the calibrated WLR to measure the first independent extragalactic distance. We then propose additional imaging of six ACS/WFC fields in M 101 to select blue supergiant candidates for spectroscopic follow-up. Having recently discovered more than a hundred new Cepheids in NGC 300, the

high-resolution imaging proposed for the photometry of blue supergiants can also be used, with no additional observing effort, to verify the effects of blending on the Cepheid distance to this galaxy, an important calibrator of secondary distance indicators."

This Hubble Space Telescope proposal was submitted by Fabio Bresolin of the University of Hawaii.

D.5 Proposal 9676

"This is the generic target version of the WFPC2 Archival Pure Parallel program. The program will be used to take parallel images of random areas of the sky, following the recommendations of the 2002 Parallels Working Group."

This Hubble Space Telescope proposal was submitted by James Rhoads of Arizona State University.

D.6 Proposal 9677

"This is a POMS test proposal designed to simulate scientific plans."

This Hubble Space Telescope proposal was submitted by James Rhoads of Arizona State University.

D.7 Proposal 10915

"Existing HST observations of nearby galaxies comprise a sparse and highly non-uniform archive, making comprehensive comparative studies among galaxies essentially impossible. We propose to secure HST's lasting impact on the study of nearby galaxies by undertaking a systematic, complete, and carefully crafted imaging survey of ALL galaxies in the Local Universe outside the Local Group. The resulting images will allow unprecedented measurements of: (1) the star formation history (SFH) of a > 100 Mpc^3 volume of the Universe with a time resolution of $\Delta[log(t)] = 0.25$; (2) correlations between spatially resolved SFHs and environment; (3) the structure and properties of thick disks and stellar halos; and (4) the colour distributions, sizes, and specific frequencies of globular and disk clusters as a function of galaxy mass and environment. To reach these goals, we will use a combination of wide-field tiling and pointed deep imaging to obtain uniform data on all 72 galaxies within a volume-limited sample extending to $\sim$3.5 Mpc, with an extension to the M 81 group. For each galaxy, the wide-field imaging will cover out to $\sim$1.5 times the optical radius and will reach photometric depths of at least 2 magnitudes below the tip of the red giant branch throughout the limits of the survey volume. One

additional deep pointing per galaxy will reach SNR 10 for red clump stars, sufficient to recover the ancient SFH from the colour-magnitude diagram. This proposal will produce photometric information for ∼100 million stars (comparable to the number in the SDSS survey) and uniform multi-colour images of half a square degree of sky. The resulting archive will establish the fundamental optical database for nearby galaxies, in preparation for the shift of high-resolution imaging to the near-infrared."

This Hubble Space Telescope proposal was submitted by Julianne Dalcanton of the University of Washington.

Appendix E

DS9 Settings for Figures

The following tables show the DS9 program options settings used to create figures Figure 7.4 through Figure 7.7, Figure 7.14 and Figure 7.28.

Table E.1: For Figure 7.4, page 122.

Parameter	**Setting**
Zoom level	4
Scale	Linear, 98%
Colour	SLS
WCS	Equatorial, J2000.0
Analysis:	
Contours	8
Smooth Parameters	3, Gaussian

Table E.2: For Figure 7.5, page 123:

Parameter	**Setting**
Zoom level	4
Scale	Linear, 98%
Colour	SLS
WCS	Equatorial, J2000.0
Analysis:	
Contours	8
Smooth Parameters	3, Gaussian

Table E.3: For Figure 7.6, page 125:

Parameter	**Setting**
Zoom level	4
Scale	Linear, 99.5%
Colour	SLS
WCS	Equatorial, J2000.0
Analysis:	
Contours	10
Smooth Parameters	3, Gaussian

Table E.4: For Figure 7.7, page 127:

Parameter	**Setting**
Zoom level	4
Scale	Linear, 95%
Colour	SLS
WCS: Equatorial, J2000.0	
The contours were not used on this image.	

Table E.5: For Figure 7.14, page 152.

Parameter	**Setting**
Colour Scale	AIPS0
Zoom	4
Scale	ZScale, Squared

Table E.6: For Figure 7.28, page 175.

Parameter	**Setting**
Colour Scale	AIPS0
Zoom	4
Scale	ZScale, Squared

Appendix F

Author's Publications List

Here is a list of publications released while working on this research degree.

1. Galvin, T. J., Filipović, M. D., Crawford, E. J., Wong, G., Payne, J. L., De Horta, A., White, G. L., Tothill, N., Drašković, D., Pannuti, T. G., Grimes, C. K., Cahall, B. J., Millar, W. C., & Laine, S., 2012, "Radio-continuum study of the Nearby sculptor group galaxies. Part 1: NGC 300 at $\lambda = 20$ cm" Astrophysics & Space Sciences, Mar, 101.

2. Millar, W. C., White, G. L., & Filipovic, M. D., 2012, "A Study of Optical Observing Techniques for Extra-Galactic Supernova Remnants: Case of NGC 300" Serbian Astronomical Journal, 184, 19

3. Millar, W. C., White, G. L., Filipović, M. D., Payne, J. L., Crawford, E. J., Pannuti, T. G., Staggs, W. D., 2011, "Optical spectra of supernova remnant candidates in the Sculptor Group galaxy NGC 300" Astrophysics & Space Sciences, 332, 221-239.

4. Payne, J. L., Filipović, M. D., Millar, W. C., Crawford, E. J., de Horta, A. Y., Stootman, F. H., Urosevic, D., 2008, "Optical Spectra of Radio Planetary Nebulae in the Large Magellanic Cloud" Serbian Astronomical Journal, 177, 53-59.

5. Kahabka, P., Haberl, F., Pakull, M., Millar, W. C., White, G. L., Filipović, M. D., Payne, J. L., 2008, "Faint super-soft X-ray sources in XMM-Newton Large Magellanic Cloud fields", Astronomy and Astrophysics, 482, 237-245.

6. Millar, W. C., Filipović, M. D., Payne, J. L., White, G. L., Crawford, E., De Horta, A., Stootman, F., 2008, "Optical Spectra of Radio Planetary Nebulae in the Large Magellanic Cloud" American Astronomical

Society Meeting Abstracts #212, Bulletin of the American Astronomical Society, 40, 207.

7. Millar, W., White, G. L., Filipović, M. D., Hons, A., 2008, "The Collection of Data for the Research Component of the Internet-Based, 'Doctor of Astronomy' Professional Degree Program at James Cook University" *EPO and a Changing World: Creating Linkages and Expanding Partnerships*, Astronomical Society of the Pacific Conference Series, Eds. Garmany, C., Gibbs, J. W., Moody, M. G., #389, 367.

8. Millar, W., 2007, "Book Betterment" Sky & Telescope, 114, #2, 20

9. Millar, W., 2006, "The Amateur Astronomer's Introduction to the Celestial Sphere" Cambridge, UK: Cambridge University Press

References

Abdo, A. A., Ackermann, M., Ajello, M., et al. 2010, Science, 327, 1103

Aharonian, F., Akhperjanian, A. G., Aye, K.-M., et al. 2005, Astronomy and Astrophysics, 437, 135

Aller, L. H. 1991, Atoms, Stars, and Nebulae (Cambridge, UK: Cambridge University Press)

Andersen, D. R., Walcher, C. J., Böker, T., et al. 2008, Astrophysical Journal, 688, 990

Arnault, P., Kunth, D., & Schild, H. 1989, Astronomy and Astrophysics, 224, 73

Arp, H. 1985, Astronomical Journal, 90, 1012

Asvarov, A. I. 2000, ArXiv Astrophysics e-prints

Baade, W. & Zwicky, F. 1934, Proceedings of the National Academy of Science, 20, 254

Badenes, C., Borkowski, K. J., Hughes, J. P., Hwang, U., & Bravo, E. 2005, ArXiv Astrophysics e-prints

Baldwin, J. A. & Stone, R. P. S. 1984, Monthly Notices of the Royal Astronomical Society, 206, 241

Balsara, D. S., Tilley, D. A., & Howk, J. C. 2006, ArXiv Astrophysics e-prints

Bamba, A., Koyama, K., & Tomida, H. 2000, Publications of the Astronomical Society of Japan, 52, 1157

Bamba, A., Yamazaki, R., Yoshida, T., Terasawa, T., & Koyama, K. 2005, Astrophysical Journal, 621, 793

Barth, A. J., Strigari, L. E., Bentz, M. C., Greene, J. E., & Ho, L. C. 2009, Astrophysical Journal, 690, 1031

Beifiori, A., Sarzi, M., Corsini, E. M., et al. 2009, Astrophysical Journal, 692, 856

Benetti, S., Meikle, P., Stehle, M., et al. 2004, Monthly Notices of the Royal Astronomical Society, 348, 261

Berger, E., Soderberg, A. M., Chevalier, R. A., et al. 2009, Astrophysical Journal, 699, 1850

Bianchi, S. & Schneider, R. 2007, Monthly Notices of the Royal Astronomical Society, 378, 973

Biermann, P. L., Becker, J. K., Dreyer, J., et al. 2010, Astrophysical Journal, 725, 184

Blair, W. P. & Davidsen, A. F. 1993, Publications of the Astronomical Society of the Pacific, 105, 494

Blair, W. P., Ghavamian, P., Sankrit, R., & Danforth, C. W. 2006, Astrophysical Journal Supplement Series, 165, 480

Blair, W. P., Kirshner, R. P., & Chevalier, R. A. 1981, Astrophysical Journal, 247, 879

Blair, W. P. & Long, K. S. 1997, (BL97) Astrophysical Journal Supplement Series, 108, 261

Blair, W. P. & Long, K. S. 2004, Astrophysical Journal Supplement Series, 155, 101

Bland-Hawthorn, J., Vlajić, M., Freeman, K. C., & Draine, B. T. 2005, Astrophysical Journal, 629, 239

Böker, T., Laine, S., van der Marel, R. P., et al. 2002, Astronomical Journal, 123, 1389

Böker, T., Lisenfeld, U., & Schinnerer, E. 2003a, Astronomy and Astrophysics, 406, 87

Böker, T., Sarzi, M., McLaughlin, D. E., et al. 2004, Astronomical Journal, 127, 105

Böker, T., Stanek, R., & van der Marel, R. P. 2003b, Astronomical Journal, 125, 1073

Bond, H. E., Bedin, L. R., Bonanos, A. Z., et al. 2009, Astrophysical Journal Letters, 695, L154

Borkowski, K. J., Rho, J., Reynolds, S. P., & Dyer, K. K. 2001, Astrophysical Journal, 550, 334

Bouchet, P. & Danziger, J. 2010, in 38th COSPAR Scientific Assembly, Vol. 38, 2725–+

Braun, R. & Walterbos, R. A. M. 1993, Astron. Astrophys. Suppl. Ser., 98, 327

Bresolin, F., Gieren, W., Kudritzki, R., et al. 2009, Astrophysical Journal, 700, 309

Bresolin, F., Pietrzyński, G., Gieren, W., & Kudritzki, R. 2005a, Astrophysical Journal, 634, 1020

Bresolin, F., Pietrzyński, G., Gieren, W., & Kudritzki, R.-P. 2005b, Astrophysical Journal, 634, 1020

Breysacher, J., Azzopardi, M., Testor, G., & Muratorio, G. 1997, Astronomy and Astrophysics, 326, 976

Brown, R. L. 1987, in Spectroscopy of Astrophysical Plasmas, ed. A. Dalgarno & D. Layzer, 35–58

Burrows, A. S. 1990, in Supernovae, ed. A. G. Petschek, 143–181

Butler, D. J., Martínez-Delgado, D., & Brandner, W. 2004, Astronomical Journal, 127, 1472

Canizares, C. R. 1990, in NATO ASIC Proc. 300: Physical Processes in Hot Cosmic Plasmas, ed. W. Brinkmann, A. C. Fabian, & F. Giovannelli, 17–28

Cao, C. & Wu, H. 2007, Astronomical Journal, 133, 1710

Carpano, S., Wilms, J., Schirmer, M., & Kendziorra, E. 2004, Mem. Soc. Astron. Italiana, 75, 486

Carpano, S., Wilms, J., Schirmer, M., & Kendziorra, E. 2005, (C05) Astronomy and Astrophysics, 443, 103

Carpano, S., Wilms, J., Schirmer, M., & Kendziorra, E. 2006a, in ESA Special Publication, Vol. 604, The X-ray Universe 2005, ed. A. Wilson, 445–+

Carpano, S., Wilms, J., Schirmer, M., & Kendziorra, E. 2006b, in ESA Special Publication, Vol. 604, The X-ray Universe 2005, ed. A. Wilson, 445–+

Carroll, B. W. & Ostlie, D. A. 1996, An Introduction to Modern Astrophysics (New York: Addison-Wesley Publishing)

Case, G. L. & Bhattacharya, D. 1998, Astrophysical Journal, 504, 761

Chevalier, R. A. 1974, Astrophysical Journal, 188, 501

Chevalier, R. A. 1977, Annual Review of Astronomy and Astrophysics, 15, 175

Chevalier, R. A. 1990, in Supernovae, ed. A. G. Petscheck (New York: Springer-Verlag), 91–110

Chevalier, R. A. & Soderberg, A. M. 2010, Astrophysical Journal Letters, 711, L40

Chomiuk, L. & Wilcots, E. M. 2009, Astronomical Journal, 137, 3869

Christensen, T., Petersen, L., & Gammelgaard, P. 1997, Astronomy and Astrophysics, 322, 41

Chu, Y.-H. 1997, Astronomical Journal, 113, 1815

Cioffi, D. F. 1990, in Physical Processes in Hot Cosmic Plasmas, ed. W. Brinkmann, A. C. Fabian, & G. F. (Boston: Kluwer Academic Publishers), 1–16

Cioffi, D. F., McKee, C. F., & Bertschinger, E. 1988, Astrophysical Journal, 334, 252

Cox, D. P. 1972, Astrophysical Journal, 178, 159

da Silva, L. A. L. 1993, Ap&SS, 202, 215

Dai, H. & Wang, T. 2008, Chinese Journal of Astronomy and Astrophysics, 8, 245

Dalcanton, J. J., Williams, B. F., Seth, A. C., et al. 2009, Astrophysical Journal Supplement Series, 183, 67

de Grijs, R., Wilkinson, M. I., & Tadhunter, C. N. 2005, Monthly Notices of the Royal Astronomical Society, 361, 311

de Mello, D. F., Smith, L. J., Sabbi, E., et al. 2008, Astronomical Journal, 135, 548

de Vaucouleurs, G., de Vaucouleurs, A., Corwin, Jr., H. G., et al. 1991, Third Reference Catalogue of Bright Galaxies (New York: Springer-Verlag)

Deharveng, L., Caplan, J., Lequeux, J., et al. 1988, Astron. Astrophys. Suppl. Ser., 73, 407

Diehl, R., Halloin, H., Kretschmer, K., et al. 2006, Nature, 439, 45

D'Odorico, S., Benvenuti, P., & Sabbadin, F. 1978, Astronomy and Astrophysics, 63, 63

D'Odorico, S., Dopita, M. A., & Benvenuti, P. 1980, Astron. Astrophys. Suppl. Ser., 40, 67

D'Odorico, S., Rosa, M., & Wampler, E. J. 1983, Astron. Astrophys. Suppl. Ser., 53, 97

Dohm-Palmer, R. C. & Jones, T. W. 1996, Astrophysical Journal, 471, 279

Dopita, M. A., Binette, L., Dodorico, S., & Benvenuti, P. 1984, Astrophysical Journal, 276, 653

Dopita, M. A., Blair, W. P., Long, K. S., et al. 2010a, Astrophysical Journal, 710, 964

Dopita, M. A., Calzetti, D., Maíz Apellániz, J., et al. 2010b, Ap&SS, 148

Drury, O. L., Aharonian, F. A., Malyshev, D., & Gabici, S. 2009, Astronomy and Astrophysics, 496, 1

Dunne, L., Eales, S., Ivison, R., Morgan, H., & Edmunds, M. 2003, Nature, 424, 285

Duric, N. 2000a, in Proceedings 232. WE-Heraeus Seminar, ed. E. M. Berkhuijsen, R. Beck, & R. A. M. Walterbos, 179–186

Duric, N. 2000b, in Proceedings 232. WE-Heraeus Seminar, ed. E. M. Berkhuijsen, R. Beck, & R. A. M. Walterbos, 127–130

Dwarkadas, V. 2005a, in ASP Conf. Ser. 332: The Fate of the Most Massive Stars, ed. R. Humphreys & K. Stanek, 418–+

Dwarkadas, V. V. 2005b, Astrophysical Journal, 630, 892

Dyer, K. K., Cornwell, T. J., & Maddelena, R. J. 2005, American Astronomical Society Meeting Abstracts, 207, 172.13

Edelstein, J., Min, K. W., Han, W., et al. 2006, ArXiv Astrophysics e-prints

Edmunds, M. G. & Pagel, B. E. J. 1984, Monthly Notices of the Royal Astronomical Society, 211, 507

Elias, J. H., Matthews, K., Neugebauer, G., & Persson, S. E. 1985, Astrophysical Journal, 296, 379

Fesen, R. A. 1996, in IAU Colloq. 145: Supernovae and Supernova Remnants, ed. McCray, R. and Wang, Z. (Cambridge University Press), 381–+

Fesen, R. A., Blair, W. P., & Kirshner, R. P. 1985, Astrophysical Journal, 292, 29

Fesen, R. A. & Hurford, A. P. 1996, Astrophysical Journal Supplement Series, 106, 563

Filipović, M. D., Haberl, F., Winkler, P. F., et al. 2008, Astronomy and Astrophysics, 485, 63

Filipović, M. D., Haynes, R. F., White, G. L., & Jones, P. A. 1998, Astron. Astrophys. Suppl. Ser., 130, 421

Filippenko, A. V. 1997, Annual Review of Astronomy and Astrophysics, 35, 309

Filippenko, A. V. 2005, in Astronomical Society of the Pacific Conference Series, Vol. 332, The Fate of the Most Massive Stars, ed. R. Humphreys & K. Stanek, 33

Filippenko, A. V. & Sargent, W. L. W. 1986, Astronomical Journal, 91, 691

Franco, J., Tenorio-Tagle, G., Bodenheimer, P., & Rozyczka, M. 1991, Publications of the Astronomical Society of the Pacific, 103, 803

Freedman, W. L., Madore, B. F., Gibson, B. K., et al. 2001, Astrophysical Journal, 553, 47

Freedman, W. L., Madore, B. F., Hawley, S. L., et al. 1992, Astrophysical Journal, 396, 80

Freeman, P. E., Kashyap, V., Rosner, R., & Lamb, D. Q. 2002, Astrophysical Journal Supplement Series, 138, 185

Fruscione, A., McDowell, J. C., Allen, G. E., et al. 2006, in Society of Photo-Optical Instrumentation Engineers (SPIE) Conference Series, Vol. 6270, Society of Photo-Optical Instrumentation Engineers (SPIE) Conference Series

Fryer, C. L. & Kusenko, A. 2006, Astrophysical Journal Supplement Series, 163, 335

Gaensler, B. M., Hendrick, S. P., Reynolds, S. P., & Borkowski, K. J. 2003, Astrophysical Journal Letters, 594, L111

Gaetz, T. J., Butt, Y. M., Edgar, R. J., et al. 2000, Astrophysical Journal Letters, 534, L47

Ganda, K., Falcón-Barroso, J., Peletier, R. F., et al. 2006, Monthly Notices of the Royal Astronomical Society, 367, 46

Ghavamian, P., Blair, W. P., Sankrit, R., Danforth, C., & Sembach, K. 2006, in Astronomical Society of the Pacific Conference Series, ed. G. Sonneborn, H. W. Moos, & B.-G. Andersson, 331–+

Ghosh, K. K., Saripalli, L., Gandhi, P., et al. 2009, Astronomical Journal, 137, 3263

Giacani, E., Loiseau, N., Dubner, G., & Smith, M. J. S. 2005, ArXiv Astrophysics e-prints

Gieren, W., Pietrzyński, G., Soszyński, I., et al. 2005, Astrophysical Journal, 628, 695

Gieren, W., Pietrzyński, G., Walker, A., et al. 2004, Astronomical Journal, 128, 1167

Gil de Paz, A., Boissier, S., Madore, B. F., et al. 2007, Astrophysical Journal Supplement Series, 173, 185

Girardi, L., Dalcanton, J., Williams, B., et al. 2008, Publications of the Astronomical Society of the Pacific, 120, 583

Gliozzi, M., Satyapal, S., Eracleous, M., Titarchuk, L., & Cheung, C. C. 2009, Astrophysical Journal, 700, 1759

Gogarten, S. M., Dalcanton, J. J., Murphy, J. W., et al. 2009a, Astrophysical Journal, 703, 300

Gogarten, S. M., Dalcanton, J. J., Williams, B. F., et al. 2010, Astrophysical Journal, 712, 858

Gogarten, S. M., Dalcanton, J. J., Williams, B. F., et al. 2009b, Astrophysical Journal, 691, 115

Goldsmith, D. 1989, Supernova! The Exploding Star of 1987 (New York: St. Martin's Press)

González Delgado, R. M., Pérez, E., Cid Fernandes, R., & Schmitt, H. 2008, Astronomical Journal, 135, 747

Graham, A. W., Erwin, P., Caon, N., & Trujillo, I. 2001, Astrophysical Journal Letters, 563, L11

Green, D. A. 2009, Bulletin of the Astronomical Society of India, 37, 45

Guerrero, M. A. & Chu, Y. 2008, Astrophysical Journal Supplement Series, 177, 216

Gull, S. F. 1973, Monthly Notices of the Royal Astronomical Society, 161, 47

Haberl, F. & Pietsch, W. 1999, Astron. Astrophys. Suppl. Ser., 139, 277

Hamuy, M., Suntzeff, N. B., Heathcote, S. R., et al. 1994, Publications of the Astronomical Society of the Pacific, 106, 566

Hanayama, H. & Tomisaka, K. 2006, Astrophysical Journal, 641, 905

Harkness, R. P. & Wheeler, J. C. 1990, in Supernovae, ed. A. G. Petscheck (New York: Springer-Verlag), 1–28

Harnett, J. I. 1986, Proceedings of the Astronomical Society of Australia, 6, 325

Harrus, I. M., Slane, P. O., Smith, R. K., & Hughes, J. P. 2001, Astrophysical Journal, 552, 614

Harwit, M. 1988, Astrophysical Concepts, 2nd edn. (New York: Springer-Verlag)

Heald, Jr., G. H. 2006, PhD thesis, The University of New Mexico, New Mexico, USA

Heng, K., McCray, R., Zhekov, S. A., et al. 2006, ArXiv Astrophysics e-prints

Herant, M., Colgate, S. A., Benz, W., & Fryer, C. 1997, Los Alamos Science, 25, 64

Hillebrandt, W. & Niemeyer, J. C. 2000, Annual Reviews, 38, 191

Holwerda, B. W., Keel, W. C., Williams, B., Dalcanton, J. J., & de Jong, R. S. 2009, Astronomical Journal, 137, 3000

Hoopes, C. G., Walterbos, R. A. M., & Greenwalt, B. E. 1996, Astronomical Journal, 112, 1429

Immler, S. & Kuntz, K. D. 2005, Astrophysical Journal Letters, 632, L99

Isensee, K., Olmschenk, G., Rudnick, L., et al. 2012, Astrophysical Journal, 757, 126

Jin, Y. K., Zhang, S. N., & Wu, J. F. 2006, Astrophysical Journal, 653, 1566

Jones, T. W., Rudnick, L., Jun, B.-I., et al. 1997, ArXiv Astrophysics e-prints

Karachentsev, I. D., Grebel, E. K., Sharina, M. E., et al. 2003, Astronomy and Astrophysics, 404, 93

Kesteven, M. J. & Caswell, J. L. 1987, Astronomy and Astrophysics, 183, 118

Kiewe, M., Gal-Yam, A., Arcavi, I., et al. 2010, ArXiv e-prints

Kim, S. C., Sung, H., Park, H. S., & Sung, E.-C. 2004, Chinese Journal of Astronomy and Astrophysics, 4, 299

Kirshner, R. P. 1990, in Supernovae, ed. A. G. Petscheck (New York: Springer-Verlag), 59–75

Kong, A. K. H., Sjouwerman, L. O., & Williams, B. F. 2004, Astronomical Journal, 128, 2783

Koo, B.-C. & Heiles, C. 1995, Astrophysical Journal, 442, 679

Kornei, K. A. & McCrady, N. 2009, Astrophysical Journal, 697, 1180

Kudritzki, R., Urbaneja, M. A., Bresolin, F., et al. 2008, Astrophysical Journal, 681, 269

Kuntz, K. D. & Snowden, S. L. 2010, Astrophysical Journal Supplement Series, 188, 46

Kwok, S. 2000, The Origin and Evolution of Planetary Nebulae (Cambridge; New York: Cambridge University Press)

Lacey, C. K. & Duric, N. 2001, Astrophysical Journal, 560, 719

Lang, K. R. 1980, Astrophysical Formulae. A Compendium for the Physicist and Astrophysicist. (New York: Springer-Verlag)

Lang, M. G., Diehl, R., Wang, W., et al. 2010, Journal of Physics Conference Series, 202, 012032

Larsen, S. S. 2004, Astronomy and Astrophysics, 416, 537

Lauer, T. R., Faber, S. M., Gebhardt, K., et al. 2005, Astronomical Journal, 129, 2138

Lauer, T. R., Faber, S. M., Richstone, D., et al. 2007a, Astrophysical Journal, 662, 808

Lauer, T. R., Gebhardt, K., Faber, S. M., et al. 2007b, Astrophysical Journal, 664, 226

Lazendic, J. S., Dewey, D., Schulz, N. S., & Canizares, C. R. 2006, ArXiv Astrophysics e-prints

Lianou, S., Grebel, E. K., & Koch, A. 2009, Astronomische Nachrichten, 330, 995

Long, K. S. 1996, in IAU Colloq. 145: Supernovae and Supernova Remnants, ed. R. McCray & Z. Wang, 349–+

Long, K. S., Blair, W. P., Winkler, P. F., et al. 2010, Astrophysical Journal Supplement Series, 187, 495

Lopez, L. A., Ramirez-Ruiz, E., Badenes, C., et al. 2010, in Bulletin of the American Astronomical Society, Vol. 42, AAS/High Energy Astrophysics Division #11, 696–+

Lopez, L. A., Ramirez-Ruiz, E., Huppenkothen, D., Badenes, C., & Pooley, D. A. 2011, Astrophysical Journal, 732, 114

Maeder, A. 1991, Astronomy and Astrophysics, 242, 93

Marschall, L. A. 1988, The Supernova Story (Princeton, NJ: Princeton University Press)

Mathewson, D. S. & Clarke, J. N. 1972, Astrophysical Journal Letters, 178, L105+

Mathewson, D. S. & Clarke, J. N. 1973a, Astrophysical Journal, 179, 89

Mathewson, D. S. & Clarke, J. N. 1973b, Astrophysical Journal, 180, 725

Mathewson, D. S. & Clarke, J. N. 1973c, Astrophysical Journal, 182, 697

Mathewson, D. S., Cleary, M. N., & Murray, J. D. 1975, Astrophysical Journal Letters, 195, L97

Matonick, D. M. & Fesen, R. A. 1997, Astrophysical Journal Supplement Series, 112, 49

Maund, J. R. & Smartt, S. J. 2009, Science, 324, 486

McKee, C. F. & Ostriker, J. P. 1977, Astrophysical Journal, 218, 148

McNeil, E. K. & Winkler, P. F. 2006, in Bulletin of the American Astronomical Society, Vol. 38, Bulletin of the American Astronomical Society, 80–+

Melbourne, J., Williams, B., Dalcanton, J., et al. 2010, Astrophysical Journal, 712, 469

Mickaelian, A. M. 2004, Astronomy and Astrophysics, 426, 367

Millar, W. C., Filipovic, M. D., Payne, J. L., et al. 2008, in Bulletin of the American Astronomical Society, Vol. 40, American Astronomical Society Meeting Abstracts #212, 207–+

Millar, W. C., White, G. L., & Filipovic, M. D. 2012, Serbian Astronomical Journal, 184, 19

Millar, W. C., White, G. L., Filipović, M. D., et al. 2011, (MWF11) Ap&SS, 332, 221

Milone, A. P., Villanova, S., Bedin, L. R., et al. 2006, Astronomy and Astrophysics, 456, 517

Minkowski, R. 1941, Publications of the Astronomical Society of the Pacific, 53, 224

Mitton, S. 1978, The Crab Nebula (New York: Charles Schribner's Sons)

Montes, G., Pérez-Torres, M. A., Alberdi, A., & González, R. F. 2009, Astrophysical Journal, 705, 899

Morris, P. W., Stolovy, S., Wachter, S., et al. 2006, Astrophysical Journal Letters, 640, L179

Mould, J. & Sakai, S. 2008, Astrophysical Journal Letters, 686, L75

Murray, S. S., Austin, G. K., Chappell, J. H., et al. 2000, in Society of Photo-Optical Instrumentation Engineers (SPIE) Conference Series, Vol. 4012, Society of Photo-Optical Instrumentation Engineers (SPIE) Conference Series, ed. J. E. Truemper & B. Aschenbach, 68–80

Nantais, J. B., Huchra, J. P., Barmby, P., & Olsen, K. A. G. 2010, Astronomical Journal, 139, 1178

Osterbrock, D. E. & Ferland, G. J. 2006, Astrophysics of gaseous nebulae and active galactic nuclei (Sausalito, CA: University Science Books)

Paerels, F. B. S. & Kahn, S. M. 2003, Annual Reviews, 41, 291

Pagel, B. E. J., Edmunds, M. G., Blackwell, D. E., Chun, M. S., & Smith, G. 1979, Monthly Notices of the Royal Astronomical Society, 189, 95

Panagia, N., Van Dyk, S. D., Weiler, K. W., et al. 2006, Astrophysical Journal, 646, 369

Pannuti, T., Filipović, M. D., Duric, N., Pietsch, W., & Read, A. 2001, in AIP Conf. Proc. 565: Young Supernova Remnants, ed. S. S. Holt & U. Hwang, 445–448

Pannuti, T. G., Duric, N., Lacey, C. K., et al. 2002, Astrophysical Journal, 565, 966

Pannuti, T. G., Duric, N., Lacey, C. K., et al. 2000, (PD00) Astrophysical Journal, 544, 780

Pannuti, T. G., Schlegel, E. M., Filipović, M. D., et al. 2011, Astronomical Journal, 142, 20

Pannuti, T. G., Schlegel, E. M., & Lacey, C. K. 2007, Astronomical Journal, 133, 1361

Park, S., Zhekov, S. A., Burrows, D. N., et al. 2006, ArXiv Astrophysics e-prints

Payne, J. L., Filipović, M. D., Crawford, E. J., et al. 2008a, Serbian Astronomical Journal, 176, 65

Payne, J. L., Filipovic, M. D., Millar, W. C., et al. 2008b, Serbian Astronomical Journal, 177, 53

Payne, J. L., Filipović, M. D., Pannuti, T. G., et al. 2004, (PF04) Astronomy and Astrophysics, 425, 443

Payne, J. L., Filipović, M. D., Pannuti, T. G., et al. 2005, in X-ray and Radio Connections (eds. L. O. Sjouwerman and K.K Dyer) Published electronically by NRAO, http://www.aoc.nrao.edu/events/xraydio Held 3-6 February 2004 in Santa Fe, New Mexico, USA, (E4.15) 8 pages

Payne, J. L., Filipović, M. D., & White, G. L. 2006, Supernovae: One Millennium After SN1006, 26th meeting of the IAU, Joint Discussion 9, 17-18 August 2006, Prague, Czech Republic, JD09, #45, 9

Payne, J. L., White, G. L., & Filipović, M. D. 2008c, Monthly Notices of the Royal Astronomical Society, 383, 1175

Payne, J. L., White, G. L., Filipović, M. D., & Pannuti, T. G. 2007, Monthly Notices of the Royal Astronomical Society, 376, 1793

Peña, M. 2010, in IAU Symposium, Vol. 265, IAU Symposium, ed. K. Cunha, M. Spite, & B. Barbuy, 155–158

Peña, M. 2011, in Asymmetric Planetary Nebulae 5 Conference, A260000+

Peeples, M. S. & Martini, P. 2006, Astrophysical Journal, 652, 1097

Petuchowski, S. J. & Bennett, C. L. 1995, Astrophysical Journal, 438, 735

Pietrzyński, G., Gieren, W., Fouqué, P., & Pont, F. 2001a, Astronomy and Astrophysics, 371, 497

Pietrzyński, G., Gieren, W., Fouqué, P., & Pont, F. 2001b, Astronomy and Astrophysics, 371, 497

Prantzos, N. 2007, ArXiv e-prints, 709

Prantzos, N., Vangioni-Flam, E., & Chauveau, S. 1994, Astronomy and Astrophysics, 285, 132

Puche, D., Carignan, C., & Bosma, A. 1990, Astronomical Journal, 100, 1468

Rakowski, C. E., Badenes, C., Gaensler, B. M., et al. 2006, ArXiv Astrophysics e-prints

Ralchenko, Y., Kramida, A. E., Reader, J., & NIST ASD Team (2011). 2012, NIST Atomic Spectra Database (ver. 4.1.0). http://physics.nist.gov/asd [2012, February 27] (Gaithersburg, MD.: National Institute of Standards and Technology)

Reach, W. T. & Rho, J. 1999, in Bulletin of the American Astronomical Society, Vol. 31, American Astronomical Society Meeting Abstracts #194, 973

Read, A. M. & Pietsch, W. 2001, (RP01) Astronomy and Astrophysics, 373, 473

Read, A. M., Ponman, T. J., & Strickland, D. K. 1997, (RPS97) Monthly Notices of the Royal Astronomical Society, 286, 626

Reid, W. A. & Parker, Q. A. 2006, Monthly Notices of the Royal Astronomical Society, 373, 521

Reynoso, E. M., Gomez, H. L., & Dunne, L. 2010, Highlights of Astronomy, 15, 425

Rhee, M. & Chun, M. 1992, Journal of Korean Astronomical Society, 25, 11

Rho, J., Andersen, M., Tappe, A., et al. 2011, in EAS Publications Series, Vol. 46, EAS Publications Series, 169–175

Rho, J. & Petre, R. 1998, Astrophysical Journal Letters, 503, L167+

Rho, J., Reach, W. T., Tappe, A., et al. 2009, in Astronomical Society of the Pacific Conference Series, Vol. 414, Astronomical Society of the Pacific Conference Series, ed. T. Henning, E. Grün, & J. Steinacker, 22–+

Richstone, D. 2000, in HST Proposal, 8591–+

Rizzi, L., Bresolin, F., Kudritzki, R., Gieren, W., & Pietrzyński, G. 2006, Astrophysical Journal, 638, 766

Rizzi, L., Tully, R. B., Makarov, D., et al. 2007, Astrophysical Journal, 661, 815

Rodgers, A. W., Conroy, P., & Bloxham, G. 1988, Publications of the Astronomical Society of the Pacific, 100, 626

Rogstad, D. H., Chu, K., & Crutcher, R. M. 1979, Astrophysical Journal, 229, 509

Rosolowsky, E. & Blitz, L. 2005, Astrophysical Journal, 623, 826

Rossa, J., van der Marel, R. P., Böker, T., et al. 2006, Astronomical Journal, 132, 1074

Roussel, H., Gil de Paz, A., Seibert, M., et al. 2005, Astrophysical Journal, 632, 227

Russell, K. S. 1989, Bulletin d'Information du Centre de Donnees Stellaires, 37, 5

Ryle, M., Elsmore, B., & Neville, A. C. 1965, Nature, 205, 1259

Ryle, M. & Smith, F. G. 1948, Nature, 162, 462

Sandie, W. G., Nakano, G. H., Chase, Jr., L. F., et al. 1988, Astrophysical Journal Letters, 334, L91

Sankrit, R., Blair, W. P., & Raymond, J. C. 2003, Astrophysical Journal, 589, 242

Schild, H., Crowther, P. A., Abbott, J. B., & Schmutz, W. 2003a, Astronomy and Astrophysics, 397, 859

Schild, H., Crowther, P. A., Abbott, J. B., & Schmutz, W. 2003b, Astronomy and Astrophysics, 397, 859

Schild, H. & Testor, G. 1991, Astronomy and Astrophysics, 243, 115

Schild, H. & Testor, G. 1992, Astronomy and Astrophysics, 266, 145

Schinnerer, E., Böker, T., Emsellem, E., & Lisenfeld, U. 2006, Astrophysical Journal, 649, 181

Schinnerer, E., Böker, T., & Meier, D. S. 2003, Astrophysical Journal Letters, 591, L115

Sedov, L. I. 1993, Similarity and Dimensional Methods in Mechanics, 10th edn. (Boca Raton, FL: CRC Press)

Seielstad, G. A. & Whiteoak, J. B. 1965, Astrophysical Journal, 142, 616

Sérsic, J. L. 1966, Zeitschrift für Astrophysik, 64, 212

Seth, A., Agüeros, M., Lee, D., & Basu-Zych, A. 2008, Astrophysical Journal, 678, 116

Shaw, R. A., Reid, W. A., & Parker, Q. A. 2007, Publications of the Astronomical Society of the Pacific, 119, 19

Shaw, R. A., Stanghellini, L., Villaver, E., & Mutchler, M. 2006, Astrophysical Journal Supplement Series, 167, 201

Shearer, A., O'Connor, P., & Tuairisg, S. Ó. 2006, in IAU Symposium, Vol. 232, The Scientific Requirements for Extremely Large Telescopes, ed. P. Whitelock, M. Dennefeld, & B. Leibundgut, 281–285

Shelton, R. L. 2006, Astrophysical Journal, 638, 206

Shelton, R. L., Kuntz, K. D., & Petre, R. 2004, Astrophysical Journal, 615, 275

Shklovskii, I. S. 1960, Cosmic radio waves (Cambridge: Harvard University Press)

Shklovsky, I. S. 1968, Supernovae (New York: John Wiley & Sons)

Shobbrook, R. R. & Robinson, B. J. 1967, Australian Journal of Physics, 20, 131

Siopis, C., Gebhardt, K., Lauer, T. R., et al. 2009, Astrophysical Journal, 693, 946

Skrutskie, M. F., Cutri, R. M., Stiening, R., et al. 2006, Astronomical Journal, 131, 1163

Smartt, S. J., Maund, J. R., Hendry, M. A., et al. 2004, Science, 303, 499

Smith, R. C. 1995, Observational Astrophysics (Cambridge, UK: Cambridge University Press)

Soffner, T., Mendez, R. H., Jacoby, G. H., et al. 1996, Astronomy and Astrophysics, 306, 9

Soffner, T., Mendez, R. H., Jacoby, G. H., et al. 2003, VizieR Online Data Catalog, 330, 60009

Sramek, R. A. & Weiler, K. W. 1990, in Supernovae, ed. A. G. Petscheck (New York: Springer-Verlag), 76–90

Stanimirović, S., Bolatto, A. D., Sandstrom, K., et al. 2005, Astrophysical Journal Letters, 632, L103

Stone, R. P. S. & Baldwin, J. A. 1983, Monthly Notices of the Royal Astronomical Society, 204, 347

Straka, W. C. & Lada, C. J. 1975, Astrophysical Journal, 195, 563

Strom, R. C. 1996, in IAU Colloq. 145: Supernovae and Supernova Remnants, ed. McCray, R. and Wang, Z. (Cambridge University Press), 333–+

Stupar, M., Parker, Q. A., & Filipović, M. D. 2008, Monthly Notices of the Royal Astronomical Society, 390, 1037

Su, Y., Chen, Y., Yang, J., et al. 2011, Astrophysical Journal, 727, 43

Sugerman, B. E. K. 2005, Astrophysical Journal Letters, 632, L17

Sugerman, B. E. K., Ercolano, B., Barlow, M. J., et al. 2006, Science, 313, 196

Tam, C. & Roberts, M. S. E. 2003, Astrophysical Journal Letters, 598, L27

Tang, S. & Wang, Q. D. 2005, Astrophysical Journal, 628, 205

Temim, T., Slane, P., Arendt, R. G., & Dwek, E. 2012, Astrophysical Journal, 745, 46

Tikhonov, N. A. & Galazutdinova, O. A. 2005, Astrophysics, 48, 221

Tikhonov, N. A. & Galazutdinova, O. A. 2009, Astronomy Letters, 35, 748

Tikhonov, N. A., Galazutdinova, O. A., & Drozdovsky, I. O. 2005, Astronomy and Astrophysics, 431, 127

Torii, K., Uchida, H., Hasuike, K., et al. 2006, Publications of the Astronomical Society of Japan, 58, L11

Torres-Peimbert, S. & Peimbert, M. 1971, Boletin de los Observatorios Tonantzintla y Tacubaya, 6, 101

Trushkin, S. A. 1998, Bull. Special Astrophys. Obs., 46, 62

Tsunemi, H., Miyata, E., Aschenbach, B., Hiraga, J., & Akutsu, D. 2000, Publications of the Astronomical Society of Japan, 52, 887

Tüllmann, R., Breitschwerdt, D., Rossa, J., Pietsch, W., & Dettmar, R.-J. 2006a, Astronomy and Astrophysics, 457, 779

Tüllmann, R., Pietsch, W., Rossa, J., Breitschwerdt, D., & Dettmar, R. 2006b, in ESA Special Publication, Vol. 604, The X-ray Universe 2005, ed. A. Wilson, 415–+

Tüllmann, R., Pietsch, W., Rossa, J., Breitschwerdt, D., & Dettmar, R.-J. 2006c, Astronomy and Astrophysics, 448, 43

Tully, R. B. & Fisher, J. R. 1988, Catalog of Nearby Galaxies (Cambridge, UK: Cambridge University Press)

Tully, R. B., Rizzi, L., Dolphin, A. E., et al. 2006, Astronomical Journal, 132, 729

Uchiyama, Y. 2011, On behalf of the Fermi LAT collaboration, ArXiv e-prints

Uomoto, A. 1986, Astrophysical Journal Letters, 310, L35

Urosevic, D., Duric, N., & Pannuti, T. 2003a, Serbian Astronomical Journal, 166, 61

Urosevic, D., Duric, N., & Pannuti, T. 2003b, Serbian Astronomical Journal, 166, 67

Urošević, D. & Pannuti, T. G. 2005, Astroparticle Physics, 23, 577

Urošević, D., Pannuti, T. G., Duric, N., & Theodorou, A. 2005, Astronomy and Astrophysics, 435, 437

Urošević, D., Vukotić, B., Arbutina, B., & Sarevska, M. 2010, Astrophysical Journal, 719, 950

van den Bergh, S. 1973, Publications of the Astronomical Society of the Pacific, 85, 335

van den Bergh, S., Li, W., & Filippenko, A. V. 2003, Publications of the Astronomical Society of the Pacific, 115, 1280

Van Dyk, S. D., Li, W., & Filippenko, A. V. 2003, Publications of the Astronomical Society of the Pacific, 115, 1289

Vink, J. 2005, in AIP Conf. Proc. 774: X-ray Diagnostics of Astrophysical Plasmas: Theory, Experiment, and Observation, ed. R. Smith, 241–251

Vink, J. 2006, ArXiv Astrophysics e-prints

Wadadekar, Y., Casertano, S., Hook, R., et al. 2006, Publications of the Astronomical Society of the Pacific, 118, 450

Walcher, C. J., van der Marel, R. P., McLaughlin, D., et al. 2005, Astrophysical Journal, 618, 237

Wang, Z.-R. 1996, in IAU Colloq. 145: Supernovae and Supernova Remnants, ed. R. McCray & Z. Wang, 323

Weiler, K. W. & Panagia, N. 1978, Astronomy and Astrophysics, 70, 419

Weisskopf, M. C., Brinkman, B., Canizares, C., et al. 2002, Publications of the Astronomical Society of the Pacific, 114, 1

Wheeler, J. C. 1996, in NATO ASIC Proc. 477: Evolutionary Processes in Binary Stars, ed. R. A. M. J. Wijers, M. B. Davies, & C. A. Tout, 307–+

Wheeler, J. C. & Benetti, S. 2000, Supernovae (Springer: New York), 451–470

Whiteoak, J. B. & Gardner, F. F. 1977, Australian Journal of Physics, 30, 187

Williams, B. F., Dalcanton, J. J., Dolphin, A. E., Holtzman, J., & Sarajedini, A. 2009a, Astrophysical Journal Letters, 695, L15

Williams, B. F., Dalcanton, J. J., Seth, A. C., et al. 2009b, Astronomical Journal, 137, 419

Williams, B. F., Dalcanton, J. J., Stilp, A., et al. 2010, Astrophysical Journal, 709, 135

Williams, B. J., Blair, W. P., Blondin, J. M., et al. 2011, Astrophysical Journal, 741, 96

Williams, R. M., Chu, Y.-H., Dickel, J. R., et al. 2005, Astrophysical Journal, 628, 704

Williams, R. M., Chu, Y.-H., & Gruendl, R. 2006, Astronomical Journal, 132, 1877

Wilms, J., Allen, A., & McCray, R. 2000, Astrophysical Journal, 542, 914

Wilson-Hodge, C. A., Cherry, M. L., Case, G. L., et al. 2011, Astrophysical Journal Letters, 727, L40

Windhorst, R. A., Taylor, V. A., Jansen, R. A., et al. 2002, Astrophysical Journal Supplement Series, 143, 113

Woltjer, L. 1972, Annual Review of Astronomy and Astrophysics, 10, 129

Woosley, S. E. 1990, in Supernovae, ed. A. G. Petscheck (New York: Springer-Verlag), 182–212

Xu, J., Wang, J., & Miller, M. 2011, Astrophysical Journal, 727, 81

Zang, Z., Warwick, R. S., & Meurs, E. J. A. 1997, Irish Astronomical Journal, 24, 45

Zwicky, F. 1938, ApJ, 88, 28

Zwicky, F. 1939, Proceedings of the National Academy of Science, 25, 338